

Crystal Structure of Transition Metal Coordination Polymers and Their Applications

THESIS SUBMITTED FOR THE DEGREE OF
DOCTOR OF PHILOSOPHY



By

SRIKANTRA JANA, M. Tech (CSPT)

DEPARTMENT OF CHEMISTRY

JADAVPUR UNIVERSITY

KOLKATA -700032, INDIA

2021

Dedicated to

Dearest AND Nearest

**Prof. (Dr.) C. Sinha, Ph. D.,
Professor,
Department of Chemistry,
Inorganic Chemistry Section**



**JADAVPUR UNIVERSITY
KOLKATA - 700 032, I N D I A
Telephone: 91+033+ 2414-6666.
Ext.2453 (O),
Mobile: +91-7044231277
e-mail: crsjuchem@gmail.com**

CERTIFICATE FROM THE SUPERVISOR

This is to certify that the thesis entitled “*Crystal Structure of Transition Metal Coordination Polymers and Their Applications*” submitted by *Mr. Srikanta Jana*, M.Tech., who got his name registered on *12.02.2018 (Registration No.- SCHEM1107418)* for the award of Ph.D. (Science) degree of Jadavpur University, is absolutely based upon his own work under the supervision of Dr. Chittaranjan Sinha, Professor, Department of Chemistry, Jadavpur University, Kolkata-700 032 and that neither this thesis nor any part of it has been submitted for either any degree / diploma or any other academic award anywhere before.

It is also certified that he has fulfilled all the requirements of the regulations relating to the nature and period of research.

C. Sinha

(Supervisor)

Declaration

I declare that this written submission suggests my creative approaches in my own words and where other's ideas have been included. I have properly cited with suitable reference from the authentic sources. I also declare that I have adhered to all origins of academic principle and honesty and have not misled or fabricated or falsified any approach/ data/ origin in my submission. I understand such violation of the above will cause for disciplinary action by University and can evoke penal action from the sources which have thus not been properly cited or from whom proper permission has not been taken when needed.

Date:

Srikanta Jana

Reg. no. **SCHEM1107418**

Index No. **74/18/Chem/25**

Acknowledgement

In the very beginning, I would like to take the opportunity to convey my deepest gratitude to my research supervisor, Prof. Chittaranjan Sinha, for his continuous precious guidance, support, and motivation throughout my Ph.D. tenure. I greatly admire his valuable guidance has propelled my research attitude in a forward direction. It has been an immense opportunity for me to work under his supervision. I understand that his inspiring guidance and intellectual support has assisted me to design and fulfil several research projects successfully. Thank you very much Sir for all your constant efforts, trust in me and most importantly for being such a wonderful guide at every stage of my Ph.D. career.

I am also extremely thankful to my research advisory committee (RAC) members, Prof. Tapan Kanti Paine (Subject Expert, School of Chemical Science, IACS, Kolkata), Prof. Swapan K Bhattacharya (Chairman, JU, Kolkata, HOD, Dept. of Chemistry) and Prof. Chittaranjan Sinha (Supervisor, JU, Kolkata, Dept. of Chemistry) for their valuable suggestions, advices and support during the annual RAC meetings. I am also grateful to Prof. Chittaranjan Sinha (JU, Kolkata, Former HOD, Department of Chemistry) and all other faculty members of the department of chemistry for being approachable for any assistance and maintaining such research friendly environment in the department.

I sincerely thank all the collaborators – especially Dr. Partha Pratim Ray (Department of Physics, Jadavpur University, Kolkata), Prof. Ayan Datta (School of Chemical Sciences, IACS, Kolkata), Prof. Sachindranath Das (Department of Instrumentation Science, Jadavpur University, Kolkata), Prof. M. Salah El Fallah (Universitat de Barcelona, Martí i Franquès, 1-11, 08028-Barcelona, Spain), Prof. Debasis Das (Department of Chemistry, University of Calcutta), Prof. Dipankar Mandal (Institute of Nano Science and Technology, Mohali), Prof. Ennio Zangrando (University of Trieste, Via L. Giorgieri 1, 34127 Trieste, Italy), and Prof. Takashiro Akitsu (Department of Chemistry, Tokyo University of Science, Japan) who assisted me in completion of research work. It has been a great privilege to come in contact with Prof. Subrata Mukherjee, Dr. Md. Hedayetullah Mir, Mr. Partha Mitra and Dr. Bhibhutibhuson show, I am delighted for their great contributions.

It has been a great pleasure for me to be a part of the Research group of Prof. Sinha and I am extremely grateful to all the past and present members of the team. Especially, I would like to thank Dr. Suwendu Maity, Dr. Souvik Pandey, Dr. Chiranjit Patra, Dr. Faruk

Ahmed, Dr. Anup Kr. Bhanja, Dr. Debashis Mallick, Dr. Kuheli Das, Dr. Chandana Sen, Dr. Nilima Sahu, Dr. Bharati Chowdhury, Dr. Basudeb Dutta, Dr. Kaushik Naskar, Dr. Sunanda Dey, Sukanya Paul, Angeera Chandra, Suprava Bhunia, Manik Shit, Arup Adak, Gurupada Bairy, Shambhu Bera. Thank you very much all for their significant co-operation, help and providing eco-friendly environment in the lab.

I would like to convey my deepest gratitude and regards to all of my school teachers of Ma Saradamoyee Siksha Sadan, Ichhabari High School and Contai High School especially Tarun master, Tuhin sir, Himankshu sir, Biring sir, Ashish sir who have encouraged me throughout different stages of life. I am grateful to all the professor especially S. B sir, A. S sir, C. K. B. sir of Ramakrishna Mission Vivekananda Centenary College, Rahara, Dept. of Chemistry for their constant support and motivation to pursue higher study. I am thankful to 'Be and Make Students Home' (Estd 2010) especially Suven Bhowmick and Rina Bhowmick for giving me opportunity to stay there during my Bachelor Degree. I would like to express my sincere regards towards all the faculty members of University of Delhi, CSPT, especially Rawat sir, Kapil sir and Sujata madam for their lessons and support during my Masters study.

I acknowledge Council of Scientific & Industrial Research (CSIR) EMR-I, Govt. of India for providing me fellowship. I would also like to thank American Chemical Society (ACS), Royal Society of Chemistry (RSC), Elsevier, Wiley, for the various research articles that I managed to publish during the tenure of my Ph.D.

I wish to thank all my friends and seniors especially, Antara, Nikita, Malika, Debashis, Pabitra, Raj, Santanu, Suvo, Rahul, Suhana, Krittis, Samik, Susanta, Moti, Abhijit, Namit, Perwej, Kunal, Kuntal, Chotan, Sayantan da, Joydeep da, Apurba da, Amit da, for their constant support and help at different stages of my life. Last but not the least; I am really grateful to my whole family, my parents, my sisters, brothers, Uncles, and Aunties who stood beside me at every moment of my life so far. Without their sacrifices, motivation, and support, I would not have reached here.

Date:

Srikanta Jana

Contents

	Pages
1. Introduction	1-33
1.1. Coordination Polymers	1
1.2. Crystal Engineering	5
1.3. Supramolecular Chemistry	7
1.4. Supramolecular Interactions	10
1.5. Applications of CPs	12
1.6. Schottky Diode and Schottky Barrier	14
1.7. Dielectric and Dielectric polarization	15
1.8. Supercapacitor	16
1.9. Catalyst and Catalysis	18
1.10. Magnetism	19
1.11. Characterization Technique	20
1.12. Aim and Scope of the Dissertation	21
1.13. References	24
2. Influence of Axial Linkers on Polymerization in Paddle Wheel Cu(II) Coordination Polymers for the Application of Optoelectronics Devices	34-58
Abstract	34
2.1. Introduction	35
2.2. Results and Discussion	50
2.3. Experimental Section	52
2.4. Conclusion	52
2.5. References	52
3. Studies on Magnetic and Dielectric Properties of Antiferromagnetically Coupled Dinuclear Cu(II) in one Dimensional Cu(II) Coordination Polymer (CP)	59-77
Abstract	59
3.1. Introduction	60
3.2. Results and Discussion	61

3.3. Experimental Section	70
3.4. Conclusion	71
3.5. References	72
4. Tetrameric and Polymeric Zn(II) Coordination Complexes of 4-Diallylaminobenzoic Acid and their Applications in the Electroreduction of CO₂ and Schottky Diode Behavior	78-102
Abstract	78
4.1. Introduction	79
4.2. Results and Discussion	80
4.3. Experimental Section	91
4.4. Conclusion	93
4.5. References	93
5. Carboxylato bridging Cu(II) coordination polymer : Structure, magnetism and catalytic reduction of nitrophenols	103-122
Abstract	103
5.1. Introduction	104
5.2. Results and Discussion	105
5.3. Experimental Section	114
5.4. Conclusion	117
5.5. References	117
6. A Cu(II)-Metal Organic Framework with tetranuclear core : Structure, Magnetism and Supercapacitor Activity	123-144
Abstract	123
5.1. Introduction	124
5.2. Results and Discussion	125
5.3. Experimental Section	134
5.4. Conclusion	136
5.5. References	136
7. Summary of Research Work	145-150
7.1. Summary	145

Abbreviations

CP	Coordination Polymer
MOF	Metal-Organic Framework
PCP	Porous Coordination Polymer
ICP	Intercatenated Coordination Polymer
HDABA	4-Diallylamino-benzoic acid
4,4'-BPY	4,4'-Bipyridine
PYZ	Pyrazine
5-N-IPA	5-nitroisophthalic acid
4-APY	4-aminopyridine
H ₃ BTC	1,3,5-benzenetricarboxylic acid
DMF	N,N'-dimethylformamide
MeOH	Methanol
EtOH	Ethanol
THF	Tetrahydrofuran
DCM	Dichloromethane
DMSO- <i>d</i> ₆	Dimethyl sulfoxide- <i>d</i> ₆
Et ₃ N	Triethylamine
NaH	Sodium hydride
FESEM	Field Emission Scanning Electron Microscopy
TGA	Thermo-gravimetric Analysis
NMR	Nuclear Magnetic Resonance
FT-IR	Fourier transform infra-red spectroscopy
UV-Vis	Ultraviolet-visible
PXRD	Powder X-Ray Diffraction
TDDFT	Time-Dependent Density Functional Theory
SBD	Schottky Barrier Diode
ITO	Indium tin oxide
MS	Metal-Semiconductor
SCLC	Space-Charge-Limited-Current
eV	Electronvolt
g	Gram
mg	Milligram
h	Hours
min	Minutes
Sec	Seconds
mL	Milliliter
mM	Millimolar
mol	Moles
RT	Room Temperature

1.1 Coordination Polymers

1.1.1 Overview

For the last few decades, there has been enormous progress in research on coordination polymers (CPs).¹⁻³ Coordination polymers have drawn a great deal of attention from the researchers because of its diverse application and has proved to be useful because of its flexible architecture, tunable chemical structure, high surface area and high pore volume, multifunctional properties, etc. The applicability of CPs can be seen in many fields such as control and treatment of gaseous pollutants, such as volatile organic compounds (VOCs), through capture, gas storage, catalysis, photocatalysis.⁴⁻⁶ Electrolytic production of H₂ gas is also a very important application of CPs in generating renewable energy. In due course of producing CPs there has been many challenges for e.g high cost of synthesis, poor selectivity, and also difficulty in regeneration. On this objective our work mainly focusses on the use of the CPs in such a way that it can be regenerated easily and also there should be a greener approach in performing different applications.⁷⁻¹⁰

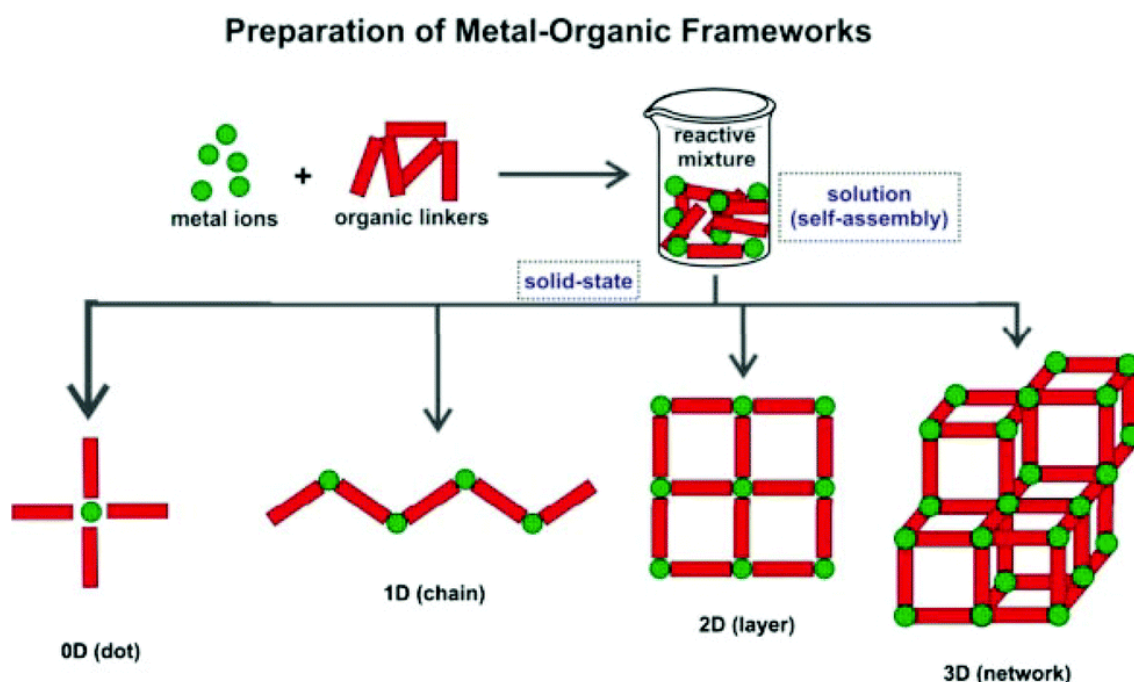


Figure 1.1 Illustration of different dimensional MOFs/CPs formation (1D, 2D and 3D) from the same primary building units (PBUs).¹⁰ Reprinted with permission.

Metal–organic frameworks (MOFs) represent a class of porous coordination polymers (CPs) that consist of metal ions or metal clusters linked together by organic bridgers (neutral, cationic or anionic).¹¹⁻¹³ The CPs/MOFs are crystalline in nature and are synthesized mainly

by self-assembly process (Figure 1.1). The high surface area and excellent physical and chemical properties make it a future precursor for development of advanced material.¹⁴⁻¹⁶ Although most of the reported MOFs in the literature are non-conducting, crystalline ordered forms of inorganic-organic hybrid materials containing single metal or metal clusters extended by the coordination of ligands (e.g. neutral or anionic linkers) with repeating coordination entities extending in one, two and three (1D, 2D and 3D)-dimensional array through various covalent and non-covalent interactions.¹⁷⁻¹⁸ According to IUPAC, its definition is “A coordination compound continuously extending in 1, 2 or 3 dimensions through coordination bonds.”¹⁹⁻²⁰

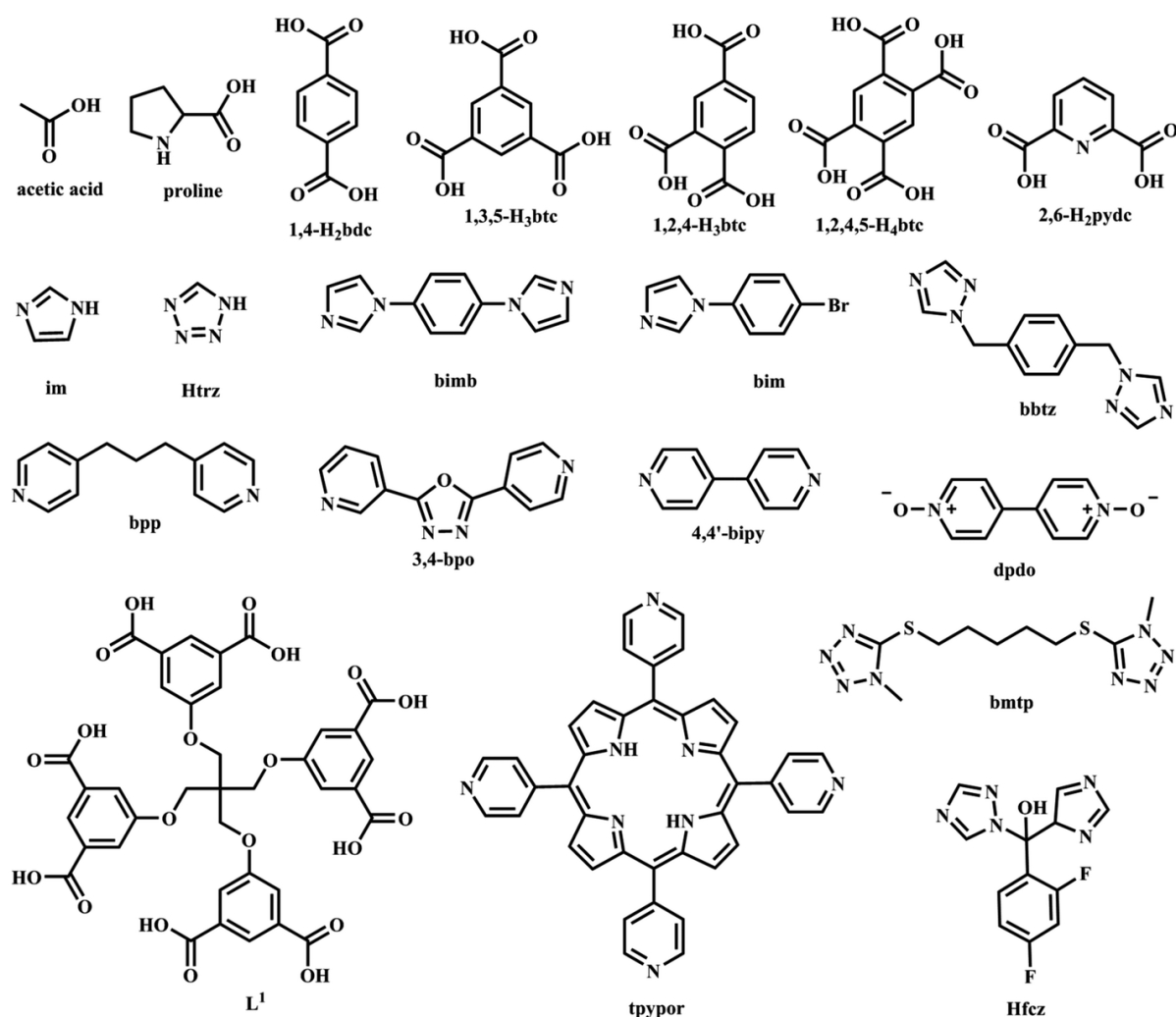


Figure 1.2 Literature reported organic linkers used to construct CPs/MOFs.²¹ Reprinted with permission.

The development of coordination compounds dates back when Warner in 1913, was awarded the Noble Prize for the introduction of coordination compounds as a part of Inorganic

chemistry. It was established that coordination compounds were connected through coordinate bonds. With researchers investigating and experimenting paved way for the development of **much** scientific advancement in the field of coordination chemistry. The Coordination Polymers were introduced by J.C. Bailar with the originating of relationship between organic polymers and inorganic coordination polymeric species.¹⁷ He established rules for the architecture and the crucial properties of new species which linked to organic ligands and metal ions. The design and synthesis of metal-organic coordination polymers have been explored in various fields of application gas storage, separation of gases and industrially important liquids, carbon capture and conversion, electrical conductivity, drug delivery, heterogeneous catalysis, **ion and molecular sensing (Figure 1.3)** etc.²²⁻²⁶

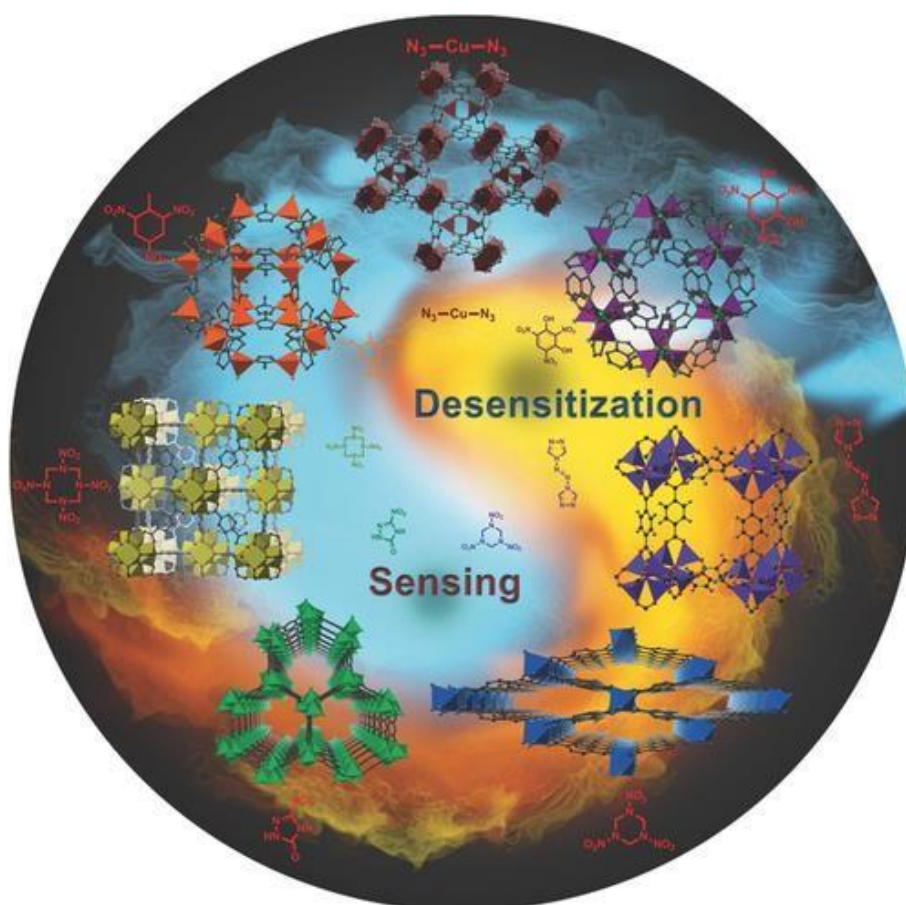


Figure 1.3 Coordination Polymers for sensing and desensitization of high-energy materials.²⁷ Reprinted with permission.

The transition metals are the most used metal precursor in building coordination polymers and the organic part being the linkers forming clusters with different geometry around the central metal atom. Literature reported organic linkers used to construct CPs/MOFs are summarized in Figure 1.2.

The versatility of CPs are initially studied and was found that by varying the metal atoms and even by changing the size of the organic linkers there were difference in the functionality and topology of the newly designed CPs.²⁸⁻²⁹ Thus, carboxylate linkers or the Nitrogen linker group 2,2 0-bipyridine BIPY are commonly used organic linkers and their derivatives became popularized in the field of coordination chemistry. They were initially used for the storage of gas. But they require a favourable condition for the maximum utilisation of the surface area and thus increase the storage capacity. Thus there has been advancement in the last 15 years for modifying the plans of coordination polymers and their drawbacks.³⁰

Omar M Yaghi and coworkers have developed the term 'reticular chemistry' for understanding the molecular chemistry and its accuracy in making and breaking bonds of a solid-state framework structure.³¹

In 1995, MOF-5 ($Zn_4O(BDC)_3$, where BDC^{2-} =1,4-benzodicarboxylate) has been first reported by Yaghi et al and with this the development of a new polymer having robust, high surface area for sorption like that of carbontubes was introduced. Since then MOFs have turn into a hottest topic in material chemistry and it has experienced a unique growth over the past few decades.³²⁻³³

In the earlier stage, researchers are interested in controlling to optimize several structural factors like (i) the large pore aperture, (ii) the high surface area and (iii) the strong metal-based adsorption property in metal-organic frameworks (MOFs) or porous coordination polymers (PCPs) for gas storage material.³⁴⁻³⁵

In the year 1998, Kitagawa et al. have been generally classified as PCPs (Figure 1.4) based on their generation. Moreover, the classified PCPs are namely - 1st, 2nd and 3rd generations (Figure 1.4).³⁶⁻³⁷ In the case of 1st generation materials, upon exclusion of the occluded guest molecules from the networks, this indicates that the frameworks have been completely collapsed. The 2nd generation PCPs is found to be stable and rigid after the removal of the guest molecules from the framework. Moving apart 2nd generation to the 3rd generation materials are flexible and dynamic nature that can reversibly remove guest molecules from the framework.³⁸⁻⁴⁰

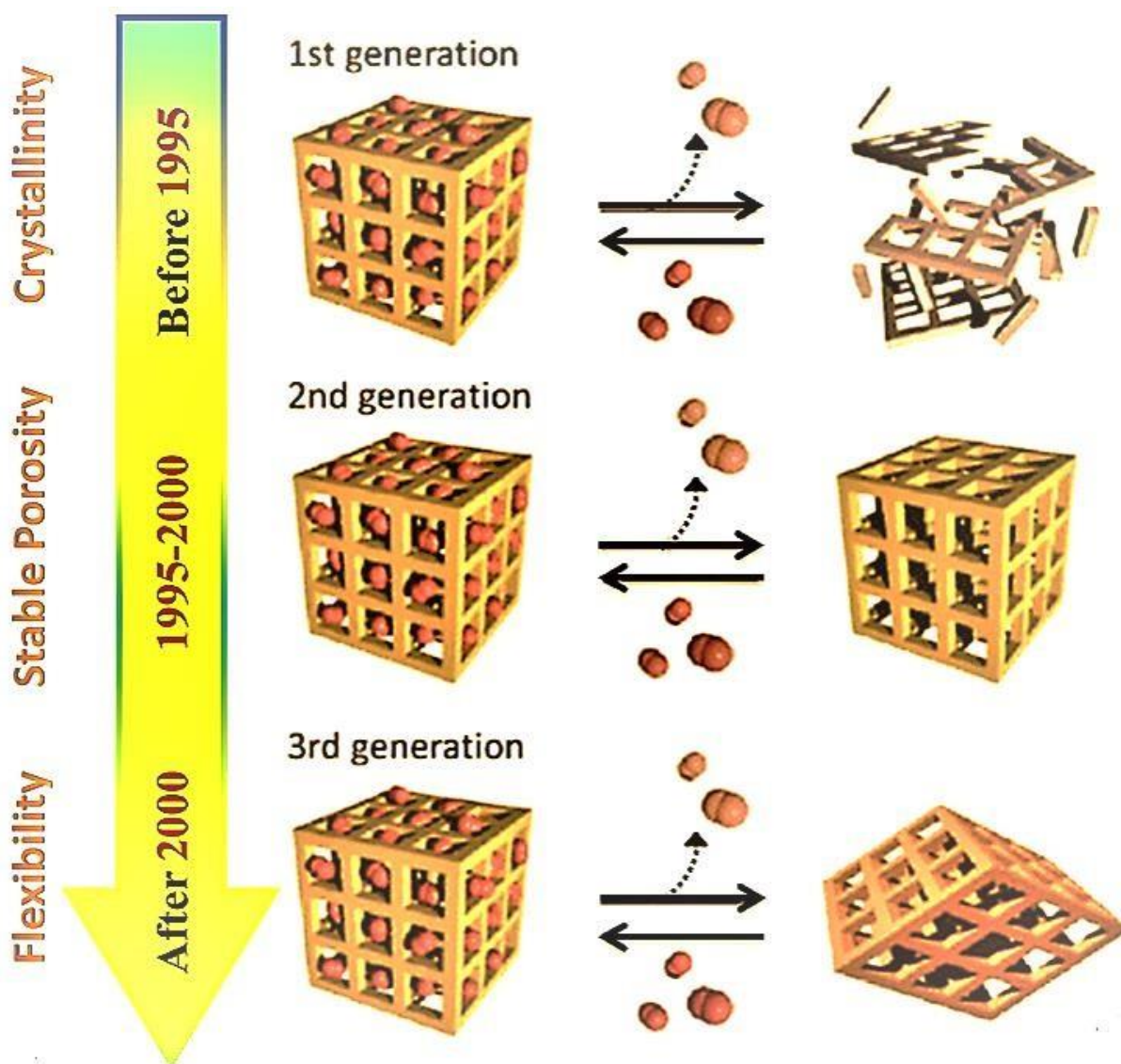


Figure 1.4 Classifications of PCPs by Kitagawa *et al.*

1.2 Crystal Engineering

R. Pepinsky in 1955 used the term Crystal Engineering but it was Gerald Schmidt who utilized it in the photodimerization of cinnamic acids.⁴¹⁻⁴² Moreover, crystal engineering has been linking between the molecular crystallography and chemistry. Chemistry is the science of crystallographic skill to control the associations of molecules into a solid crystalline form (Figure 1.5).⁴³

In the earlier stage of crystal engineering is solely based on organic systems, but from the late 1990s, a large number of organic-inorganic hybrid compounds have been explored widely in various structural architecture and topologies (Figure 1.6).⁴⁴⁻⁴⁵

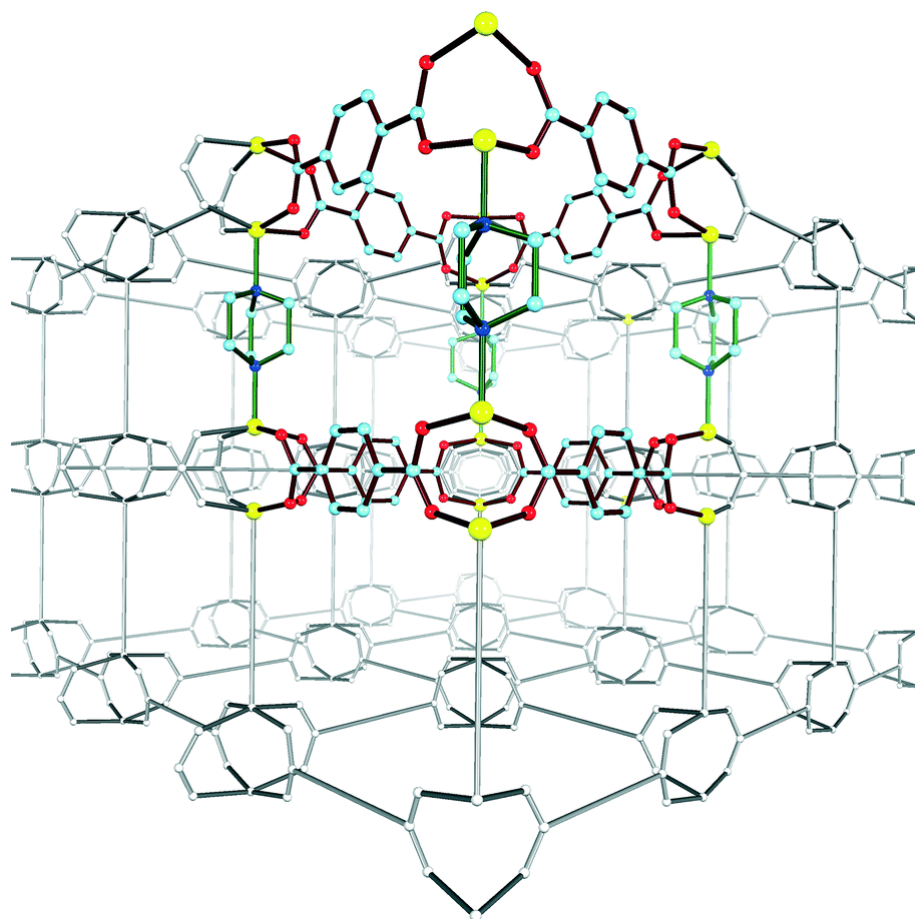


Figure 1.5 Crystal structure of paddlewheel pillared MOF ($\text{Zn}_2(\text{NH}_2\text{BDC})_2\text{DABCO}$). Zinc (yellow), oxygen (red), carbon (light blue), nitrogen (dark blue).⁴⁶ Reprinted with permission.

The design strategy of the crystal engineering facilitates to bring material science, molecular biology and pharmaceutical science together under a single umbrella.⁴⁷ The association of such supramolecular synthon like organic molecule (linker) and inorganic (cation) into a solid-state through the non-covalent and self-assembly which is become the heart of the crystal engineering. Organic crystal engineering is mostly dealing with weak intermolecular forces like hydrogen bond, pi-pi, etc. while those are associated with constructing the metal-organic building blocks later it is familiar as inorganic crystal engineering.⁴⁸

Nowadays, inorganic crystal engineering becomes the most powerful tool which is widely utilized by the implementation of the weak intermolecular force like hydrogen bond compared to organic crystal engineering. Besides the hydrogen bonding, crystal engineering studies have explored weak intermolecular forces of aromatic π -system, for example, pi...pi and C-H...pi interactions. The roles of halogen-halogen interactions not been explored extensively as a supramolecular interaction but its importance has risen day by day. Beyond a

constructive approach, three-dimensional crystals have been rationally designed but the predictions over such 3D crystal structure are still attractive.⁴⁹⁻⁵⁰

Crystal engineering⁵¹ is one of the rapidly growing topics that play a major role in the appearance of several high impacts international scientific journals like *Crystal Growth and Design* (American Chemical Society) and *CrystEngComm* (Royal Society of Chemistry). To reflect the importance of this modern topic, two new open access journals have been created IUCrJ from the International Union of Crystallography and Crystals from MDPI.

1.3 Supramolecular Chemistry

Supramolecular chemistry is the modern domain in chemical science it deals with many chemical systems composed of a discrete number of molecules. In the early stage, this term has highlighted the interactions among macromolecules and the arrangements of enzyme and membrane systems. In 1987, Donald J. Cram, Jean-Marie Lehn, and Charles J. Pedersen has been shared Nobel Prize in Chemistry for establishing this area.⁵² In this consequence, Jean-Marie Lehn proposed a modern sense about the supramolecular chemistry as “chemistry of the intermolecular bond, covering the structure and functions of the entities formed by the association of two or more chemical species.”⁵³ Conventional molecular chemistry mostly focusing on the covalent bonds, whereas supramolecular chemistry deals with some weaker and non-covalent interactions like $\pi \dots \pi$ interactions, hydrogen bonding, metal coordination, van der Waals forces.⁵⁴

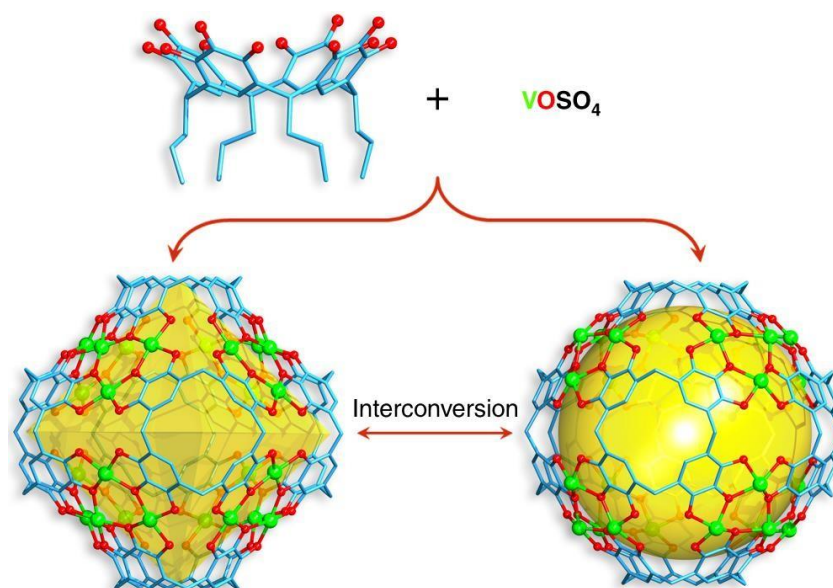


Figure 1.6 Supramolecular structure of hexameric pyrogallol[4]arene V_{24} octahedron, 24 vanadium ions and V_{24} ball from 6 PgC_3 ligands.⁵⁵ Reprinted with permission.

In the late 1990s, the field of research on supramolecular chemistry becomes more sophisticated by executing innovative ideas in the interface of electronic and biological science. During this period, several concepts like molecular self-assembly,⁵⁶ molecular recognition,⁵⁷ host-guest chemistry,⁵⁸ and mechanically-interlocked⁵⁹ molecular designs have been integrated into the supramolecular systems for several potential applications like catalysis, drug delivery, data storage, and processing, etc.

1.3.1 Molecular Self-assembly

The term ‘molecular self-assembly’ becomes more attractive in supramolecular chemistry. The classical sense regarding the self-assembly process can be defined as “The spontaneous and reversible organization of molecular units into ordered structures by non-covalent interactions.”⁶⁰ Three unique key features of self-assembly: (i) order (ii) interactions and (iii) building blocks to make a distinct concept. The non-covalent interactions like hydrogen bonds, $\pi\cdots\pi$, ionic bonds, and $C-H\cdots\pi$ and van der Waals interactions are typically integrated to assemble stable framework structure (Figure 1.7). Collectively these interactions can play a major role in harvesting materials with high stability by the large supramolecular association rather than their distinct interactions. Moreover, self-assembly can be classified into two categories, (i) intermolecular self-assembly which usually forms a supra-molecule and (ii) intramolecular self-assembly where folding conformation observed in the foldamers and polypeptides. In recent times, molecular self-assembly becomes one of the most important fields in crystal engineering, it can fix the several targets in designing of various macromolecules.⁶¹

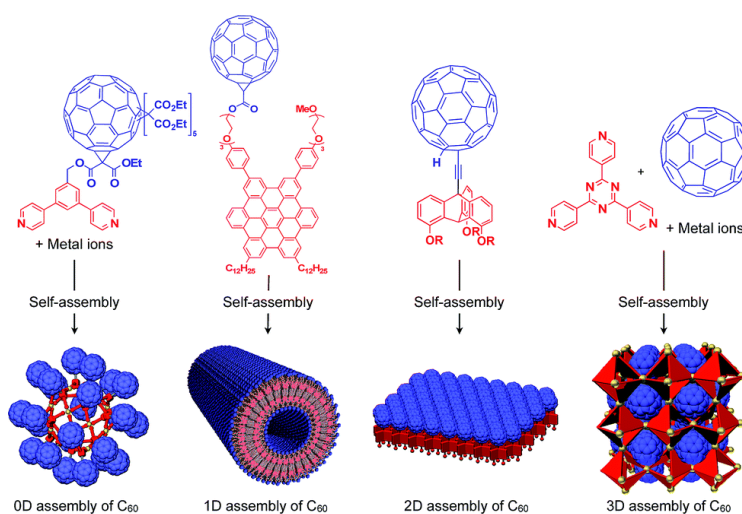


Figure 1.7 Controlled self-assembly (0D to 3D) of C₆₀ units (blue) by supramolecular scaffolds (red).⁶² Reprinted with permission.

1.3.2 Molecular Recognition

The term ‘molecular recognition’ is one of the well discussed terminologies in supramolecular chemistry so far. It refers the specific binding between two or more molecules through non-covalent interactions such as hydrogen bonding (Figure 1.8), $\pi\cdots\pi$ interactions, metal coordination, halogen...halogen interactions, van der Waals forces, etc.⁶³ Beyond such direct interaction, solvents also leading an indirect role for molecular recognition in the solution state.⁶⁴⁻⁶⁵ Most recently researchers draw their attention in designing several functional organic and inorganic artificial supramolecular systems through such molecular recognition process.⁶⁶ Dynamic molecular recognition has been studied so far for such applications as chemical sensors, catalysis, and molecular devices.⁶⁷

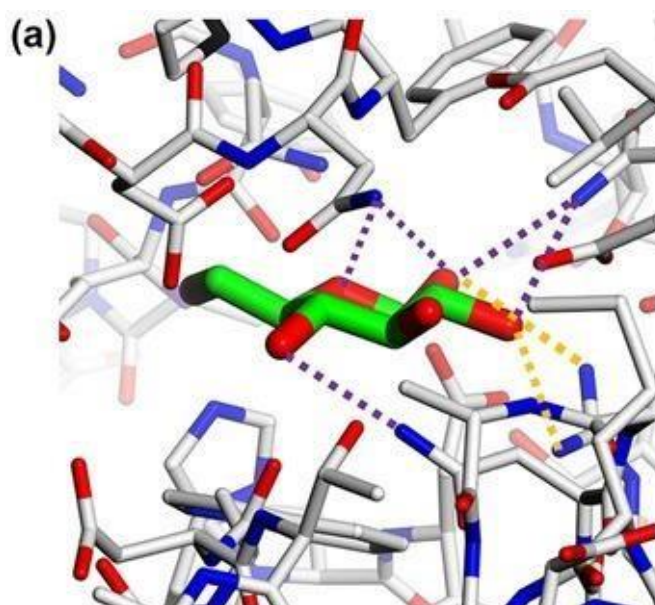


Figure 1.8 Hydrogen bonding mediated molecular recognition. a) X-Ray structure of periplasmic galactose-binding protein of glucose complexed from *E. coli* (PDB: 2GBP).⁶⁸ Reprinted with permission.

1.3.3 Host-guest Chemistry

Host-guest chemistry is a branch of supramolecular chemistry. Moreover, it combines the idea of molecular recognition and self-assembly through non-covalent bonding to maintain the 3D structures. Usually, most of the 'host' component has been considered as a larger molecule, while the smaller component is 'guest' molecule. According to Donald Cram, “The host component is defined as an organic molecule or ion whose binding sites converge in the complex...The guest component is any molecule or ion whose binding sites diverge in the

complex”.⁶⁹ In 1967, Charles Pedersen discovered a simple method of synthesizing crown ether but he had shared the Nobel Prize in Chemistry in 1987 for extensive research over crown ethers and advancement in the field of host-guest chemistry.⁷⁰

In reality, host-guest interactive forces allow the host molecule to occupy appropriate binding sites of the guest molecule to bind. To achieve the maximum stability they should orient in such a way that multiple interactions between host and guest may occur.

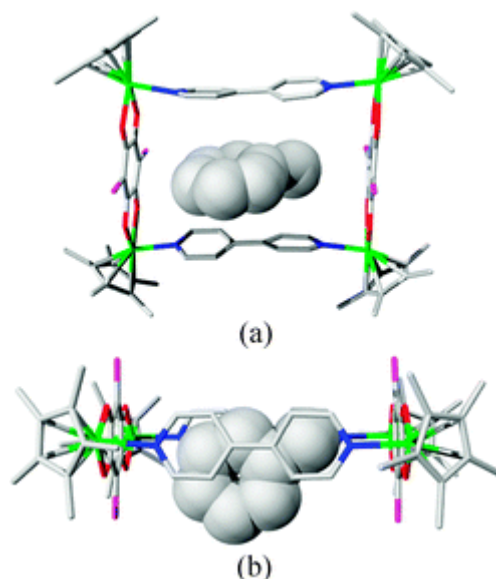


Figure 1.9 Structures of encapsulated toluene guest molecule in cation H39 host, (a) side view and (b) top view.⁷¹

For example, if the donor sites of the host molecule acquire a large number of hydrogen bonds, then the guest must enclose with an equal number of acceptor sites. Most recently, host-guest chemistry (Figure 1.9) has been extensively implemented over metal-organic frameworks (MOFs) and coordination polymers (CPs) to explore various stimuli-responsive applications such as drug delivery, photochromic device, selective gas adsorption, etc.⁷²⁻⁷⁴

1.4 Supramolecular Interactions

In general, supramolecular chemistry is an interface where supramolecular building blocks are held by a large number of supramolecular interactions or, non-covalent interactions. The term ‘supramolecular interaction’ covers by a substantial range of attractive and repulsive forces. These types of interactions stabilize many important systems like organic molecules, biological macromolecules, and the structural motif of the coordination polymers.⁷⁵⁻⁷⁶ Moreover, they have also responsible for the orientations of molecular species in crystalline

lattices. From the crystal engineering point of view, non-covalent interactive forces lead an important role in the design and synthesis of molecular crystals and also conserving the three-dimensional structure. The dynamic nature of such non-covalent forces significantly implicated in many interdisciplinary subjects like chemistry, biology, physics, and engineering.⁷⁷

Most recently, these weaker forces such as hydrogen bonding, halogen•••halogen interactions, π ••• π stacking, hydrophobic forces, van der Waals forces, and C-H••• π interactions have been widely investigated so far in designing of 3D architecture (Figure 1.10). These types of interaction along with their approximate strength indications are listed below (Table 1.1).

Table 1.1 Different types of supramolecular interactions and its stabilization energy.

Type of interactions	Energy (KJ/mol)
Ion•••Ion	100-350
Covalent	350-950
Ion•••Dipole	50-200
Dipole•••Dipole	≤ 50
Halogen•••Halogen	5-180
H-bonding	≤ 120
π ••• π	≤ 50
C-H••• π	6-13
Cation••• π	≤ 80
Anion••• π	≤ 80
Van der Waals	≤ 5
Metal•••Ligand	0-400
Hydrophobic	Hardly accessible

There are some important and general properties of weak forces regarding crystal engineering which is included below:

- The strength of acting forces may be strong, weak, or moderate. To reflect the attractive force interaction must possess energy value above $0.6 \text{ kcal mol}^{-1}$ at room temperature.

ii) The directionality of the interaction is very essential and helps in designing of several desired crystalline supramolecules.

iii) The process of nucleation and crystallization is an important factor which depends upon distance.⁷⁸

However, in our present discussion, we will focus over such supramolecular interactions summarized in **Figure 1.10** and explained their properties.

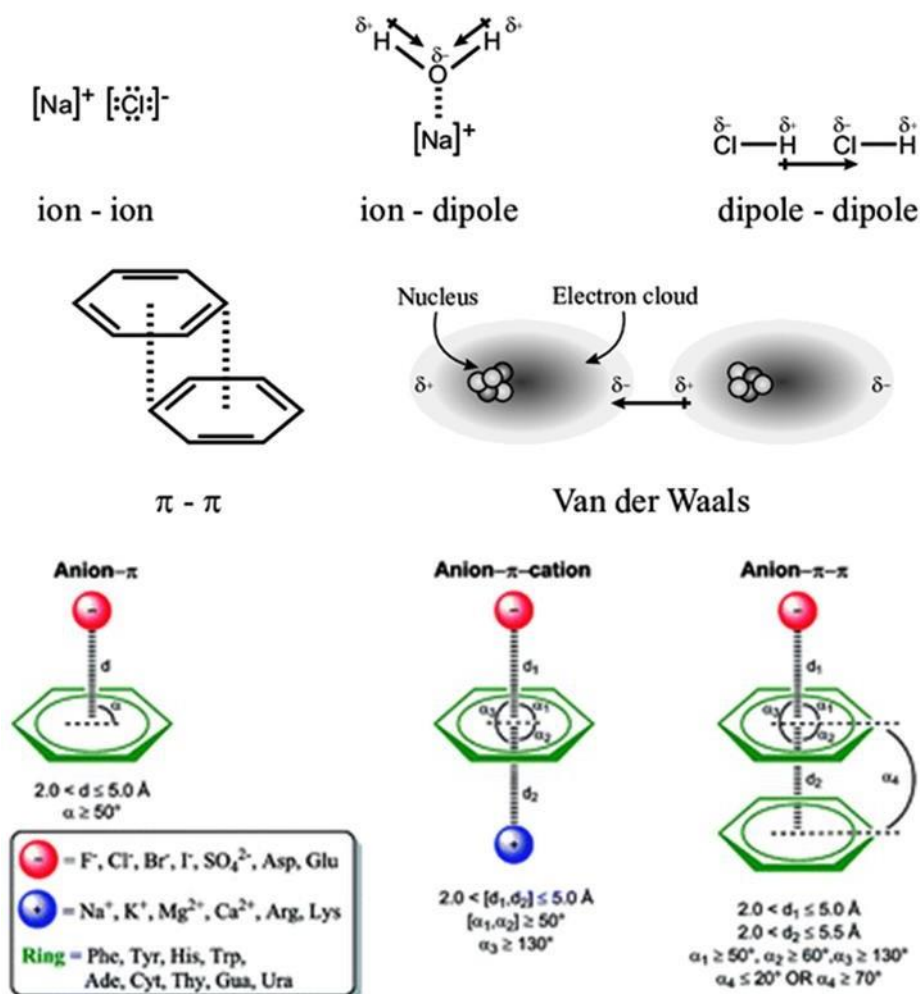


Figure 1.10 Examples of different types of supramolecular interactions.

1.5 Applications of CPs

Nowadays, the substantial growth of environmental issues like pollution, degradation, and climate change has drawn their attention to the environmentalists and analytical chemists for the remediation of such global concerns. Determination of organic (e.g. dyes, oils, pharmaceuticals products, pesticides, etc.) and hazardous inorganic pollutants (heavy metal

ions, radioactive species, oxy anions, etc.) and the capturing of such pollutants from the aquatic source are found to be the biggest concern over the past few years.

In this domain, coordination polymers/metal-organic frameworks (CPs/MOFs) become an esteemed class of material in the families of porous materials (e.g. zeolites, activated carbons, porous silica, mesoporous clay materials, etc.), for their tuneable porosity and large surface area.⁷⁹ Owing of such unique features in CP/MOF materials have been aggressively exploited in the last 20 years in various fields of applications such as gas storage and separation, sensor application, electrical conductivity, photochromic application, heterogeneous catalyst, electrochemical application, etc. shown in **Figure 1.11**.⁸⁰

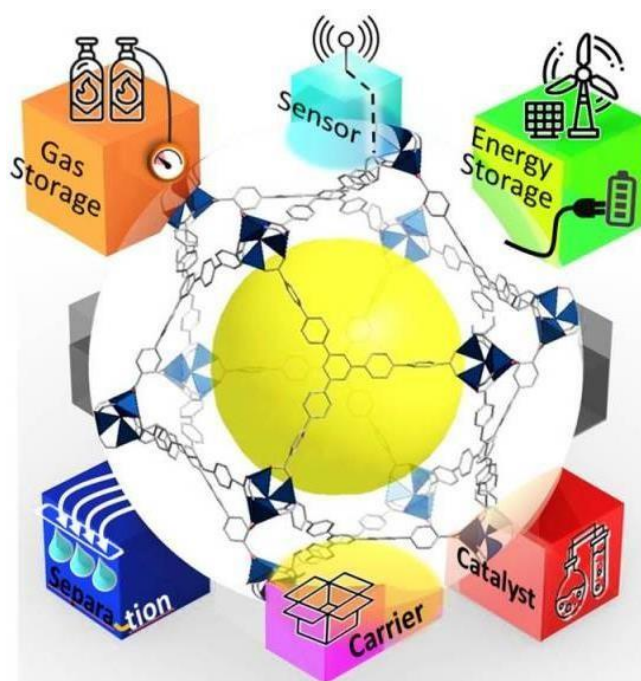


Figure 1.11 Various applications of MOFs. From Metal-Organic Frameworks – International Commission.

Although MOFs, have widely used in the above-mentioned applications, among them electrical conductivity and photochromic applications have been rarely explored so far. In this regard, electro-conductive MOFs or PCPs have been earned new opportunities to improve device performance as an energy storage application, for the remediation of the global energy crisis. In the last five years, the extensive growth of electro-conductive MOFs have been manifested by new approaches to exhibit both porosity and high electrical conductivity (**Figure 1.12**).⁸¹

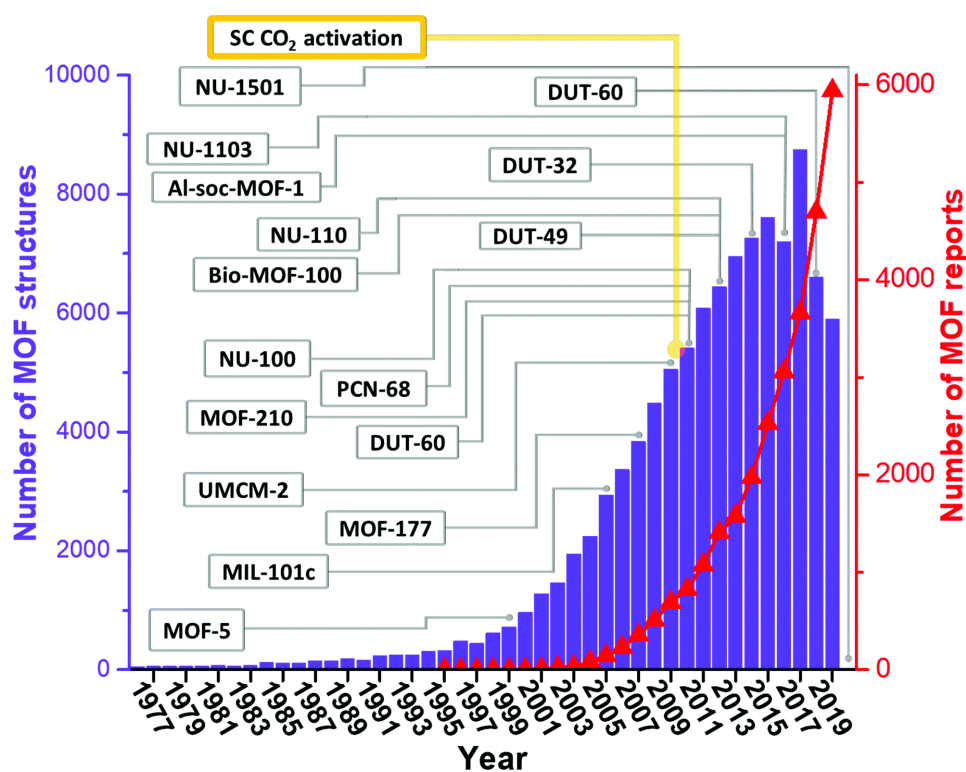


Figure 1.12 Overview of the reported metal–organic frameworks from 1977 to 2019.⁸²

Apart from MOFs, nowadays, most of the researchers are involved in the exploration of this property in CPs, which is still very scarce. Some results regarding CPs have been motivated towards the rational design of novel electro-conductive CPs by the incorporation of theoretical and experimental calculations.⁸³⁻⁸⁴

1.6 Schottky Diode and Schottky Barrier

Here we have performed Schottky diode applications by applying electrical voltage. Schottky diode is a electronic device which permits current to flow in one direction while opposes the current in the opposite direction with a high resistance.⁸⁵ Schottky diode is a kind of semiconductor which is known as hot carrier diode also and It has a low forward bias voltage. This lower bias voltage drop offers improved efficiency and switching speed of the system. In general, Schottky diode is made by generating a Schottky barrier between semiconductor and metal. In Schottky diode, cathode acts as n-type semiconductor and the metallic part behaves as anode material of the diode.⁸⁶⁻⁸⁷

The electrostatic barrier between semiconductor and metal in a diode rectifies it's property. Metal and semiconductor have different work functions which emerges the electrostatic barrier in a Schottky diode (Figure 1.13). For n type, electron transfer occur semiconductor to metal and reached equilibrium between the Fermi levels and forms a

depletion region, when the work function of metal (ϕ_m) exceeds the work function of the semiconductor (ϕ_s).⁸⁸⁻⁸⁹

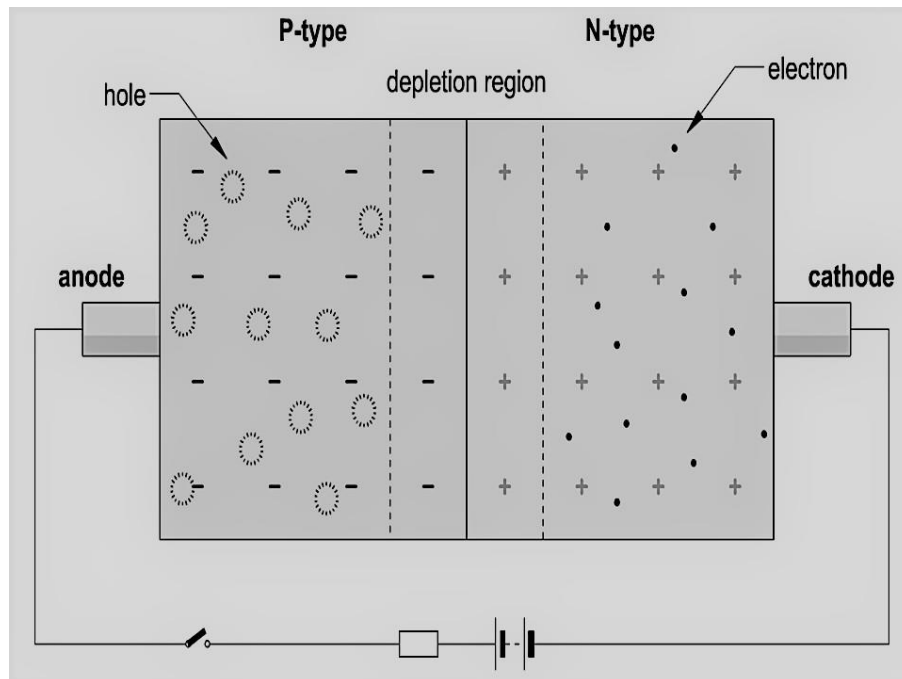


Figure 1.13 Schottky barriers and work function for semiconductors.

We can write the diffusion potential V_{do} as

$$V_{do} = \phi_m - \phi_s \quad (1)$$

For n-type semiconductor, when $\phi_m > \phi_s$, and the bands are bent upwards; the electrons have to overcome the electrostatic barrier to transfer semiconductor into metal. For p-type semiconductor, the band-bending due to no barrier to the holes motion, and an 'ohmic' contact formation taking place. When $\phi_m < \phi_s$, downwards bending of band provides an ohmic contact for a n-type semiconductor Whereas, a rectifying contact is formed for a p-type semiconductor.⁹⁰

1.7 Dielectric and Dielectric polarization

In electromagnetism, an electrical insulator has polarized when is placed in an external electrical field and such type of materials is known as dielectric material.⁹¹ Unlike electrical conductor no charges flow through the material, instead due to dielectric polarization slightly shifting of their average equilibrium positions takes place.⁹² Because of polarization, negative charges are attracted in the positive direction of the field and positive charges are attracted in

the negative direction to the field and thus an internal electric field generated that shrinks the overall electric field within the dielectric material itself.

From the classical approach of a dielectric material, each atom has negative charges cloud (electrons) which is bound by a positive point charge (proton) and when an external electric field applied, the cloud of negative charge is distorted, as shown in the figure 1.14. Using the superposition principle, this distorted negative cloud and positive point charge form a simple dipole. Dipole moment have generated due to dipole formation, dipole moment a vector quantity shown in the figure 1.14 as labeled M . Dielectric behaviour of a dielectric material is the connection between the applied electric field and the generated dipole moment of the material.

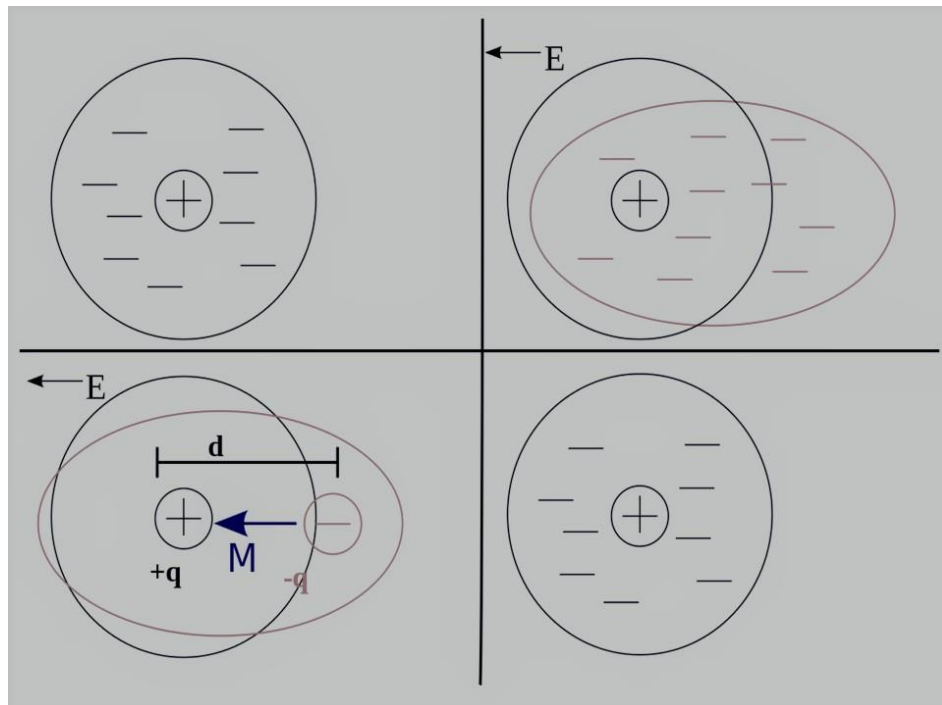


Figure 1.14 Interaction of an atom with electric field.

1.8 Supercapacitor

High capacitance value with low voltage limits bridges the gap between rechargeable batteries and electrolytic capacitors is known as supercapacitor/ultracapacitor (Figure 1.15). Storage capacity of supercapacitor is 10 to 100 times greater than electrolytic capacitors per unit volume or mass, charge transfer and receive rate is much higher than batteries, and cycling charge and discharge stability far better than rechargeable batteries.⁹³ They are used in energystorage, reformative braking, burst-mode power delivery and as power backup for static

random-access memory where fast charge/discharge cycles are required.⁹⁴ Supercapacitors use electrochemical pseudocapacitance and electrostatic double-layer capacitance where normal capacitors use the solid dielectric.⁹⁵

Carbon type electrodes are used as electrostatic double-layer capacitors (EDLCs) has much more EDLC than electrochemical pseudocapacitance, they store charge at the electrode and electrolyte interface by charge separation in a Helmholtz layer and the charge separation lies in 0.3nm–0.8 nm, which is very less compare to a conventional capacitor (Figure 1.16).

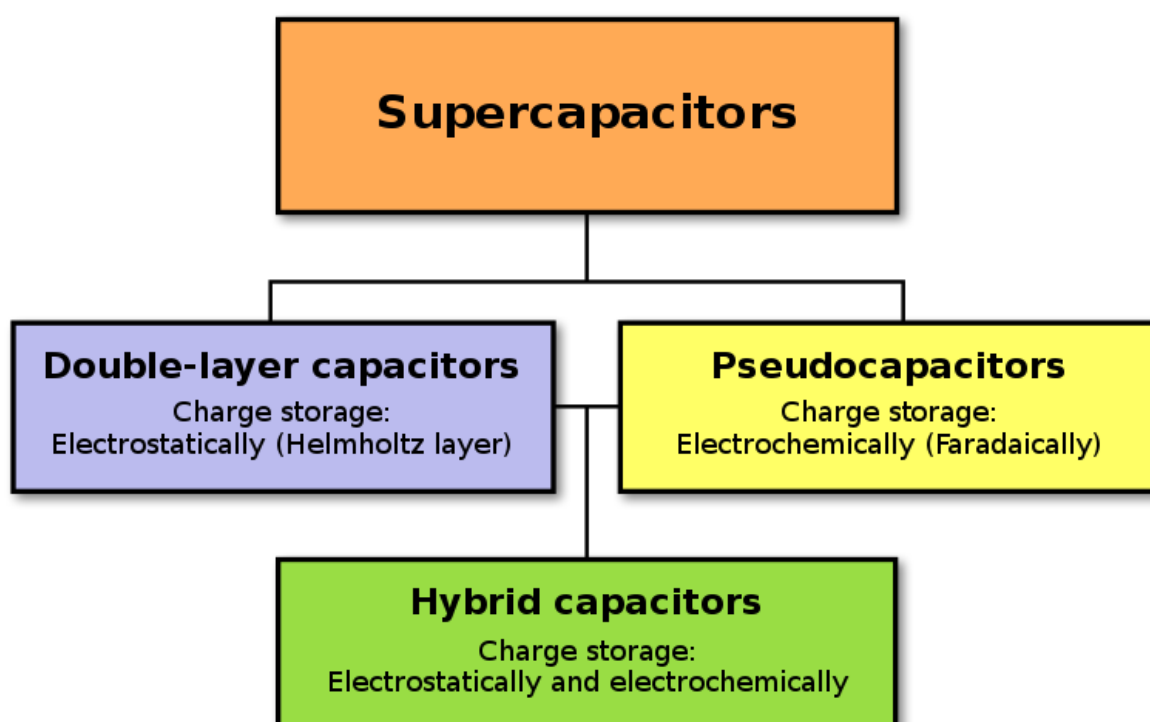


Figure 1.15 Different types of supercapacitors.

Electrochemical use metal oxide or conducting polymer or metal oxide have been used as pseudocapacitors electrodes, which has very high value of electrochemical pseudocapacitance with the electrical double-layer capacitance. Redox reactions with faradaic electron charge-transfer are responsible for pseudocapacitance. Lithium-ion capacitor which is used as hybrid capacitor electrodes has differing features: one showing typically electrostatic double-layer capacitance and the other electrochemical pseudocapacitance.



Figure 1.16 Hybrid supercapacitor application of MOF-based materials.⁹⁶ Reprinted with permission.

1.9 Catalyst and Catalysis

Catalysis is the process in which the rate of a reaction is increased by many fold by the use of a catalyst.⁹⁷⁻⁹⁸ Catalysts that participate in the reaction forms substrate with the reactant and decreases the activation energy and thus fastens the reaction without getting consumed. If the temperature and other favourable conditions are maintained, a small quantity of catalyst is sufficient. The final product is obtained easily with the regeneration of the catalyst.⁹⁹ The use of a catalyst is usually seen in about 90% of commercially produced chemical goods.¹⁰⁰ There are two types of Catalysis homogenous where phase of the catalyst and the reactant are same and heterogeneous where the reactant and catalysts are in different phase. Nowadays two important catalytic reaction such as electrochemical carbon dioxide reduction (CO_2RR) and oxygen evolution reaction (OER) have drawn great attention to scientific communities (Figure 1.17). Design of coordination polymers for CO_2RR and OER catalyst are very challenging job for researcher and also for sustainable environment. Due to structural diversity of coordination polymers/metal-organic frameworks they serve as a very good catalyst. Figure 1.17 describes electrochemical reduction of CO_2 to methanol using cobalt complex as a catalyst and another example of CP materials as a OER catalyst are given at figure 1.18.

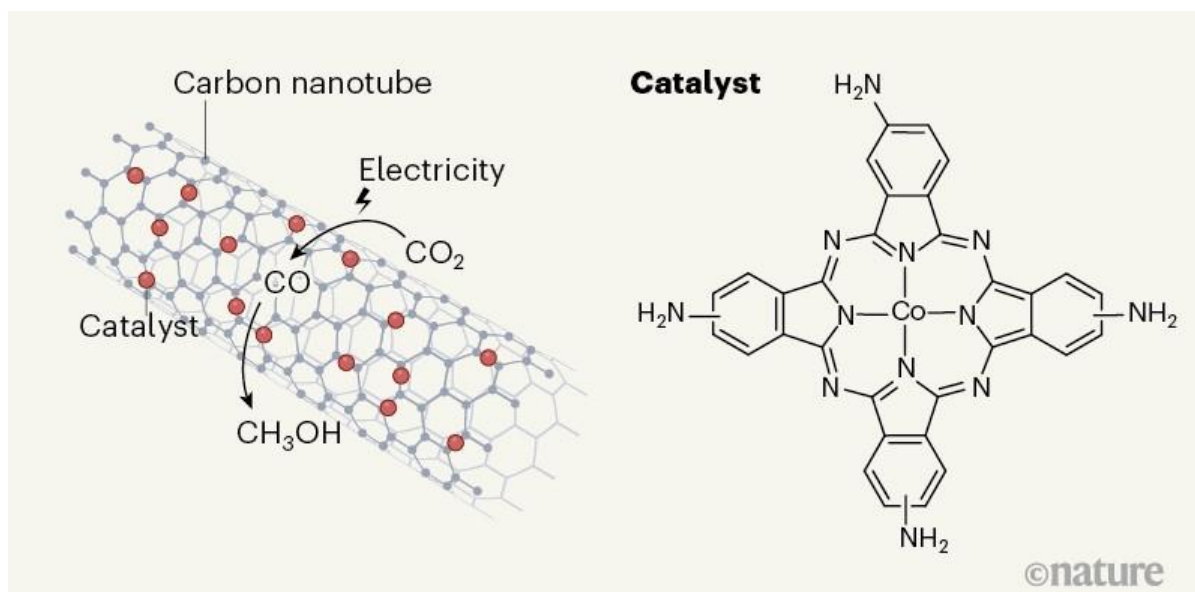


Figure 1.17 Electrochemical carbon dioxide reduction and manufacture of methanol.¹⁰¹

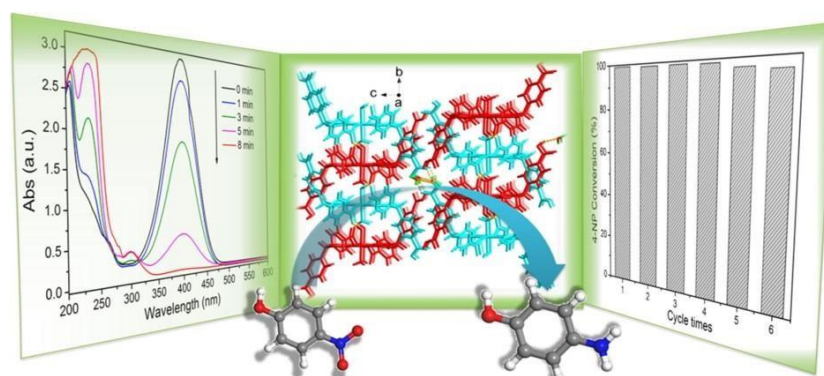


Figure 1.18 Schematic presentation of catalytic reduction of 4-nitrophenol using cobalt(II) coordination polymer.¹⁰² Reprinted with permission.

1.10 Magnetism

Magnetism arises due to the interaction of spin motion of elementary particles with the applied external magnetic field. Magnetic moment arises due to the alignment of spin of electrons in different direction.¹⁰³ The substances that interact with the applied magnetic field are called paramagnetic substances. Depending on the concentration of magnetically active ions present the paramagnetic substances can be distinguished as ferromagnetic and antiferromagnetic. Ferromagnetic substances are strongly attracted by external magnetic field. The electron spins align up in the same direction as the applied magnetic field. Due to this property even after the withdrawal of external magnetic field we observe a phenomenon called hysteresis.¹⁰⁴ Ferromagnetic substances can be permanently magnetized. Most common

example of Ferromagnetic substance is magnetite Fe_3O_4 . The usual ferromagnetism is shown by paramagnetic substances up to Curie point.

Paramagnetic substances are weakly attracted to external magnetic field. Antiferromagnetism is also observed in paramagnetic substances with metal ions whose spins are paired up in presence of external magnetic field. From the magnetic point of view coordination polymers/ metal-organic frameworks (Figure 1.19) is one of the most important magnetic materials for daily life application due to its various dimensional structural architecture and tuneable properties.

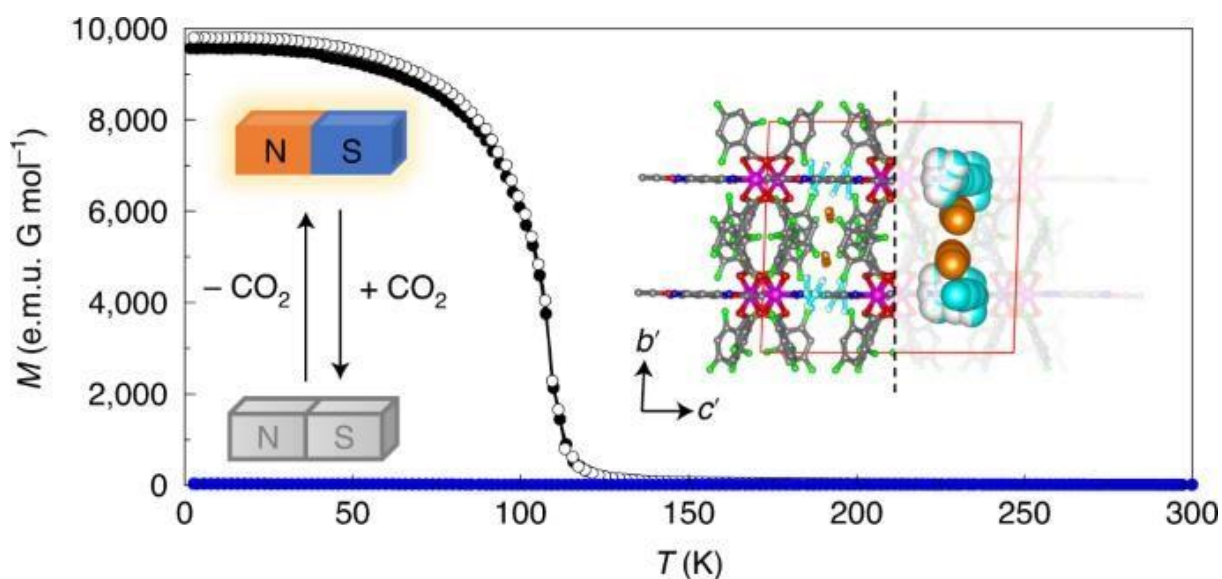


Figure 1.19 CO_2 -induced transitions between paramagnetism and ferrimagnetism of a MOF material.¹⁰⁵ Reprinted with permission.

1.11 Physicochemical Measurements

Transition metal salts in requisite form are procured and using the metal salt, suitable metal precursors are synthesized, required ligands will be prepared using standard techniques. These ligands will be used to synthesize Coordination polymers. Structural characterization will be carried out using single crystal X-Ray technique and Purity of compounds have checked by powder X-ray analysis (PXRD). Several spectral techniques and elemental analysis will be used to carry out bulk characterization. NMR spectral technique may be used for titrimetric study of composition of the complexes. IR spectra will be used to obtain some signature peak of some particular functional group. UV-Vis spectra could be useful to obtain the electronic transition. DFT calculations will be adopted to identify the electronic structure and hence the origin of the lowest energy spectral transition. Electrochemical analysis may also be carried out to gain idea about redox centers and others activity of MOFs/CPs (HER,

OER, CO₂ reduction).

1.12 Aim and Scope of the Dissertation

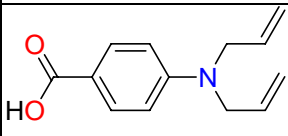
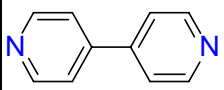
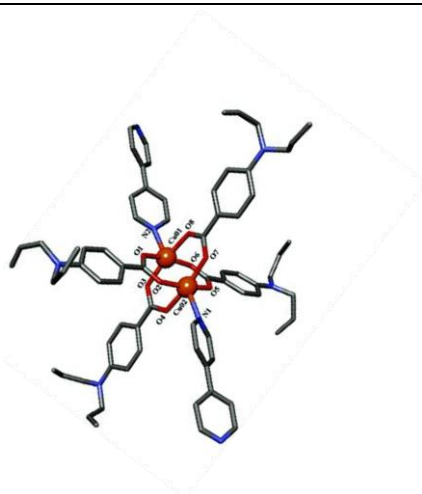
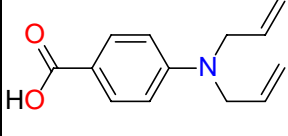
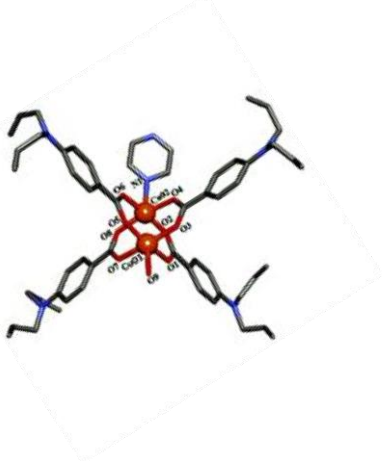
The research work presented in this thesis explores the design, synthesis and structural characterization of transitional metal based metal coordination polymers (Cu(II), Zn(II), Ni(II)). The dissertation study focuses on (i) Design and synthesis of coordination polymers of interesting structural architecture, (ii) Exploring the role of different supramolecular interactions in the production of coordination polymers, (iii) Finding out the physical significance of the supramolecular interactions in terms of their application in electrical conductivity study, magnetic and electrochemical study (iv) Photo-reactivity of coordination polymers. In this thesis work, various mono, di, tri-carboxylic acids will be employed along with multidentate nitrogen donor ligands for the formation of different dimensional coordination polymer.

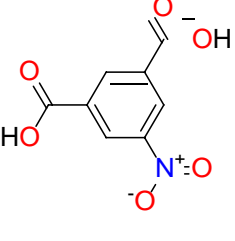
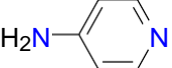
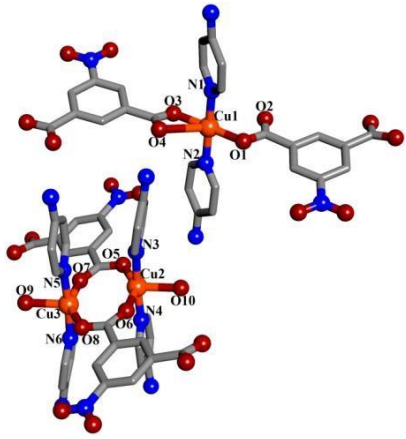
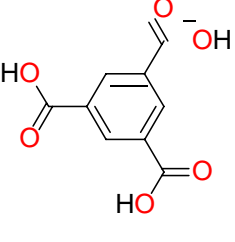
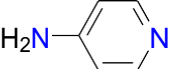
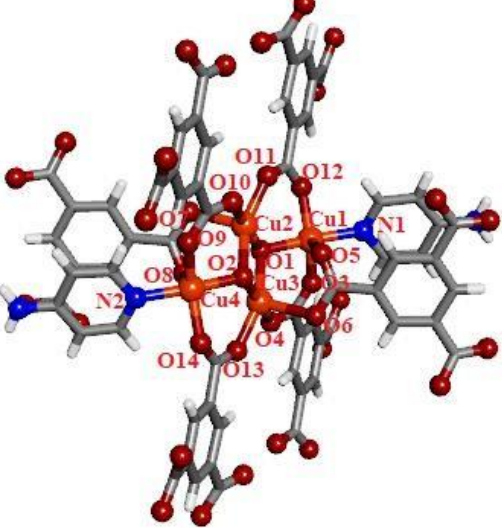
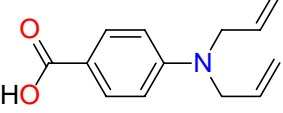
The chapter 2 describes copper based coordination polymers for electrical conductivity and magnetic study. Charge transportation taking place through space via noncovalent interactions in 0D and 1D network. In this regards the role of different supramolecular interactions in conductivity has been revealed and also metal–coordination polymer junction Schottky barrier diode has been successfully fabricated and studied in detail.

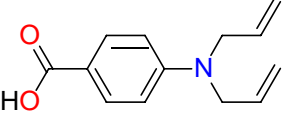
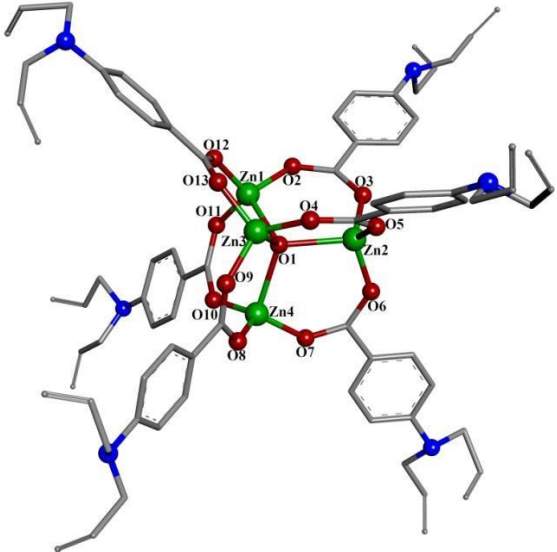
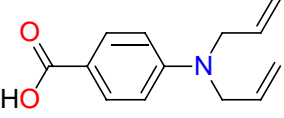
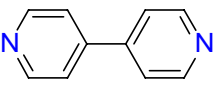
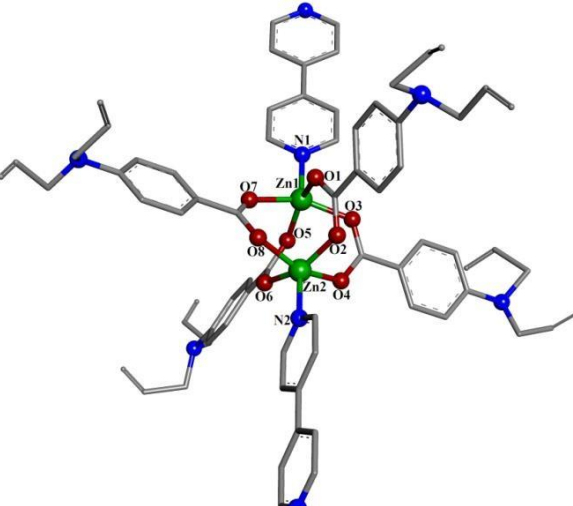
In the successive chapters we have successfully studied the role of π – π stacking interactions, C–H \cdots π interactions and hydrogen bonding interactions in the construction of coordination polymers. In chapter 3, dielectric properties and magnetic coupling interaction have been studied of a copper coordination polymer. This compound shows variable temperature dielectric properties and antiferromagnetic coupling between copper centers. The chapter 4 reveals the synthesis of two Zn(II) based coordination compounds for the application of catalytic CO₂ reduction and schottky diode properties. This compound electrochemically reduced carbon dioxide to methanol and also shows conducting behaviour in solid state. The chapter 5 reveals 1D Cu(II) coordination polymers using 4-diallylaminobenzoic acid as a highly electron rich N-donor ligand. Strong intramolecular H-bonding, various supramolecular interactions and hydroxide bridging are responsible for 1D conformation. This hybrid material shows weak antiferromagnetic interaction between copper centres and efficient nitrophenol reduction reaction in aqueous solution. Therefore this material has great importance as a catalyst for reduction of environmentally hazardous aromatic nitrophenols. The chapter 6 contains detail study of supercapacitor application and magnetic coupling interaction of a tetranuclear copper based metal-organic frameworks. This compound

exhibited antiferromagnetic coupling interaction and the capacitance is 547 F g^{-1} at 2mVS^{-1} . The high value of capacitance and charge/discharge cycling stability makes this material useful for the energy storage application as a supercapacitor electrode. Finally chapter (chapter 7) discusses the conclusions and suggestions for the future work.

Table 1.2 Metal salts and organic linkers are used for the synthesis of CPs.

Sl. No.	Metal salts	Organic linkers	Single unit of CPs
1	$\text{Cu}(\text{NO}_3)_2 \cdot 3\text{H}_2\text{O}$	 And 	
2	$\text{Cu}(\text{NO}_3)_2 \cdot 3\text{H}_2\text{O}$	 And 	

3	$\text{Cu}(\text{NO}_3)_2 \cdot 3\text{H}_2\text{O}$	 <p>And</p> 	
4	$\text{Cu}(\text{NO}_3)_2 \cdot 3\text{H}_2\text{O}$	 <p>And</p> 	
5	$\text{Cu}(\text{NO}_3)_2 \cdot 3\text{H}_2\text{O}$		

6	$\text{Zn}(\text{NO}_3)_2 \cdot 6\text{H}_2\text{O}$		
7	$\text{Zn}(\text{NO}_3)_2 \cdot 6\text{H}_2\text{O}$	 And 	

1.13 References

- (1) Xu, Q.; Sun, J.-K.; Li, J.-Y.; Yin, Y.-X.; Guo, Y.-G. Scalable Synthesis of Spherical Si/C Granules with 3D Conducting Networks as Ultrahigh Loading Anodes in Lithium-Ion Batteries. *Energy Storage Mater.* **2018**, *12*, 54–60.
- (2) Li, P.; Hwang, J.-Y.; Sun, Y.-K. Nano/Microstructured Silicon Graphite Composite Anode for High-Energy-Density Li-Ion Battery. *ACS Nano* **2019**, *13*, 2624–2633.
- (3) Zhang, W.; Li, J.; Guan, P.; Lv, C.; Yang, C.; Han, N.; Wang, X.; Song, G.; Peng, Z. One-Pot Sol-Gel Synthesis of Si/C Yolk-shell Anodes for High Performance Lithium-Ion Batteries. *J. Alloys Compd.* **2020**, *835*, 155135–155141.

- (4) Wu, Y.; Li, M.; Wahyudi, W.; Sheng, G.; Miao, X.; Anthopoulos, T. D.; Huang, K.-W.; Li, Y.; Lai, Z. Performance and Stability Improvement of Layered NCM Lithium-Ion Batteries at High Voltage by a Microporous Al₂O₃ Sol-Gel Coating. *ACS Omega* **2019**, *4*, 13972–13980.
- (5) Bien, C. E.; Chen, K. K.; Chien, S.-C.; Reiner, B. R.; Lin, L.-C.; Wade, C. R.; Ho, W. S. W. Bioinspired Metal-Organic Framework for Trace CO₂ Capture. *J. Am. Chem. Soc.* **2018**, *140*, 12662–12666.
- (6) Yang, L. Z.; Yan, L. T.; Wang, Y.; Liu, Z.; He, J. X.; Fu, Q. J.; Liu, D. D.; Gu, X.; Dai, P. C.; Li, L. J.; Zhao, X. B. Adsorption Site Selective Occupation Strategy within a Metal-Organic Framework for Highly Efficient Sieving Acetylene from Carbon Dioxide. *Angew. Chem., Int. Ed.* **2021**, *60*, 4570–4574.
- (7) Jiang, L. Y.; Wu, N. N.; Li, Q.; Li, J.; Wu, D. P.; Li, Y. S. Heterometallic Strategy for Enhancing the Dynamic Separation of C₂H₂/CO₂: A Linear Pentanuclear Cluster-Based Metal-Organic Framework. *Inorg. Chem.* **2019**, *58*, 4080–4084.
- (8) Li, Y.-T.; Zhang, J.-W.; Lv, H.-J.; Hu, M.-C.; Li, S.-N.; Jiang, Y.-C.; Zhai, Q.-G. Tailoring the Pore Environment of a Robust Ga-MOF by Deformed [Ga₃O(COO)₆] Cluster for Boosting C₂H₂ Uptake and Separation. *Inorg. Chem.* **2020**, *59*, 10368–10373.
- (9) Yang, H. J.; Trieu, T. X.; Zhao, X.; Wang, Y. X.; Wang, Y.; Feng, P. Y.; Bu, X. H. Lock-and-Key and Shape-Memory Effects in an Unconventional Synthetic Path to Magnesium Metal-Organic Frameworks. *Angew. Chem., Int. Ed.* **2019**, *58*, 11757–11762.
- (10) Mendes, F. R.; Paz, A. F. Transforming metal–organic frameworks into functional materials. *Inorg. Chem. Front.*, **2015**, *2*, 495-509.
- (11) Hong, M. C.; Chen, L. *Design and Construction of Coordination Polymers*, ed. John Wiley & Sons, Inc. Hoboken, New Jersey, **2009**.
- (12) Janiak, C. Engineering coordination polymers towards applications. *Dalton Trans.*, **2003** 2781-2804.
- (13) Kitagawa, S.; Kitaura, R.; Noro, S.-I. Functional Porous Coordination Polymers. *Angew. Chem., Int. Ed.*, **2004**, *43*, 2334-2375.
- (14) Batten, S. R.; Neville, S. M.; Turner, D. R. *Coordination polymers: design, analysis and application*. RSC: Cambridge, **2009**.

- (15) Eddaoudi, M.; Moler, D. B.; Li, H. L.; Chen, B. L.; Reineke, T. M.; O'Keeffe, M.; Yaghi, O. M. Modular Chemistry: Secondary Building Units as a Basis for the Design of Highly Porous and Robust Metal–Organic Carboxylate Frameworks. *Acc. Chem. Res.* **2001**, *34*, 319–330.
- (16) Biradha, K.; Ramanan, A.; Vittal, J. J. Coordination polymers versus metal-organic frameworks. *Cryst. Growth Des.*, **2009**, *9*, 2969-2970.
- (17) Bailar, J. C. Jr. *Prep, Inorg. React.* **1964**, *1*, 1–27.
- (18) Karmakar, A.; Desai, A. V.; Ghosh, S. K. Ionic metal-organic frameworks (iMOFs): Design principles and applications. *Coord. Chem. Rev.*, **2016**, *307*, 313–341.
- (19) Batten, S. R.; Champness, N. R.; Chen, X.-M.; Garcia-Martinez, J.; Kitagawa, S.; Öhrström, L.; O'Keeffe, M.; Suh, M. P.; Reedijk, J. Coordination polymers, metal-organic frameworks and the need for terminology guidelines. *CrystEngComm*, **2012**, *14*, 3001–3004.
- (20) Batten, S. R.; Champness, N. R.; Chen, X.-M.; Garcia-Martinez, J.; Kitagawa, S.; Öhrström, L.; O'Keeffe, M.; Suh, M. P.; Reedijk, J. Terminology of metal–organic frameworks and coordination polymers (IUPAC Recommendations 2013). *Pure Appl. Chem.*, **2013**, *85*, 1715–1724.
- (21) Du, -Y. D.; Qin, J.; Li, S.; Su, Z. Lan, Y. Recent advances in porous polyoxometalatebased metal–organic framework materials. *Chem. Soc. Rev.*, 2014, *43*, 4615.
- (22) Horike, S.; Shimomura, S.; Kitagawa, S. Soft porous crystals. *Nat. Chem.*, **2009**, *1*, 695-704.
- (23) Sun, L.; Campbell, M. G.; Dincă, M. Electrically Conductive Porous Metal-Organic Frameworks. *Angew. Chem., Int. Ed.* **2016**, *55*, 3566.
- (24) Keskin, S.; van Heest, T. M.; Sholl, D. S. Can Metal-Organic Framework Materials Play a Useful Role in Large-Scale Carbon Dioxide Separations?. *ChemSusChem*, **2010**, *3*, 879–891.
- (25) Danaci, D.; Bui, M.; Mac Dowell, N.; Petit, C. Exploring the limits of adsorption-based CO₂ capture using MOFs with PVSA - from molecular design to process economics. *Mol. Syst. Des. Eng.* **2020**, *5*, 212-231.

- (26) Li, J.-R.; Kuppler, R. J.; Zhou, H.-C. Selective gas adsorption and separation in metal-organic frameworks. *Chem. Soc. Rev.*, **2009**, *38*, 1477-1504.
- (27) Wang, S.; Wang, Q.; Feng, X.; Wang, B.; Yang, L. Explosives in the Cage: Metal-Organic Frameworks for High-Energy Materials Sensing and Desensitization. *Advanced Materials*, **2017**, *29*, 1701898.
- (28) Zhang, L.; Zou, C.; Zhao, M.; Jiang, K.; Lin, R.; He, Y.; Wu, C.-D.; Cui, Y.; Chen, B.; Qian, G. Doubly Interpenetrated Metal-Organic Framework for Highly Selective C₂H₂/CH₄ and C₂H₂/CO₂ Separation at Room Temperature. *Cryst. Growth Des.* **2016**, *16*, 7194–7197.
- (29) Xue, N.; Zheng, L.-N.; Wang, H.; Li, H.-M.; Ding, T. Highly selective C₂H₂ and CO₂ capture and photoluminescence properties of two Tb(III)-based MOFs. *J. Solid State Chem.* **2020**, *285*, 121257.
- (30) Yang, J.; Yang, Y.-W. Metal-Organic Frameworks for Biomedical Applications. *Small*, **2020**, *16*, 1906846.
- (31) Yaghi, O. M.; Kalmutzki, M. J.; Diercks, C. S. *Introduction to Reticular Chemistry: Metal-Organic Frameworks and Covalent Organic Frameworks*. Wiley-VCH, Weinheim, Germany, **2019**.
- (32) Yaghi, O. M.; O’Keeffe, M.; Ockwig, N. W.; Chae, H. K.; Eddaoudi, M.; Kim J. Reticular synthesis and the design of new materials. *Nature* **2003**, *423*, 705.
- (33) Li, H.; Eddaoudi, M.; O’Keeffe, M.; Yaghi, O. M. Design and synthesis of an exceptionally stable and highly porous metal-organic framework. *Nature* **1999**, *402*, 276.
- (34) Kitagawa, S.; Matsuda, R. Chemistry of coordination space of porous coordination polymers. *Coord. Chem. Rev.* **2007**, *251*, 2490.
- (35) Kitagawa, S.; Uemura, K. Dynamic porous properties of coordination polymers inspired by hydrogen bonds. *Chem. Soc. Rev.* **2005**, *34*, 109.
- (36) Ghosh, S. K.; Zhang, J. P.; Kitagawa, S. Reversible topochemical transformation of a soft crystal of a coordination polymer. *Angew. Chem., Int. Ed.* **2007**, *46*, 7965.
- (37) Matsuda, R.; Kitaura, R.; Kitagawa, S.; Kubota, Y.; Belosludov, R. V.; Kobayashi, T. C.; Sakamoto, H.; Chiba, T.; Takata, M.; Kawazoe, Y.; Mita, Y. Highly controlled acetylene accommodation in a metal-organic microporous material. *Nature* **2005**, *436*, 238.

- (38) Ghosh, S. K.; Bureekaew, S.; Kitagawa, S. A dynamic, isocyanurate-functionalized porous coordination polymer. *Angew. Chem., Int. Ed.* **2008**, *47*, 3403.
- (39) Seo, J.; Matsuda, R.; Sakamoto, H.; Bonneau, C.; Kitagawa, S. A Pillared-Layer Coordination Polymer with a Rotatable Pillar Acting as a Molecular Gate for Guest Molecules. *J. Am. Chem. Soc.* **2009**, *131*, 12792.
- (40) Kitagawa, S.; Kitaura, R.; Noro, S.-i. Functional porous coordination polymers. *Angew. Chem. Int. Ed.* **2004**, *43*, 2334–2375.
- (41) Pepinsky, R. Crystal Engineering - New Concept in Crystallography, *Physical Review*, **1955**, *100*, 971.
- (42) Schmidt, G. M. Photodimerization in the solid state. *Pure Appl. Chem.*, **1971**, *27*, 647.
- (43) Desiraju, G. R. *Crystal Engineering: The design of Organic Solids*, Elsevier, Amsterdam, The Netherlands, 1989.
- (44) Desiraju, G. R. Crystal Engineering: From Molecule to Crystal. *J. Am. Chem. Soc.* **2013**, *135*, 9952.
- (45) Almarsson, O.; Zaworotko, M. J. Crystal engineering of the composition of pharmaceutical phases. Do pharmaceutical co-crystals represent a new path to improved medicines?. *Chem. Commun.* **2004**, *17*, 1889-1896.
- (46) McGrath, T. D.; V. A. Downing, A. V.; Katz, J. M. Investigating the crystal engineering of the pillared paddlewheel metal–organic framework $Zn_2(NH_2BDC)_2DABCO$. *CrystEngComm*, **2018**, *20*, 6082-6087.
- (47) Hosseini, M. W. Molecular Tectonics: From Simple Tectons to Complex Molecular Networks. *Acc. Chem. Res.* **2005**, *38*, 313.
- (48) Desiraju, G. R.; Vittal, J. J.; Ramanan, A. *Crystal Engineering: A Text Book*, World Scientific: Singapore, **2011**.
- (49) Cooper, A. I. Molecular Organic Crystals: From Barely Porous to Really Porous. *Angew. Chem., Int. Ed.* **2012**, *51*, 7892.
- (50) Nangia, A. Organic nanoporous structures. *Solid State Mater. Sci.* **2001**, *5*, 115.
- (51) Steed, J. W.; Atwood, J. L., *Supramolecular Chemistry*. Wiley: Chichester, **2000**.

- (52) Schmeck, Harold M. Jr. "Chemistry and Physics Nobels Hail Discoveries on Life and Superconductors; Three Share Prize for Synthesis of Vital Enzymes". *New York Times*, **1987**.
- (53) Lehn, J. M. Cryptates: inclusion complexes of macropolycyclic receptor molecules. *Pure Appl. Chem.* **1978**, *50*, 871.
- (54) Atwood, J. L.; Steed, J. W. *Supramolecular chemistry*, Wiley, **2013**.
- (55) Su, K., Wu, M., Yuan, D. *et al.* Interconvertible vanadium-seamed hexameric pyrogallol[4]arene nanocapsules. *Nat Commun*, **2018**, *9*, 4941.
- (56) Hasenknopf, B.; Lehn, J. M.; Kneisel, B. O.; Baum, G.; Fenske, D. Self-assembly of a circular double helicate. *Angew. Chem., Int. Ed.* **1996**, *35*, 1838–1840.
- (57) Lehn, J.-M. *Angew. Chem., Int. Ed.* **1990**, *29*, 1304-1319.
- (58) Day, A. I.; Blanch, R. J.; Arnold, A. P.; Lorenzo, S.; Lewis, G. R.; Dance, I. A cucurbituril-based gyroscane: a new supramolecular form. *Angew. Chem., Int. Ed.* **2002**, *41*, 275.
- (59) Ikeda, T.; Stoddart, J. F. *Sci. Technol.* Electrochromic materials using mechanically interlocked molecules. *Adv. Mater.* **2008**, *9*, 014104.
- (60) Whitesides, G. M., Simanek, E. E.; Gorman, C. B. in NATO Advanced Study Institute on Chemical Synthesis: Gnosis to Prognosis, Chatgililoglu, C.; Snieckus, V. Eds.; Kluwer, Dordrecht, the Netherlands, **1996**.
- (61) Ariga, K.; Hill, J. P.; Lee, M. V.; Vinu ,A.; Charvet, R.; Acharya S. Challenges and breakthroughs in recent research on self-assembly. *Sci. Technol. Adv. Mater.* **2008**, *9*, 014109.
- (62) Ishiwari, F.; Shoji, Y.; Fukushima, T. Supramolecular scaffolds enabling the controlled assembly of functional molecular units. *Chem. Sci.*, **2018**, *9*, 2028-2041.
- (63) Lehn, J. M. *Supramolecular chemistry – concepts and perspectives*, New York: VHC, **1995**.
- (64) Baron, R. ; Setny, P.; Mc Cammon, J. A.; Water in Cavity-Ligand Recognition. *J. Am. Chem. Soc.* **2010**, *132*, 12091–12097.

- (65) Baron, R.; McCammon, J. A.; Molecular recognition and ligand association. *Annu. Rev. Phys. Chem.* **2013**, *64*, 151–175.
- (66) Nørgaard, K.; Bjornholm, T. Supramolecular chemistry on water - towards self-assembling molecular electronic circuitry. *Chem. Commun.* **2005**, 1812.
- (67) Shinkai, S.; Ikeda, M.; Sugasaki, A.; Takeuchi, M. Positive Allosteric Systems Designed on Dynamic Supramolecular Scaffolds: Toward Switching and Amplification of Guest Affinity and Selectivity. *Acc. Chem. Res.* **2001**, *34*, 494.
- (68) Dong, J.; Davis, P. A. Molecular Recognition Mediated by Hydrogen Bonding in Aqueous Media. *Angew. Chem., Int. Ed.* **2021**, *133*, 8113-8126.
- (69) Cram, D. J. *Angew. Chem., Int. Ed. Engl.* **1986**, *25*, 1039.
- (70) Pedersen, C. J. Cyclic polyethers and their complexes with metal salts. *J. Am. Chem. Soc.* **1967**, *89*, 7017–7036.
- (71) Han, Y.; Lia, H.; Jin, G. Host–guest chemistry with bi- and tetra-nuclear macrocyclic metallasupramolecules. *Chem. Commun.*, **2010**, *46*, 6879-6890.
- (72) Cai, W.; Wang, J.; Chu, C.; Chen, W.; Wu, C.; Liu, G. Metal-Organic Framework-Based Stimuli-Responsive Systems for Drug Delivery. *Adv. Sci.* **2019**, *6*, 1801526.
- (73) Garai, B.; Mallick, A.; Banerjee, R. Photochromic metal-organic frameworks for inkless and erasable printing. *Chem. Sci.*, **2016**, *7*, 2195-2200.
- (74) Fan, C. B.; Gong, L. L.; Huang, L.; Luo, F.; Krishna, R.; Yi, X. F.; Zheng, A. M.; Zhang, L.; Pu, S. Z.; Feng, X. F.; Luo, M. B.; Guo, G. C. Significant Enhancement of C₂H₂/C₂H₄ Separation by a Photochromic Diarylethene Unit: A Temperature- and Light-Responsive Separation Switch. *Angew Chem Int Ed.* **2017**, *56*, 7900–7906.
- (75) Desiraju, G. R. Chemistry beyond the molecule. *Nature.* **2001**, *412*, 397.
- (76) Desiraju, G. R. Supramolecular synthons in crystal engineering - a new organic synthesis. *Angew. Chem., Int. Ed. Engl.* **1995**, *34*, 2311.
- (77) Steed, J.; Atwood, J. L. *Supramolecular Chemistry*. John Wiley, New York, **2001**.
- (78) Desiraju, G. R.; Vittal, J. J.; Ramanan, A. *Crystal Engineering: A Text Book, World Scientific*: Singapore, **2011**.

- (79) Slater, A. G.; Cooper, A. I. *Science*, **2015**, *348*, 8075.
- (80) Ferey, G.; Serre, C.; Devic, T.; Maurin, G.; Jobic, H.; Llewellyn, P. L.; De Weireld, G.; Vimont, A.; Daturi, M.; Chang, J.-S. Why hybrid porous solids capture greenhouse gases?. *Chem. Soc. Rev.* **2011**, *40*, 550.
- (81) Sun, L.; Campbell, M. G.; Dinca, M. Electrically Conductive Porous Metal-Organic Frameworks. *Angew. Chem. Int. Ed.* **2016**, *55*, 3566-3579.
- (82) Zhang, X.; Chen, Z.; Liu, X.; Hanna, S.; Wang, X.; Taheri-Ledari, R.; Maleki, A.; Li, P.; Omar, K. Farha. A historical overview of the activation and porosity of metal-organic frameworks. *Chem. Soc. Rev.*, **2020**, *49*, 7406-7427.
- (83) Welte, L.; Calzolari, A.; di Felice, R.; Zamora, F.; Gómez-Herrero, J. *Nat. Nanotechnol.*, **2010**, *5*, 110-115.
- (84) Mas-Balleste, R.; Castillo, O.; Miguel, P. J. S.; Olea, D.; Gomez-Herrero, J.; Zamora, F. Towards Molecular Wires Based on Metal-Organic Frameworks. *Eur. J. Inorg. Chem.*, **2009**, 2885-2896.
- (85) Dutta, B.; Das, D.; Datta, J.; Chandra, A.; Jana, S.; Sinha, C.; Ray, P. P.; Mir, M. H. Synthesis of a Zn(II)-based 1D zigzag coordination polymer for the fabrication of optoelectronic devices with remarkably high photosensitivity. *Inorg. Chem. Front.* **2019**, *6*, 1245-1252.
- (86) Dutta, B.; Dey, A.; Sinha, C.; Ray, P. P.; Mir, M. H. Photochemical Structural Transformation of a Linear 1D Coordination Polymer Impacts the Electrical Conductivity. *Inorg. Chem.* **2018**, *57*, 8029-8032.
- (87) Naskar, K.; Maity, S.; Jana, S.; Dutta, B.; Tanaka, S.; Mallick, D.; Akitsu, T.; Sinha, C. Arylazoimidazole Coordinated and Naphthalene-Dicarboxylato Bridged Polymers of Co(II) and Photochromic Zn(II) Complexes. *Cryst. Growth. Des.* **2018**, *18*, 2986-2997.
- (88) Dutta, B.; Jana, R.; Sinha, C.; Ray, P. P.; Mir, M. H. Synthesis of a Cd(II) based 1D coordination polymer by in situ ligand generation and fabrication of a photosensitive electronic device. *Inorg. Chem. Front.* **2018**, *5*, 1998-2005.
- (89) Naskar, K.; Dey, A.; Maity, S.; Bhunia, K. M.; Ray, P. P.; Sinha, C. Novel porous polycatenated Iodo-cadmium coordination polymer for iodine sorption and electrical conductivity measurement. *Cryst. Growth. Des.* **2018**, *19*, 2206-2218.

- (90) Chandra, A.; Das, M.; Pal, K.; Jana, S.; Dutta, B.; Ray, P. P.; Jana, K.; Sinha, C. 3D-Coordination Polymer of Zn(II)-carboxylate : Structural Elucidation, Photo-electrical Conductivity and Biological Activity. *ACS Omega*, **2019**, *4*, 17649-1766.
- (91) Dutta, B.; Ghosh, S.; Apurba Ray, Jana, S.; Sinha, C.; Das, S.; Jana, A.; Mir, M. H. Stabilization of cyclic water tetramers and dimers in the crystal host of 2D coordination networks: electrical conductivity and dielectric studies. *New J. Chem.*, **2020**, *44*, 15857-15870.
- (92) Thoms, E.; Sippel, P.; et., al. Dielectric study on mixtures of ionic liquids. *Sci.* **2017**, *7*, 7463.
- (93) Fredrik, H.; Jerker, D. Energy Harvesting and Systems. **2018**, *5*, 43–51. doi:10.1515/ehs-2018-0010.
- (94) Tehrani, Z.; Thomas, D.J.; Korochkina, T.; Phillips, C.O.; Lupo, D.; Lehtimäki, S.; O'Mahony, J.; Gethin, D.T. Large-area printed supercapacitor technology for low-cost domestic green energy storage. *Energy*, **2017**, *118*, 1313–1321.
- (95) Bueno, P. R. Nanoscale origins of super-capacitance phenomena. *Journal of Power Sources*, **2019**, *414*, 420–434.
- (96) Wang, -G. D.; Liang, Z.; Gao, S.; Qu, C.; Zou, R. Metal-organic framework-based materials for hybrid supercapacitor application. *Coord. Chem. Rev.*, **2020**, *404*, 213093.
- (97) IUPAC Compendium of Chemical Terminology. Catalyst, Oxford: Blackwell Scientific Publications. **2009**, doi:10.1351/goldbook.
- (98) Richard, I. M. Chemical Kinetics and Catalysis. New York: Wiley-Interscience. **2001**.
- (99) Louise, L. 7 things you may not know about catalysis. Argonne National Laboratory. **2011**.
- (100) Iqrash, S.; Sumeer, S.; Parveen, A.; Wenshu, Y.; Murid, H. "Recent developments in alumina supported hydrodesulfurization catalysts for the production of sulfur-free refinery product. *Catalysis Reviews*. **2020**, *0*, 1–86.
- (101) Hu, -M. X.; Daasbjerg, K. Molecular catalyst converts carbon dioxide to methanol. *Nature*, **2019**, *575*, 598-599.

(102) Zhang, Xiuling.; Jin, Feng. A cobalt(II) coordination polymer based on a carboxyl-triazolyl-bifunctional ligand: Synthesis, characterization and catalytic reduction of 4-nitrophenol. *Inorg. Chem. Commun.* **2020**, *119*, 108075.

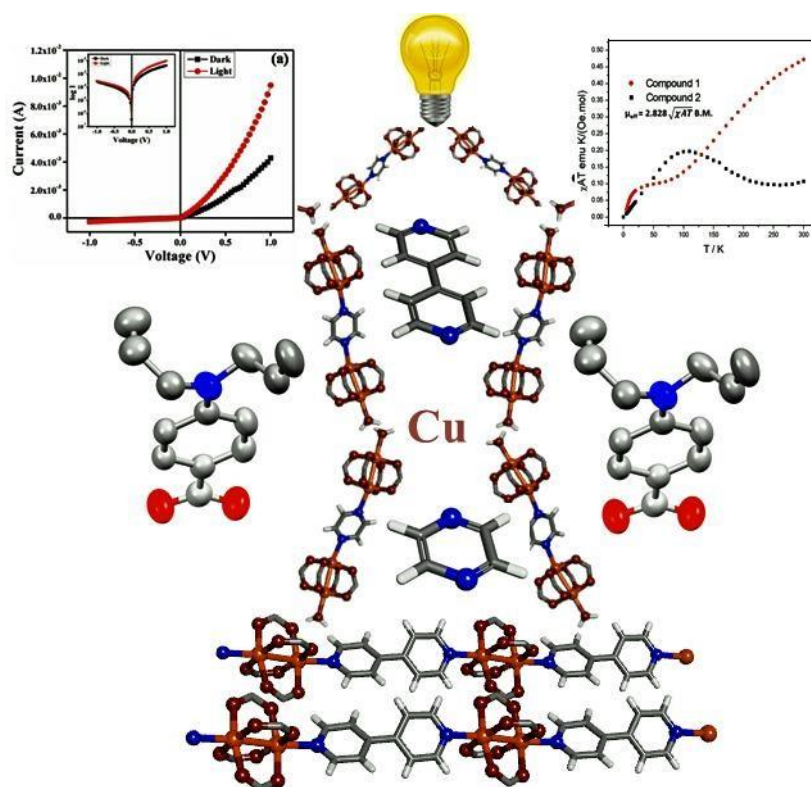
(103) David, J. Introduction to magnetism and magnetic materials (Third ed.). Boca Raton. **2015**.

(104) Westbrook, C.; Kaut, C.; Kaut-Roth, C. MRI (Magnetic Resonance Imaging) in practice (2 ed.). Wiley-Blackwell. **1998**.

(105) Zhang, J.; Kosaka, W.; Kitagawa, Y.; Miyasaka, H. A metal–organic framework that exhibits CO₂-induced transitions between paramagnetism and ferrimagnetism. *Nature*, **2021**, *13*, 191–199.

Abstract

Carboxylato bridged paddle wheel Cu(II) coordination polymers $[\text{Cu}_2(\text{DABA})_4(4,4'\text{-BPY})]_n$ (**1**) and $[\text{Cu}_4(\text{DABA})_8(\text{PYZ})(\text{H}_2\text{O})_2]$ (**2**) (HDABA = 4-Diallylamino-benzoic acid) have been synthesized by varying axial linkers, 4,4'-Bipyridine (4,4'-BPY) and Pyrazine (PYZ). The single crystal X-ray structure of **1** is 1D polymer while **2** is 0D tetranuclear Cu(II) complex. Upon light irradiation the thin film of the compounds increases the electrical conductivity with respect to the dark phase and the conductivity of **1** is ~150 times higher than **2**. Magnetic properties were investigated at an applied field 0.5 T in a temperature range 5–300 K. Compound **1** exhibits ferromagnetic behavior and compound **2** is antiferromagnetic at 300 K and the effective magnetic moment at 300 K, is 1.94 and 0.93 BM, respectively. The capability to switch photoelectricity and magnetism by changing the crystal structure via axial linker's modification has been rationalized through DFT calculations.



2.1. Introduction

Coordination polymers (CPs)¹⁻⁷ have been extensively used in various fields such as in super capacitor,⁸ battery,⁹ gas storage and separation, sensing¹⁰ and electrocatalysis.¹¹ But CPs with distinct magnetic and electrical conductivities are of great interest as next-generation functional materials due to their potential applications for electromagnetic interference shielding,¹² biomedicine¹³ and microwave absorption.¹⁴ In order to achieve long-range charge transport and strong paramagnetic character, it is crucial for these complexes to have strong intermolecular ordering and strong intramolecular coupling. One of the remarkable features of CP is its ability to adopt different structural architecture under varying conditions. The length of organic spacer and the functional groups of the ligands, the nature of metal ions and the oxidation state along with the reaction condition greatly influence the structure of the CPs. Out of the nine 3d transition metal ions nontoxic Cu(II) (d^9) exhibit a large variation of nuclearity and structures. The magnetic super-exchange interactions between copper centers through the bridging ligands of paddle wheel Cu(II) complexes are well known.¹⁵ But the electrical conductivity and photosensitivity of such type of complexes have not been much investigated. Loh et al.¹⁶ and Zuo et al.¹⁷ reported recently the conductivity and magnetic property of copper based supramolecules.

In this work, we report 1D and 0D paddle wheel Cu(II) complexes, ($[\text{Cu}_2(\text{DABA})_4(4,4'\text{-BPY})]_n$ (**1**) and $[\text{Cu}_4(\text{DABA})_8(\text{PYZ})(\text{H}_2\text{O})_2]$ (**2**)), where DABA acts as carboxylate bridger and BPY, PYZ are N-heterocyclic spacer of similar conjugated π systems with subtle difference in π -acidity and different degrees of σ -donating ability. Selective N-allylation of 4-amino benzoic acid helps to form aliphatic C-H... π interaction which can help single crystal formation. Diallyl group (have +I effect) of HDABA also increases the electron density on metal centre, which has an effect on conductivity and magnetic properties. These type of CPs are exciting for two main reasons: (i) the paramagnetic Cu(II) (d^9) center and the conducting electrons are linked by a chemical bridge and (ii) the metal is a very good electron transporter between organic linkers.¹⁸ The CPs simultaneously exhibit photosensitive¹⁹ semiconducting nature²⁰⁻²² and paramagnetic behavior to make them viable for use in optoelectronic²³, photovoltaic²⁴ and electromagnetic devices.

2.2. Results and Discussion

2.2.1. Structural analysis of HDABA, $[\text{Cu}_2(\text{DABA})_4(4,4'\text{-BPY})]_n$, (1) and $[\text{Cu}_4(\text{DABA})_8(\text{PYZ})(\text{H}_2\text{O})_2]_n$, (2)

HDABA crystallizes in the monoclinic $C 2/c$ space group with $Z = 8$ and exists as a dimer through strong hydrogen bonding with $\text{O}\cdots\text{H}$ distance 1.80 Å (Figure 2.1) which has been confirmed by Single-crystal X-ray diffraction experiment.

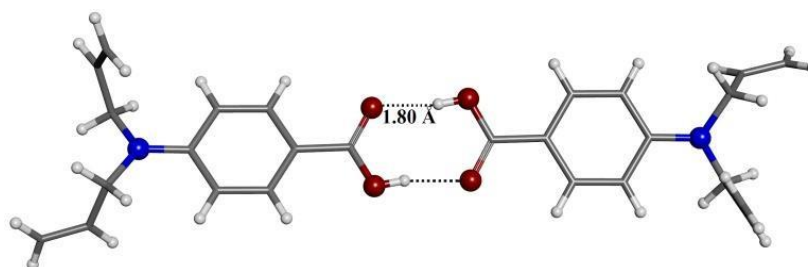


Figure 2.1 Dimeric form of 4-Diallylamino benzoic acid.

The structure analyses of **1** and **2** have revealed that the asymmetric unit have identical motif, a discrete carboxylato bridged Cu(II) paddle wheel $[\text{Cu}_2(\text{DABA})_4]$ unit which is capped by the N-heterocycles at the axial coordination position. (Figure 2.2a and 2.3a) Both the compounds have distorted square pyramidal geometry around Cu centers with metal...metal interaction, where $\text{Cu}\cdots\text{Cu}$ distance lies in the range 2.579-2.641 Å. Compound **1** crystallizes in the monoclinic $P 2_1/n$ space group with $Z = 4$, where **2** crystallizes in the triclinic $P-1$ with $Z = 1$ (Table 2.1).

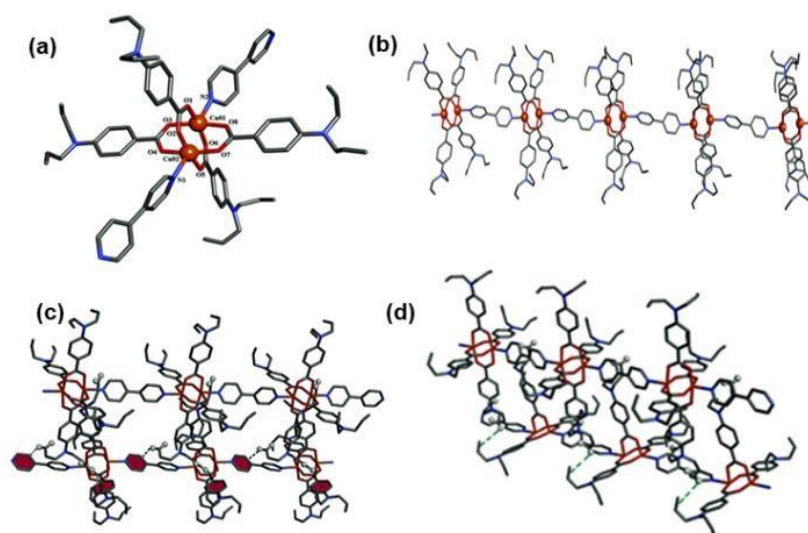


Figure 2.2 A portion of the compound **1** displaying the coordination atmospheres of the Cu(II) atoms (a). A schematic diagram displaying the connectivity of the structure (b). A portion of the 2D connectivity displaying C-H... π interactions (b) - (d).

Compound **1** forms 1D polymeric chain by repeating the asymmetric unit and pyridine ring of 4,4'-BPY (Figure 2.2b) are twisted along X-axis that may assist efficient charge delocalization through metal orbitals.

Table 2.1 Crystallographic Data of **1** and **2**.

Compound	Compound-1	Compound-2
CCDC No.	1871434	1871433
Formula	C ₆₂ H ₆₄ Cu ₂ N ₆ O ₈	C ₁₀₈ H ₁₂₀ Cu ₄ N ₁₀ O ₁₈
fw	1148.30	2100.34
crystalsyst	monoclinic	Triclinic
space group	<i>P</i> 21/ <i>n</i>	P-1
<i>a</i> (Å)	12.5450(8)	13.1365(11)
<i>b</i> (Å)	34.762(2)	14.0314(12)
<i>c</i> (Å)	13.9615(9)	16.3546(13)
α(deg)	90	66.462(2)
β(deg)	112.248(3)	74.865(2)
γ (deg)	90	87.755(3)
<i>V</i> (Å ³)	5635.2(6)	2660.6(4)
<i>Z</i>	4	1
<i>D</i> _{calcd} (g/cm ³)	1.354	1.311
μ(mm ⁻¹)	0.816	0.858
λ(Å)	0.71073	0.71073
data[<i>I</i> > 2σ(<i>I</i>)]/Npar	9888/703	9295/631
GOF on <i>F</i> ²	1.077	1.122
Final <i>R</i>	<i>R</i> ₁ = 0.0466	<i>R</i> ₁ = 0.0479
indices[<i>I</i> > 2σ(<i>I</i>)] ^{<i>a,b</i>}	<i>wR</i> ₂ = 0.1180	<i>wR</i> ₂ = 0.1539

$$^a R_1 = \frac{\sum ||F_o| - |F_c||}{\sum |F_o|}, \quad ^b wR_2 = \left[\frac{\sum w(F_o^2 - F_c^2)^2}{\sum w(F_o^2)^2} \right]^{1/2}$$

The compound **2** forms tetranuclear Cu(II) complex and water molecules act as capping ligands. These coordinating water molecules enables strong hydrogen bonding with bridging carboxylate groups with O...O distances in the range ~ 2.8 Å leading to the formation of the 1D polymeric network (Figure 2.3b). These complexes are capable of forming higher dimensional structures through H-bonding and Supramolecular²⁵ (aliphatic, aromatic C-H... π) interactions (3.066–3.454 Å) (Figures 2.2c-d, 2.3c- d).

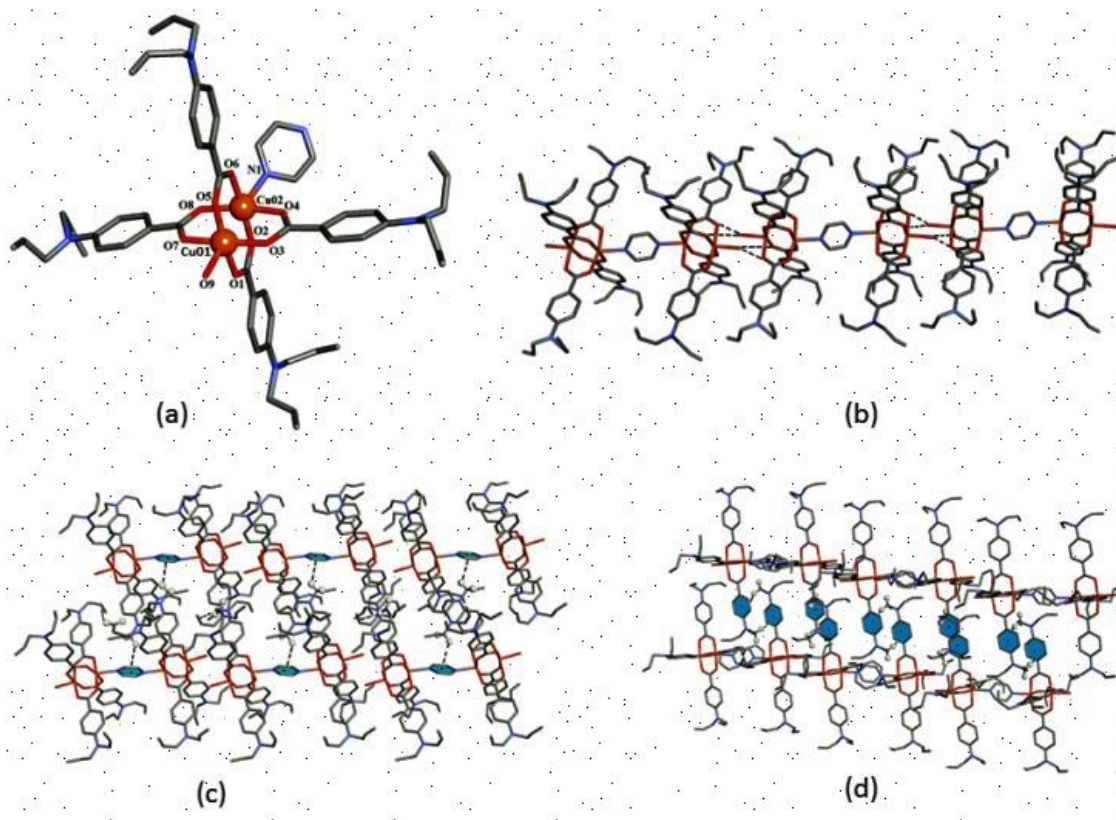


Figure 2.3 (a) A portion of the compound **2** displaying the coordination atmospheres of the Cu(II) atoms; (b) A portion of the 2D connectivity displaying hydrogen bonding interactions; (c) A portion of the 2D connectivity displaying C-H... π interactions; (d) A portion of the 2D connectivity displaying π ... π interactions.

The intramolecular N-N distance in the heterocyclic bridger (in 4,4'-BPY of **1** it is 7.08 Å much longer than 2.75 Å in PYZ of **2**) may be the major driving force for the formation of 1D superstructure for **1** and 0D for **2**. Smaller size of PYZ allows large steric hindrance and may not permit the formation of 1D polymeric chain in **2**.

Single-crystal X-ray diffraction data is well supported by density functional theory (DFT) study, performed using plane wave technique as implemented in Vienna Ab Initio Simulation Package (VASP) (details are given in supporting information).

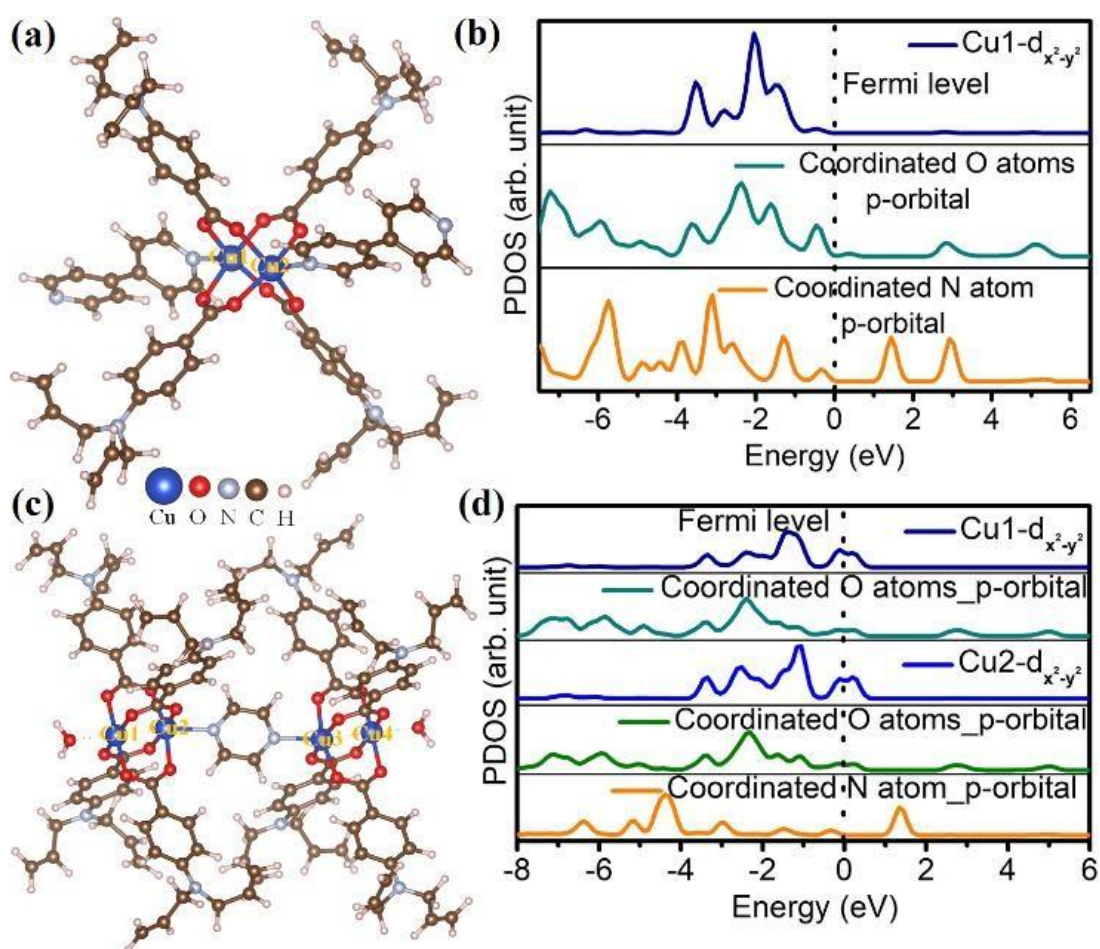


Figure 2.4 Optimized structures of compound **1** (a) and **2** (c), PDOS plots for Cu- $d_{x^2-y^2}$ and p-orbitals of Cu coordinated oxygen and nitrogen atoms in compound **1** (b) and **2** (d).

Cu \cdots Cu distances (in the range 2.579-2.641 Å) determined from the SC-XRD experiment is also well matched with DFT optimized structures which show Cu \cdots Cu distances are 2.70 and 2.56 Å respectively for compounds **1** and **2** (Figure 2.4a and c). In accordance with SC-XRD, DFT optimized structures reveals Cu1 center in compound **1** is coordinated with four oxygen atoms of the carboxylato groups (Cu-O bond length \sim 2.0 Å) and one nitrogen atom from N-heterocycle (Cu-N bond length \sim 2.28 Å) whereas in compound **2** Cu1 center is covalently linked with four oxygen atom of the carboxylato groups (Cu-O \sim 2.05Å) and one oxygen atom from water through hydrogen bonding interaction (Cu \cdots O \sim 2.33Å). On the other hand Cu2 center in compound **2** shows bonding interaction with four oxygen atoms of the carboxylate groups (Cu-O \sim 2.03Å) and one nitrogen atom from N- heterocycle (Cu-N \sim 2.23 Å). Projected density of states (PDOS) analysis clearly reveals that the bonding interaction between Cu and coordinated atoms originates from Cu- $d_{x^2-y^2}$ orbitals and p-orbitals of nitrogen and oxygen atoms both in compound **1** and **2** (Figure 2.4 b-d).

2.2.2. Magnetic Properties

Paddle-wheel copper(II) carboxylato CPs [Cu(II), d^9] are well-known to possess magnetic super exchange interactions²⁶ between the two copper(II) centers through the bridging ligands. The extent of the exchange interaction is known to be controlled by several factors, including the geometry of the Cu(II) ions, the bond angles and the bond lengths of the bridging atoms, the bridging mode of the ligand and also the type of bridging linkers^{27,28}. The spin super-exchange interaction of the binuclear copper(II) complexes can be understood in terms of the natural (non-orthogonalized) magnetic orbitals.²⁹⁻³¹ At 300 K, the effective magnetic moment for **1**, and **2** are 1.94, and 0.93 B.M., respectively, which correspond to spin only values of $S=1/2$ for Cu(II) (1.73 B. M.). It is noted that the effective magnetic moment of compound **1** is greater than that of single uncoupled Cu(II) ion and compound **2** shows much less value than that of one-electron spin uncoupled Cu(II) ion. The compound **1** exhibits χ_{AT} value 0.0223 emu K/(Oe . mol) at 5 K and is increased linearly upto 20 K followed by sigmoidal change in the χ_{AT} value to 0.472 emu K/(Oe . mol) at 300 K (Figure 2.5). For compound **2** χ_{AT} becomes 0.0098 emu K/(Oe . mol) at 5 K and follows paramagnetic change (χ_{AT} vs T is linear) upto 100 K.

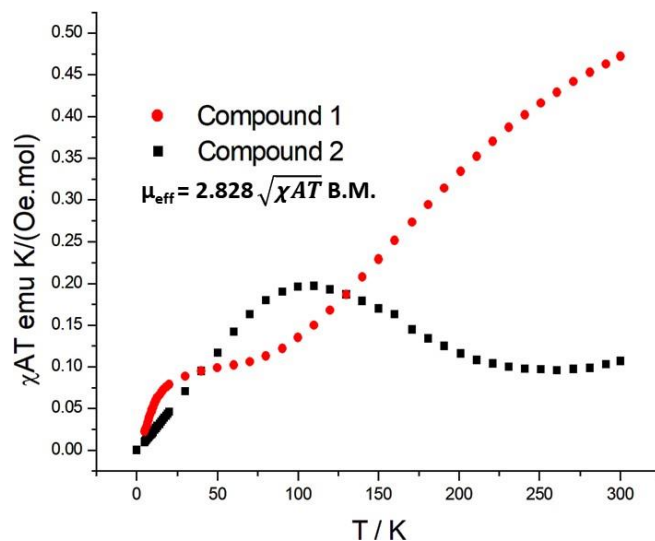


Figure 2.5 Variation of χ_{AT} value with temperature for compounds **1** and **2** (where χ_A refers to diamagnetic correction of χ_M).

Then it is gradually decreased until around 250 K and the χ_{AT} value is reached to 0.107 emu K/(Oe . mol) at 300 K (Figure 2.5). Therefore, compound **1** becomes ferromagnetic at room temperature while the compound **2** is antiferromagnetic at 300 K. To further rationalize the

strong antiferromagnetic coupling interactions between the Cu^{2+} ions as well as among the covalently linked atoms with Cu^{2+} ions (coordinated N and O atoms) at low temperature, we have performed DFT and calculated magnetic moment values at low temperature (~ 0 K) for both the compounds **1** and **2**.

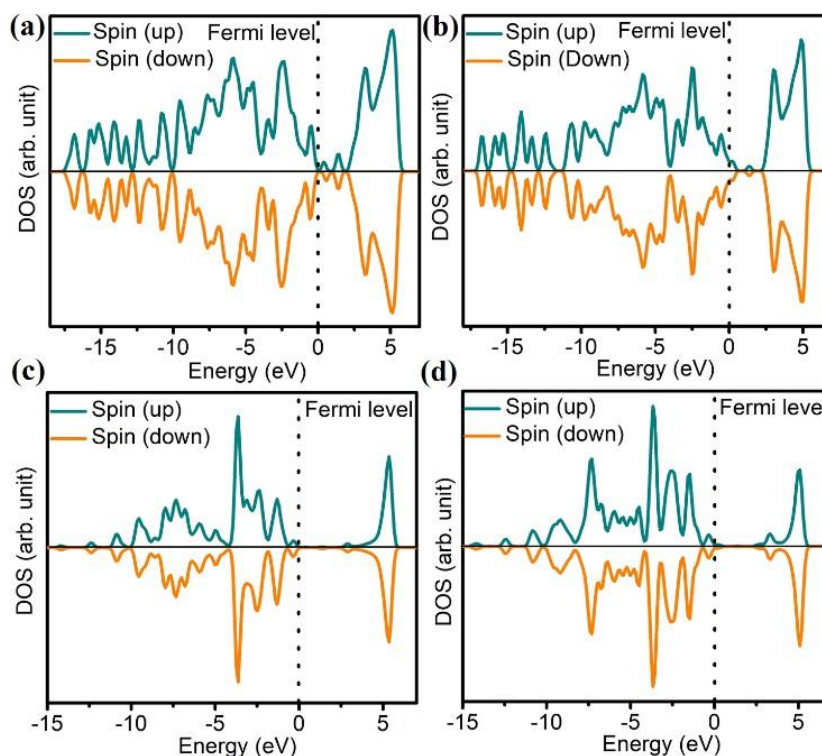


Figure 2.6 DOS plots for (a) compound **1** (b) compound **2**, LDOS plots for Cu^{2+} ions in compound **1** (c) and **2** (d).

Charge transfer from Cu^{2+} ions to the ligand orbitals results ferromagnetic coupling in the ambient temperature. DFT calculations on both compounds **1** and **2**, reveal that strong charge transfer from coordinated atoms to Cu^{2+} centers (~ 0.9 e on average for both compounds) results in strong anti-ferromagnetic coupling with the more localization of electrons on Cu^{2+} centers (magnetic moment = $0.000 \mu\text{B}$) at low temperature (~ 0 K). The anti-ferromagnetic coupling phenomenon is well understood from total as well as localized density of states (TDOS, LDOS) analysis (Figure 2.6). The perfectly symmetric nature of electron density of spin up and down clearly indicates that there are strong antiferromagnetic coupling interactions among the Cu^{2+} ions as well as between Cu^{2+} and coordinated ligands (Figure 2.6a-b) for compounds **1** and **2**. The LDOS of Cu^{2+} ions and coordinated nitrogen and oxygen atoms of compounds **1** and **2** clearly demonstrates that the spin on the atoms are all antiferromagnetically coupled (Figure 2.6 c-d).

Apart from this, d^9 configuration of Cu(II) being more than half-filled has significant orbital contribution and also the presence of hydrogen bonding and other supramolecular interactions can also influence the magnetic properties.³²

2.2.3. Electrical Characterization

Impedance Spectroscopy study and current-voltage (I-V) measurement

Impedance Spectroscopy (IS) study is performed in frequency range 40 Hz-10 MHz at room temperature. **Figure 2.7a** shows the Nyquist plot for two compounds in the dark condition. The higher frequency semicircular arc depicts the bulk contribution and intermediate or low frequency semicircular arc represents the grain-boundary or electrode-specimen effect.³³ The intercept of the semicircular arc on real axis Z' depicts the bulk resistance R_b (dc resistance) of the sample. From **Figure 2.7a** and inset of **Figure 2.7a**, it is clearly seen that compound **1** has lower resistance than compound **2**.

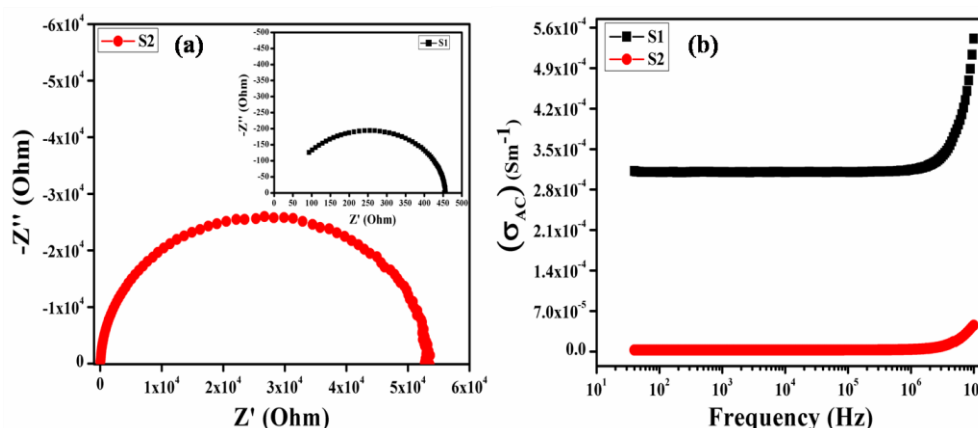


Figure 2.7 (a) Nyquist plot and (b) frequency dependent ac conductivity plot for compounds **1** and **2**.

The lower resistance signifies the better possibility of charge transfer. **Figure 2.7b** represents ac conductivity vs. frequency (log scale) plot for compound **1** and **2**. At lower frequency region, the extrapolation of Y-axis gives the value of dc conductivity (σ_{DC}), which is attributed to the long range translational motion of the charge carriers. In high frequency region the term $A\omega^n$ is responsible for the frequency dependent behaviour and the dispersion nature.³⁴ The frequency dependence of ac conductivity (σ_{AC}) may be because of free and bound carriers.³⁵ The frequency dependent conductivity can be expressed by the following power law equation .^{36, 37}

$$(\omega) = \sigma_{dc} + \sigma_{ac} \quad (1)$$

Where, $\sigma(\omega)$ is the total conductivity, σ_{DC} is the dc conductivity and σ_{AC} is the ac conductivity. At high frequency region, the increase of conductivity described through Jonscher's power law [1] and it is defined as:

$$\sigma_{ac} = [\mathbf{1} + (_)\omega_H^n] \quad (2)$$

Where, n is the dimensionless frequency component, ω ($\omega=2\pi f$) is the angular frequency and ω_H is the hopping frequency of the charge carrier. At room temperature, the dc conductivity (σ_{DC}) of the compound **1** and **2** are calculated as $3.12 \times 10^{-4} \text{ Sm}^{-1}$ and $2.65 \times 10^{-6} \text{ Sm}^{-1}$ respectively which was also verified by computationally and the corresponding theoretical band gap are 1.36 eV and 1.75 eV respectively (Figure 2.8). The DFT calculated DC electrical current conductivity ($\sigma_{dc, DFT}$) of the compound **1** is 1.1×10^{-4} whereas that of compound **2** is $8.5 \times 10^{-7} \text{ Sm}^{-1}$ that agrees with the experimentally determined electrical conductivity value. Both the experimental and DFT study shows that compound **1** is more conducting (in order of magnitude) compared to compound **2**. Motivated from these results, the current-voltage (I-V) characteristics of Al/Compound/ITO sandwich structure have been performed within the voltage range $\pm 1 \text{ V}$.

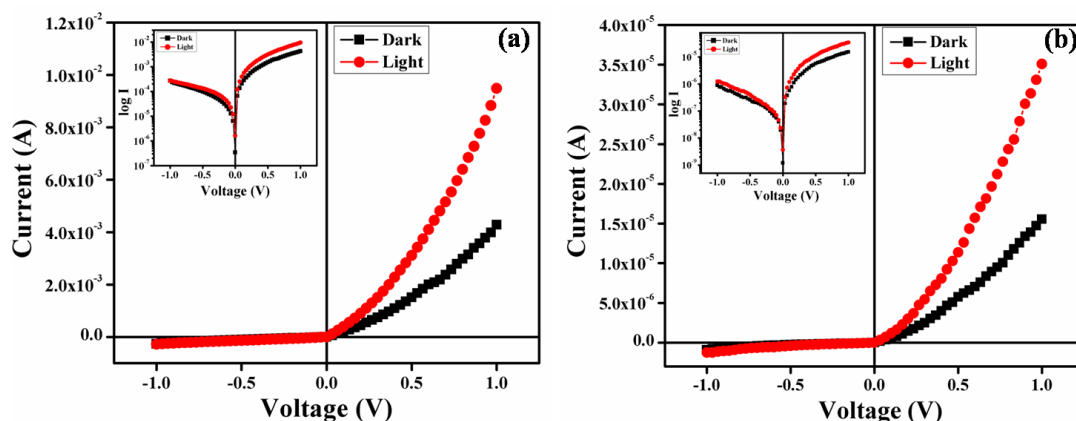


Figure 2.8 Current-Voltage (I-V) characteristic curves for (a) compound 1 and (b) compound 2 under dark and light condition.

Figure 2.8a-b show the current-voltage characteristic curves of devices (compounds **1** and **2**) in the dark/under irradiation with white light (irradiance $\sim 1000 \text{ Wm}^{-2}$). Figure 2.8 shows that the fabricated devices based on the samples exhibit non-linear rectifying behavior, similar to the Schottky diode behavior. The rectification ratio (i.e., On/Off ratio) of the devices in the dark/under illumination condition are found to be 16.00, 17.39 and 34.64, 28.25 for the compound **1-2** respectively. Logarithmic presentation of I as a function of V is shown in inset of Figure 2.8.

We have analyzed the I-V characteristic curves by introducing standard thermionic emission (TE) theory³⁸ for exploring the charge transport phenomena by considering the following standard equations.³⁹

$$I = I_0 \exp\left(\frac{V}{\eta kT}\right) [1 - \exp\left(\frac{-qV}{\eta kT}\right)] \quad (3)$$

Where, I_0 is the saturation current derived from the straight line intercept of $\ln(I)$ at $V = 0$ and is given by Eq. 4.

$$I_0 = AA^*T^2 \exp\left(\frac{-q\phi_B}{kT}\right) \quad (4)$$

Where, q stands for the electronic charge, k is the Boltzmann constant, T is the temperature in Kelvin, V is the forward bias voltage, A is the effective diode area, η is the ideality factor and A^* is the effective Richardson constant respectively. The effective diode area is estimated as $7.065 \times 10^{-6} \text{ m}^2$ and the effective Richardson constant is considered as $1.20 \times 10^6 \text{ AK}^{-2}\text{m}^{-2}$ for all the devices. At low bias, linearity in current is observed which is consistent with Eq. (3), while the deviation from linearity at higher bias voltages occurred due to the change in diode series resistance. From Cheung, the forward bias I-V characteristics in term of series resistance can be expressed as (Eq. 5),⁴⁰

$$I = I_0 \exp\left[\frac{(V - IR_S)}{\eta kT}\right] \quad (5)$$

Where, the IR_S term is the voltage drop across series resistance of device.

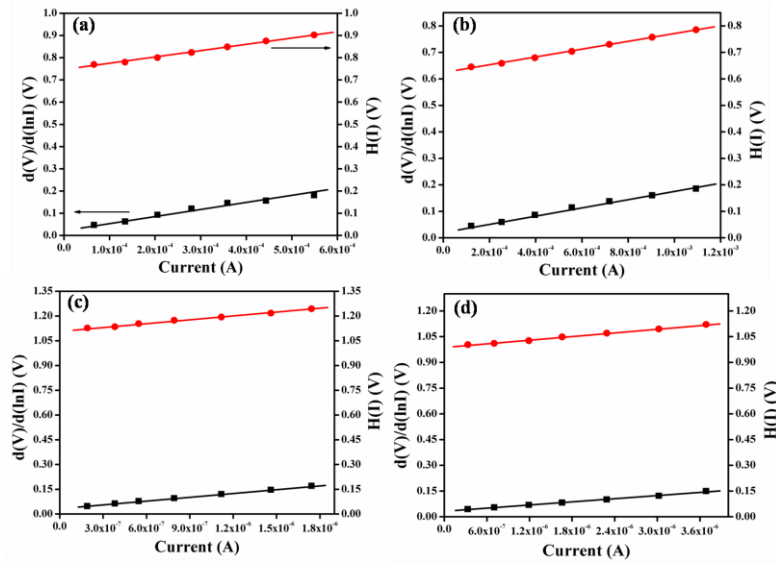


Figure 2.9 $dV/d(\ln I)$ vs. I and $H(I)$ vs. I curve for compound 1 and 2 based Schottky barrier diode under dark (a), (c) and photo (b), (d) condition.

In this circumstance, the values of the series resistance can be determined from following equations (Eqs. 6, 7) ⁴¹

$$\frac{dV}{d\ln(I)} = \left(\frac{nKT}{q}\right) + s \quad (6)$$

$$(I) = R_s I + \eta \phi_B \quad (7)$$

and $H(I)$ can be represented as (Eq. 8):

$$(I) = V - \left(\frac{\eta kT}{q}\right) \ln\left(\frac{I}{AA^*T^2}\right) \quad (8)$$

The plot of $dV/d\ln(I)$ vs. I (Figure 2.9) gives the value of series resistance (R_s) as the slope and the ideality factor (η) as the y-axis intercept. The $dV/d\ln(I)$ vs. I graph for all devices in the dark/under light condition have been portrayed in Figure 2.9. The potential barrier height for all devices are evaluated from the y-axis intercept of $H(I)$ vs. I curve (Figure 2.9). The slope of this plot also furnishes a second determination of the series resistance. The obtained values of ideality factor, barrier height and series resistance are listed in Table-2.2. The values of ideality factor (η) in the dark condition deviated from ideal behavior and this difference is due to the presence of inhomogeneities of Schottky barrier height, high probability of electron and hole recombination in the depletion region, existence of interface states and series resistance.^{42,43} But, under the illumination of light the value of ideality factor approaches unity. Series resistance (R_s) of all the compounds in both cases decrease after soaking light, these results indicate a certain reduction in carrier density in the depletion region of the rectifier through the introduction of traps and recombination centres associated with illumination effect, which signifies its applicability in the field of optoelectronics devices.

For a better insight into the charge transport phenomena through the metal-semiconductor (MS) junction, we investigate the forward I-V curves in details by employing the space charge limited current (SCLC) theory.

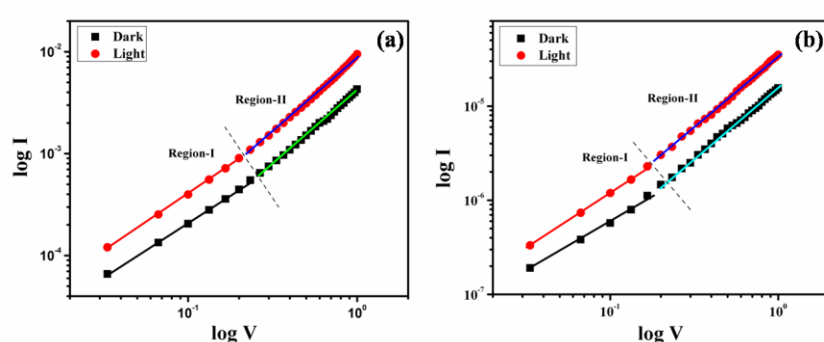


Figure 2.10 log I versus log V plot for (a) compound 1 and (b) compound 2 under dark and light condition.

The characteristic I-V curves in the dark/under light conditions in the logarithmic scale portrayed in Figure 2.10. Figure 2.10 clearly demonstrates two regions with different slopes, indicating different conduction mechanisms. The current conduction mechanism is governed

by the power law ($I \propto V^m$),⁴⁴ where m is the slope of the I vs. V curve. At low bias voltage (region-I), the sample exhibits an ohmic behavior, i.e., the current is directly proportional to the applied bias voltage ($I \propto V$). The I - V characteristics in this region can be attributed due to the thermionic emission and the current is dominated by bulk generated electrons of the film, rather than the injected free carriers.⁴⁵ The region II corresponds to the higher ordered magnitude of slope, exhibits variation of current with square of forward bias voltage ($I \propto V^2$) (Figure 2.11). In this region the current is governed by space charge, designated as space charge limited current (SCLC).⁴⁶ The trap distribution is the key factor in this type of charge transport mechanism.

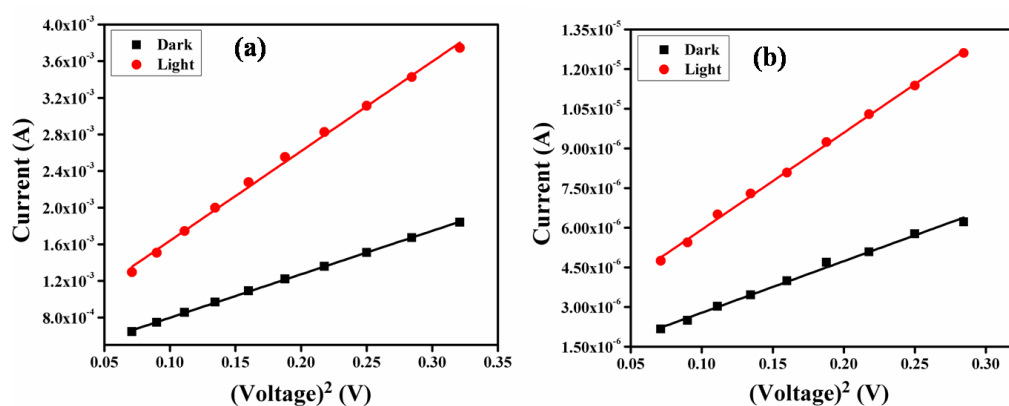


Figure 2.11 I vs V^2 plot of SCLC region under dark and photo condition for (a) compound 1 and (b) compound 2.

As the traps are exponentially distributed in this region, current increases rapidly. Moreover, to check the performance of the devices effective carrier mobility are evaluated from I vs V^2 plot (Figure 2.11) from the SCLC region, by evaluating the slope with the help of Mott-Gurney space-charge-limited-current (SCLC) equation (Eq. 9).^{47, 48}

$$I = \frac{9\mu_{\text{eff}}\epsilon_0\epsilon_r A}{8} \left(\frac{V^2}{d^3}\right) \quad (9)$$

Where, I is the current, ϵ_0 is the permittivity of free space and ϵ_r the dielectric constant.

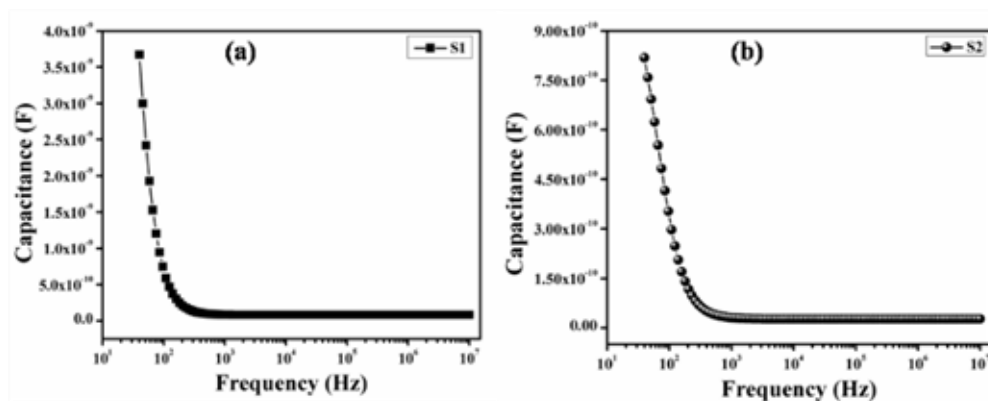


Figure 2.12 Capacitance versus frequency plot for (a) compound 1 and (b) compound 2.

The value of dielectric constant of the material is measured from capacitance versus frequency plot (C-f) (Figure 2.12) with the help of following equation:⁴⁹

$$\epsilon_r = \frac{Cd}{\epsilon_0 A} \quad (10)$$

Where, C is the capacitance (at saturation), d is the thickness and rest are same as defined previously. We have also theoretically determined dielectric constant of the compound **1** and **2**. Compound **1** has dielectric constant of 1.36 while for the compound **2** it is 1.25 which agrees well with the experimentally determined dielectric constants. The frequency dependent dielectric constant plot has been given in the supporting information. Mobility and transit time are the prime factor to determine the device performance. Transit time (τ) is defined as the time required by a carrier to travel from anode to cathode. It can be expressed as the summation of average total time spent by each electron as a free carrier plus total time spent in the trap.⁵⁰ The transit time (τ) of the charge carrier is deduced by using the equation (Eq. 11):⁵¹

$$\tau = \frac{9\epsilon_0\epsilon_r A}{8d} \left(\frac{V}{I}\right) \quad (11)$$

The effective mobility of the carriers under dark condition is evaluated as $5.21 \times 10^{-5} \text{ m}^2\text{V}^{-1}\text{s}^{-1}$ and $6.48 \times 10^{-7} \text{ m}^2\text{V}^{-1}\text{s}^{-1}$ for compound **1** and **2**. After irradiation of light the values of effective carrier mobility (μ_{eff}) improved to $1.07 \times 10^{-4} \text{ m}^2\text{V}^{-1}\text{s}^{-1}$ and $1.21 \times 10^{-6} \text{ m}^2\text{V}^{-1}\text{s}^{-1}$ for those compounds respectively. Longer transit time in dark condition leads to higher trapping probabilities⁵² but after illumination of light the situation is reverse due to the higher carrier mobility. The values of effective carrier mobility and transit time of compound **1** and **2** based

devices are tabulated in **Table-2.2**. Hence, compound **1** is better candidate than compound **2** for the application in photovoltaic devices.

Table 2.2 Schottky Diode Parameters.

Sample Name	Measured Condition	On/Off ratio	d(V)/d(lnI) vs. I Graph		H(I) vs. I Graph	
			Ideality Factor (η)	Series Resistance (R_s) (Ohm)	Barrier Height (ϕ_b) (eV)	Series Resistance (R_s) (Ohm)
Compound 1	Dark	16.00	1.23	286.71	0.60	287.30
	Light	34.64	1.05	148.09	0.58	147.56
Compound 2	Dark	17.39	2.23	7.57×10^4	0.76	7.49×10^4
	Light	28.25	1.42	3.28×10^4	0.74	3.59×10^4

2.2.4. DFT calculations

VASP as well as GAUSSIAN-09 program package⁵⁵ has been executed during all the theoretical calculations for the verification of experimental results. All the DFT calculations are periodic (performed using VASP package) except the HOMO-LUMO calculation where GAUSSIAN-09 program package has been used. In case of periodic calculation, unit cell of the compound **1** and **2** are considered as a repeating unit whereas HOMO-LUMO calculations are performed in the molecular level considering discrete monomer unit of compound **1** and **2**. The generalized gradient approximation method (GGA) parameterized by the Perdew-Burke-Ernzerhof (PBE) was used to account the exchange-correlation energy for computation using VASP package.⁵⁶⁻⁵⁷

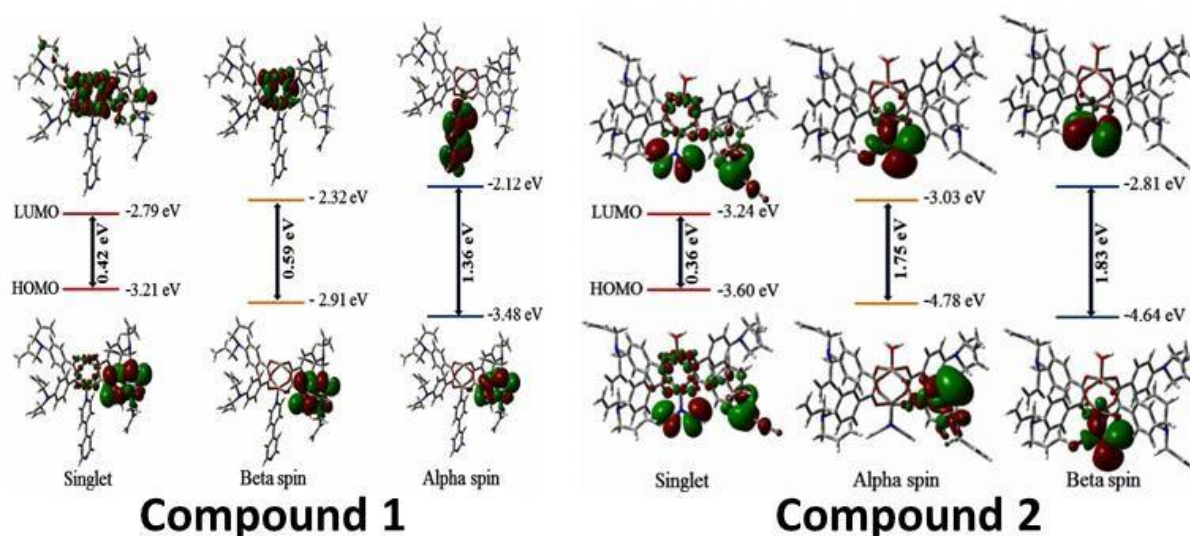


Figure 2.13 DFT calculated energy of molecular orbitals (MOs) and the energy difference between HOMO and LUMO of compound **1** and **2**.

The on-site coulomb repulsion U term (DFT+ U method) was used to improve the description of localized Cu d-electrons as well as on-site coulomb interaction in Cu based systems with $U_{\text{eff}} = 3.0$ eV as reported in the literature.⁵⁸⁻⁵⁹ The projector augmented wave potential (PAW) was used to treat the ion-electron interactions. The effect of van der Waals interactions were considered using empirical correction method proposed by Grimme (DFT-D2).⁶⁰ In all computations the kinetic energy cut off is set to be 500 eV in the plane-wave expansion. All the structures were fully relaxed (lattice constant and atomic position) using the conjugated gradient method and the convergence threshold was set to be 10^{-4} eV in energy and 0.01 eV/Å in force considering spin-polarization effect. For geometry optimization, the Brillouin zone is sampled with a $3 \times 3 \times 3$ Monkhorst-Pack grid. Density of states (DOS) was computed with the the Brillouin zone sampled with the same grid. In order to calculate the charge transfer between the Cu^{2+} cluster and different surfaces, we choose Bader charge-population analysis method.⁶¹ On the otherhand GAUSSIAN-09 program package have been executed for spin state calculation using the hybrid B3LYP/LanL2DZ exchange–correlation function as implemented. Here the lattice equivalent and deformation potentials were used to obtain the Schottky electrical contact. The deformation commonly refers to the energy gap between valence and conduction band which is the difference between highest occupied and lowest unoccupied molecular orbitals ($\Delta E = E_{\text{HOMO}} - E_{\text{LUMO}}$, eV). The band gap⁶² of CPs can be obtained by using absolute deformation potentials (ADPs). The calculated band gaps for compound **1** and **2** are 1.36 eV and 1.75 eV

(Figure 2.13) respectively. Therefore, the validity of verification of the electrical and magnetic

properties of the molecules has been successfully performed.

2.3. Experimental Section

2.3.1. Materials and general method

Sigma Aldrich helped us by providing all the required chemicals. Micro-analytical data (C, H, N) were collected on Perkin-Elmer 2400 CHNS/O elemental analyzer. Thermogravimetric analysis was recorded on a Perkin-Elmer Pyris Diamond TG/DTA in the temperature range between 30 °C and 600 °C under a nitrogen atmosphere at a heating rate of 12 °C min⁻¹. Single crystal of the compound 1 and 2 was used for data collection using a Bruker SMART APEX II diffractometer equipped with graphite-monochromated MoK α radiation ($\lambda = 0.71073 \text{ \AA}$). The crystal structure was solved using the SHELX-97 package. The PXRD data was collected on a Bruker D8 Advance X-ray diffractometer using Cu K α radiation ($\lambda = 1.548 \text{ \AA}$) generated at 40 kV and 40 mA. The PXRD spectrum was recorded in a 2θ range of 5–50. Magnetic properties were investigated using a Quantum Design MPMS-XL superconducting quantum interference device magnetometer (SQUID) at an applied field 0.5 T in a temperature range 5–300 K. The diamagnetic correction was carried out by using Pascal constants. The di-electrical study was carried out by evaluating capacitance (C), impedance (Z), and phase angle (θ) of the sample as a function of frequency (40 Hz–10 MHz) using a computer-controlled Agilent make precision 4294A LCR meter. The Current-Voltage (I-V) characteristics of two devices are recorded under dark and light (AM 1.5 radiation) condition with the help of Keithley 2635B source meter interfaced with PC by applying bias voltage in the range of -1 V to +1 V. All the measurements are performed at room temperature.

2.3.2. Synthesis of 4-Diallylamino-benzoic acid allyl ester

Allylations of 4-amino benzoic acid were carried out by using the literature procedure.⁵³ The obtained white solid (2.347 g, 97%) was recrystallized from methanol and tri allylation was characterised by ¹H NMR spectrum. ¹H NMR (300 MHz, CDCl₃): d 3.94 (d, 4H), d 4.75 (d, 2H), d 5.20 (m, 4H), d 5.33 (m, 2H), d 5.81 (m, 2H), d 6.01 (m, 1H), d 6.60 (m, 2H), d 7.90 (d, 2H) (Fig. 2.14)



Figure 2.14 The ^1H NMR spectrum of 4-Diallylamino-benzoic acid allyl ester.

2.3.3. Synthesis of 4-Diallylamino-benzoic acid

We have synthesized these reported compound⁵⁴ with modified procedure. Selective deallylation of 4-Diallylamino-benzoic acid allyl ester was carried out using the following procedure. To a 250 mL round bottom flask the 4-Diallylamino-benzoic acid allyl ester (2.347 g 9.72 mmol) was dissolved in a solution of NaOH (3.11 g, 8 equiv) in 50 mL MeOH and 50 mL H₂O and stirred at room temperature for 12 h. The reaction mixture was then acidified with 6N HCl, white precipitate comes out, filtered and residue was recrystallized from methanol, gives pure 4-Diallylamino-benzoic acid (2.015, g 95%) (Figure 2.15).

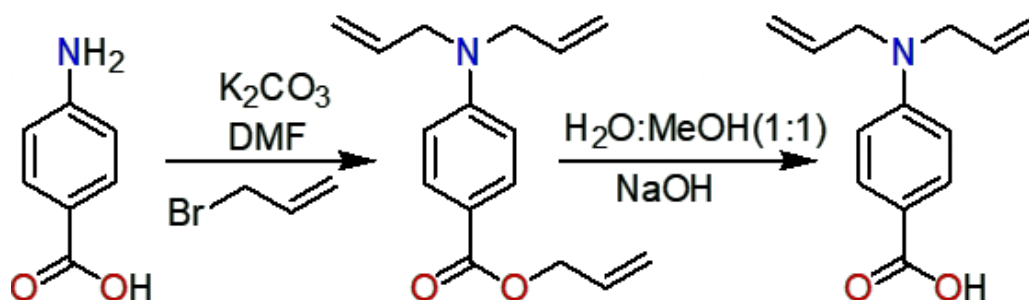


Figure 2.15 Schematic representation of the preparation of 4-Diallylamino-benzoic acid.

2.3.4. Synthesis of compound 1 and 2

A methanolic solution of (1 ml) of 4,4-BPY (15.619 mg, 0.1 mmol) was carefully layered by the help of water-methanol mixed solvent over the aqueous solution of (1 ml) of

$\text{Cu}(\text{NO}_3)_2 \cdot 3\text{H}_2\text{O}$, (24.16 mg, 0.1 mmol). HDABA (21.726 mg, 0.1 mmol) in ethanol (1 ml) was neutralized with Et_3N (10.119 mg, 0.1 mmol) and was layered cautiously over the 4,4-BPY followed by water-methanol mixed solvent to make an undisturbed layer. It was then allowed to diffuse for a week. The blue coloured needle-shaped crystals were deposited on the glass wall. The crystals were separated mechanically under a microscope and washed with methanol and water (1:1) mixture, and dried. The yield of $[\text{Cu}_2(\text{DABA})_4(4,4'\text{-BPY})]_n$, **1** was 75 % (45.934 mg). Elemental analysis calculated for (**1**); C, 58.23; H, 9.46; N, 7.75% and found C, 58.11; H, 9.53; N, 7.82%. The same synthetic procedure has been applied for compound **2** as adopted for **1**, except PYZ (8.009 mg, 0.1 mmol). The blue coloured block-shaped crystals were deposited on the glass wall. The yield of $[\text{Cu}_4(\text{DABA})_8(\text{PYZ})(\text{H}_2\text{O})_2]$, **2** was 80 % (43.158 mg). Elemental analysis calculated for (**2**); C, 59.23; H, 9.74; N, 6.42 % and found C, 59.32; H, 9.68; N, 6.37 %.

2.4. Conclusions

We have successfully synthesized two structurally distinct Cu based coordination polymers having 1D and 0D structures respectively with fascinating electrical and magnetic properties. These properties can be further tailored by modifying the axial linkers. Tuning of axial linkers leads to the formation of charge transfer complexes which significantly enhances its magnetic moment and improves its electrical properties.

2.5. References

- (1) Batten, S. R.; Neville, S. M.; Turner, D. R. Coordination Polymers. Design, Analysis and Application, *Royal Society of Chemistry*, London, **2009**.
- (2) Desiraju, G. R.; Vittal, J. J.; Ramanan, A. *Crystal Engineering*. A Textbook, World Scientific, Singapore, **2011**.
- (3) Zhou, H.-C.; Long, J. R.; Yaghi, O. M. Introduction to Metal–Organic Frameworks. *Chem. Rev.* **2012**, *112*, 673–674.
- (4) Moulton, B.; Zaworotko, M. J. From Molecules to Crystal Engineering: Supramolecular Isomerism and Polymorphism in Network Solids. *Chem. Rev.* **2001**, *101*, 1629–1658.
- (5) Natarajan, S.; Mahata, P.; Sarma, D. J. The relevance of metal organic frameworks (MOFs) in inorganic materials chemistry. *Chem. Sci.* **2012**, *124*, 339–353.

- (6) Biradha, K.; Su C.-Y.; Vittal, J. J. Recent Developments in Crystal Engineering. *Cryst. Growth. Des.* **2011**, *11*, 875–886.
- (7) Kitagawa, S.; Kitaura, R.; Noro, S.-I. Functional Porous Coordination Polymers. *Angew. Chem. Int. Ed.* **2004**, *43*, 2334–2375.
- (8) Choi, K. M.; Jeong, H. M.; Park, J. H.; Zhang, Y.; Kang, J. K.; Yaghi, O. M. Supercapacitors of nanocrystalline metal-organic frameworks. *ACS Nano.* **2014**, *8*, 7451-7457.
- (9) Férey, G.; Millange, F.; Morcrette, M.; Serre, C.; Doublet, M.; Grenèche, J.; Tarascon, J. Mixed-Valence Li/Fe-Based Metal–Organic Frameworks with Both Reversible Redox and Sorption Properties. *Angew. Chem. Int. Ed.* **2007**, *46*, 3259-3263.
- (10) Campbell, M. G.; Sheberla, D.; Liu, S.; Swager, T. M.; Dincă, M. Cu_3 (hexaiminotriphenylene)₂: an electrically conductive 2D metal-organic framework for chemiresistive sensing. *Angew. Chem. Int. Ed.* **2015**, *54*, 4349-4352.
- (11) Nohra, B.; Moll, H. E.; Albelo, M. R.; Mialane, P.; Marrot, J.; Mellot-Draznieks, C.; O’Keeffe, M.; Biboum, R. N.; Lemaire, J.; Keita, B.; Nadjo, L.; Dolbecq, A. Polyoxometalate-Based Metal Organic Frameworks (POMOFs): Structural Trends, Energetics, and High Electrocatalytic Efficiency for Hydrogen Evolution Reaction. *J. Am. Chem. Soc.* **2011**, *133*, 13363-13374.
- (12) Bayat, M.; Yang, H.; Ko, F. K.; Michelson, D.; Mei, A. Electromagnetic interference shielding effectiveness of hybrid multifunctional Fe₃O₄/carbon nanofiber composite. *Polymer.* **2014**, *55*, 936-943.
- (13) Wuang, S. C.; Neoh, K. G.; Kang, E.-T.; Pack, D. W.; Leckband, D. E. Synthesis and functionalization of polypyrrole-Fe₃O₄ nanoparticles for applications in biomedicine. *J. Mater. Chem.* **2007**, *17*, 3354-3362.
- (14) Zhang, D. Q.; Cheng, J. Y.; Yang, X. Y.; Zhao, B.; Cao, M. S. Electromagnetic and microwave absorbing properties of magnetite nanoparticles decorated carbon nanotubes/polyaniline multiphase hetero structures. *J. Mater. Sci.* **2014**, *49*, 7221-7230.
- (15) Mohideen, M. I. H.; Lei, C.; Tuc̃ek, J.; Malina, O.; Brivio, F.; Kasneryk, V.; Huang, Z.; Mazur, M.; Zou, X.; Nachtigall, P.; C̃ejka, J.; Morris, R. E. Magneto-structural

correlations of novel kagome'-type metal organic frameworks. *J. Mater. Chem. C.* **2019**, *7*, 6692-6697.

(16) Sengupta, A.; Datta, S.; Su, C.; Heng, T. S.; Ding, J.; Vittal, J. J.; Loh, K. P. Tunable Electrical Conductivity and Magnetic Property of the Two Dimensional Metal Organic Framework [Cu(TPyP)Cu₂(O₂CCH₃)₄]. *ACS Appl. Mater. Interfaces.* **2016**, *8*, 16154–16159.

(17) Yu, F.; Kurmoo, M.; Zhuang, G.-L.; Zuo, J.-L. Hierarchical tandem assembly of planar [3×3] building units into {3×[3×3]} oligomers: mixed-valency, electrical conductivity and magnetism. *Chem. Sci.* **2018**, *9*, 7498.

(18) Benbellat, N.; Gavrilenko, K. S.; Gal, Y. L.; Cador, O.; Golhen, S.; Gouasmia, A.; Fabre, J.-M.; Ouahab, L. Co(II)–Co(II) Paddlewheel Complex with a Redox-Active Ligand Derived from TTF. *Inorg. Chem.* **2006**, *45*, 10440-10442.

(19) Dutta, B.; Das, D.; Datta, J.; Chandra, A.; Jana, S.; Sinha, C.; Ray, P. P.; Mir, M. H. Synthesis of a Zn(II)-based 1D zigzag coordination polymer for the fabrication of optoelectronic devices with remarkably high photosensitivity. *Inorg. Chem. Front.* **2019**, *6*, 1245-1252.

(20) Dutta, B.; Dey, A.; Sinha, C.; Ray, P. P.; Mir, M. H. Photochemical Structural Transformation of a Linear 1D Coordination Polymer Impacts the Electrical Conductivity. *Inorg. Chem.* **2018**, *57*, 8029–8032.

(21) Naskar, K.; Maity, S.; Jana, S.; Dutta, B.; Tanaka, S.; Mallick, D.; Akitsu, T.; Sinha, C. Arylazoimidazole Coordinated and Naphthalene-Dicarboxylato Bridged Polymers of Co(II) and Photochromic Zn(II) Complexes. *Cryst. Growth. Des.* **2018**, *18*, 2986–2997.

(22) Dutta, B.; Jana, R.; Sinha, C.; Ray, P. P.; Mir, M. H. Synthesis of a Cd(II) based 1D coordination polymer by in situ ligand generation and fabrication of a photosensitive electronic device. *Inorg. Chem. Front.* **2018**, *5*, 1998-2005.

(23) Das, S.; Presselt, M. Progress and development in structural and optoelectronic tunability of supramolecular nonbonded fullerene assemblies. *J. Mater. Chem. C.* **2019**, 10.1039/C9TC00889F.

- (24) Lu, K.; Zhao, C.; Luan, L.; Duan, J.; Xie, Y.; Shao, M.; Hu, B. Exploring the role of spin-triplets and trap states in photovoltaic processes of perovskite solar cells. *J. Mater. Chem. C*, **2018**, *6*, 5055–5062.
- (25) Dutta, B.; Pratik, S. M.; Jana, S.; Sinha, C.; Datta, A.; Mir, M. H. Novel Br \cdots π (Chelate) Interaction in a 1D Coordination Polymer Revealing Aromaticity. *ChemistrySelect*. **2018**, *3*, 4289 – 4291.
- (26) Li, X.; Cheng, D.; Lin, J.; Li, Z.; Zheng, Y. Di-, Tetra-, and Hexanuclear Hydroxy-Bridged Copper(II) Cluster Compounds: Syntheses, Structures, and Properties. *Cryst. Growth. Des.* **2008**, *8*, 2853-2861.
- (27) Wannarit, N.; Siriwong, K.; Chaichit, N.; Youngme, S.; Costa, R.; Moreira, I. P. R.; Illas, F. New Series of Triply Bridged Dinuclear Cu(II) Compounds: Synthesis, Crystal Structure, Magnetic Properties, and Theoretical Study. *Inorg. Chem.* **2011**, *50*, 10648–10659.
- (28) Reyes-Ortega, Y.; Alcantara-Flores, J.; Hernandez-Galindo, M.; Ramírez-Rosales, D.; Berne's, S.; Ramírez-García, J.; Zamorano-Ulloa, R.; Escudero, R. Magnetic Properties and Crystal Structure of a One-Dimensional Phase of Tetrakis (μ_2 -benzoato O, O')-bis (dimethyl sulfoxide) dicopper(II). *J. Am. Chem. Soc.* **2005**, *127*, 16312-16317.
- (29) Costa, R.; Lo'pez, C.; Molins, E.; Espinosa, E. Synthesis, Structure, and Properties of a Tetrametallic Ferrocenecarboxylato-Bridged Copper(II) Complex. *Inorg. Chem.* **1998**, *37*, 5686-5689.
- (30) Lo'pez, C.; Costa, R.; Illas, F.; Molins, E.; Espinosa, E. Ferromagnetic Copper(II) Complex Containing Ferrocenecarboxylato Bridging Ligands. *Inorg. Chem.* **2000**, *39*, 4560-4565.
- (31) Huang, P.-J.; Natori, Y.; Kitagawa, Y.; Sekine, Y.; Kosaka, W.; Miyasaka, H. One-Dimensional Chains of Paddlewheel-Type Dichromium(II,II) Tetraacetate Complexes: Study of Electronic Structure Influenced by σ - and π - Donation of Axial Linkers. *Inorg. Chem.* **2018**, *57*, 5371–5379.
- (32) Reger, D. L.; Debreczeni, A.; Smith, M. D. Copper(II) Carboxylate Dimers Prepared from Ligands Designed to Form a Robust $\pi\cdots\pi$ Stacking Synthons: Supramolecular Structures and Molecular Properties. *Inorg. Chem.* **2012**, *51*, 1068–1083.

- (33) Sil, S.; Datta, J.; Das, M.; Jana, R.; Halder, S.; Biswas, A.; Sanyal, D.; Ray, P. P. Bias dependent conduction and relaxation mechanism study of Cu₅FeS₄ film and its significance in signal transport network. *J. Mater. Sci.* **2018**, *29*, 5014-5024.
- (34) Dökme, İ.; Altındal, Ş.; Gökçen, M. Frequency and gate voltage effects on the dielectric properties of Au/SiO₂/n-Si structures, *Microelectron. Eng.* **2008**, *85*, 1910-1914.
- (35) Kamalasanan, M. N.; Kumar, N. D.; Chandra, S. Dielectric and ferroelectric properties of BaTiO₃ thin films grown by the sol-gel process. *J. Appl. Phys.* **1993**, *74*, 5679-5686.
- (36) Mukherjee, R.; Dutta, A.; Sinha, T. P. Dielectric Relaxation of Rare Earth Ordered Double Perovskite Oxide Ba₂ErTaO₆. *J. Electron. Mater.* **2016**, *45*, 846-852.
- (37) Chanda, S.; Saha, S.; Dutta, A.; Irfan, B.; Chatterjee, R.; Sinha, T. P. Magnetic and dielectric properties of orthoferrites La_{1-x}Pr_xFeO₃ (x = 0, 0.1, 0.2, 0.3, 0.4 and 0.5). *J. Alloys. Compd.* **2015**, *649*, 1260-1266.
- (38) Rhoderick, E. H.; Williams, R. H. Metal-Semiconductor Contacts, Clarendon Press, Oxford, 2nd edn, **1988**.
- (39) Sze, S. M. Physics of Semiconductor Devices, Wiley, New York. **1981**.
- (40) Dey, A.; Layek, A.; Roychowdhury, A.; Das, M.; Datta, J.; Middya, S.; Das, D.; Ray, P. P. Investigation of Charge Transport Properties in Less Defective Nanostructured ZnO Based Schottky Diode. *RSC Adv.* **2015**, *5*, 36560-36567.
- (41) Das, M.; Datta, J.; Dey, A.; Jana, R.; Layek, A.; Middya, S.; Ray, P. P. One step hydrothermal synthesis of a rGO-TiO₂ nanocomposite and its application on a Schottky diode: improvement in device performance and transport properties. *RSC Adv.* **2015**, *5*, 101582-101592.
- (42) Jana, R.; Dey, A.; Das, M.; Datta, J.; Das, P.; Ray, P. P. Improving performance of device made up of CuO nanoparticles synthesized by hydrothermal over the reflux method. *Appl. Surf. Sci.* **2018**, *452*, 155-164.
- (43) Gupta, R. K.; Yakuphanoglu, F.; Photoconductive Schottky Diode Based on Al/p-Si/SnS₂/Ag for Optical Sensor Applications. *Sol. Energy.* **2012**, *86*, 1539-1545.
- (44) Hwang, W.; Kao, K. Electrical transport in solids, Pergamon Press, Oxford/New York, **1981**.

- (45) Tasçioğlu, I.; Aydemir, U.; Altındal, S.; Barrier height fluctuations in InGaN polarization dipole diodes. *J. Appl. Phys.* **2010**, *108*, 064506.
- (46) Jain, A.; Kumar, P., S. Jain, C.; Kumar, V.; Kaur, R., Mehra, R. M. Trap Filled Limit Voltage (VTFL) and V^2 Law in Space Charge Limited Currents. *J. Appl. Phys.* **2007**, *102*, 94505-94509.
- (47) Soylu, M.; Abay, B. Analysing space charge-limited conduction in Au/n-InP Schottky diodes, *Physica E Low Dimens. Syst. Nanostruct.* **2010**, *43*, 534-538.
- (48) Das, M.; Datta, J.; Jana, R.; Sil, S.; Halder, S.; Ray, P. P. Synthesis of rGO-Zn_{0.8}Cd_{0.2}S Via In Situ Reduction of GO For the Realization Of a Schottky Diode With Low Barrier Height and Highly Enhanced Photoresponsivity. *New J. Chem.* **2017**, *41*, 5476-5486.
- (49) Middy, S.; Layek, A.; Dey, A.; Datta, J.; Das, M.; Banerjee, C.; Ray, P.P. Role of zinc oxide nanomorphology on Schottky diode properties. *Chem. Phys. Lett.* **2014**, *610*, 39-44.
- (50) Sil, S.; Dey, A.; Datta, J.; Das, M.; Jana, R.; Halder, S.; Dhar, J.; Sanyal, D.; Ray, P. P. Analysis of interfaces in Bornite (Cu₅FeS₄) fabricated Schottky diode using impedance spectroscopy method and its photosensitive behaviour. *Mater. Res. Bull.* **2018**, *106*, 337-345.
- (51) Datta, J.; Das, M.; Dey, A.; Halder, S.; Sil, S.; Ray, P. P. Network analysis of semiconducting Zn_{1-x}Cd_xS based photosensitive device using impedance spectroscopy and current-voltage measurement. *Appl. Surf. Sci.* **2017**, *420*, 566-578.
- (52) Kao, K.C. Dielectric phenomena in solids, Academic press, **2004**.
- (53) Nawghare, B. R.; Sakate, S. S.; Lokhande, P. D. A New Method for the Facile Synthesis of Hydroxylated Flavones by Using Allyl Protection. *J. Heterocyclic Chem.* **2014**, *51*, 291-302.
- (54) Konda, S. G.; Humne, V. T.; Lokhande, P. D. Rapid and selective deallylation of allyl ethers and esters using iodine in polyethylene glycol-400. *Green Chem.* **2011**, *13*, 2354-2358.
- (55) Frisch, M. J.; Trucks, G. W.; Schlegel, H. B.; Scuseria, G. E.; Robb, M. A.; Cheeseman, J. R.; Scalmani, G.; Barone, V.; Mennucci, B.; Petersson, G. A.; Nakatsuji, H.; Caricato, M.; Li, X.; Hratchian, H. P.; Izmaylov, A. F.; Bloino, J.; Zheng, G.; Sonnenberg, J. L.; Hada, M.; Ehara, M.; Toyota, K.; Fukuda, R.; Hasegawa, J.; Ishida, M.; Nakajima, T.; Honda, Y.; Kitao, O.; Nakai, H.; Vreven, T.; Montgomery, J. A.; Peralta, J. E.; Ogliaro, F. M.; Bearpark, J.;

Heyd, J.; Brothers, E.; Kudin, K. N.; Staroverov, V. N.; Kobayashi, R.; Normand, J.; Raghavachari, K.; Rendell, A.; Burant, J. C.; Iyengar, S. S.; Tomasi, J.; Cossi, M.; Rega, N.; Millam, J. M.; Klene, M.; Yazyev, O.; Austin, A. J.; Cammi, R.; Pomelli, C.; Ochterski, J. W.; Martin, R. L.; Morokuma, K.; Zakrzewski, V. G.; Salvador, G. A. P.; Dannenberg, J. J.; Dapprich, S.; Daniels, A. D.; Farkas, Ö.; Foresman, J. B.; Ortiz, J. V.; Cioslowski, J.; Fox, D. J. Gaussian, Inc., CT Wallingford, **2009**.

(56) Kresse, G.; Hafner, J. Ab initio molecular dynamics for liquid metals. *Phys. Rev. B.* **1993**, *47*, 558.

(57) Perdew, J. P.; Burke, K.; Ernzerhof, M. Generalized gradient approximation made simple. *Phys. Rev. Lett.* **1996**, *77*, 3865.

(58) Mishra, A. K.; Roldan, A.; Leeuw, N. H. CuO Surfaces and CO₂ Activation: A Dispersion-Corrected DFT+*U* Study. *J. Phys. Chem. C.* **2016**, *120*, 2198–2214.

(59) Journal of Physics: Conference Series , **2016**, *739*, 012040.

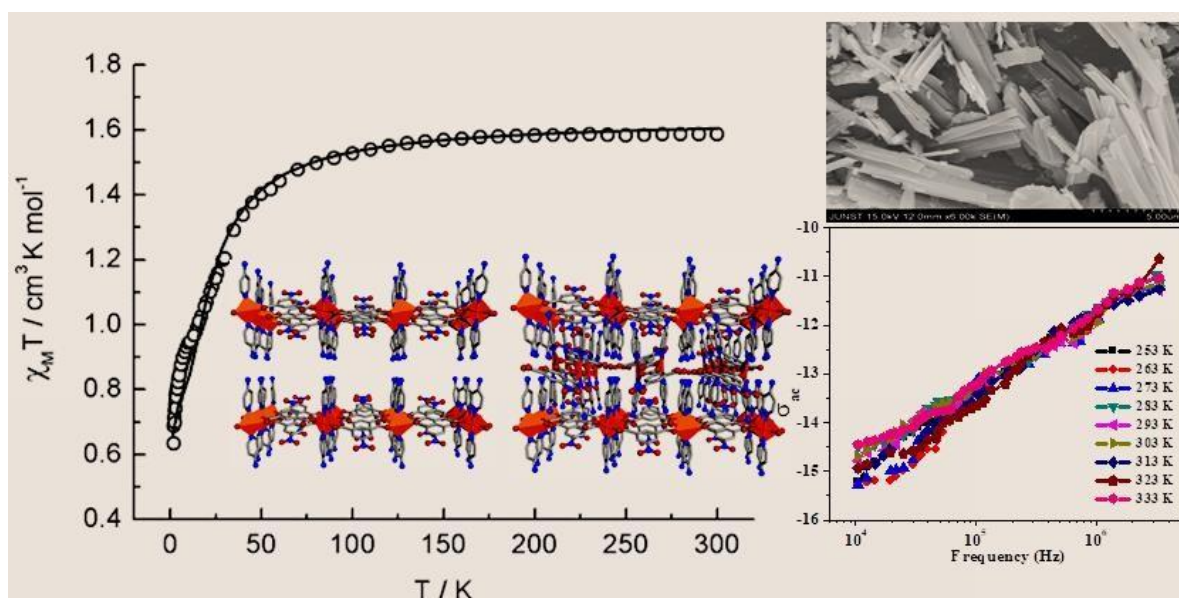
(60) Grimme, S. Semiempirical GGA- type density functional constructed with a long- range dispersion correction. *J. Comput. Chem.* **2006**, *27*, 1787-1799.

(61) Henkelman, G.; Arnaldsson, A.; Jónsson, H. A fast and robust algorithm for Bader decomposition of charge density. *Comput. Mater. Sci.* **2006**, *36*, 354-360.

(62) Li, Y.-H.; Gong, X. G.; Wei, S.-H. Ab Initio Calculation of Hydrostatic Absolute Deformation Potential of Semiconductors. *Appl. Phys. Lett.* **2006**, *88*, 042104–042106.

Abstract

One Dimensional Cu(II) coordination polymer with encapsulated antiferromagnetically coupled binuclear Cu(II) has been synthesized by using 5-nitroisophthalic acid (5-N-IPA) and 4-aminopyridine (4-APY) $[\text{Cu}_2(5\text{-N-IPA})_2(4\text{-APY})_4]_n$ (**1**). Electrical properties are examined by Complex impedance (Z^*), dielectric permittivity (ϵ^*), and ac conductivity studies at different frequencies (10 kHz–5MHz) and temperature (253 K–333 K). The contribution of grain and grain boundary have been explained by different theoretical model. The variable temperature magnetic susceptibility data for compound **1** were recorded between 300 and 2 K. The shape of the curve ($\chi_M T$ vs T) indicates dominant antiferromagnetic coupling, which results from the interaction between the copper(II) atoms.



3.1. Introduction

Coordination polymers (CPs)¹⁻⁷ have been commodiously used in various fields (**Chapter 1**) such as in supercapacitor,⁸⁻¹¹ batteries,¹² gas storage and separation, sensing¹³ and electrocatalysis.¹⁴ But CPs with prominent magnetic and dielectric properties are of great attention as functional materials due to their embryonic applications in the fields such as for electromagnetic interference shielding,¹⁵ capacitors,^{16,17} microwave tunable devices^{18,19} and broadband electric-field tunable devices.²⁰ Dielectric spectroscopy is routinely used to accumulate the information on the ac conduction mechanism and dielectric relaxation in a immense frequency range for different temperatures. The flexible qualitative delineation often provides new intuition into the field of dielectric behavior. For example, localized (i.e., long range conductivity) and non-localized (i.e., dielectric relaxation) conduction processes inside the material can be esteemed by the non-existence or existence of relaxation peak in frequency dependent hypothetical modulus plot. Performance of dielectric parameter has been explored on transition metal oxide amorphous semiconductor, oxide perovskite materials, ionically conducting polymer, and conducting glass.²¹⁻²³ Recently, comprehensive study on ac conductivity and dielectric relaxation of $\text{CH}_3\text{NH}_3\text{PbX}_3$ (X=Br, I) has been reported, which shows the dominance of non-Debye type relaxation inside the material.^{24,25} In order to acquire long-range charge conduct and obvious magnetic behaviour, it is pivotal for these compounds to have tough intramolecular coupling and strong intermolecular ordering. One of the incredible characteristics of CP is its potentiality to acquire distinct structural architecture under varying environments. The functional groups of the ligands and the length of organic spacer, the reaction condition, the nature and the oxidation of metal ions immensely control the structure of the CPs. Among the 3d transition metal ions nontoxic Cu(II) (d^9) can display a wide distinction of structures and nuclearity. The magnetic superexchange interactions in the middle of copper centres across the bridging ligands of Cu(II) compounds are established.^{26,51} But the charge transfer Mechanism and Dielectric behaviour of coordination polymers have not been much explored. Recently Zuo et al.²⁸ and Loh et al.²⁷ reported the magnetic and conductivity property of copper based CPs.

In this Chapter, the 5-nitroisophthalate ion forms 1D coordination polymer with Cu(II) metal knot and two axial positions are occupied by 4-aminopyridine. The structure shows encapsulation of dinuclear Cu(II) in the 1D coordination polymer. The multinuclear Cu(II)-CP shows antiferromagnetic coupling and temperature dependent dielectric properties.

3.2. Results and Discussion

3.2.1. Structure and Morphology of compound 1, $[\text{Cu}_2(5\text{-N-IPA})_2(4\text{-APY})_4]_n$

$[\text{Cu}_2(5\text{-N-IPA})_2(4\text{-APY})_4]_n$ crystallizes in the monoclinic $P 21/c$ space group with $Z = 4$ and the details of refinement parameters and crystal data for compound 1 are tabulated in Table 3.1. The structure analysis of 1 has revealed that two types of copper centres are there (Figure 3.1a). One of them forms 1D polymeric network via carboxylato bridging in the square of 5-N-IPA. 4-APY is appended to the axial coordination site of Cu(II) in the dimensional network and are hydrogen bonded (3.32 Å) with amino group of another 1D network to form porous 2D network (Figure 3.1b-c). In the pore of these 2D network dinuclear Cu(II) are encapsulated by the help of hydrogen bonding and $\pi \cdots \pi$ interactions (Figure 3.1d).

Table 3.1 Crystal data and refinement parameters for compound 1.

Formula	$\text{C}_{36} \text{H}_{31} \text{Cu}_2 \text{N}_{10} \text{O}_{13}$
CCDC No.	1920033
Fw	938.81
Crystalsyst	Monoclinic
space group	$P 21/c$
a (Å)	15.485(3)
b (Å)	20.386(4)
c (Å)	12.655(2)
α (deg)	90
β (deg)	101.146(5)
γ (deg)	90
V (Å ³)	3919.5(13)
Z	4
D_{calcd} (g/cm ³)	1.591
μ (mm ⁻¹)	1.165
λ (Å)	0.71073
data[$I > 2\sigma(I)$]/params	6895/551
GOF on F^2	1.100
final R indices[$I > 2\sigma(I)$] ^{a,b}	$R1 = 0.0451$ $wR2 = 0.1265$

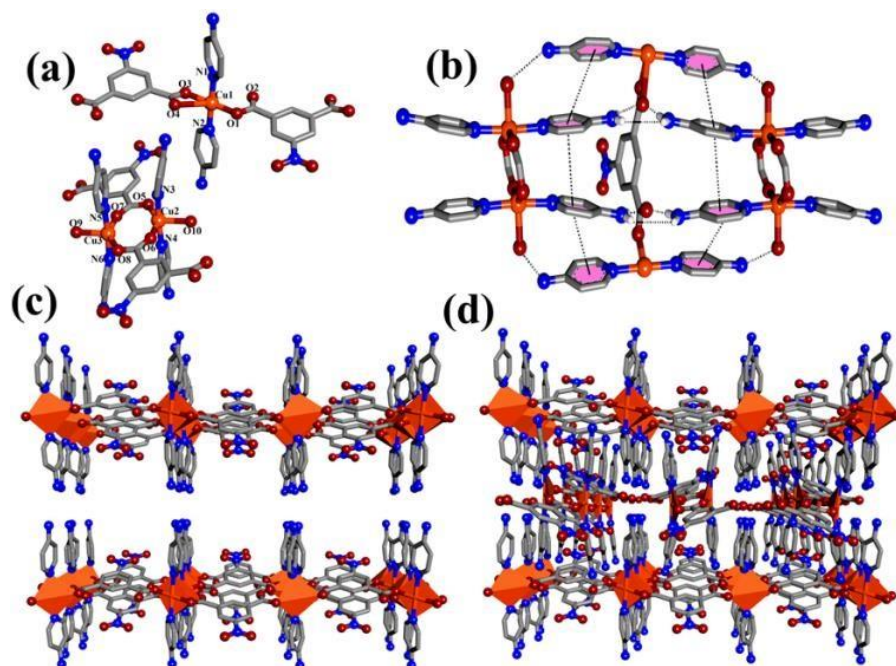


Figure 3.1 (a) The coordination spheres of the Cu(II) atoms, (b) a schematic presentation displaying the presence of $\pi \cdots \pi$ interactions and hydrogen bonding in the compound. (c) A portion of the 2D connectivity, (d) one Dimensional Cu(II) CP with Encapsulated dinuclear Cu(II).

The geometry around Cu centres in dinuclear Cu(II) are distorted square pyramidal, where Cu \cdots Cu separation lies in the range 3.388 Å. This complex have the potential to form higher dimensional structures throughout H-bonding (2.865–3.3320 Å) and Supramolecular (aromatic $\pi \cdots \pi$) interactions (3.869–4.148 Å), (Figure 3.1b).^{29-32,51-52} Furthermore, morphologies of 1 was examined by field emission scanning electron microscopy (FESEM). **Figure 3.2** is displays that the nanosheets are firmly stacked and intertwined with each other.

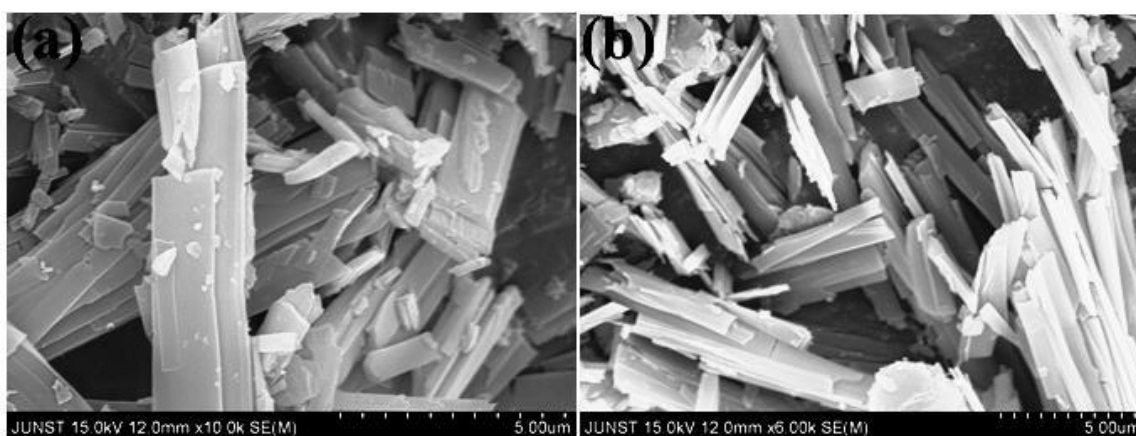


Figure 3.2 FESEM images of compound 1.

3.2.2. TGA and PXRD analysis

Thermogravimetric analysis (TGA) of compound **1** is displayed that the compound is thermally stable up to 373 K (Figure 3.3). Therefore, no decomposition or deformation occurs of the compound **1** at examined temperatures. The PXRD patterns of as synthesized compound exhibit broad diffraction peaks at 2θ (degree) are 9.34, 10.55, 11.56, 14.38, 16.80, 19.48, 20.43, 22.55, 23.66, 26.28 and 30.23 which correspond to (111), (120), (200), (102), (122), (132), (302), (042), (113), (322) and (502) planes respectively, were matched with the corresponding peaks of simulated pattern, which confirmed the bulk sample have uncontaminated (Figure 3.4).

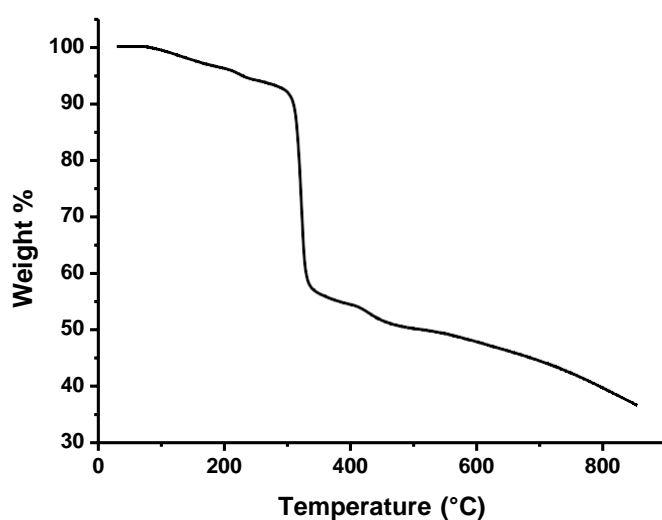


Figure 3.3 TGA curves of compound **1**.

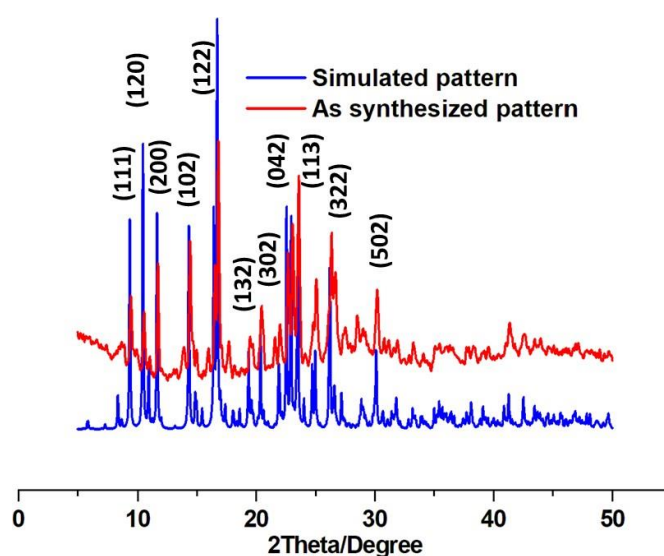


Figure 3.4 PXRD patterns of compound **1**: simulated pattern (black), as synthesized pattern (red).

3.2.3. Magnetic Study

The variable temperature magnetic susceptibility data for compound **1** were recorded between 300 and 2 K. A plot of $\chi_M T$ versus T is shown in **Figure 3.5**. At room temperature $\chi_M T$ is equal to $1.586 \text{ cm}^3 \text{ K mol}^{-1}$, which is close to four uncoupled copper(II) ions with local spin $S = 1/2$ and $g \approx 2.06$.

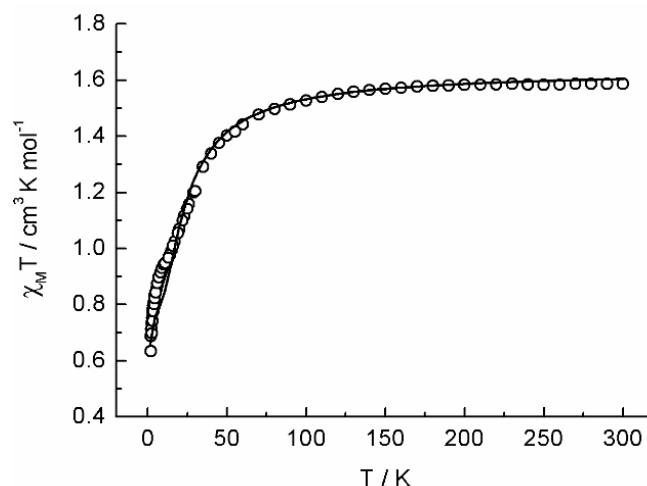


Figure 3.5 Plot of the $\chi_M T$ vs T for compound **1** (per four Cu atoms). Solid line shows the best fit of the data (see text).

When the sample is cooled, the $\chi_M T$ decreases slowly and below 75 K decreases more rapidly to value of $0.634 \text{ cm}^3 \text{ K mol}^{-1}$ at 2 K, which is slightly less for two isolated Cu(II) ions ($0.75 \text{ cm}^3 \text{ K mol}^{-1}$). The shape of this curve indicates dominant antiferromagnetic coupling, which results from the interaction between the copper(II) atoms. To fit the magnetic data, we consider two copper of the four present in the elemental cell as isolated from the magnetic point of view.

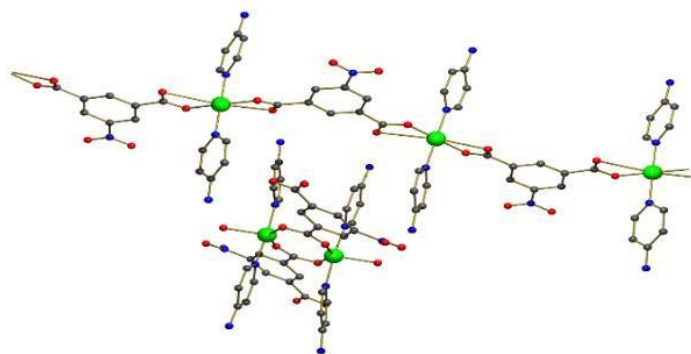


Figure 3.6 Structure of compound **1** showing the dinuclear and catena Cu(II) fragments formed.

The interaction through the 5-Nitroisophthalate ligand in the monodimensional fragment must be negligible ($\text{Cu}\cdots\text{Cu} = 10.225 \text{ \AA}$) (Figure 3.6), following, thus, the Curie law for each isolated Cu(II). This part can be subtracted from the global magnetic susceptibility to give only that corresponding to the dinuclear fragment $[\text{Cu(II)}]_2$ which is antiferromagnetically coupled. Considering the above, the experimental data were fitted to the Bleaney-Bowers expression for an isotropically coupled pair of $S = 1/2$ ions (eq 1),³³ in conjunction with an additional mean field correction term, χ_{MF} (eq 2), where N is Avogadro's number, μ_{B} is the Bohr magneton, k is the Boltzmann constant, and z is the number of nearest neighbors.

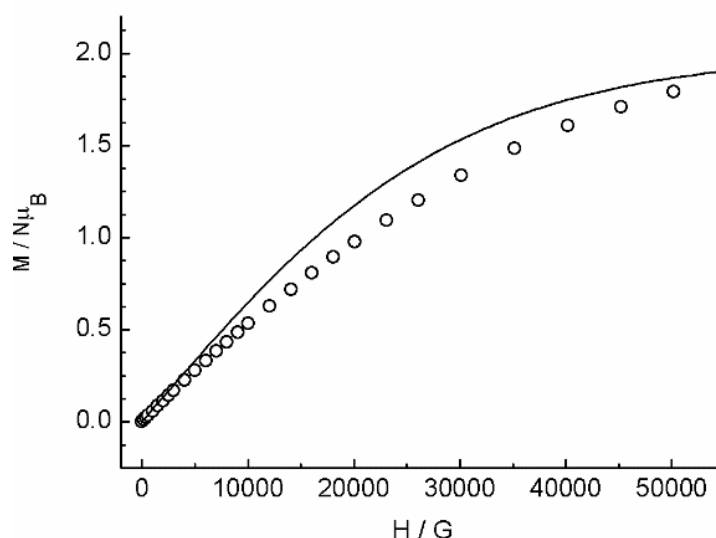


Figure 3.7 The field dependence of reduced magnetization at 2 K for compound **1** (per four Cu atoms), continuous line correspond to the Brillouin function for two isolated $S = 1/2$ and $g = 2.0$

The best least-squares fit parameters gave $J = -29.5 \text{ cm}^{-1}$, $zJ' = -0.5 \text{ cm}^{-1}$, $g = 2.09$ and $R = 8.21 \cdot 10^{-5} = \sum_i (\chi_{\text{M}} T_{\text{cal}} - \chi_{\text{M}} T_{\text{obs}})^2 / (\chi_{\text{M}} T_{\text{obs}})^2$.

$$\chi_{\text{M}} = \frac{Ng^2\mu_{\text{B}}^2}{KT} \frac{2 \exp(J/kT)}{1 + 3 \exp(J/kT)} \quad (1)$$

$$\chi_{\text{MF}} = \frac{\chi_{\text{M}}}{1 - \chi_{\text{M}} \left(\frac{-zJ'}{Ng^2\mu_{\text{B}}^2} \right)} \quad (2)$$

The field dependence of magnetization (0-5 T) measured at 2 K for compound **1** is shown in Figure 3.7, in the form of $M/N\mu_{\text{B}}$ (per Cu_4 unit) vs H . The magnetization reaches a value of $1.79 M/N\mu_{\text{B}}$ at 5 T, which is slightly less to the expected $S = 1/2$ value of two isolated copper (II) atom.

3.2.4. Dielectric studies

The complex dielectric permittivity, ε^* , of a material can be expressed as eq. (3)^{34,35}

$$\varepsilon^*(\omega) = \varepsilon'(\omega) - j\varepsilon''(\omega) \quad (3)$$

where $\varepsilon'(\omega)$ and $\varepsilon''(\omega)$ are the real and imaginary part of complex dielectric constant and $\omega = 2\pi f$. Here, $\varepsilon'(\omega)$ and $\varepsilon''(\omega)$ represent the amount of electrical potential energy stored and the amount of energy dissipated due to polarization, respectively.^{36,37} The real and imaginary dielectric constant of the complex can be calculated from the measured capacitance in parallel mode by using following eqs. (4, 5)

$$\varepsilon'(\omega) = \frac{C_p d}{\varepsilon_0 A} \quad (4)$$

$$\varepsilon''(\omega) = \varepsilon'(\omega) \tan\delta \quad (5)$$

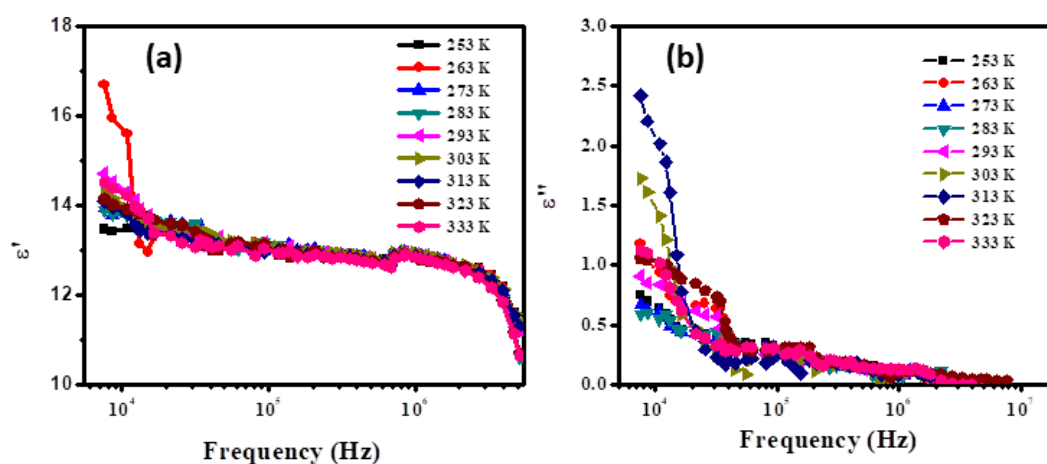


Figure 3.8 (a) Frequency dependence $\varepsilon'(\omega)$ at different temperatures, (b) Frequency dependence $\varepsilon''(\omega)$ at different temperatures of compound **1**.

Where C_p is known as the capacitance of the sample, ε_0 (8.85×10^{-14} F/cm) is the dielectric permittivity in vacuum, A is the effective surface area of the pellet and d is the thickness of the pellet, $\tan\delta$ is the loss tangent or dissipation factor. The frequency dependence $\varepsilon'(\omega)$ for the compound **1** depicts (Figure 3.8a) that $\varepsilon'(\omega)$ decreases gradually with increasing frequency. This behavior is in agreement with the natural properties of organic and inorganic hybrid materials.⁴⁴⁻⁴⁷ At low frequency, it has been observed that $\varepsilon'(\omega)$ is increased with increasing temperature. Generally, there are four types of polarization such as electronic, ionic, orientation and space charge polarization, which are mainly responsible for high dielectric constant of the material.^{35,50} This dielectric constant also strongly depends on the

purity and perfection of the synthesized samples. The increases of $\epsilon'(\omega)$ of this material may be due to the presence of metal ions with organic moieties and non-bridging oxygen atom, which generate dangling bond.^{48,49} These metal ions contribute to the space charge polarization which leads to the increase of $\epsilon'(\omega)$. The small change in $\epsilon'(\omega)$ with increasing applied temperatures also observed for all samples which may be due to the increase of ionic polarization at low frequency region.^{38,39} The frequency and temperature dependence $\epsilon''(\omega)$ (Figure 3.8b) for this material shows that $\epsilon''(\omega)$ decreases with increasing frequency at all temperatures. It has been observed that $\epsilon''(\omega)$ increases faster with temperature at low frequency region. This may be due to the crystal defects in the material generate potential barriers for charge transport process. As a result the contribution of space charges becomes limited until they are stopped at grain boundary. In low frequency region four types of polarizations contribute significantly to $\epsilon''(\omega)$ but contribution of ionic and orientational polarizations reduce at higher frequency region. This effect decreases $\epsilon''(\omega)$ with increase of frequency for the examined temperatures.^{40,41}

3.2.5. Complex impedance study

The complex impedance properties of the compound **1** has been performed over an extensive range of frequency from 10 kHz to 5 MHz for different temperatures (253 K – 333 K) using complex impedance spectroscopy (CIS). This impedance spectroscopy method is the most important method to explain the ionic movement mechanism of a material and the contribution of grain boundary and grain.⁴² The details information about the resistive and capacitive properties of the material can be obtained from this study. The frequency dependence complex impedance (Z^*) can be obtained using this model and represented as eq. (6)

$$Z^*(\omega) = Z'(\omega) + jZ''(\omega) \quad (6)$$

Where, the frequency dependence real part of impedance $Z'(\omega)$ and imaginary part of impedance $Z''(\omega)$ can be expressed in eqs. (7, 8)

$$Z'(\omega) = \frac{R_g}{[1+(\omega R_g C_g)^2]} + \frac{R_{gb}}{[1+(\omega R_{gb} C_{gb})^2]} \quad (7)$$

$$Z''(\omega) = \frac{\omega C_g R_g^2}{[1+(\omega R_g C_g)^2]} + \frac{\omega C_{gb} R_{gb}^2}{[1+(\omega R_{gb} C_{gb})^2]} \quad (8)$$

Where, $\omega = 2\pi f$, R_g = grain resistance, C_g = grain capacitance, R_{gb} = grain boundary resistance and C_{gb} = grain boundary capacitance.^{34,35,42}

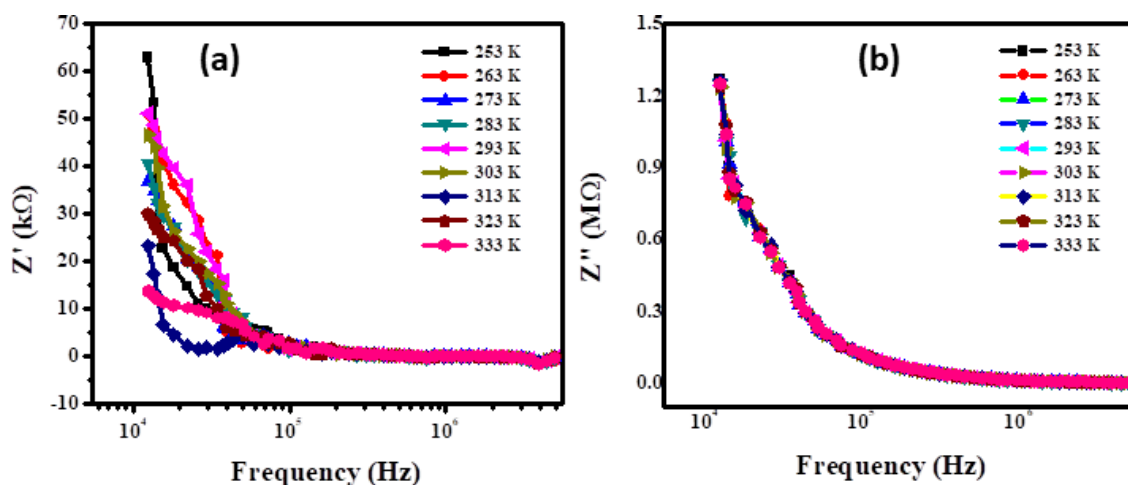


Figure 3.9 (a) Frequency dependence $Z'(\omega)$ at different temperatures, (b) Frequency dependence $Z''(\omega)$ at different temperatures of compound **1**.

The variation of $Z'(\omega)$ as a function of frequency and temperature (Figure 3.9a) for this compound **1** follows a sigmoidal type variation with increase in frequency. The $Z'(\omega)$ values show higher in low frequency region and consequently decrease with increase of frequency and temperature. This nature reveals the increase of ac conductivity as well as the presence of negative temperature coefficient of resistance (NTCR) of this material, which can generally suggest the semiconducting nature of this compound. Higher values of $Z'(\omega)$ in the low frequency and temperature significantly reveal the effect of large polarization. The decrease in $Z'(\omega)$ value at higher frequency and temperature clearly indicates the less contribution of grain boundaries in total resistance, leading to increase of ac conductivity with increase of temperature as well as frequency.³⁵

3.2.6. AC Conductivity

To explain the effect of Cu centres on the electrical conductivity of the one dimensional Cu(II) CP with encapsulated antiferromagnetically coupled dinuclear Cu(II), the electrical conductivity measurement has also been done. Figure 3. 10 reveals the variation of ac conductivity for the compound **1**. The lower conductivity for the material could be attributed to low level of protonation of the carboxylate, nitro and/or amino groups of the coordination polymer. The enhancement of ac conductivity for this material comes from the effective dispersion of compound in the matrix, which favours improved electronic transport. It can be observed that the conductivity of the one dimensional Cu(II) CP with encapsulated

antiferromagnetically coupled dinuclear Cu(II) increases with frequency and the slope becomes higher at higher frequency region. The ac conductivity is also considered to be the combine effect of intrinsic electric dipole polarization and interface charge polarization.

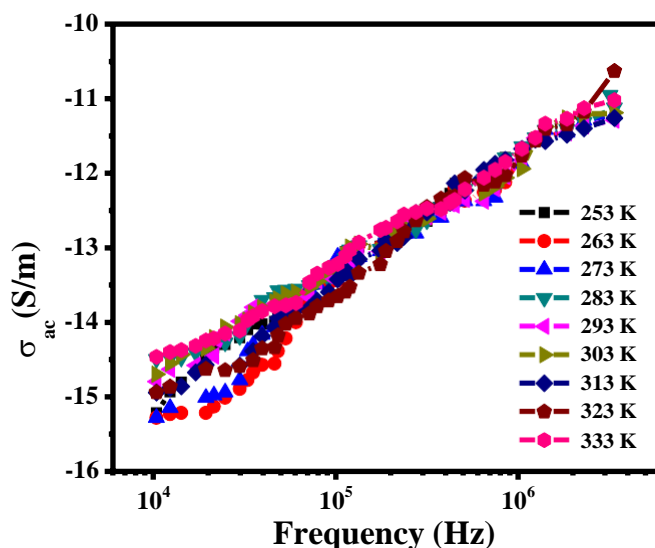


Figure 3.10 Frequency dependence of $\sigma_{ac}(\omega)$ at different temperatures of compound **1**.

The phenomenon appears in metal organic polymeric system. The reason behind this is the piling of mobile charges at the interfaces and as a result, large dipoles on metal particles or clusters are made. Polarization as well as ac conduction inside the coordination polymer is found to be dependent on the concentration of these metal particles.^{34,36,43}

3.2.7. DFT calculations

GAUSSIAN-09 program package⁵³ have been executed for spin state calculation using the hybrid B3LYP/LanL2DZ exchange–correlation function as implemented. In case of theoretical calculation, asymmetric unit of the single crystal of the compound are considered as a repeating unit and also HOMO-LUMO calculation are performed on this unit. Here the lattice equivalent and deformation potentials were used to obtain the band gap. The deformation commonly refers to the energy gap between valence and conduction band which is the difference between highest occupied and lowest unoccupied molecular orbitals ($\Delta E = E_{\text{HOMO}} - E_{\text{LUMO}}$, eV). The band gap⁵⁴ of CPs can be obtained by using absolute deformation potentials (ADPs). The calculated band gap for the compound is 0.32 eV (Figure 3.11). Therefore, the validity of verification of the electrical properties of the compound has been successfully performed.

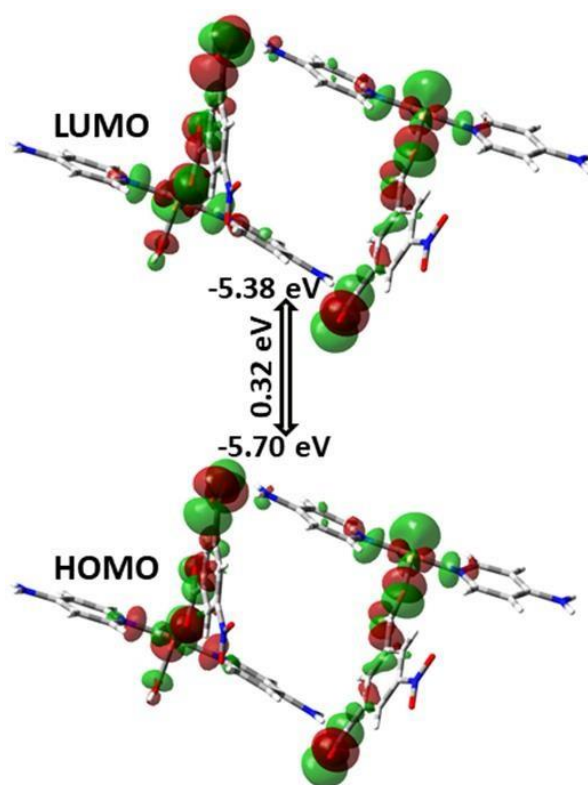


Figure 3.11 DFT calculated energy of molecular orbitals (MOs) and the energy difference between HOMO and LUMO of compound **1**.

3.3. Experimental Section

3.3.1. Materials and general method

Sigma Aldrich has provided all the required chemicals. Micro-analytical data (C, H, N) was collected on Perkin- Elmer 2400 CHNS/O elemental analyzer. Suitable single crystal of compound **1** was used for single crystal diffraction. Bruker SMART APEX II diffractometer equipped with graphite-monochromated MoK α radiation ($\lambda = 0.71073 \text{ \AA}$) was used for data collection. The crystal structure was solved by the SHELX-97 package. Field emission scanning electron microscope (FESEM, S-4800, Hitachi) was used for the morphological study and the PXRD data was collected on a Bruker D8 advance X-ray diffractometer using Cu K α radiation ($\lambda = 1.548 \text{ \AA}$) generated at 40 kV and 40 mA and in a 2θ range of 5–50. Magnetic susceptibility measurements for the compound **1** was carried out on polycrystalline samples, at the Servei de Magnetoquímica of the Universitat de Barcelona, with a Quantum Design SQUID MPMS-XL susceptometer apparatus working in the range 2-300 K under two magnetic field of 500 G and 10000 G. Diamagnetic corrections were estimated from Pascal Tables. Frequency and temperature dependent electrical conductivity and dielectric properties

of the compound **1** was measured in the form of pellets (0.44 mm thick and 8.0 mm diameter). The samples are compressed under 5 tons/inch² pressure using hydraulic press. The pellet is placed between two copper electrodes and inserted with a holder vertically into a cylindrical furnace. All electrical measurements was performed in the frequency range 10 kHz- 5 MHz in the temperature range 253 K to 333 K using LCR meter model Hioki IM3536. The entire measurements have been performed at different temperatures under in the dark condition and the temperatures have been controlled by a indigenous liquid nitrogen cryostat.

3.3.2. Synthesis of compound

Figure 11 shows the schematic representation of the preparation of compound **1**. A methanolic solution (2 ml) of 4-Aminopyridine (4-APY, 18.82 mg, 0.2 mmol) was judiciously layered using water-metahnol (1:1) mixed solvent above the aqueous solution (2 ml) of Cu(NO₃)₂. 3H₂O, (48.32 mg, 0.2 mmol). 5-Nitroisophthalic acid (5-N-IPA, 42.226 mg, 0.2 mmol) in ethanol (2 ml) was deprotonated by Et₃N (40.476 mg, 0.2 mmol) and was layered carefully above the 4-Aminopyridine to build an uninterrupted layer. It was then allowed to diffuse and the deep blue coloured block-shaped crystals were settled on the glass Wall after a week. Under a microscope, the crystals were separated and washed with methanol and water (1:1) mixed solvent, and dried. The yield of [Cu₂(5-N-IPA)₂(4-APY)₄]_n, was 84 % (91.84 mg).

3.4. CONCLUSIONS

We have successfully synthesized one dimensional Cu(II) CP with encapsulated antiferromagnetically coupled dinuclear Cu(II) with fascinating dielectrical and magnetic properties. The charge transfer mechanism and dielectric relaxation throughout the CP have been established. However, the overall electromagnetic properties and the effect of temperature on electromagnetic behaviour of compound **1** reveals that our as synthesized polymer will be a suitable for energy storage applications in future still the more enhancements yet to be done to achieve optimized energy storage device.

3.5. References

- (1) Batten, S. R.; Neville, S. M.; Turner, D. R. Coordination Polymers. Design, Analysis and Application. *Royal Society of Chemistry* : London, **2009**; pp 1-18.
- (2) Desiraju, G. R.; Vittal, J. J.; Ramanan, A. *Crystal Engineering*. A Textbook, World Scientific: Singapore, **2011**; pp 131–153.
- (3) Zhou, H.-C.; Long, J. R.; Yaghi, O. M. Introduction to Metal–Organic Frameworks. *Chem. Rev.* **2012**, *112*, 673–674.
- (4) Moulton, B.; Zaworotko, M. J. From molecules to crystal engineering: supramolecular isomerism and polymorphism in network solids. *Chem. Rev.* **2001**, *101*, 1629–1658.
- (5) Natarajan, S.; Mahata, P.; Sarma, D. J. The relevance of metal organic frameworks (MOFs) in inorganic materials chemistry. *Chem. Sci.* **2012**, *124*, 339–353.
- (6) Biradha, K.; Su, C.-Y.; Vittal, J. J. Recent developments in crystal engineering. *Cryst. Growth. Des.* **2011**, *11*, 875–886.
- (7) Kitagawa, S.; Kitaura, R.; Noro, S.-I. Functional porous coordination polymers. *Angew. Chem. Int. Ed.* **2004**, *43*, 2334–2375.
- (8) Choi, K. M.; Jeong, H. M.; Park, J. H.; Zhang, Y.; Kang, J. K.; Yaghi, O. M. Supercapacitors of nanocrystalline metal–organic frameworks. *ACS Nano*, **2014**, *8*, 7451-7457.
- (9) Yang, T.; Teng, B.; Han, S.; Li, M.; Xu, Z.; Li, Y.; Liu, Y.; Luo, J.; Sun, Z. Structural phase transition and dielectric anisotropy properties of a lead-free organic–inorganic hybrid. *Inorg. Chem. Front.* **2019**, *6*, 1761-1766.
- (10) Zhao, S.; Wu, H.; Li, Y.; Li, Q.; Zhou, J.; Yu, X.; Chen, H.; Tao, K.; Han, L. Core–shell assembly of carbon nanofibers and a 2D conductive metal–organic framework as a flexible free-standing membrane for high-performance supercapacitors. *Inorg. Chem. Front.* **2019**, *6*, 1824-1830.
- (11) Liu, J.; Ren, X.; Kang, X.; He, X.; Wei, P.; Wen, Y.; Li, X. Fabrication of nitrogen-rich three-dimensional porous carbon composites with nanosheets and hollow spheres for efficient supercapacitors. *Inorg. Chem. Front.* **2019**, *6*, 2082-2089.

- (12) Férey, G.; Millange, F.; Morcrette, M.; Serre, C.; Doublet, M.; Grenèche, J.; Tarascon, J. Mixed-Valence Li/Fe-Based Metal–Organic Frameworks with Both Reversible Redox and Sorption Properties. *Angew. Chem. Int. Ed.* **2007**, *46*, 3259-3263.
- (13) Campbell, M. G.; Sheberla, D.; Liu, S.; Swager, T. M.; Dincă, M. Cu₃(hexaiminotriphenylene)₂: An Electrically Conductive 2D Metal–Organic Framework for Chemiresistive Sensing. *Angew. Chem. Int. Ed.* **2015**, *54*, 4349-4352.
- (14) Nohra, B.; Moll, H. E.; Albelo, M. R.; Mialane, P.; Marrot, J.; Mellot-Draznieks, C.; O’Keeffe, M.; Biboum, R. N.; Lemaire, J.; Keita, B.; Nadjo, L.; Dolbecq, A. Polyoxometalate-based metal organic frameworks (POMOFs): structural trends, energetics, and high electrocatalytic efficiency for hydrogen evolution reaction. *J. Am. Chem. Soc.* **2011**, *133*, 13363-13374.
- (15) Bayat, M.; Yang, H.; Ko, F. K.; Michelson, D.; Mei, A. Electromagnetic interference shielding effectiveness of hybrid multifunctional Fe₃O₄/carbon nanofiber composite. *Polymer.* **2014**, *55*, 936-943.
- (16) Wuang, S. C.; Neoh, K. G.; Kang, E.-T.; Pack, D. W.; Leckband, D. E. Synthesis and functionalization of polypyrrole-Fe₃O₄ nanoparticles for applications in biomedicine. *J. Mater. Chem.* **2007**, *17*, 3354-3362.
- (17) Müssig, Joachim, H. Semiconductor capacitor with praseodymium oxide as dielectric. **2003**.
- (18) Zhang, D. Q.; Cheng, J. Y.; Yang, X. Y.; Zhao, B.; Cao, M. S. Electromagnetic and microwave absorbing properties of magnetite nanoparticles decorated carbon nanotubes/polyaniline multiphase heterostructures. *J. Mater. Sci.* **2014**, *49*, 7221-7230.
- (19) Cole, M. W.; Geyer, R. G. Novel tunable acceptor doped BST thin films for high quality tunable microwave devices. *Revista Mexicana de Física*, **2004**, *50*.
- (20) Nair, K. M.; Guo, R.; Bhalla, A. S.; Hirano, S.-I.; Suvorov, D. Developments in Dielectric Materials and Electronic Devices Ceramic Transactions Series. **2006**, *167*.
- (21) Das, S.; Ghosh, A. Charge carrier relaxation in different plasticized PEO/PVDF-HFP blend solid polymer electrolytes. *J. Phys. Chem. B.* **2017**, *121*, 5422-5432.

- (22) Tealdi, C.; Chiodelli, G.; Malavasi, L.; Flor, G.; Fisica, C.; Unita, I. C. N. R.; Taramelli, V.; Pavia, I. Effect of alkaline-doping on the properties of $\text{La}_2\text{Mo}_2\text{O}_9$ fast oxygen ion conductor. *J. Mater. Chem.* **2004**, *14*, 3553-3557.
- (23) Paul, T.; Ghosh, A. Structural and electrical transport properties of $\text{La}_2\text{Mo}_2\text{O}_9$ thin films prepared by pulsed laser deposition. *J. Appl. Phys.* **2017**, *121*, 135106.
- (24) Sheikh, M. S.; Sakhya, A. P.; Dutta, A.; Sinha, T. P. Dielectric relaxation of $\text{CH}_3\text{NH}_3\text{PbI}_3$ thin film. *Thin Solid Films*, **2017**, *638*, 277-281.
- (25) Sheikh, M. S.; Sakhya, A. P.; Sadhukhan, P.; Dutta, A.; Das, S.; Sinha, T. P. Dielectric relaxation and Ac conductivity of perovskites $\text{CH}_3\text{NH}_3\text{PbX}_3$ (X = Br, I). *Ferroelectrics*, **2017**, *514*, 146-157.
- (26) Mohideen, M. I. H.; Lei, C.; Tuc̃ek, J.; Malina, O.; Brivio, F.; Kasneryk, V.; Huang, Z.; Mazur, M.; Zou, X.; Nachtigall, P.; C̃ejka, J.; Morris, R. E. Magneto-structural correlations of novel kagom -type metal organic frameworks. *J. Mater. Chem. C.* **2019**, *7*, 6692-6697.
- (27) Sengupta, A.; Datta, S.; Su, C.; Heng, T. S.; Ding, J.; Vittal, J. J.; Loh, K. P. Tunable Electrical Conductivity and Magnetic Property of the Two Dimensional Metal Organic Framework $[\text{Cu}(\text{TPyP})\text{Cu}_2(\text{O}_2\text{CCH}_3)_4]$. *ACS Appl. Mater. Interfaces.* **2016**, *8*, 16154–16159.
- (28) Yu, F.; Kurmoo, M.; Zhuang, G.-L.; Zuo, J.-L. Hierarchical tandem assembly of planar $[3 \times 3]$ building units into $\{3 \times [3 \times 3]\}$ oligomers: mixed-valency, electrical conductivity and magnetism. *Chem. Sci.* **2018**, *9*, 7498-7504.
- (29) Naskar, K.; Dey, A.; Dutta, B.; Ahmed, F.; Sen, C.; Mir, M. H.; Roy, P. P.; Sinha, C. Intercatenated coordination polymers (ICPs) of carboxylato bridged Zn (II)-isoniazid and their electrical conductivity. *Cryst. Growth Des.* **2017**, *17*, 3267-3276.
- (30) Naskar, K.; Maity, S.; Jana, S.; Dutta, B.; Tanaka, S.; Mallick, D.; Akitsu, T.; Sinha, C. Arylazoimidazole Coordinated and Naphthalene-Dicarboxylato Bridged Polymers of Co (II) and Photochromic Zn (II) Complexes. *Cryst. Growth Des.* **2018**, *18*, 2986-2997.
- (31) Siddiqui, M. M.; Saha, R.; Mukherjee, P. S. Ruthenium(II) Metalla[2]catenanes and Macrocycles via Donor-Dependent Self-Assembly. *Inorg. Chem.* **2019**, *58*, 4491-4499.
- (32) Dutta, B.; Jana, R.; Bhanja, A. K.; Ray, P. P.; Sinha, C.; Mir, M. H. Supramolecular aggregate of Cadmium (II)-based one-dimensional coordination polymer for device fabrication and sensor application. *Inorg. Chem.* **2019**, *58*, 2686-2694.

- (33) Bleaney, B.; Bowers, K. D. Anomalous paramagnetism of copper acetate. *Proc. R. Soc. Lond. A.* **1952**, *214*, 451-465.
- (34) Maji, P.; Ray, A.; Sadhukhan, P.; Chatterjee, S.; Das, S. Study on charge transfer mechanism and dielectric relaxation of cesium lead bromide (CsPbBr₃). *J. Appl. Phys.* **2018**, *124*, 124102.
- (35) Ray, A.; Roy, A.; Bhattacharjee, S.; Jana, S.; Ghosh, C. K.; Sinha, C.; Das, S. Correlation between the dielectric and electrochemical properties of TiO₂-V₂O₅ nanocomposite for energy storage application. *Electrochim. Acta.* **2018**, *266*, 404-413.
- (36) Maji, P.; Chatterjee, S.; Das, S. Study on charge transportation and scaling behavior of CsPbI₃ microwires. *Ceram. Int.* **2019**, *45*, 6012-6020.
- (37) Dhara, A.; Sain, S.; Das, S.; Pradhan, S. K. Microstructure, optical and electrical characterizations of Mn doped ZnS nanocrystals synthesized by mechanical alloying. *Mater. Res. Bull.* **2018**, *97*, 169-175.
- (38) Acharya, T.; Choudhary, R. N. P. Dielectric and electrical characteristics of La_{0.5}Na_{0.5}Ga_{0.5}V_{0.5}O₃. *Phys. Lett. A.* **2016**, *380*, 2437-2444.
- (39) Mandal, S. K.; Singh, S.; Dey, P.; Roy, J. N.; Mandal, P. R.; Nath, T. K. Frequency and temperature dependence of dielectric and electrical properties of TFe₂O₄ (T= Ni, Zn, Zn_{0.5}Ni_{0.5}) ferrite nanocrystals. *J. Alloys Compd.* **2016**, *656*, 887-896.
- (40) Das, M. R.; Mukherjee, A.; Mitra, P. Structural, optical and ac electrical characterization of CBD synthesized NiO thin films: Influence of thickness. *Phys. E Low-dimensional Syst. Nanostructures*, **2017**, *93*, 243-251.
- (41) Jana, P. K.; Mukherjee, S.; Chaudhuri, B. K. Existence of internal domains in Li_xTi_yNi_{1-x-y}O and their effects on dielectric behaviour. *J. Phys. D. Appl. Phys.* **2014**, *47*, 365302.
- (42) Fang, T. T.; and Liu, C. P. Evidence of the Internal Domains for Inducing the Anomalous High Dielectric Constant of CaCu₃Ti₄O₁₂. *Chem. Mater.* **2005**, *17*, 5167-5171.
- (43) Dong, W.; Hu, W.; Berlie, A.; Lau, K.; Chen, H.; Withers, R. L.; Liu, Y. Colossal Dielectric Behavior of Ga+Nb Co-Doped Rutile TiO₂. *ACS Appl. Mater. Interfaces.* **2015**, *7*, 25321-25325.

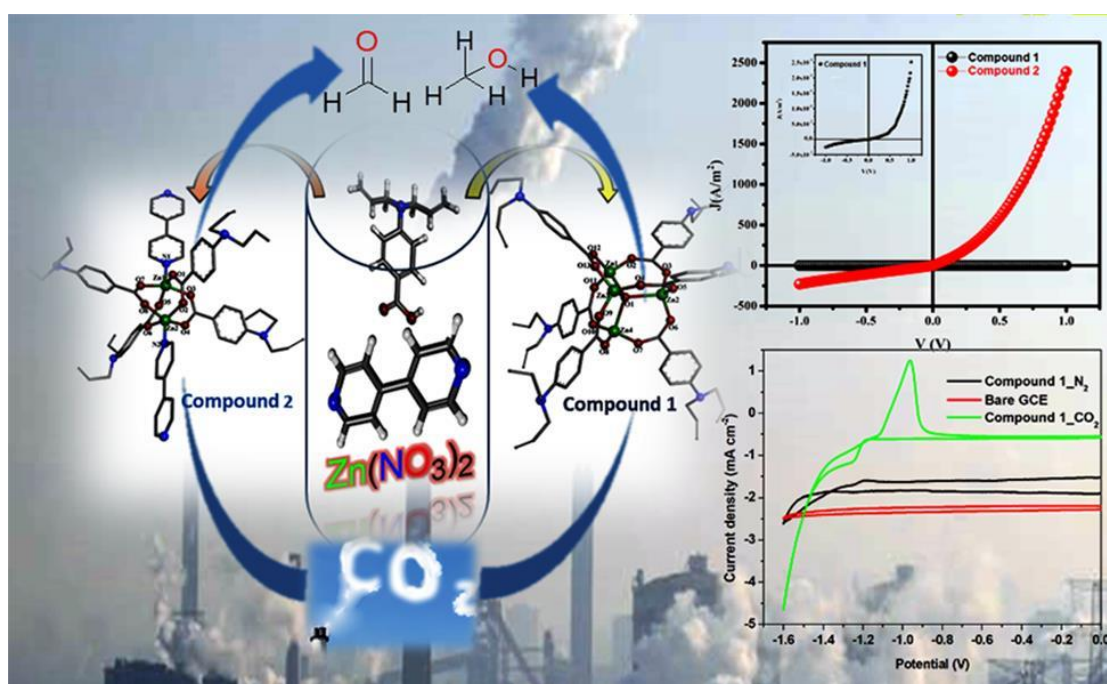
- (44) Galli, S.; Cimino, A.; Ivy, J. F.; Giacobbe, C.; Arvapally, R. K.; Vismara, R.; Checchia, S.; Rawshdeh, M. A.; Cardenas, C. T.; Yaseen, W. K.; Maspero, A.; Omary, M. A. Fluorous Metal–Organic Frameworks and Nonporous Coordination Polymers as Low- κ Dielectrics. *Adv. Funct. Mater.* **2019**, *29*, 1904707.
- (45) Balendra, Banday, A.; Tewari, S.; Singh, B.; Murugavel, S.; Ramanan, A. Alkaline-earth metal based coordination polymers assembled from two different V-shaped ligands: Synthesis, structure, and dielectric properties. *Inorganica Chimica Acta*, **2019**, *495*, 118940.
- (46) Ashalatha, A.; Sudarsanakumar, M. R.; Prasad, S. S.; Suma, S.; Kurup, M. R. P.; Rahul, S. Synthesis, crystal structure and dielectric properties of a new acetate bridged coordination polymer: $\{[\text{La}(\mu\text{-CH}_3\text{COO})(\text{PDC})(\text{H}_2\text{O})_2]\cdot 2\text{H}_2\text{O}\}_n$. *Journal of Molecular Structure*, **2019**, *1195*, 522-527.
- (47) Zhang, M.; Tan, Y.-L.; Chen, X.-R.; Yu, H.; Zhang, W.-H.; Lang, J.-P. A cationic $[\text{Ag}_{12}\text{S}_{12}]$ cluster-based 2D coordination polymer and its dye composite with enhanced photocurrent and dielectric responses. *Dalton Trans.*, **2019**, *48*, 8546-8550.
- (48) Balendra, B. A.; Kumar, V.; Murugavel, S.; Ramanan, A. Strontium- Carboxylate-Based Coordination Polymers: Synthesis, Structure and Dielectric Properties. *Chemistry Select*, **2019**, *4*, 4756-4766.
- (49) Sima, J.-Y.; Li, H.-X.; Young, D. J.; Braunstein, P.; Lang, J.-P. Reversible dielectric switching behavior of a 1D coordination polymer induced by photo and thermal irradiation. *Chem. Commun.* **2019**, *55*, 3532-3535.
- (50) Kao, Y.-C.; Mendiratta, S.; Usman, M.; Wen, Y.-S.; Wang, C.-M.; Zhao, L.; Wu, M.-K.; Lu, K.-L. Exceptional Low Dielectric Behavior of Chemically Robust, Guest-Free Co- and Mn-Based Coordination Polymers. *ChemElectroChem*, **2019**, *6*, 623– 626.
- (51) Jana, S.; Jana, R.; Sil, S.; Dutta, B.; Sato, H.; Ray, P. P.; Datta, A.; Akitsu, T.; Sinha, C. Influence of Axial Linkers on Polymerization in Paddle-Wheel Cu(II) Coordination Polymers for the Application of Optoelectronics Devices. *Cryst. Growth Des.* **2019**, *11*, 6283-6290.
- (52) Chandra, A.; Das, M.; Pal, K.; Jana, S.; Dutta, B.; Ray, P. P.; Jana, K.; Sinha, C. Three-Dimensional-Coordination Polymer of Zn(II)-Carboxylate: Structural Elucidation, Photoelectrical Conductivity, and Biological Activity. *ACS Omega*, **2019**, *4*, 17649–17661.

(53) Frisch, M. J.; Trucks, G. W.; Schlegel, H. B.; Scuseria, G. E.; Robb, M. A.; Cheeseman, J. R.; Scalmani, G.; Barone, V.; Mennucci, B.; Petersson, G. A.; Nakatsuji, H.; Caricato, M.; Li, X.; Hratchian, H. P.; Izmaylov, A. F.; Bloino, J.; Zheng, G.; Sonnenberg, J. L.; Hada, M.; Ehara, M.; Toyota, K.; Fukuda, R.; Hasegawa, J.; Ishida, M.; Nakajima, T.; Honda, Y.; Kitao, O.; Nakai, H.; Vreven Jr, T.; Montgomery, J. A.; Peralta, J. E.; Ogliaro, F. M.; Bearpark, J.; Heyd, J.; Brothers, E.; Kudin, K. N.; Staroverov, V. N.; Kobayashi, R.; Normand, J.; Raghavachari, K.; Rendell, A.; Burant, J. C.; Iyengar, S. S.; Tomasi, J.; Cossi, M.; Rega, N.; Millam, J. M.; Klene, M.; Yazyev, O.; Austin, A. J.; Cammi, R.; Pomelli, C.; Ochterski, J. W.; Martin, R. L.; Morokuma, K.; Zakrzewski, V. G.; Salvador, G. A. P.; Dannenberg, J. J.; Dapprich, S.; Daniels, A. D.; Farkas, Ö.; Foresman, J. B.; Ortiz, J. V.; Cioslowski, J.; Fox, D. J. Gaussian, Inc., CT Wallingford, **2009**.

(54) Li, Y.-H.; Gong, X. G.; Wei, S.-H. Ab Initio Calculation of Hydrostatic Absolute Deformation Potential of Semiconductors. *Appl. Phys. Lett.* **2006**, 88, 042104–042106.

Abstract

Electrochemical reduction of CO₂ into C-fuels using Metal and Metal oxides Nano particles, molecular complexes etc. are challenging task in view of sustainable environment, renewable energy sources and transformation of waste-to-wealth. Zn(II), d¹⁰ redox-innocent, coordination complexes have recently been used as efficient and selective catalysts in the electroreduction of CO₂. Towards this goal, we have synthesized two complexes, tetranuclear (0D) [Zn₄(μ₄-O)(DABA)₆] (**1**) and polynuclear (1D) [Zn₂(DABA)₄(4,4'-BPY)]_n (**2**), in one pot (HDABA = 4-Diallylamino-benzoic acid and 4,4'-BPY = 4,4'-Bipyridine) and characterized by single crystal X-ray diffraction measurements and other spectroscopic data. The electroreduction of CO₂ (CO₂RR) using the complexes **1** and **2** as catalyst has synthesized HCOOH, HCHO and CH₃OH. The reduced products are identified by ¹³C NMR spectral data. It is observed that Compound **1** is catalytically more efficient than compound **2** when compound **1** demonstrates the current -5.63 mA mg⁻¹, the compound **2** shows much lower value (-22.27 mA mg⁻¹). Impedance spectroscopy shows that in the complex **2**, the Z' decreases with diminishing frequency than that of the complex **1**; this implies that the dc resistivity of **2** is lower than that of **1**. Theoretically calculated energy gap (ΔE(HOMO-LUMO)) are 4.4 eV (**1**) and 2.81 eV (**2**) and the conductivity is 2.29×10⁻⁷ S/m (**1**) and 2.54×10⁻³ S/m (**2**). About 10⁴ times enhancement of conductivity of **2** is not only due to coordination of 4,4'-BPY to Zn(II) but also subsidized by the coordination polymer and noncovalent superstructure.



4.1. Introduction

Two key issues faced by the global economics and Science & Technology for the sustainability of the civilization in this century are the depletion of energy resources and global warming. As a program of ‘Waste-to-Wealth’, conversion of CO₂ to C-fuels and commercially useful synthetic chemicals is one of the attractive scheme in ‘Chemistry for Better Future’.¹⁻¹⁰ CO₂ reduction may be carried out using superheated steam to syngas or H₂ to methanol or other chemicals; reduction may be catalyzed by metal and/or metal oxide NPs, molecular complexes etc.¹¹⁻²⁴ Alternative plan proposed to alleviate CO₂ accumulation in the atmosphere, and consequently impact on the global climate by the Carbon Capture and Utilization (CCU) technologies is the electrocatalytic CO₂ reduction reaction (CO₂RR) to generate C-fuels.²⁵⁻²⁹ As a distinctive product of CO₂ reduction with 6e-6H⁺ is CH₃OH which is one of the challenging processes.³⁰⁻³¹ Methanol is an encouraging energy carrier since, as a liquid, it is easier to store, transport and safely handle than hydrogen and natural gas.³²⁻³⁵

Electrocatalysis is largely influenced by the well-distributed metal centers in the electrode deposited metal complexes, metal clusters, metal-organic frameworks etc.³⁶⁻⁴¹ Due to the closed shell electronic configuration of Zn (II) (d¹⁰, redox-innocent), the main electrocatalytic active sites in the CO₂RR process of the Zn-based complex or MOFs may not be the metal center, but the electron rich ligands coordinating to Zn(II).⁴²⁻⁵¹ An electron-rich active center could assist the activation of stable C=O bond in CO₂ by supporting electron movement from the active sites to the antibonding orbitals followed by the reduction to different products.⁵²⁻⁵⁶ Thus, accumulation of the charge concentration on the catalytic sites would be an encouraging approach to boost selectivity, catalytic activity and durability of electrocatalysts for heterogeneous CO₂ reduction, and has been considered ideal for the practical applications.⁵⁷⁻⁵⁹

Herein, we report a facile synthesis and structural characterization of tetranuclear (0D), [Zn₄(μ₄-O)(DABA)₆] (**1**), and one-dimensional (1D) polynuclear, [Zn₂(DABA)₄(4,4'-BPY)]_n (**2**) (DABA, 4-diallylaminobenzoic acid; 4,4'-BPY, 4,4'-bipyridine) nanomaterials (average particle size : 300 nm (**1**) and 250 nm (**2**)). Catalytic electrochemical CO₂ reduction followed by ¹³C NMR spectra proves the formation of CH₃OH and HCHO using **1** and CH₃OH, HCHO and HCOOH using **2** as catalyst. The conductivity study based on diode derived from J-V characteristics has shown Schottky Diode Behavior and is promising for the coordination polymer, **2** (2.54×10⁻³ S/m) than **1** (2.29×10⁻⁷ S/m), 10⁴ times higher in polymer (**2**) than monomer (**1**). The electronic properties have been explained by DFT computation of the compounds.

4.2. Results and Discussion

4.2.1. General Information of the Compounds

Aqueous solution of $\text{Zn}(\text{NO}_3)_2$ diffuses to methanol solution of 4,4'-bipyridine (4,4'-BPY) followed by the injection of 4-diallylaminobenzoic acid (HDABA) in ethanol in presence of very small amount of Et_3N to isolate tetranuclear $[\text{Zn}_4(\mu_4\text{-O})(\text{DABA})_6]$ (**1**) and a coordination polymer $[\text{Zn}_2(\text{DABA})_4(4,4'\text{-BPY})]_n$ (**2**). The composition of the compounds is supported by microanalytical data. FTIR spectrum of **1** shows a characteristic high intense stretch at 1580 cm^{-1} along with a strong broad band at 1380 cm^{-1} which correspond to $\nu(\text{COO})$ while the complex **2** generates two sharp asymmetric high intense stretches at 1560 and 1650 cm^{-1} which refer to bridging carboxylate (Zn-OCO-Zn) and pyridyl C=N (bridged 4,4'-BPY) in the polymeric structure (Figure 4.1).⁶⁰ The ^1H and ^{13}C NMR spectra of the complexes are compared with free ligand data and support the coordination to $\text{Zn}(\text{II})$ (Figure 4.2).

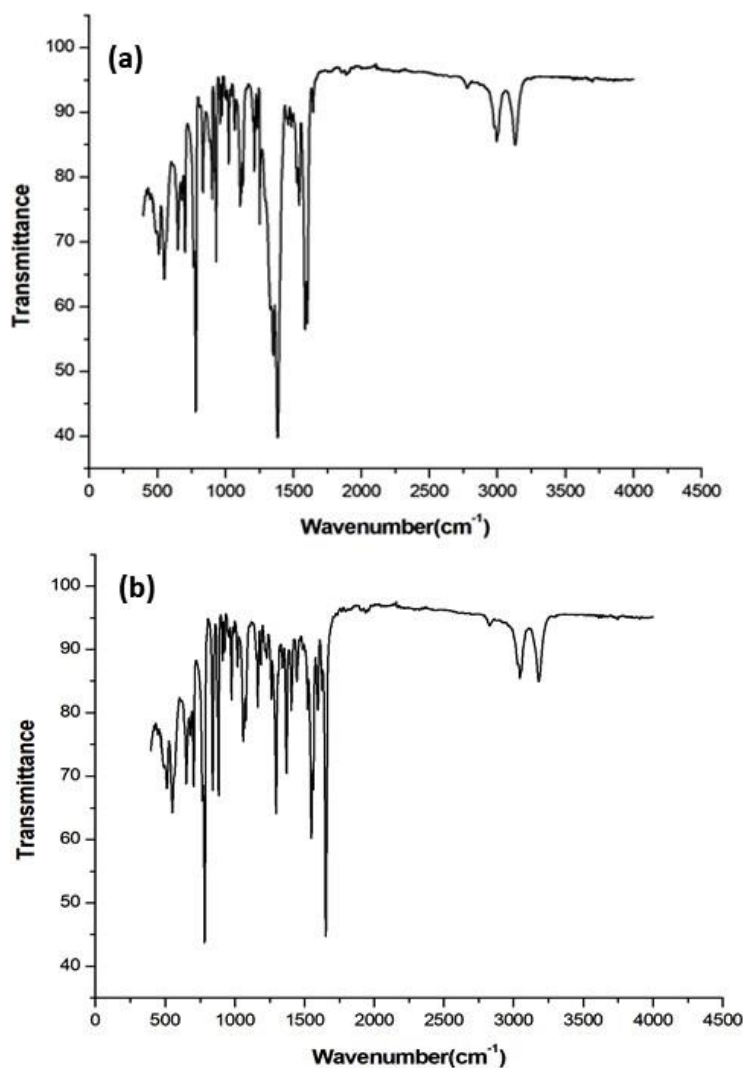


Figure 4.1 (a) IR spectrum of compound **1**, (b) IR spectrum of compound **2**.

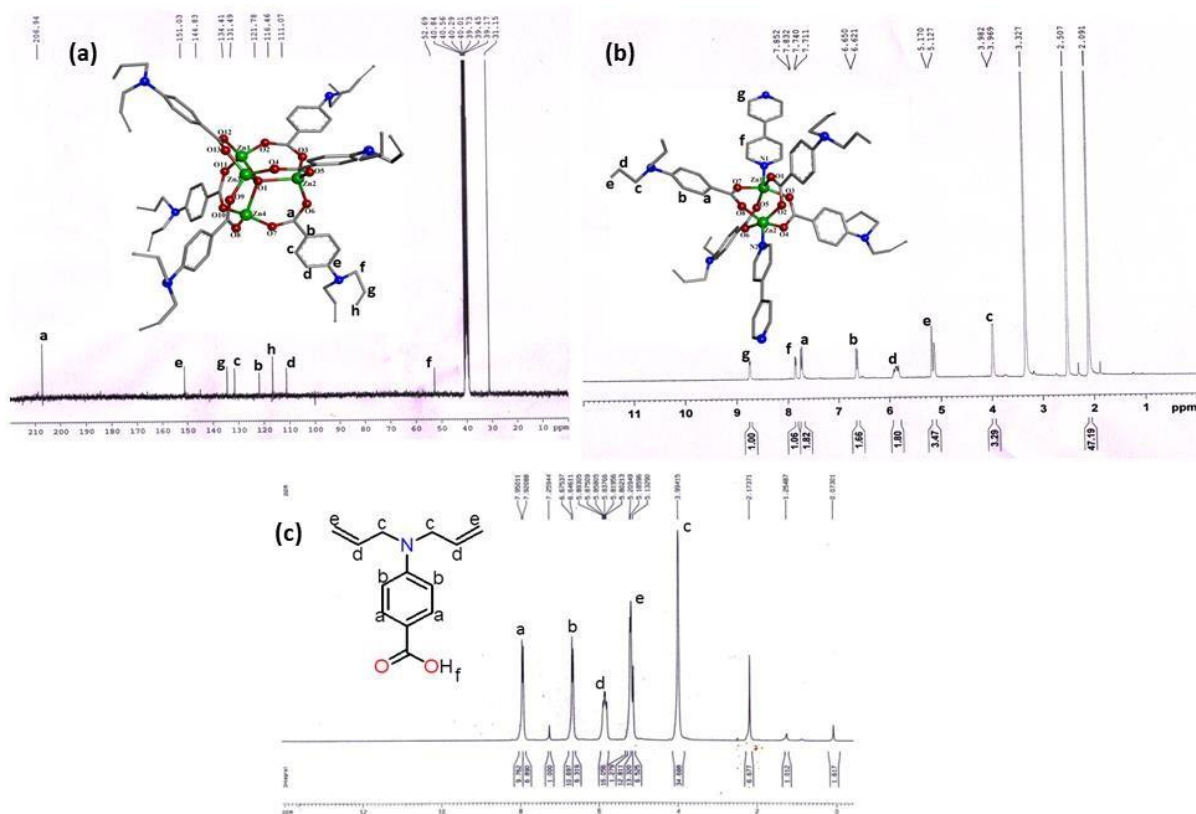


Figure 4.2 (a) The ^{13}C NMR spectrum of compound 1. (b) The ^1H NMR spectrum of compound 2. (c) The ^1H NMR spectrum of 4-Diallylamino-benzoic acid.

The SEM image of the synthesized compounds exhibit irregular spherical type shapes (Figure 4.3(a-b)). Using Gaussian function, the fittings show the average particle size as 300 nm (1) and 250 nm (2) (Figure 4.3(c-d)). Structural feature of the compounds slowly degrades during electrolysis and agglomeration occurs. Thus, the active component becomes complicated during long-time durability test in the electrocatalytic CO_2 reduction.⁶¹⁻⁶⁴

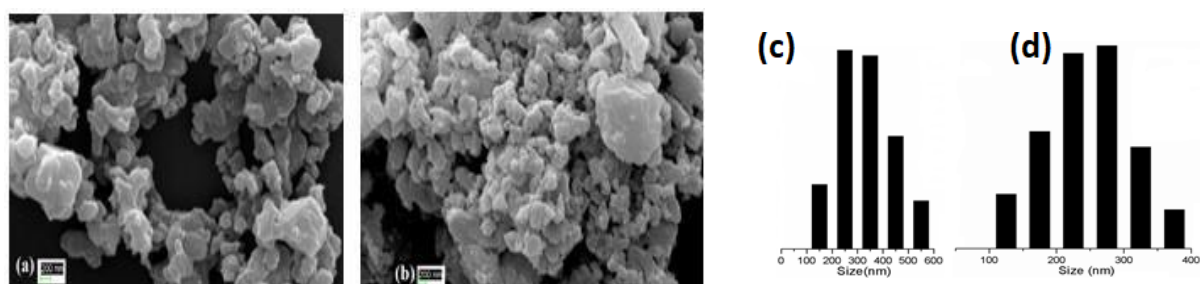


Figure 4.3 SEM images of compounds (a) 1 and (b) 2 along with their particle distribution pattern ((c) 1 and (d) 2).

Therefore, the particle size of the compound 2 is found smaller than that of the compound 1. Diminishing particle size indicates the lower grain size and higher grain boundary which may

affect the conductivity of the samples.^{65,66} In general, the trapping ability of grains (or grain boundaries) at the localized states directly impacts upon the gathering of charge carriers. The Debye length of the material can determine the trapping ability. The 4 times higher grain size than the Debye length is sufficient to make the grain conductivity dominant in total conductivity of the material.⁶⁷ In present example, the grain resistivity of compound **1** is 2.5 times higher than compound **2**, whereas, the grain boundary resistivity is almost same for both materials. So, the lower grain size of compound **1** directly impacts on the conductivity than the contribution of grain boundary.

4.2.2. Structural description of $[\text{Zn}_4(\mu_4\text{-O})(\text{DABA})_6]$ (**1**) and $[\text{Zn}_2(\text{DABA})_4(4,4'\text{-BPY})]_n$ (**2**)

The single-crystal X-ray diffraction analysis of **1** shows that in the asymmetry unit, the Zn(II) centres are bridged by carboxylato groups to form a 0D tetranuclear complex with $\mu_4\text{-O}$ bridging to stabilize tetrahedrally oriented geometry (Figure 4.4). The tetranuclear Zn(II) complex (**1**) shows Zn \cdots Zn separation in the range 3.122-3.186 Å, and the $\mu_4\text{-O}$ Zn distance lies in the range 1.927-1.944 Å (Figure 4.4). The structure analysis of **2** shows that a carboxylato bridged Zn(II) paddle wheel $[\text{Zn}_2(\text{DABA})_4]$ unit is connected by the 4, 4'-bipyridine at the axial coordination position and helps to form 1D polymeric chain (Figure 4.4 and 4.6a). The compound **2** has distorted square pyramidal geometry around Zn centers with Zn–Zn distance, 3.058 Å, and pyridine ring of 4, 4'-BPY assist efficient charge delocalization through metal orbitals (Figure 4.4). These complexes are capable of forming higher dimensional structures through various classical and nonclassical supramolecular (van der Waals, aliphatic, aromatic C-H \cdots π) interactions (3.066–3.454 Å, (Figure 4.5(a-c) and 4.6(b-c)).⁶⁷⁻⁷⁴ Compound **1** crystallizes in the monoclinic $Ci\ 2/c1$ space group, with $Z = 8$, whereas **2** crystallizes in the monoclinic $P\ 21/c$, with $Z = 4$ (Table 4.1).

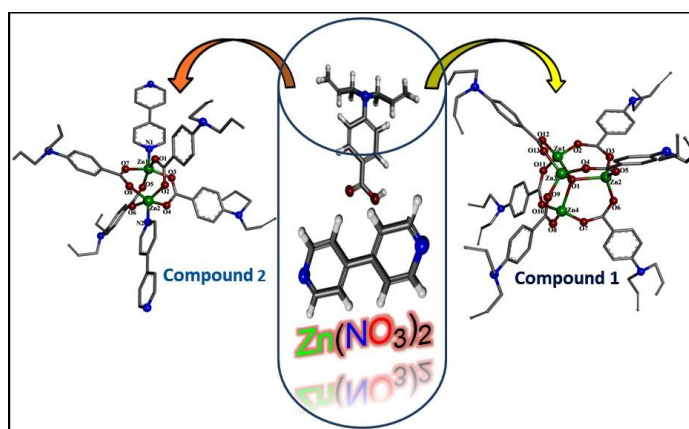


Figure 4.4 Schematic representation of the synthesis and structural unit of compounds **1** and **2**.

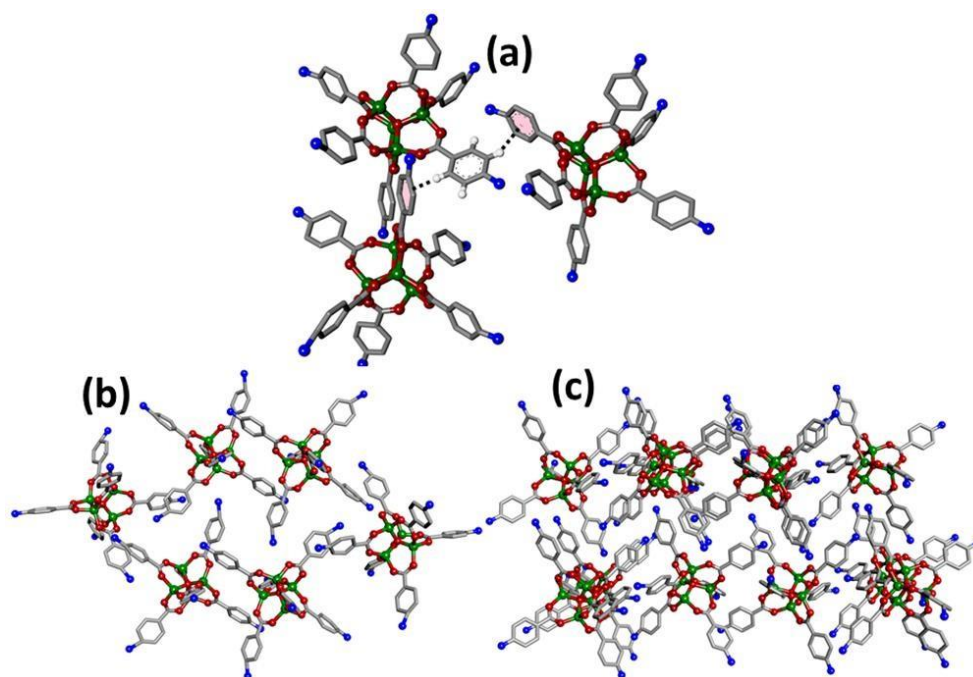


Figure 4.5 (a) C-H... π interaction, (b) and (c) Supramolecular aggregate structure (3D view) of compound **1**. Allyl groups have omitted for clarity.

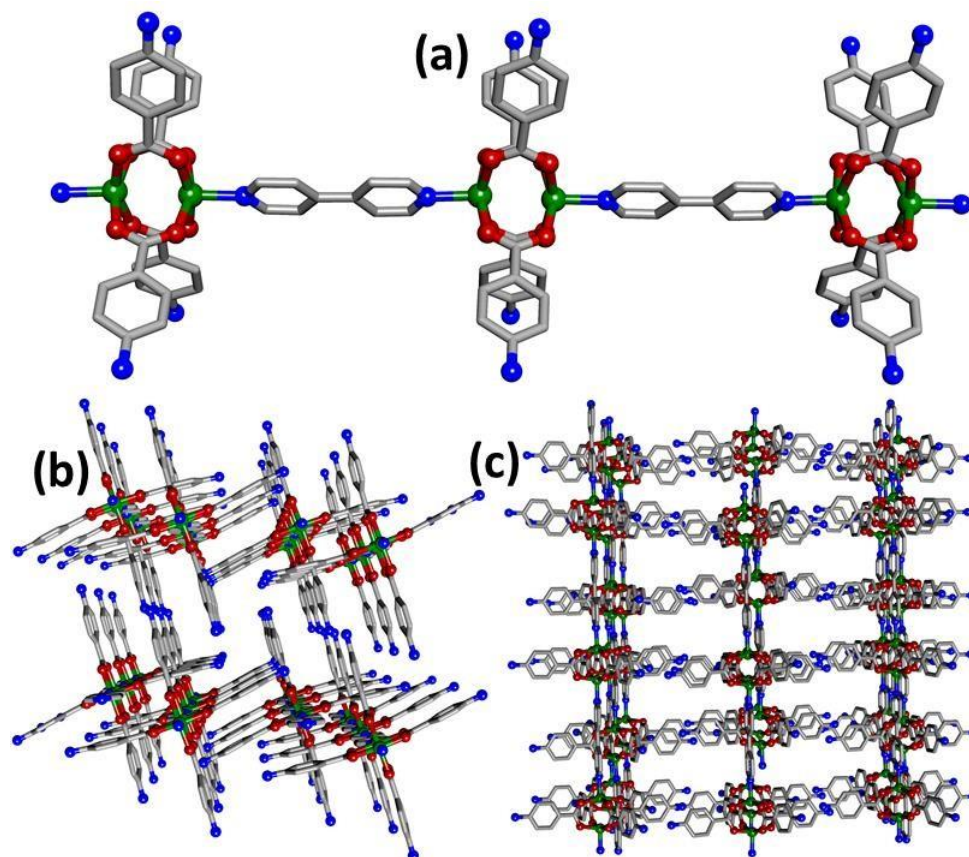


Figure 4.6 (a) 1D polymeric chain, (b),(c) Supramolecular aggregate structure (3D view) of compound **2**. Allyl groups have omitted for clarity.

Table 4.1. Crystal data and refinement parameters for compound **1** and **2**.

CCDC No.	1937038	1915446
Formula	C _{71.45} H _{15.08} N _{5.98} O ₁₃ Zn ₄	C ₆₂ H ₂₇ N ₆ O ₈ Zn ₂
fw	1426.60	1114.68
crystalsyst	monoclinic	monoclinic
space group	C2/c	P 21/c
a (Å)	25.071(2)	14.2834(7)
b (Å)	14.4055(12)	14.0834(6)
c (Å)	43.218(4)	28.8090(15)
α(deg)	90	90
β(deg)	101.239(4)	96.841(3)
γ (deg)	90	90
V (Å ³)	15309(2)	5753.9(5)
Z	8	4
D _{calcd} (g/cm ³)	1.238	1.287
μ(mm ⁻¹)	1.912	0.892
λ(Å)	1.54178	0.71073
data[I > 2σ(I)]/params	14301/944	10118/688
GOF on F ²	1.801	1.008
final R indices[I > 2σ(I)] ^{a,b}	R1 = 0.1355 wR2 = 0.3883	R1 = 0.0676 wR2 = 0.1855

$$^a R1 = \frac{\sum ||F_o| - |F_c||}{\sum |F_o|}, \quad ^b wR2 = \left[\frac{\sum w(F_o^2 - F_c^2)^2}{\sum w(F_o^2)^2} \right]^{1/2}$$

4.2.3. Electrochemical CO₂RR Study

The cyclic voltammetry (CV) scans of the GCE/compound **1** and GCE/compound **2** (Figure 4.7a and b), both hybrids have shown similar electrochemical behavior and the cathodic peak appears at -0.33 V and -0.32 V (vs RHE), the current densities are -1.56 mA cm⁻² and -1.97 mA cm⁻², respectively in N₂ saturated electrolyte. The cathodic peak potential is shifted to -0.24 V for **1** and -0.34 V for **2** (vs RHE) in CO₂-saturated electrolyte (compound-CO₂), which means obviously the reduction of CO₂ (CO₂RR activity) on the working electrode.⁷⁵⁻⁸¹ The current height measurement suggests that 6e⁻ transfer process is performed in presence of compound **1** and for compound **2** the 4e⁻ transfer process occurs. The ligand HDABA is catalytically inactive towards CO₂RR.

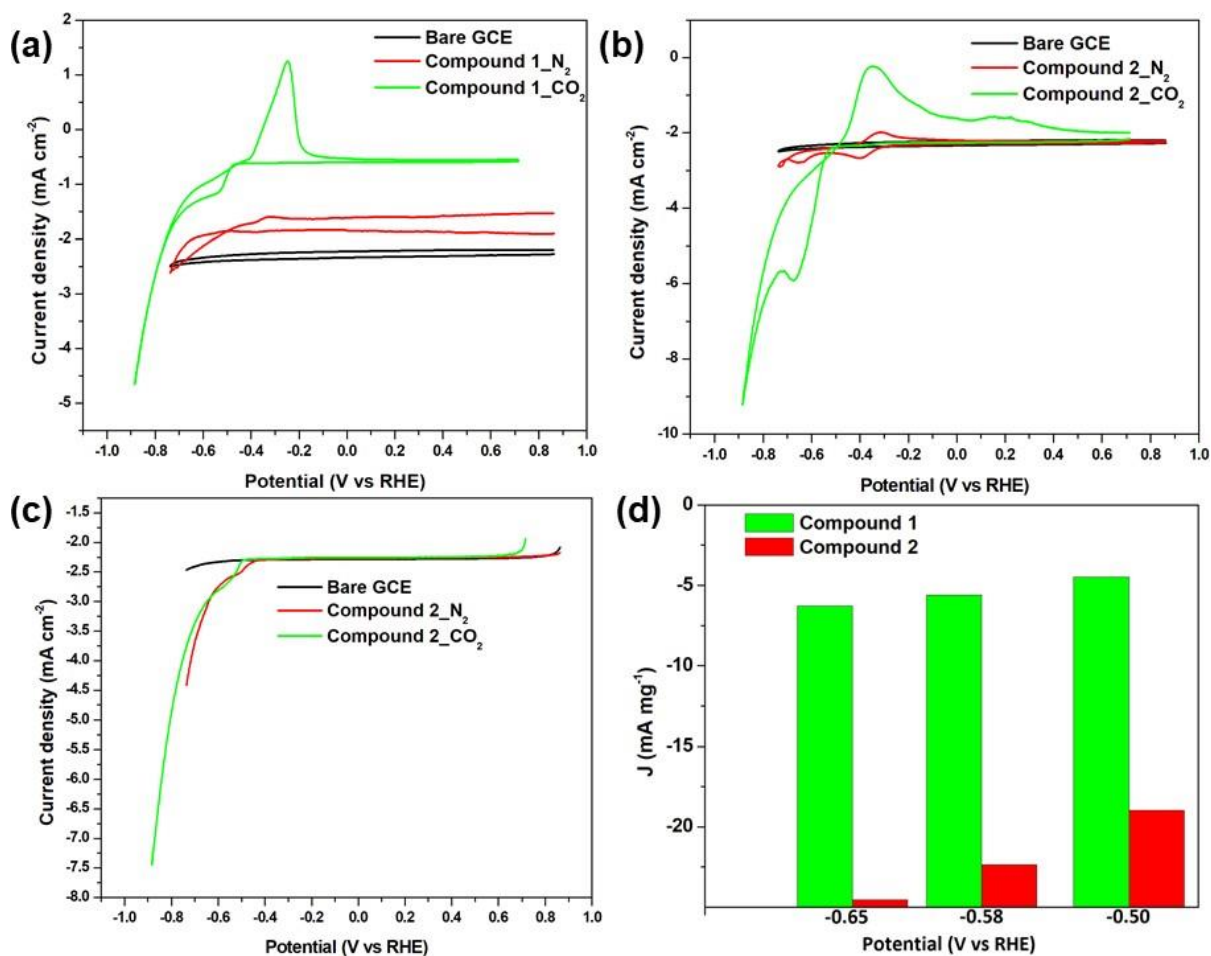


Figure 4.7 (a), (b) Cyclic voltammograms of compound **1** and **2** in N₂ and CO₂ saturated atmosphere in 0.1 M K₂CO₃ solution with scan rate of 50 mV/s. (c) Linear sweep voltammograms of **2** in N₂ and CO₂ saturated atmosphere in 0.1 M K₂CO₃ solution with scan rate of 5 mV/s. (d) Mass activity comparison plot between compound **1** and **2**.

Electrocatalytic CO₂ reduction performance has also evaluated by linear sweep voltammetry (LSV) in N₂ and CO₂-saturated electrolyte (Figure 4.7). LSV plot of **2** reveals that the current density changes from 4.4 mA cm⁻² to -7.5 mA cm⁻² from N₂-saturated electrolyte to CO₂-saturated electrolyte, which means obviously CO₂RR occurred on the electrode.⁸²⁻⁸⁴ From the mass activity relationship, Compound **1** is catalytically more efficient than compound **2** (Figure 4.7d) and it is shown that at -0.58 V (vs RHE) the compound **1** demonstrates -5.63 mA mg⁻¹ being higher compared to compound **2** (-22.27 mA mg⁻¹). The structure of compound **1** shows that four Zn(II) centres are tetrahedrally arranged where in **2** paddle wheel [Zn₂(DABA)₄] is connected through 4, 4'-bipyridine bridge that makes metal centre five coordinated. The structural feature of the compound **1** allows the easy passage of CO₂ to the active site rather than the complex **2**. Easy accession to the active sites and the number of centres makes the compound catalytically more efficient which is reflected from the higher

amount of current in case of **1** than **2** in the result in CO₂RR. Cyclic voltammograms and Mass activity comparison plot shows compound **1** has more catalytic efficiency compare to **2**, which is as our expected.

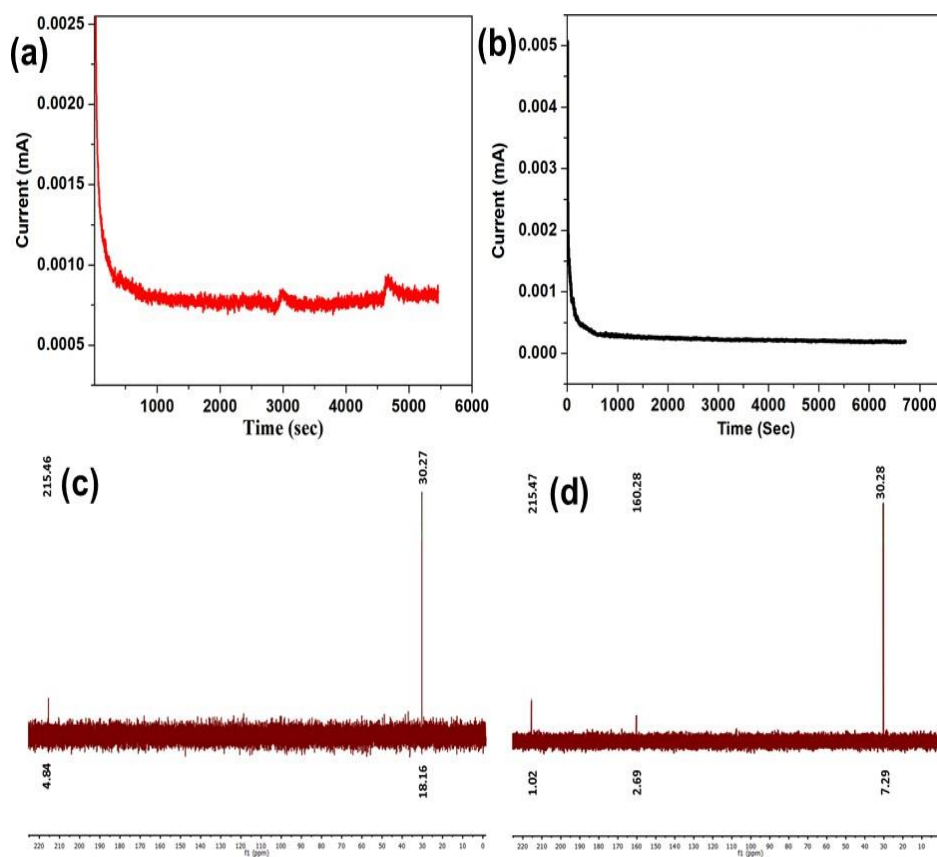
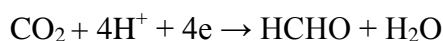
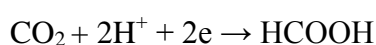
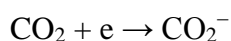
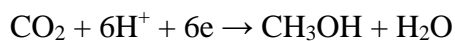


Figure 4.8 Chronoamperometric durability test of the compound **1**(a) and **2**(b) at applied potential of -0.58 V (vs RHE) in 0.1 M K₂CO₃ solution. (c-d) ¹³C NMR spectrum of the obtained liquid products after CO₂RR of the compound **1**(c) and **2**(d).

The long-term durability of the as-prepared Zn(II) catalysts for CO₂RR activity was evaluated by chronoamperometry at a potential of -0.58 V (vs RHE). The I-t curve (Figure 4.8a-b, Current vs Time) shows that the catalytic current decline after 90 min (**1**) and 112 min (**2**) of continuous measurement, which could be caused by the catalyst mass loss from the working electrode during long-term CO₂RR condition for **1** and **2** respectively.

The possible reduced products after CO₂ reduction are





The liquid products obtained in D₂O medium instead of H₂O from the CO₂ reduction experiments have also been subjected to ¹³C NMR analyses. The ¹³C NMR spectrum of reduced products obtained using compound **1** as catalyst exhibits resonance peaks at 30.27 and 215.46 ppm those are compared with the presence of ¹³CH₃OH, and H¹³CHO and the ratio of formation of methanol and formaldehyde is about 3.75 : 1 (Figure 4.8c). The ¹³C NMR spectrum of the electrocatalysis using compound **2** exhibits peaks at 30.27, 160.28 and 215.46 ppm those are referred to ¹³CH₃OH, H¹³COOH and H¹³CHO and the ratio of products follow 7.14: 2.63 : 1 (Figure 4.8d) molar ratio.

4.2.4. Impedance study

The real part of impedance (*Z'*) of the synthesized materials is plotted as a function of frequency (Figure 4.9a). There are three noticeable regions for both materials - two of them are frequency independent, and one is frequency dependent. The frequency independent *Z'* is observed at higher and lower frequency region. Among them, *Z'* at higher frequency exposes the resistive behavior of grain of the material. Another frequency independent *Z'* at lower frequency regime is observed due to the long-range movement of the carrier. In this region, charge carriers successfully hops when the neighboring particles relax at their own site. It causes the dc resistivity at lower frequency.^{85- 86} On the other hand, a dispersive frequency dependent *Z'* is found at the intermediate frequency region. This is caused by the localized movement due to the unsuccessful hopping within the relaxed neighboring sites.⁸⁵⁻⁸⁶ The outcome of this movement at the intermediate frequency region provides the frequency dependent ac conductivity. Most significantly, compound **2** displays lower *Z'* at lower frequency which illustrates the lower dc resistivity of that compound than compound **1**. The enhancement of charge carrier mobility may lower the trap density which provides the lower dc resistivity of compound **2**.⁸⁷ The imaginary part of the impedance (*Z''*) of both compounds varies significantly with frequency and it is shown in **Figure 4.9b**. Some noteworthy features are arisen from the variation which provides some lights upon the conduction mechanism. We have found the peak in *f* vs *Z''* for both materials and its broadening is asymmetric. The position of the peak is lower for compound **2** and it is slightly shifted towards the higher frequency. The peak existence signifies the electrical relaxation during conduction.⁸⁸⁻⁸⁹ The peak for compound **2** is found at higher frequency than compound **1**. This shifting of the peak for **2** indicates the faster relaxation time of this compound than the other and it escalates the conduction mechanism between two neighboring particles and this may be due to the polymeric nature of compound **2**.

To study the impact of grain and grain boundary upon the conduction behavior, we have fitted the Nyquist plot

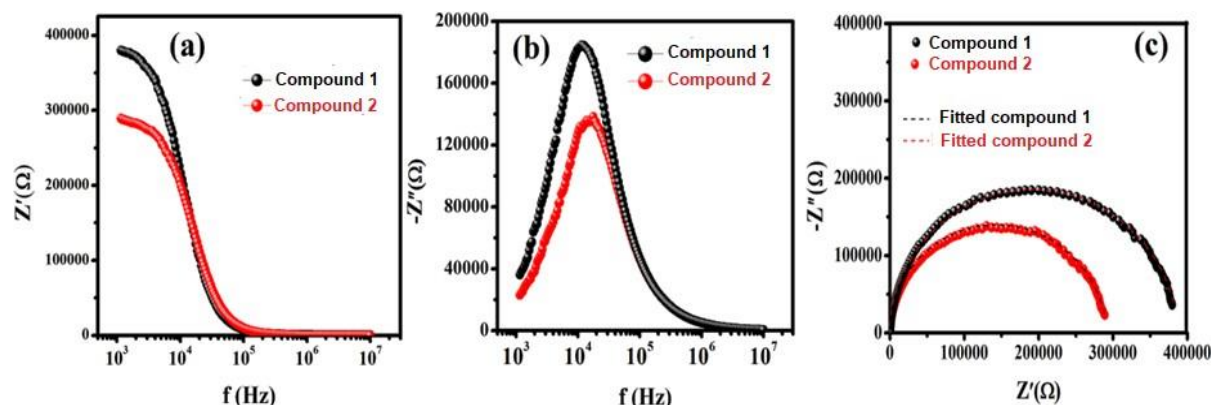
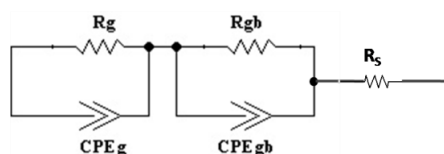


Figure 4.9 Variation of (a) Z' and (b) Z'' with frequency for compound 1 and 2; (c) Nyquist plot of compound 1 and 2 with fitted lines (dotted).

with proper equivalent circuit (Scheme 4.1). To study the Nyquist plot (Z' vs Z''), we have used simple circuit containing two R||C elements (for grain and grain boundary) along with a series resistance. In general, the R||C elements approach to semicircular Nyquist plot. But the above mention circuit does not fit our experimental data (Provided in supplementary). Therefore, we have substituted the R||C elements by R||CPE (CPE=Constant Phase Element). The CPE circuit element introduces the combination of resistance and capacitance instead of only contribution of capacitance. The CPE element consists of two parts one is empirical exponent (n) which varies from 0 to 1 and the other part is frequency independent constant impedance (Q).⁸⁶ They relate the resistance and capacitance according to the following equation,⁸⁹

$$C = Q^{1/n} R^{(1-n)/n} \quad (1)$$

The equivalent circuit (Scheme 4.1) which simulates the experimental Nyquist data can be represented mathematically. Here, the subscript 'g', and 'gb' demonstrate the grain and grain boundary, accordingly. The Nyquist plots along with the fitted data are shown in Figure 4.9c.



Scheme 4.1 The equivalent circuit to simulate the experimental Nyquist plot.

In the Nyquist plot, the intercept of arc on Z' axis decreases for compound 1 than 2 (the intercept does not touch Z' axis but it clearly approaches to Z' axis). In general, the intercept on Z' axis defines the total resistive nature of the material. So, the arc with lower radius (total resistance) of the compound 2 reveals the better intermolecular conducting behavior than compound 1.

4.2.5. Schottky diode

As the resistive behavior of compound 2 is minor in comparison to the other, we have attempted Schottky diode application to implement this phenomenon. In this regard, the aluminium electrode (0.065 μm thickness) was deposited on the films of 1 μm (approx.) thickness by evaporation technique. Hence, Al/compound/ITO configured Schottky diodes are constructed and the effective diode area was maintained as $7.065 \times 10^{-6} \text{ m}^2$.

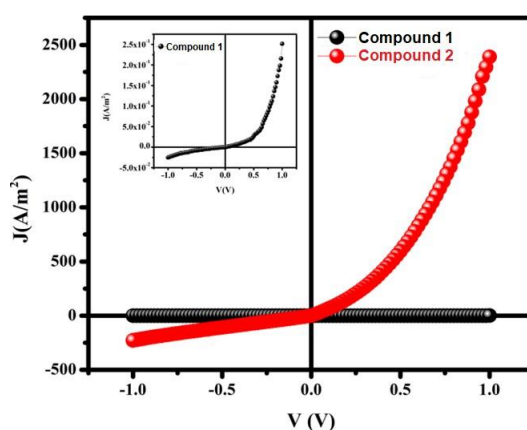


Figure 4.10 Current density vs Voltage (J-V) plot of Al/compound/ITO configured Schottky diode (Inset- J-V plot for compound 2 based diode).

The J-V characteristics (Figure 4.10) curves show rectifying behavior in forward bias. But, the enhanced current density of compound 2 based diode at forward bias clearly indicates the superior conducting nature of that compound than compound 1. DFT computational study has performed for both the compounds and it shows that the bandgap is falling in the semicon-

ductor range. The energy gap between HOMO and LUMO are 4.4 eV and 2.81 eV respectively (Figure 4.11). We have performed optical band gap measurement from UV-visible spectrum which is well supported by band gap measurement via DFT studies. We have found the value of E_g as 3.85 eV and 3.13 eV for the compound **1** and **2** respectively. Here, the synthesized compounds have performed as a semiconductor and formed a metal-semiconductor (MS Schottky) junction with Al metal. The conductivity is derived as $2.29 \times 10^{-7} \text{ Sm}^{-1}$ (**1**) and $2.54 \times 10^{-3} \text{ Sm}^{-1}$ (**2**), therefore the experimental results are verified with theoretically. The polymeric nature of the compound **2** may be the reason for lowering the band gap and hence enhancement of the conductivity. Therefore, the compound **2** is found as a better candidate for device application than **1**.

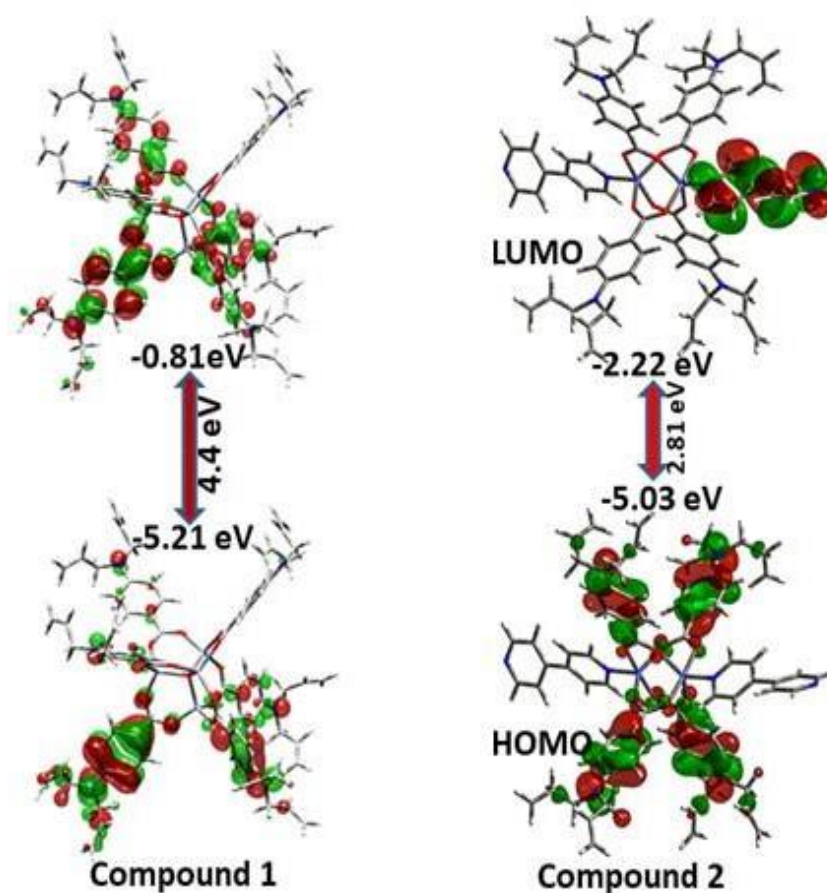


Figure 4.11 DFT computed energy of HOMO and LUMO of the compounds **1** and **2**.

4.3. EXPERIMENTAL SECTION

4.3.1. Materials and general method.

Sigma Aldrich helped us by providing all the required chemicals. Micro-analytical data (C, H, N) was collected on Perkin- Elmer 2400 CHNS/O elemental analyzer. Single crystals of the compound **1** and **2** was used for data collection using a Bruker SMART APEX II diffractometer equipped with graphite-monochromatic MoK α radiation ($\lambda = 0.71073 \text{ \AA}$). The crystal structure was solved using the SHELX-97 package. Thermogravimetric analysis was recorded on a Perkin-Elmer Pyris Diamond TG/DTA in the temperature range between 30°C and 600°C under a nitrogen atmosphere at a heating rate of 12 °C min⁻¹. The morphological study was done by field emission scanning electron microscope (FESEM, S-4800, Hitachi) and the PXRD data was collected on a Bruker D8 advance X-ray diffractometer using Cu K α radiation ($\lambda = 1.548 \text{ \AA}$) generated at 40 kV and 40 mA. The PXRD spectrum was recorded in a 2 θ range of 5–50. All the electrochemical measurements are carried out using 6038D (updated) electrochemical analyser with a scan rate of 50 mv/s. The current density-voltage (J-V) characteristics of both compounds are collected in the bias regime of $\pm 1\text{V}$ by using Keithley 2635B SMU under the dark. UV-VIS studies have performed using Perkin Elmer Lambda 25 spectrophotometer.

4.3.2. Synthesis of compounds **1** and **2**

A methanolic solution (3 ml) of 4,4'-bipyridine (4,4'-BPY, 46.84 mg, 0.3 mmol) was layered by the help of water-methanol (1:1) mixed solvent over the aqueous solution (3 ml) of Zn(NO₃)₂.6H₂O, (89.247 mg, 0.3 mmol). 4-Diallylamino-benzoic acid (HDABA, 65.18 mg, 0.3 mmol) in ethanol (3 ml) was neutralized with Et₃N (30.36 mg, 0.3 mmol) and layered above the 4,4'-bipyridine followed by water-methanol mixed solvent. It was then allowed to diffuse for a week. Two different types of crystals were deposited - the colorless block-shaped and yellow needle like crystals. The crystals were separated mechanically under the microscope and washed with methanol and water (1:1) mixture, and dried. The yield of compound **1** [Zn₄(μ_4 -O)(DABA)₆]_n, was 41% (82.52 mg) and of compound **2** [Zn₂(DABA)₄(4,4'-BPY)]_n was 46% (92.58 mg). Elemental analysis calculated for the compound **1**: C, 57.93; H, 7.87; N, 5.17 % and found C, 60.06; H, 7.73; N, 5.30 % ; calculated for the compound **2**: C, 63.66; H, 9.07; N, 8.22 % and found C, 63.60; H, 9.16; N, 8.11 %.

4.3.3. X-ray crystallographic data collection and structure determination

Crystal structure analysis of the compounds were carried out at room temperature on a Bruker Smart Apex diffractometer equipped with CCD and Mo-K α radiation ($\lambda = 0.71073 \text{ \AA}$). Cell refinement, indexing and scaling of the data set were done by using programs Bruker Smart Apex and Bruker Saint packages.⁹⁰ The structure was solved by direct methods and subsequent Fourier analyses⁹¹ and refined by the full-matrix least-squares method based on F^2 with all observed reflections.⁹² Hydrogen atoms were placed at geometrical positions. **The structure of the compound shows moderate alerts.** The completeness of data is less than the usual 99-100%, however it is only the very high angle data that is incomplete and 100% coverage is above 0.75 \AA . This will always be a problem with area detector data that is not truncated. Some bad reflections data are omitted during the refinement. **It may be the reason for high R-factor.**

4.3.4. Electrochemical measurement

The electrochemical activities of the as-prepared Zn(II) based compounds were carried out using three-electrode systems employing Ag/AgCl (filled with 1 M KCl) as reference electrode, Pt wire as counter electrode and fabricated glassy carbon as working electrode. All the reported potentials were converted with respect to the reversible hydrogen electrode (RHE) using the formula $E (\text{vs. RHE}) = E (\text{vs. Ag/AgCl}) + 0.196 \text{ V} + 0.059 \times \text{PH}$. PH of the N₂ and CO₂ saturated 0.1 M K₂CO₃ solution are 11.3 and 8.8 respectively.

4.3.5. DFT calculations

Gaussian-09 program package⁹³ has been used for spin state calculation using the hybrid B3LYP/LanL2DZ exchange–correlation function as implemented. Unit cell of the compound **1** and **2** are considered as a repeating unit whereas HOMO-LUMO calculations are performed in the molecular level considering discrete monomer unit of compound **1** and **2**. The lattice equivalent and deformation potentials were used to obtain the Schottky electrical contact. The deformation commonly refers to the energy gap between valence and conduction band which is the difference between highest occupied and lowest unoccupied molecular orbitals ($\Delta E = E_{\text{HOMO}} - E_{\text{LUMO}}$, eV). The band gap⁹⁴ of the compounds are calculated by using absolute deformation potentials (ADPs). The calculated band gaps for compound **1** and **2** are 4.4 eV and 2.81 eV respectively.

4.4. CONCLUSIONS

In summary, two Zn(II) coordination complexes with different geometry and dimension were synthesized from one-pot and separated mechanically. The structures are confirmed by X-ray measurements and one compound is tetranuclear (0D) with $(\mu_4\text{-O})\text{Zn}_4$ bridged by 4-diallylamino-benzoic acid (HDABA) and other is 1D coordination polymer in which a paddle wheel dinuclear $\text{Zn}_2(\text{DABA})_4$ is bridged by 4,4'-BPY (4,4'-Bipyridine). Due to the electron-donating nature of ligand, charge would transfer from the ligand to the metal sites in the complex, which enables faster and stronger electron injection to the antibonding orbitals of CO_2 to boost its CO_2RR activity. This research discovered the high efficiency and selectivity in electrocatalytic CO_2 reduction to methanol, formaldehyde and formic acid. Also due to the polymeric nature of compound **2** (1D), the conductivity based on diode derived from J-V characteristics has promisingly increased by 10^4 times than tetranuclear complex.

4.5. References

- (1) Manzi, A.; Simon, T.; Sonnleitner, C.; D'obliger, M.; Wyrwich, R.; Stern, O.; Stolarczyk, J.; Feldmann, J. Light-Induced Cation Exchange for Copper Sulfide Based CO_2 Reduction. *J. Am. Chem. Soc.* **2015**, *137*, 14007-14010.
- (2) Yan, D.; Dong, C.; Huang, Y.; Zou, Y.; Xie, C.; Wang, Y.; Zhang, Y.; Liu, D.; Shen, S.; Wang, S. Engineering the coordination geometry of metal–organic complex electrocatalysts for highly enhanced oxygen evolution reaction. *J. Mater. Chem.* **2018**, *6*, 805-810.
- (3) Dou, S.; Tao, L.; Wang, R.; Hankari, S.; Chen, R.; Wang, S. Plasma-Assisted Synthesis and Surface Modification of Electrode Materials for Renewable Energy. *Adv. Mater.* **2018**, *30*, 1705850.
- (4) Min, X.; Kanan, M. Pd-Catalyzed Electrohydrogenation of Carbon Dioxide to Formate: High Mass Activity at Low Overpotential and Identification of the Deactivation Pathway. *J. Am. Chem. Soc.* **2015**, *137*, 4701-4708.
- (5) Jiang, Z.; Xiao, T.; Kuznetsov, L. V.; Edwards, P. P. Turning carbon dioxide into fuel. *Phil. Trans. R. Soc. A.* **2010**, *368*, 3343–3364.
- (6) Qiao, J.; Liu, Y.; Hong, F.; Zhang, J. A Review of Catalysts for the Electroreduction of Carbon Dioxide to Produce Low-Carbon Fuels. *Chem. Soc. Rev.* **2014**, *43*, 631–675.

- (7) Zhu, D. D.; Liu, J. L.; Qiao, S. Z. Recent Advances in Inorganic Heterogeneous Electrocatalysts for Reduction of Carbon Dioxide. *Adv. Mater.* **2016**, *28*, 3423–3452.
- (8) Kondratenko, E. V.; Mul, G.; Baltrusaitis, J.; Larrazábal, G. O.; Pérez-Ramírez, J. Status and Perspectives of CO₂ Conversion into Fuels and Chemicals by Catalytic, Photocatalytic and Electrocatalytic Processes. *Energy Environ. Sci.* **2013**, *6*, 3112–3135.
- (9) Gao, S.; Lin, Y.; Jiao, X.; Sun, Y.; Luo, Q.; Zhang, W.; Li, D.; Yang, J.; Xie, Y. Partially oxidized atomic cobalt layers for carbon dioxide electroreduction to liquid fuel. *Nature*, **2016**, *529*, 68-71.
- (10) Tan, C. Y.; Lee, B. K.; Song, H.; Oh, J. Modulating Local CO₂ Concentration as a General Strategy for Enhancing C-C Coupling in CO₂ Electroreduction. *Joule*, **2020**, *4*, 1104–1120.
- (11) Artz, J.; Müller, T. E.; Thenert, K.; Kleinekorte, J.; Meys, R.; Sternberg, A.; Bardow, A.; Leitner, W. Sustainable conversion of carbon dioxide: an integrated review of catalysis and life cycle assessment. *Chem Rev.* **2018**, *118*, 434–504.
- (12) Francke, R.; Schille, B.; Roemelt, M. Homogeneously Catalyzed Electroreduction of Carbon Dioxide-Methods, Mechanisms, and Catalysts. *Chem Rev.* **2018**, *118*, 4631–4701.
- (13) Luo, W.; Zhang, J.; Li, M.; Züttel, A. Boosting CO production in electrocatalytic CO₂ reduction on highly porous Zn catalysts. *ACS Catal.* **2019**, *9*, 3783–3791.
- (14) Li, Q.; Fu, J.; Zhu, W.; Chen, Z.; Shen, B.; Wu, L.; Xi, Z.; Wang, T.; Lu, G.; Zhu, J.; Sun, S. Tuning Sn-catalysis for electrochemical reduction of CO₂ to CO via the core/shell Cu/SnO₂ structure. *J. Am. Chem. Soc.* **2017**, *139*, 4290–4293.
- (15) Liu, Y.; Chen, S.; Quan, X.; Yu, H. Efficient electrochemical reduction of carbon dioxide to acetate on nitrogen-doped nanodiamond. *J. Am. Chem. Soc.* **2015**, *137*, 11631–11636.
- (16) Lin, S.; Diercks, S. C.; Biao, Y.; Kornienko, N.; Nichols, M. E.; Zhao, Y.; Paris, R. A.; Kim, D.; Yang, P.; Yaghi, M. O.; Chang, J. C. S. Covalent organic frameworks comprising cobalt porphyrins for catalytic CO₂ reduction in water. *Science*, **2015**, *349*, 1208–1213.
- (17) Hoang, H. T. T.; Verma, S.; Ma, S.; Fister, T. T.; Timoshenko, J.; Frenkel, I. A.; Kenis, A. J. P.; Gewirth, A. A. Nanoporous copper-silver alloys by additive-controlled electrodeposition for the selective electroreduction of CO₂ to ethylene and ethanol. *J. Am. Chem. Soc.* **2018**, *140*, 5791–5797.

- (18) Zhao, C.; Dai, X.; Yao, T.; Chen, W.; Wang, X.; Wang, J.; Yang, J.; Wei, S.; Wu, Y.; Li, Y. Ionic exchange of metal-organic frameworks to access single nickel sites for efficient electroreduction of CO₂. *J. Am. Chem. Soc.* **2017**, *139*, 8078–8081.
- (19) Zhao, S.; Jin, R.; Jin, R. Opportunities and Challenges in CO₂ Reduction by Gold- and Silver-Based Electrocatalysts: From Bulk Metals to Nanoparticles and Atomically Precise Nanoclusters. *ACS Energy Lett.* **2018**, *3*, 452–462.
- (20) Kim, C.; Jeon, H. S.; Eom, T.; Jee, M. S.; Kim, H.; Friend, C. M.; Min, B. K.; Hwang, Y. J. Achieving Selective and Efficient Electrocatalytic Activity for CO₂ Reduction Using Immobilized Silver Nanoparticles. *J. Am. Chem. Soc.* **2015**, *137*, 13844–13850.
- (21) Gattrell, M.; Gupta, N.; Co, A. A review of the aqueous electrochemical reduction of CO₂ to hydrocarbons at copper. *J. Electroanal. Chem.* **2006**, *594*, 1–19.
- (22) Tamaki, Y.; Morimoto, T.; Koike, K.; Ishitani, O. Photocatalytic CO₂ reduction with high turnover frequency and selectivity of formic acid formation using Ru (II) multinuclear complexes. *Proc. Natl. Acad. Sci. U. S. A.* **2012**, *109*, 15673–15678.
- (23) Clark, L. M.; Cheung, L. P.; Lessio, M.; Carter, A. E.; Kubiak, P. C. Kinetic and mechanistic effects of bipyridine (bpy) substituent, labile ligand, and Brønsted acid on electrocatalytic CO₂ reduction by Re(bpy) complexes. *ACS Catal.* **2018**, *8*, 2021–2029.
- (24) Varela, A. S.; Ju, W.; Strasser, P. Molecular Nitrogen–Carbon Catalysts, Solid Metal Organic Framework Catalysts, and Solid Metal/Nitrogen-Doped Carbon (MNC) Catalysts for the Electrochemical CO₂ Reduction. *Adv. Energy Mater.* **2018**, *8*, 1703614.
- (25) Kang, X.; Zhu, Q.; Sun, X.; Hu, J.; Zhang, J.; Liu, Z.; Han, B. Highly efficient electrochemical reduction of CO₂ to CH₄ in an ionic liquid using a metal–organic framework cathode. *Chem. Sci.* **2015**, *7*, 266–273.
- (26) Jin, B.; Luo, L.; Xie, L. Pathways and Kinetics for Autocatalytic Reduction of CO₂ into Formic Acid with Fe under Hydrothermal Conditions. *ACS Omega*, **2021**, *17*, 11280–11285.
- (27) Liua, Y.; Fan, X.; Nayak, A.; Wang, Y.; Shan, B.; Quan, X.; Meyer, J. T. Steering CO₂ electroreduction toward ethanol production by a surface-bound Ru polypyridyl carbene catalyst on N-doped porous carbon. *PNAS*, **2019**, *116*, 26353–26358.
- (28) Luo, W.; Xie, W.; Li, M.; Zhang, J.; Züttel, A. 3D Hierarchical Porous Indium Catalyst for Highly Efficient Electroreduction of CO₂. *J. Mater. Chem. A*, **2019**, *7*, 4505–4515.

- (29) Li, J.; Kuang, Y.; Meng, Y.; Tian, X.; Hung, W.-H.; Zhang, X.; Li, A.; Xu, M.; Zhou, W.; Ku, C.-S.; Chiang, C.-Y.; Zhu, G.; Guo, J.; Sun, X.; Dai, H. Electroreduction of CO₂ to Formate on a Copper-Based Electrocatalyst at High Pressures with High Energy Conversion Efficiency. *J. Am. Chem. Soc.* **2020**, *142*, 7276–7282.
- (30) Sen, S.; Brown, M. S.; Leonard, M.; Brushett, R. F. Electroreduction of carbon dioxide to formate at high current densities using tin and tin oxide gas diffusion electrodes. *J. Appl. Electrochem.*, **2019**, *49*, 917–928.
- (31) Yin, Z.; Palmore, R. T. G.; Sun, S. Electrochemical Reduction of CO₂ Catalyzed by Metal Nanocatalysts. *Trends in Chemistry*, **2019**, *1*, 739-750.
- (32) Fiedler, E.; Grossmann, G.; Burkhard, K. D.; Weiss, G.; Witte, C. "Methanol". Ullmann's Encyclopedia of Industrial Chemistry. Weinheim, Wiley-VCH. **2005**.
- (33) Biodiesel Production Principles and Processes - extension. Retrieved 24 March, **2018**.
- (34). Evaluation of the Fate and Transport of Methanol in the Environment. Archived 16 May **2016** at the Portuguese Web Archive, Malcolm Pirnie, Inc., January **1999**.
- (35) Sánchez, G. O.; Birdja, Y. Y.; Bulut, M.; Vaes, J.; Breugelmans, T.; Pant, D. Recent advances in industrial CO₂ electroreduction. *Current Opinion in Green and Sustainable Chemistry*, **2019**, *16*, 47–56.
- (36) Yang, D.; Zhu, Q.; Chen, C.; Liu, H.; Liu, Z.; Zhao, Z.; Zhang, X.; Liu, S.; Han, B. Selective electroreduction of carbon dioxide to methanol on copper selenide nanocatalysts. *Nat Commun*, **2019**, *10*, 677.
- (37) Jiang, X.; Li, H.; Xiao, J.; Gao, D.; Si, R.; Yang, F.; Li, Y.; Wang, G.; Bao, X. Carbon dioxide electroreduction over imidazolate ligands coordinated with Zn (II) center in ZIFs. *Nano Energy*, **2018**, *52*, 345-350.
- (38) Kozachuk, O.; Luz, I.; Fx, L. I. X.; Noei, H.; Kauer, M.; Albada, H. B.; Bloch, E. D.; Marler, B.; Wang, Y.; Muhler, M. Multifunctional, defect- engineered metal–organic frameworks with ruthenium centers: sorption and catalytic properties. *Angew Chem. Int. Edit.* **2014**, *53*, 7058-7062.
- (39) Nangia, A. K.; Desiraju, G. R. Crystal Engineering: An Outlook for the Future. *Angew Chem. Int. Edit.* **2018**, *58*, 4100 – 4107.

- (40) Nath, k.; Karan, C.; Biradha, k. MOFs and MOF Derived N-doped Porous Carbon Materials as Heterogeneous Catalysts: Chemical Fixation of Carbon Dioxide under Mild Conditions and Electrochemical Hydrogen Evolution. *Cryst. Growth Des.* **2019**, *19*, 6672-6681.
- (41) Moi, r.; Nath, k.; Biradha, k. Tailoring Coordination Polymers by Substituent Effect: A Bi-functional Co(II) Doped 1D-Coordination Network with Electrochemical Water Oxidation and Nitro Aromatics Sensing. *Chem. Asian J.* **2019**, *14*, 3742–3747.
- (42) Kornienko, N.; Zhao, Y.; Kley, S. C.; Zhu, C.; Kim, D.; Lin, S.; Chang, J. C.; Yaghi, M. O.; Yang, P. Metal–Organic Frameworks for Electrocatalytic Reduction of Carbon Dioxide *J. Am. Chem. Soc.* **2015**, *137* (44), 14129–14135.
- (43) Lin, S.; Diercks, S. C.; Zhang, Y.; Kornienko, N.; Nichols, M. E.; Zhao, Y.; Paris, R. A.; Kim, D.; Yang, P.; Yaghi, M. O.; Chang, J. C. Covalent organic frameworks comprising cobalt porphyrins for catalytic CO₂ reduction in water. *Science* **2015**, *349*, 1208-1213.
- (44) Costentin, C.; Drouet, S.; Robert, M.; Savéant, J. A Local Proton Source Enhances CO₂ Electroreduction to CO by a Molecular Fe Catalyst. *Science* **2012**, *338*, 90-94.
- (45) J. Ran, M. Jaroniec, S. Qiao, Cocatalysts in Semiconductor-based Photocatalytic CO₂ Reduction: Achievements, Challenges, and Opportunities. *Adv Mater* **2018**, *30*, 1704649.
- (46) Zhong, H.; Wang, J.; Zhang, Y.; Xu, W.; Xing, W.; Xu, D.; Zhang, Y.; Zhang, X. ZIF-8 derived graphene-based nitrogen-doped porous carbon sheets as highly efficient and durable oxygen reduction electrocatalysts. *Angew Chem Int Edit* **2014**, *53*, 14235-14239.
- (47) Wang, J. Zhong, x-. H.; Qin, Y.; Zhang, X. An efficient three-dimensional oxygen evolution electrode. *Angew Chem Int Edit* **2013**, *52*, 5248-5253.
- (48) Jiang, X.; Li, H.; Xiao, J.; Gao, D.; Si, R.; Yang, F.; Li, Y.; Wang, G.; Bao, X.; Carbon dioxide electroreduction over imidazolate ligands coordinated with Zn(II) center in ZIFs. *Nano Energy* **2018**, *52*, 345-350.
- (49) Wu, Y.; Jiang, J.; Weng, Z.; Wang, M.; Broere, D.; Zhong, Y.; Brudvig, W. G.; Feng, Z.; Wang, H. Electroreduction of CO₂ Catalyzed by a Heterogenized Zn–Porphyrin Complex with a Redox-Innocent Metal Center. *ACS Cent. Sci.* **2017**, *3* (8), 847–852.
- (50) Donovan, S. E.; Barry, M. B.; Larsen, A. C.; Wirtz, N. M.; Geiger, E. W.; Kemp, A. R. Facilitated carbon dioxide reduction using a Zn(II) complex. *Chem. Commun.*, **2016**, *52*, 1685-1688.

- (51) Dou, S.; Song, J.; Xi, S.; Du, Y.; Wang, J.; Huang, Z.; Xu, Z.; Wang, X. Boosting Electrochemical CO₂ Reduction on Metal-Organic Frameworks via Ligand Doping. *Angew Chem Int Edit* **2019**, *58*, 4041-4045.
- (52) Rosen, B.; Salehi-Khojin, A.; Thorson, M.; Zhu, W.; Whipple, D.; Kenis, P.; Masel, R. Ionic liquid-mediated selective conversion of CO₂ to CO at low overpotentials. *Science*, 2011, *334*, 643-644.
- (53) Whipple, D. T.; Kenis, P. J. Prospects of CO₂ Utilization via Direct Heterogeneous Electrochemical Reduction. *J. Phys. Chem. Lett.* 2010, *1*, 3451-3458.
- (54) Jensen, M. T.; Rønne, M. H.; Ravn, A. K.; Juhl, R. W.; Nielsen, D. U.; Hu, X.-M.; Pedersen, S. U.; Daasbjerg, K.; Skrydstrup, T. Scalable Carbon Dioxide Electroreduction Coupled to Carbonylation Chemistry. *Nat. Commun.* 2017, *8*, 489.
- (55) Gong, J.; Zhang, L.; Zhao, Z. Nanostructured Materials for Heterogeneous Electrocatalytic CO₂ Reduction and their Related Reaction Mechanisms. *Angew Chem. Int. Edit.* 2017, *56*, 11326-11353.
- (56) Li, X.; Bi, W.; Chen, M.; Sun, Y.; Ju, H.; Yan, W.; Zhu, J.; Wu, X.; Chu, W.; Wu, C.; Xie, Y. Exclusive Ni-N₄ Sites Realize Near-Unity CO Selectivity for Electrochemical CO₂ Reduction. *J. Am. Chem. Soc.* 2017, *139*, 14889-14892.
- (57) Jiao, Y.; Zheng, Y.; Chen, P.; Jaroniec, M.; Qiao, S. Molecular Scaffolding Strategy with Synergistic Active Centers To Facilitate Electrocatalytic CO₂ Reduction to Hydrocarbon/Alcohol. *J. Am. Chem. Soc.* 2017, *139*, 18093-18100.
- (58) Geng, Z.; Kong, X.; Chen, W.; Su, H.; Liu, Y.; Cai, F.; Wang, G.; Zeng, J. Oxygen Vacancies in ZnO Nanosheets Enhance CO₂ Electrochemical Reduction to CO. *Angew Chem. Int. Edit.* 2018, *57*, 6054-6059.
- (59) Ran, J.; Jaroniec, M.; Qiao, S. Cocatalysts in Semiconductor-based Photocatalytic CO₂ Reduction: Achievements, Challenges, and Opportunities. *Adv. Mater.* **2018**, *30*, 1704649.
- (60) J. J. Hermans, L. Baij, M. Koenis, K. Keune, P. D. Iedema, S. 2D-IR spectroscopy for oil paint conservation: Elucidating the water-sensitive structure of zinc carboxylate clusters in ionomers, *Adv.* 2019;5: eaaw3592;
- (61) Yi, D.-J.; Xie, R.; Xie, L.-Z.; Chai, L.-G.; Liu, F.-T.; Chen, P.-R.; Huang, B.-Y.; Cao, R. Highly Selective CO₂ Electroreduction to CH₄ by In Situ Generated Cu₂O Single-Type Sites

on a Conductive MOF: Stabilizing Key Intermediates with Hydrogen Bonding. *Angew Chem Int Edit* **2020**, *59*, 23641-23648.

(62) Zhao, S.; Tan, C.; He, C.; An, P.; Xie, F.; Jiang, S.; Zhu, Y.; Wu, K.; Zhang, B.; Li, H.; Zhang, J.; Chen, Y.; Liu, S.; Dong, J.; Tang, Z. Structural transformation of highly active metal–organic framework electrocatalysts during the oxygen evolution reaction. *Nature Energy*, **2020**, *5*, 881–890.

(63) Yi, J-D.; Si, D-H.; Xie, R.; Yin, Q.; Zhang, M-D.; Wu, Q.; Chai, G-L.; Huang, Y-B.; Cao, R. Conductive Two-Dimensional Phthalocyanine-based Metal–Organic Framework Nanosheets for Efficient Electroreduction of CO₂. *Angew. Chem. Int. Ed.* **2021**, *60*, 2–9.

(64) Zhang, M-D.; Si, D-H.; Yi, J-D.; Zhao, S-S.; Huang, Y-B.; Cao, R. Conductive Phthalocyanine-Based Covalent Organic Framework for Highly Efficient Electroreduction of Carbon Dioxide. *Small*, **2020**, *16*, 2005254.

(65) Nikiforova, P. A.; Stenina, I. A.; Kulova, T. L.; Skundin, A. M.; Yaroslavtsev, A. B. Effect of particle size on the conductive and electrochemical properties of Li₂ZnTi₃O₈. *Inorg Mater*, **2016**, *52*, 1137–1142.

(66) Makhlof, S.A.; Kassem, M.A.; Abdel-Rahim, M. A. Particle size-dependent electrical properties of nanocrystalline NiO. *J Mater Sci*, **2009**, *44*, 3438–3444.

(67) Jana, S.; Jana, R.; Sil, S.; Dutta, B.; Sato, H.; Ray, P. P.; Datta, A.; Akitsu, T.; Sinha, C. Influence of Axial Linkers on Polymerization in Paddle Wheel Cu(II) Coordination Polymers for the Application of Optoelectronics Devices. *Cryst. Growth Des.* **2019**, *19*, 6283-6290.

(68) Chandra, A.; Das, M.; Pal, K.; Jana, S.; Dutta, B.; Ray, P. P.; Jana, K.; Sinha, C. 3D-Coordination Polymer of Zn(II)-carboxylate : Structural Elucidation, Photo-electrical Conductivity and Biological Activity. *ACS Omega*, **2019**, *4*, 17649-1766.

(69) Dutta, B.; Das, D.; Datta, J.; Chandra, A.; Jana, S.; Sinha, C.; Ray, P. P.; Mir, H. M. Synthesis of a Zn (ii)-based 1D zigzag coordination polymer for the fabrication of optoelectronic devices with remarkably high photosensitivity. *Inorganic Chemistry Frontiers*, **2019**, *6*, 1245-1252.

(70) Jana, S.; Ray, A.; Chandra, A.; Fallah, S. M.; Das, S.; Sinha, C. Studies on Magnetic and Dielectric Properties of Antiferromagnetically Coupled Dinuclear Cu(II) in a One-Dimensional Cu(II) Coordination Polymer. *ACS Omega*, **2020**, *5*, 274-280.

(71) Naskar, K.; Dey, A.; Dutta, B.; Ahmed, F.; Sen, C.; Mir, M. H.; Roy, P. P.; Sinha, C. Intercatenated coordination polymers (ICPs) of carboxylato bridged Zn (II)-isoniazid and their electrical conductivity. *Cryst. Growth Des.* **2017**, *17*, 3267-3276.

(72) Naskar, K.; Maity, S.; Jana, S.; Dutta, B.; Tanaka, S.; Mallick, D.; Akitsu, T.; Sinha, C. Arylazoimidazole Coordinated and Naphtha-lene-Dicarboxylato Bridged Polymers of Co (II) and Photochromic Zn (II) Complexes. *Cryst. Growth Des.* **2018**, *18*, 2986-2997.

(73) Dutta, B.; Jana, R.; Bhanja, A. K.; Ray, P. P.; Sinha, C.; Mir, M. H. Supramolecular aggregate of Cadmium (II)-based one-dimensional coordination polymer for device fabrication and sensor application. *Inorg. Chem.* **2019**, *58*, 2686-2694.

(74) Naskar, K.; Dey, A.; Maity, S.; Bhunia, M.; Ray, P. P.; Sinha, C. Novel Porous Polycatenated Iodo-Cadmium Coordination Polymer for Iodine Sorption and Electrical Conductivity Measurement. *Cryst. Growth Des.* **2019**, *19*, 2206-2218.

(75) Shawuti, S.; Can, M. M.; Gülgün, M. A.; Fırat, T. Grain Size Dependent Comparison of ZnO and ZnGa₂O₄ Semiconductors by Impedance Spectrometry. *Electrochimica Acta.* **2014**, *145*, 132-138.

(76) Ray, A.; Roy, A.; Bhattacharjee, S.; Jana, S.; Ghosh, C.; Sinha, C.; Das, S. Correlation between the dielectric and electrochemical properties of TiO₂-V₂O₅ nanocomposite for energy storage application. *Electrochimica Acta.* **2018**, *266*, 404-413.

(77) Wang, N.; Liu, Z.; Ma, J.; Liu, J.; Zhou, P.; Chao, Y.; Ma, C.; Bo, X.; Liu, J.; Hei, Y.; Bi, Y.; Sun, M.; Cao, M.; Zhang, H.; Chang, F.; Wang, H.-L.; Xu, P.; Hu, Z.; Bai, J.; Sun, H.; Hu, G.; Zhou, M. Sustainability Perspective-Oriented Synthetic Strategy for Zinc Single-Atom Catalysts Boosting Electrocatalytic Reduction of Carbon Dioxide and Oxygen. *ACS Sustainable Chem. Eng.* **2020**, *8*, 13813-13822.

(78) Cronin, P. S.; Strain, M. J.; Mashuta, S. M.; Spurgeon, M. J.; Buchanan, M. R.; Graperhaus, A. C. Exploiting Metal-Ligand Cooperativity to Sequester, Activate, and Reduce Atmospheric Carbon Dioxide with a Neutral Zinc Complex. *Inorg. Chem.* **2020**, *59*, 4835-4841.

(79) Ren, D.; Ang, B.; Yeo, S. B. Tuning the Selectivity of Carbon Dioxide Electroreduction toward Ethanol on Oxide-Derived Cu_xZn Catalysts. *ACS Catal.* **2016**, *6*, 8239-8247.

- (80) Ren, D.; Gao, J.; Grätzel, M. Understanding the Electrochemical Reduction of Carbon Dioxide at Copper Surfaces. *ACS Symposium Series*, **2019**, 1331.
- (81) Wang, P.; Li, X.; Zhang, P.; Zhang, X.; Shen, Y.; Zheng, B.; Wu, J.; Li, S.; Fu, Y.; Zhang, W.; Huo, F. Transitional MOFs: exposing metal sites with porosity for enhancing catalytic reaction performance. *ACS Appl. Mat. Interf.*, **2020**, 12, 23968–23975.
- (82) Zha, F.; Ding, J.; Chang, Y.; Ding, J.; Wang, J.; Ma, J. Cu–Zn–Al Oxide Cores Packed by Metal-Doped Amorphous Silica–Alumina Membrane for Catalyzing the Hydrogenation of Carbon Dioxide to Dimethyl Ether. *Ind. Eng. Chem. Res.* **2012**, 51, 345–352.
- (83) Jiang, X.; Wang, X.; Wang, Q.; Xiao, X.; Chen, J.; Wang, M.; Shen, Y. Efficient Activation and Electroreduction of Carbon Dioxide on an Electrocatalyst Cadmium Carbonate. *ACS Appl. Energy Mater.* **2021**, 4, 2073–2080.
- (84) Qin, B.; Li, Y.; Fu, H.; Wang, H.; Chen, S.; Liu, Z.; Peng, F. Electrochemical Reduction of CO₂ into Tunable Syngas Production by Regulating the Crystal Facets of Earth-Abundant Zn Catalyst. *ACS Appl. Mater. Interfaces*, **2018**, 10, 20530–20539.
- (85) Datta, J.; Das, M.; Dey, A. Sil, S.; Jana, R.; Halder, S.; Das, P.; Ray, P. P. Experimental and theoretical overview on bias dependent Debye relaxation and conduction mechanism of Cd_{1-x}Zn_xS film and its significance in signal transport network. *Materials Chemistry and Physics*. **2018**, 213, 23-34.
- (86) Panda, R.K.; Muduli, R.; Kar, S. K.; Behera, D. Dielectric relaxation and conduction mechanism of cobalt ferrite nanoparticles. *Journal of Alloys and Compounds*. **2014**, 615, 899-905.
- (87) Rahmouni, H.; Smari, M.; Cherif, B.; Dhahri, E.; Khirouni, K. Conduction mechanism, impedance spectroscopic investigation and dielectric behavior of La_{0.5}Ca_{0.5-x}Ag_xMnO₃ manganites with compositions below the concentration limit of silver solubility in perovskites (0 ≤ x ≤ 0.2). *Dalton Trans.* **2015**, 44, 10457-10466.
- (88) Sil, S.; Datta, J.; Das, M.; Jana, R.; Halder, S.; Biswas, A.; Sanyal, D.; Ray, P. P. Bias dependent conduction and relaxation mechanism study of Cu₅FeS₄ film and its significance in signal transport network. *Journal of Materials Science: Materials in Electronics*. **2018**, 29, 5014–5024.

(89) Ahmad, I.; Akhtar, M. J.; Younas, M.; Siddique, M.; Hasan, M. M. Small polaronic hole hopping mechanism and Maxwell-Wagner relaxation in NdFeO₃. *JOURNAL OF APPLIED PHYSICS*. **2012**, *112*, 074105.

(90) Bruker, **2000**. SMART, SAINT. Software Reference Manual Bruker AXS Inc. Madison, Wisconsin, USA.

(91) Sheldrick, G. M. *Acta Cryst A*, **2008** A64, 112-122.

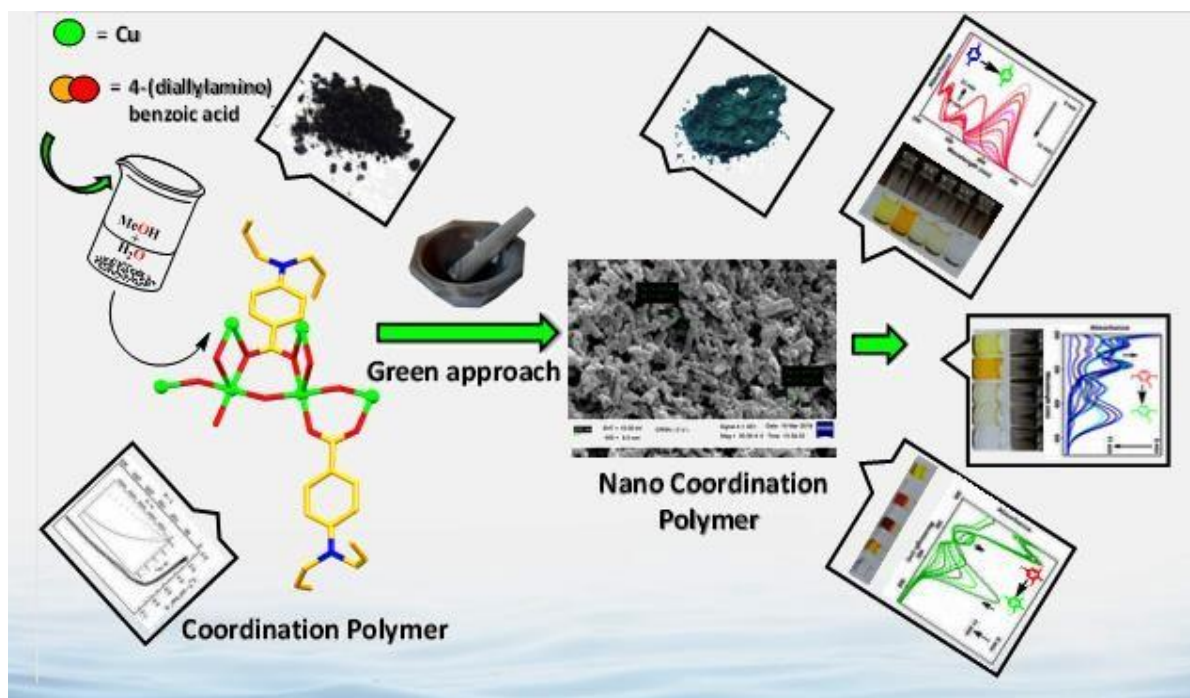
(92) Farrugia, L. J. *J. Appl. Crystallogr.* **2012**, *45*, 849-854.

(93) Frisch, M. J.; Trucks, G. W.; Schlegel, H. B.; Scuseria, G. E.; Robb, M. A.; Cheeseman, J. R.; Scalmani, G.; Barone, V.; Mennucci, B.; Petersson, G. A.; Nakatsuji, H.; Caricato, M.; Li, X.; Hratchian, H. P.; Izmaylov, A. F.; Bloino, J.; Zheng, G.; Sonnenberg, J. L.; Hada, M.; Ehara, M.; Toyota, K.; Fukuda, R.; Hasegawa, J.; Ishida, M.; Nakajima, T.; Honda, Y.; Kitao, O.; Nakai, H.; Vreven Jr, T.; Montgomery, J. A.; Peralta, J. E.; Ogliaro, F. M.; Bearpark, J.; Heyd, J.; Brothers, E.; Kudin, K. N.; Staroverov, V. N.; Kobayashi, R.; Normand, J.; Raghavachari, K.; Rendell, A.; Burant, J. C.; Iyengar, S. S.; Tomasi, J.; Cossi, M.; Rega, N.; Millam, J. M.; Klene, M.; Yazyev, O.; Austin, A. J.; Cammi, R.; Pomelli, C.; Ochterski, J. W.; Martin, R. L.; Morokuma, K.; Zakrzewski, V. G.; Salvador, G. A. P.; Dannenberg, J. J.; Dapprich, S.; Daniels, A. D.; Farkas, Ö.; Foresman, J. B.; Ortiz, J. V.; Cioslowski, J.; Fox, D. *J. Gaussian, Inc.*, CT Wallingford, **2009**.

(94) Li, Y.-H.; Gong, X. G.; Wei, S.-H. Ab Initio Calculation of Hydrostatic Absolute Deformation Potential of Semiconductors. *Appl. Phys. Lett.* **2006**, *88*, 042104–042106.

Abstract

The 1D coordination polymer, $[\text{Cu}_2(\mu_2\text{-OH})_2(\text{DABA})_2]_n$ (**1**), (HDABA = 4-Diallylamino-benzoic acid) is characterized by Single crystal X-Ray diffraction analysis. The structure switches to a 2D geometry by hydrogen bonding interactions. Hand grinding aqueous suspension of the coordination polymer, **1**, present in nano regime of av. 100 nm dimension and shows catalytic performance in the reduction of toxic nitrophenols to corresponding aminophenols by NaBH_4 . The rate constant values (κ_{app}) are 2.4×10^{-3} (4-NP), 5.3×10^{-3} (2,4-DNP) and 5.6×10^{-3} (2,4,6-TNP) s^{-1} are much higher than reduction by only NaBH_4 . The susceptibility measurements (χ_{MT}) of Cu(II) coordination polymer indicates the presence of a very weak antiferromagnetic coupling between the metal centres. The hand grinding technique and reusability of **1** makes the approach chemically green, cost effective and attracts the attention towards the real-life application.



5.1. Introduction

Nitroaromatics (NACs) are well known weedkillers and insect repellent and precursors to synthetic dyestuff.¹⁻³ These compounds are not degraded easily by microbes. Because of strong toxicity, the NACs are noted as pollutants by the Environmental Protection Agency.⁴ Conventional waste water management methods such as reverse osmosis, adsorption ion exchange,⁵ photocatalysis,⁶ membrane separation,⁷ and electro coagulation have been proposed for the detoxification of highly persistent organic pollutants. Besides, some of the nitrophenols are explosive and have been used for terroristic activity. Immediate disposal of NACs is an issue of explosive and safety departments of the Government. The conversion of toxic NACs to the secondary nontoxic and useful chemicals is very urgent issue for the forensic personals and researchers. The chemical reduction has been one of the most commonly applied techniques of detoxification of the NACs using metal nanoparticles (MNP's) as catalysts and BH_4^- as reducing agent. On the other hand, the reduced products, amino phenols (AP) are very important moiety in dyes and pigments, pharmaceuticals industry.⁸ Literature survey reports that there is no such coordination polymer that serves as catalyst bed for the reduction of NACs. Up to now, large number of nano metal catalysts (Pt, Au, Ag, Pd etc.) have been fabricated for the reduction of NACs.⁹⁻¹³ Yongsheng Fu et al.¹⁴ (2017), Nguyen et al.¹⁵ (2018) and Yukui Fu et al.¹⁶ (2019) have used expensive gold catalyst to carry out such transformation while Ying Ma et al.¹⁷ (2017) used silver catalyst for the same. Sahiner et al.¹⁸ (2010) introduced cobalt catalyst for the reduction.

Coordination Polymers (CPs) are prepared by bridging organic coordinating groups with metal ions.¹⁹⁻²² They are promising contender for catalysis,²³ drug delivery,²⁴ gas storage,²⁵ and energy storage systems.^{26,27} Some of the CPs have been serving as catalyst in the reduction of Nitrophenols (NP), (4-NP, 2,4-DNP, 2,4,6-TNP).²⁸ In this paper, we have characterized Cu(II) CP that has been used as a catalyst for the reduction of toxic and explosive NPs in aqueous medium. The easy removal of solid phase catalyst even at nm level by filtration makes this catalyst analytically useful. The efficiency of the catalyst is reflected in the rate constant (κ_{app}) data of the nitrophenol reductions. Owing to the catalytic activity we have designed the coordination polymer of Cu(II)- 4-diallylamino benzoic acid and has been structurally characterized.²⁹ The reusability of the catalyst in the several catalytic cycles of various nitrophenols, makes the compound unique. Besides, the coordination polymer of Cu(II), d^9 , may show efficient magnetic exchange behavior that has been supported by variable temperature magnetic measurements.³⁰⁻³²

5.2. Results and Discussion

5.2.1. Molecular Structure, Stability and Morphology of 1

The compound **1** crystallizes in the orthorhombic space group, $Fdd2$ and the symmetric unit comprises two independent Cu(II), two 4-(diallylamino)benzoate (DABA⁻) bridgers and two μ_2 -OH. Two copper atoms, Cu1 and Cu2, exhibit distorted square pyramidal geometry where the basal plane is formed by two bridging hydroxides and two carboxylato oxygen donors (Figure 5.1 and table 5.1).³⁴ The coordination is completed by occupying caoboxylato-O at apical position of a symmetry related species. The Cu-O bond distances in the square pyramidal base are in between 1.875(6)-1.988(4) Å, while the Cu-O (apical) are significantly longer of 2.598(5) Å and 2.609(6) Å, for Cu1 and Cu2, respectively (Figure 5.1).

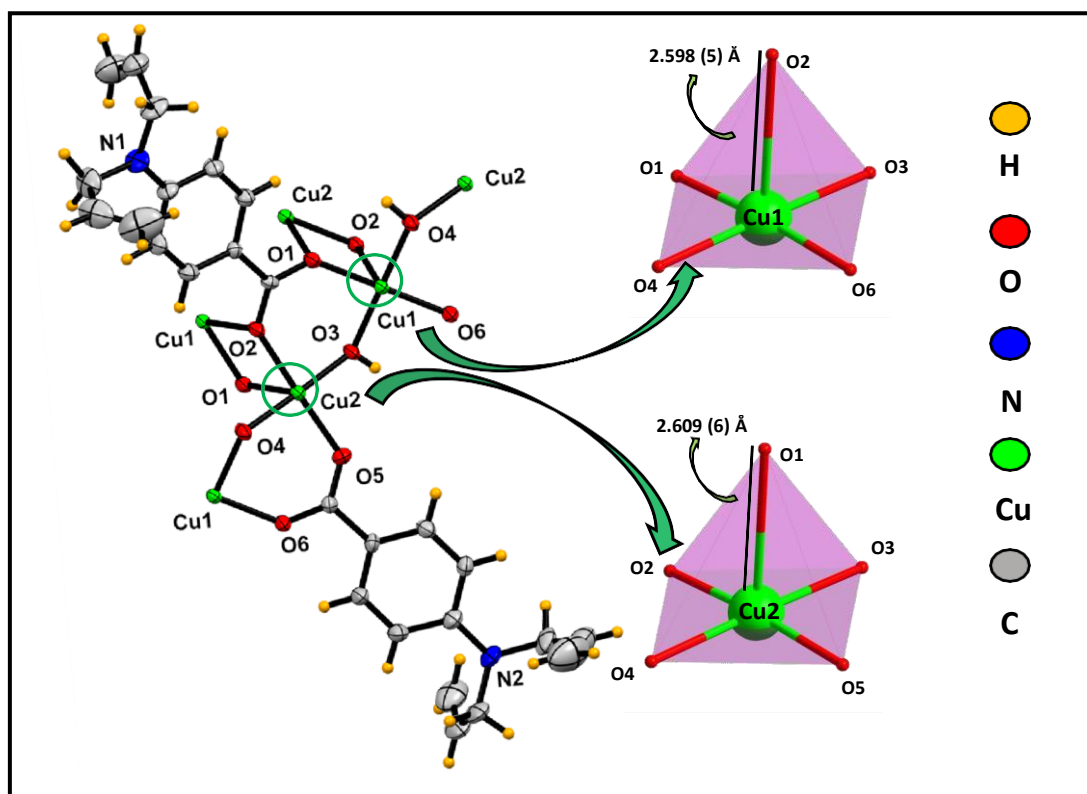


Figure 5.1 ORTEP diagram of coordination polymer $[\text{Cu}_2(\mu_2\text{-OH})_2(\text{DABA})_2]_n$ (**1**) (40% probability ellipsoids)

The 1D polymer (Figure 5.2a) is formed by two adjacent $-\text{[Cu}(\text{DABA})(\text{OH})]_n-$ chains where carboxylato-O, O1 and O2, behave as apical donors for the copper atoms to the adjacent chain. In chain, copper atoms are alternatively separated by 3.338 and 3.377 Å, sharing a vertex of the square pyramidal polyhedron (Figure 5.2b). Besides, copper atoms of the two adjacent chains are 3.389 Å far apart and share an edge of their polyhedra.³⁵

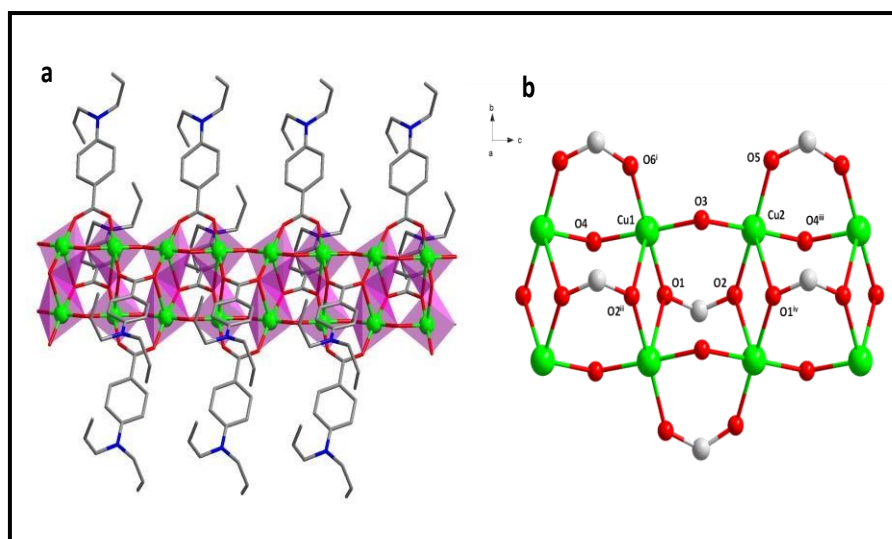


Figure 5.2 (a) The two connected 1D polymeric chains elongated along axis *c* with indication of coordination polyhedral around the copper atoms (H atoms not included for clarity) and (b) Details of the 1D chain of **1**.

Table 5.1 Crystallographic Data and Details of Refinements for **1**

CCDC No.	1896232
Formula	C ₂₆ H ₃₀ Cu ₂ N ₂ O ₆
fw	593.60
crystal system	Orthorhombic
space group	<i>F</i> dd2
<i>a</i> (Å)	34.191(4)
<i>b</i> (Å)	46.031(5)
<i>c</i> (Å)	6.7145(7)
<i>V</i> (Å ³)	10568(2)
<i>Z</i>	16
<i>D</i> _{calcd} (g/cm ³)	1.492
μ(mm ⁻¹)	1.652
<i>F</i> (000)	4896
Reflections collected	19047
Independent reflections	5391 [R(int) = 0.0526]
Data [<i>I</i> > 2σ(<i>I</i>)]	3564
parameters	331
GOF on <i>F</i> ²	1.002
final <i>R</i> indices [<i>I</i> > 2σ(<i>I</i>)] ^a	R1 = 0.0402; wR2 = 0.0969
Residuals (e Å ⁻³)	0.448, -0.473

$$^a R1 = \sum ||F_o| - |F_c|| / \sum |F_o|, wR2 = [\sum w(F_o^2 - F_c^2)^2 / \sum w(F_o^2)^2]^{1/2}$$

The particle size of the synthesized compound, **1**, diminished to nano regime by following hand grinding technique. The resultant powder **1** was characterised by scanning electron microscope. The SEM images of the powder **1** had a cubic rod like morphology (Figure 5.3a) as it is supported from the single crystal symmetry of **1**. The SEM image (Figure 5.3b) reveals the uniform distribution of the particles. Using Gaussian function, we have fitted the particle size distribution which is obtained from the SEM images.³⁶ Small particle size indicates the lower grain size and higher grain boundary which may affect the conducting electrons which helps in the reduction reaction. Intense peaks of PXRD patterns of bulk are matched with those simulated from single crystal data and nano regime form which also indicates the phase purity of the bulk sample (Figure 5.3c).

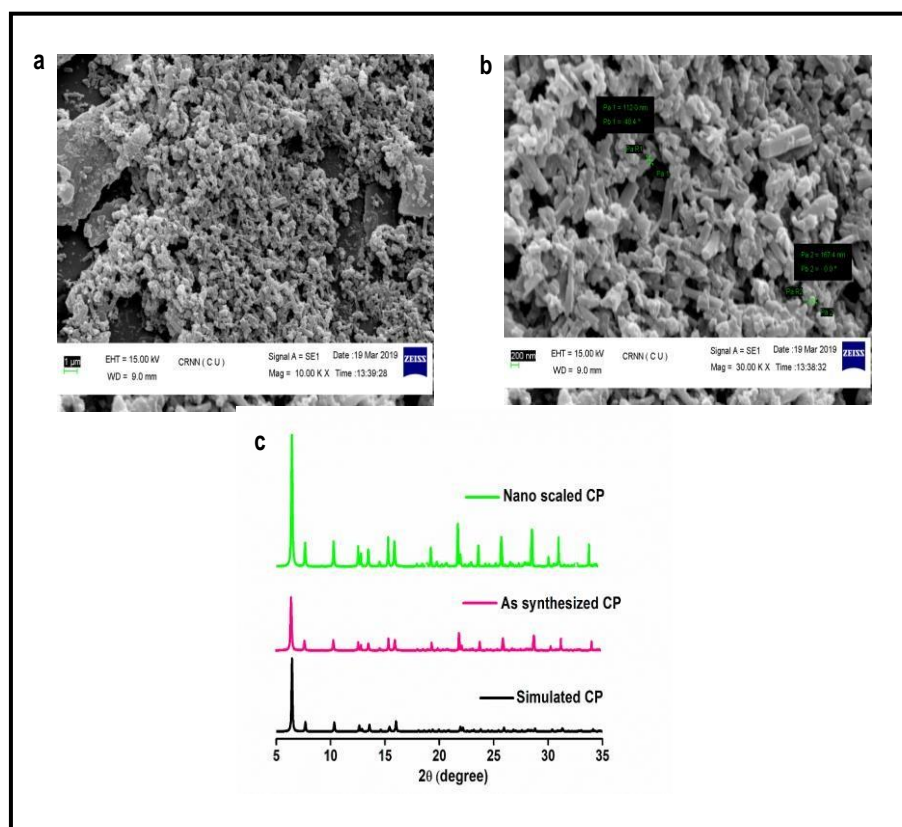


Figure 5.3 (a) Low magnificant SEM image of synthesized nano scaled compound **1**. (b) High magnificant cubic rod-shaped SEM image of nano scaled compound **1**. (c) PXRD pattern of simulated, as synthesized & nano scaled product **1** collected under air.

5.2.2. Magnetic Studies

Magnetic measurements were carried out at 2 – 300 K. The $\chi_M T$ at 300 K is $0.90 \text{ cm}^3 \text{ mol}^{-1} \text{ K}$ which is somewhat high as anticipated for two isolated Cu(II) ions ($0.75 \text{ cm}^3 \text{ K mol}^{-1}$ with $g = 2.0$). The $\chi_M T$ value decreases with temperature steadily until 50 K and then exponentially,

giving the minimum value of $0.177 \text{ cm}^3 \text{ K mol}^{-1}$ at 2K (Figure 5.4). The drop in $\chi_M T$ indicates the presence of a very weak antiferromagnetic] coupling between the Cu (II) ions.³⁷

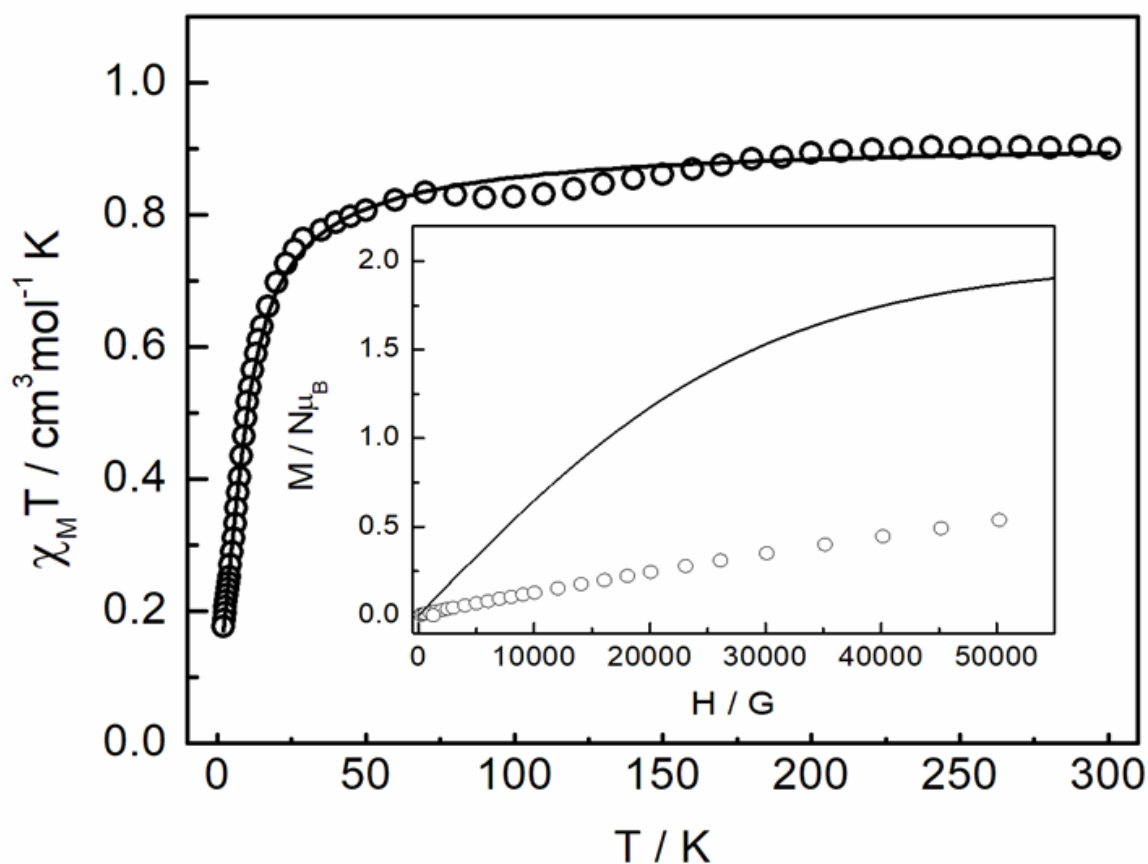


Figure 5.4 Variation of $\chi_M T$ vs T for compound **1** (per two Cu). Figure in Inset refers to the field dependence of reduced magnetization at 2K for **1** (per two Cu), continuous line corresponds to the Brillouin function simulation for two isolated ions with $S = 1/2$ and $g = 2.0$.

The structure consists of copper ions bridged by 4-(diallylamino)benzoate (DABA⁻) through the oxygen atoms (Figure 5.5), giving a system with a ladder like chain motif. The interpretation of magnetic behaviour of **1** is attended by considering two assumption : (i) a negligible contribution from the weak axial interactions through one of the 4-(diallylamino)benzoate due to the large Cu(1)-O(2) and Cu(2)-O(1) distances (2.597 Å and 2.608 Å respectively) then $J_3 = 0$ (Figure 5.5a, 5.5b), (ii) the very similar Cu1 and Cu2 geometric environment (mainly the neighbours angles Cu-O-Cu which are 123.67° and 126.71° (*vide* detailed crystallographic data).

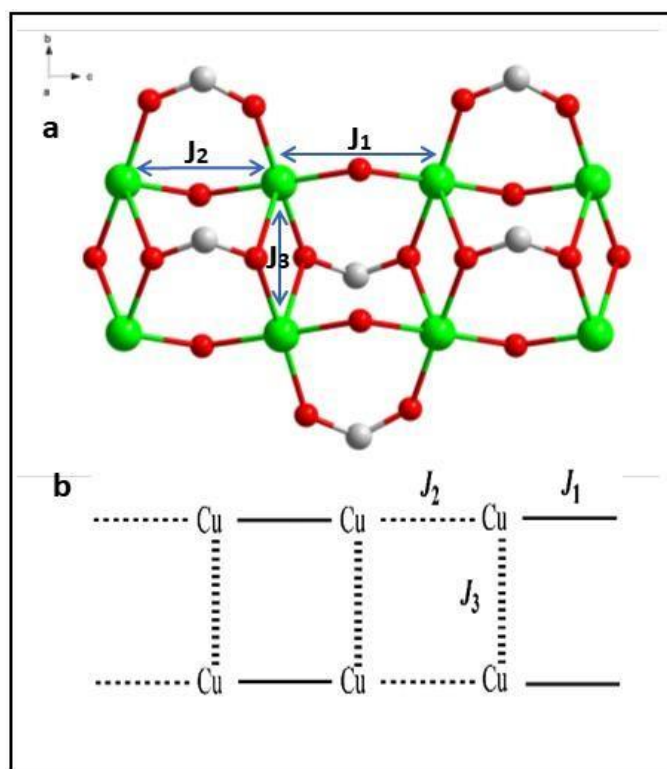


Figure 5.5 (a-b) Schematic diagram representing the exchange interaction within Cu(II) centres of **1**.

Use of one coupling parameter ($J=J_1=J_2$) must be considered to assess the possible magnetic interaction corresponding to the double oxo/carboxylato bridge. The magnetic data have been fitted using Bonner-Fisher calculation³⁷ based on the isotropic Heisenberg Hamiltonian: $H = -J \sum (S_i S_{i+1})$. The best fit parameters from 300 down to 2 K are found as $J = -8.07 \text{ cm}^{-1}$ and $g = 2.07$ with an error $R = 2.7 \times 10^{-4}$, where $R = \sum [(\chi_M T)_{\text{exp}} - (\chi_M T)_{\text{calc}}]^2 / \sum [(\chi_M T)_{\text{exp}}]^2$ (Figure 4). The small value of the super exchange parameter can be realised on considering the large Cu-O-Cu angle ($123.7^\circ/126.7^\circ$). The weak antiferromagnetic interaction was checked by magnetization measurements at 2 K up to an external field of 5 T. The magnetization in $M/N\beta$ units at higher field indicates a value of 0.54 corresponding to two isolated Cu (II) ions (Figure 4, inset). The shape of the plot is compared with the Brillouin plot (solid line plot) for two isolated ions with $S = 1/2$ system and $g = 2$; this indicates the slower magnetization which is consistent with a weak antiferromagnetic interaction.

5.2.3. Reduction of Nitrophenols

The nano regime form of the coordination polymer, **1**, acts as a competent catalyst in the reduction of toxic nitrophenols to nontoxic *p*-aminophenols compared to free Cu(II) salt while the crystalline compound **1** is insoluble in water. The Coordination polymer nano

materials (CPNM) is a new advanced area in nanoscience and nanotechnology in the last decade and have shown many applications in the field of catalysis, medicine, bioimaging, drug delivery, sensors in biomedicine, e-skin, energy harvester, etc.³⁸⁻⁴⁰ During the reduction of 4-NPs, NaBH_4 serves as a reducing agent and nano regime coordination polymer, **1** serves as a catalyst. In absence of catalyst, the reaction is unfavourable and no significant spectral change is seen even after 4 h; the nano scaled compound plays a significant role to bring reactant and reagent together during the catalysis and improves the transfer of electrons from BH_4^- to the nitro groups of 4-NPs.⁴¹⁻⁴⁶ The nano catalyst surface may decrease the kinetic energy barrier and hence makes easy to reduction.

Upon addition of NaBH_4 to NP solution, colour turned from yellow to bright yellow. The strong absorption peak at 317 nm is shifted to 401 nm (Figure 5.6a); this may be due to the generation of nitrophenolate anions under basic condition and the absorbance remained intact with time in the absence of a nano scaled catalyst **1** but decreased rapidly with a small amount of the catalyst.

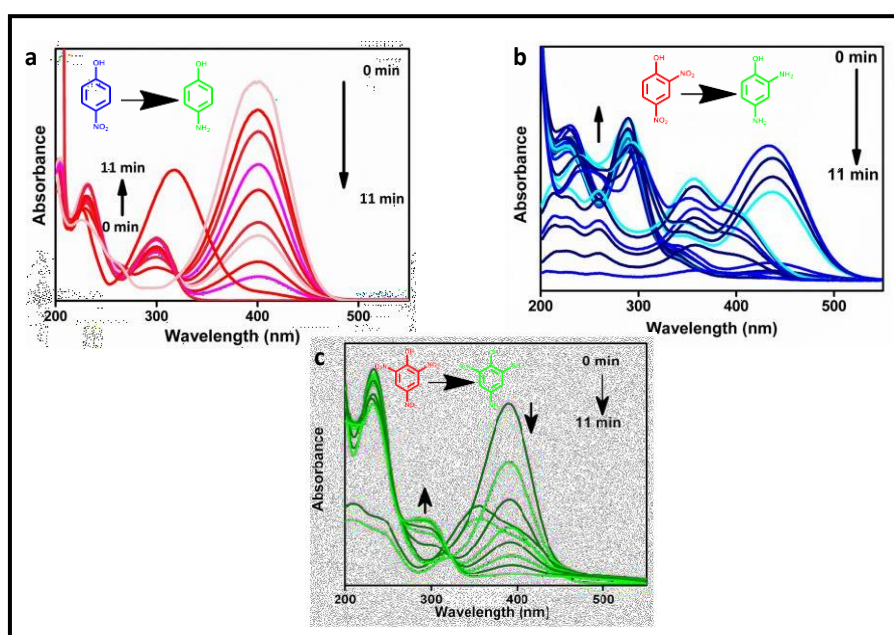


Figure 5.6 Time-dependent UV-vis spectral changes in Nitro Aromatic Compounds like (a) 4-nitrophenol (4-NP), (b) 2,4-dinitrophenol (2,4-DNP), (c) 2,4,6-trinitrophenol (2,4,6-TNP) in presence of **1** and excess NaBH_4 .

The absorption peak at 357 nm in case of 2, 4-dinitrophenol (2, 4-DNP, Figure 5.6b) decreases with concomitant increase in absorption at 450 nm (by adding NaBH_4 in reaction medium) with time followed by the decrement of intensity at 450 nm band with subsequent

development of new band at 300 nm. This implies that the two step reduction reaction : 2, 4-dinitrophenol \rightarrow intermediate 2-amino-4-nitrophenol \rightarrow 4-aminophenol. 2,4,6-Trinitrophenol (2,4,6-TNP) undergoes reduction similarly. Herein, the peak (Figure 5.6c) at 389 nm corresponds to phenolate anion and the peak at 291 nm increases with time indicates the formation of 2,4,6-triaminophenol.

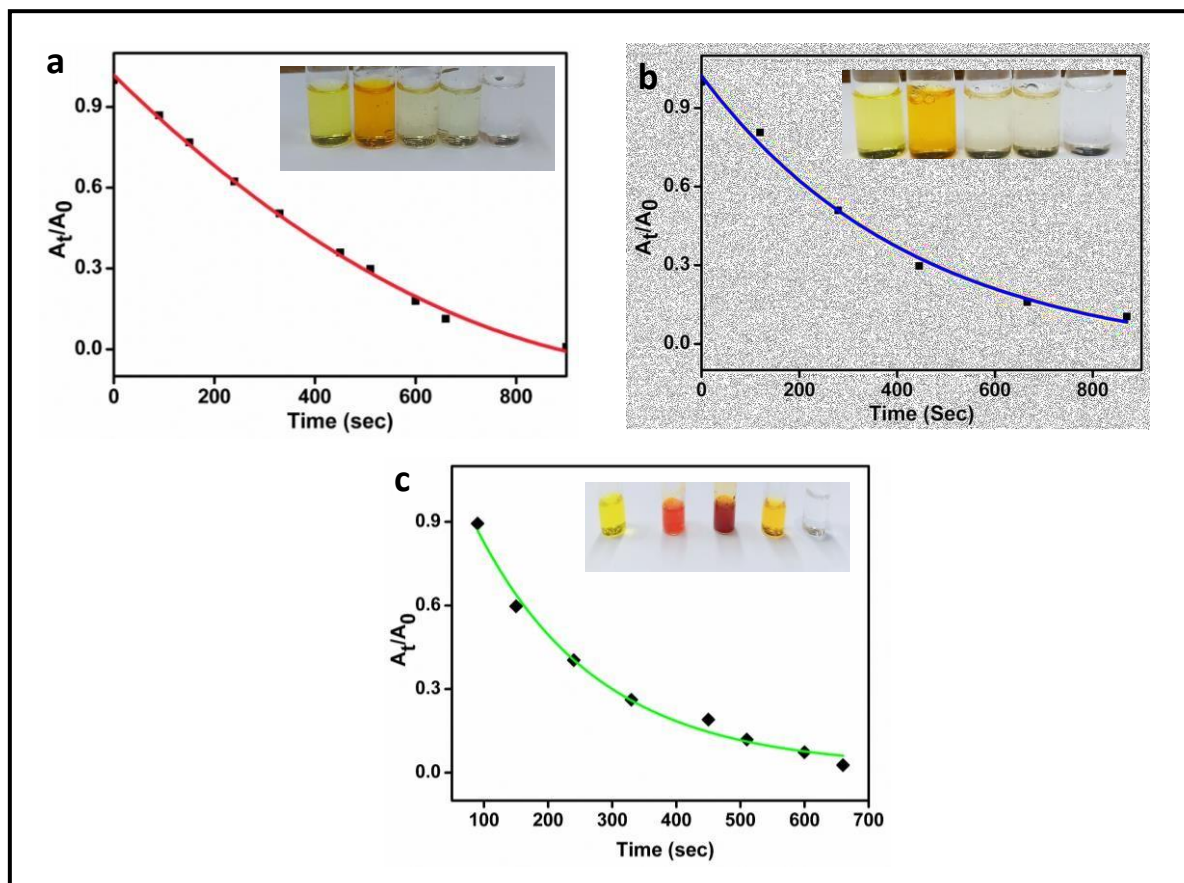


Figure 5.7 Concentration (A_t/A_0) changes in (pink solid line, nude eye test inserted in the box) 4-nitrophenol, (blue solid line) 2,4-dinitrophenol and green solid line) 2,4,6-trinitrophenol in the presence of catalyst **1**.

The pseudo first-order kinetics principle is used and it is more appropriate to assess the rate constants data for nitrophenol reduction because the concentration of NaBH_4 is higher than those of model substrate and can be considered as a constant during the reaction period (Figure 5.7). The linear relationship of $\ln(A_t/A_0)$ versus time (t) indicates that the reduction of nitrophenols by nano scaled catalyst **1** follows the pseudo first order kinetics. The rate constants for 4-nitrophenol, 2,4-dinitrophenol and 2,4,6-trinitrophenol reduction are 0.0024 sec^{-1} , 0.0053 sec^{-1} , and 0.0056 sec^{-1} respectively (Figure 5.8).⁴⁷

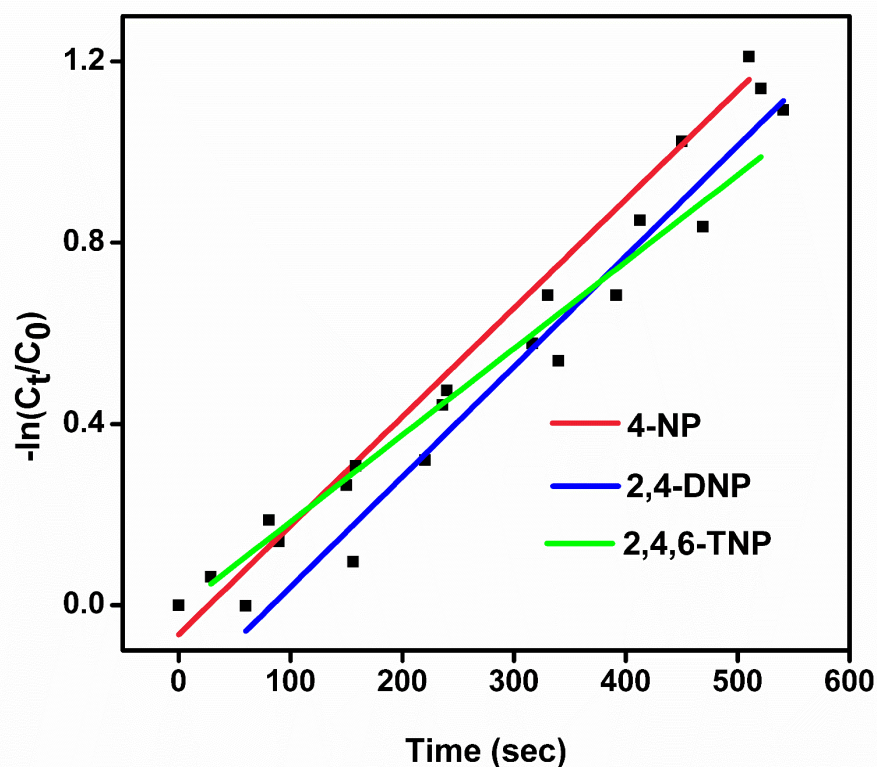


Figure 5.8 The plot of $\ln(C_t/C_0)$ vs t (time) for 4-nitrophenol (pink solid line), 2,4-dinitrophenol (blue solid line) and 2,4,6-trinitrophenol (green). C_t , the concentration of NPs at time t and C_0 , the initial concentration of nitrophenols at $t = 0$. The C_t/C_0 is measured from the relative intensity of absorbance (A_t/A_0).

The catalyst was separated after reaction by filtration method then reuse the catalyst at least 6 times (Figure 5.9). After catalytic performance, we did the SEM experiment to check its integrity (Figure 5.9 a-c) which exactly matches with the SEM image before the catalytic activity.

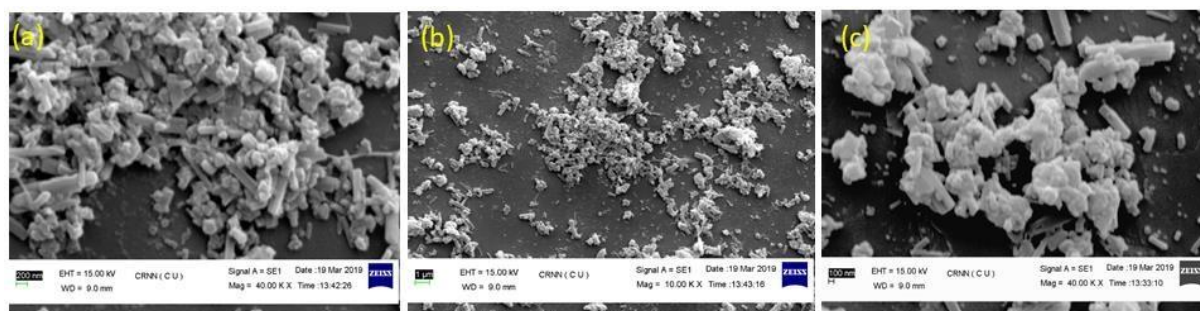


Figure 5.9 (a) SEM image of nano scaled CPP after catalysis reaction with 4-NP. (b) SEM image of nano scaled CP after catalysis reaction with 2,4-DNP. (c) SEM image of nano scaled CP after catalysis reaction with 2,4,6-TNP.

We also performed PXRD experiment after separating the catalyst. The peak-to-peak matching elaborates that the catalyst is able to hold its integrity for a long time period (Figure 5.10).

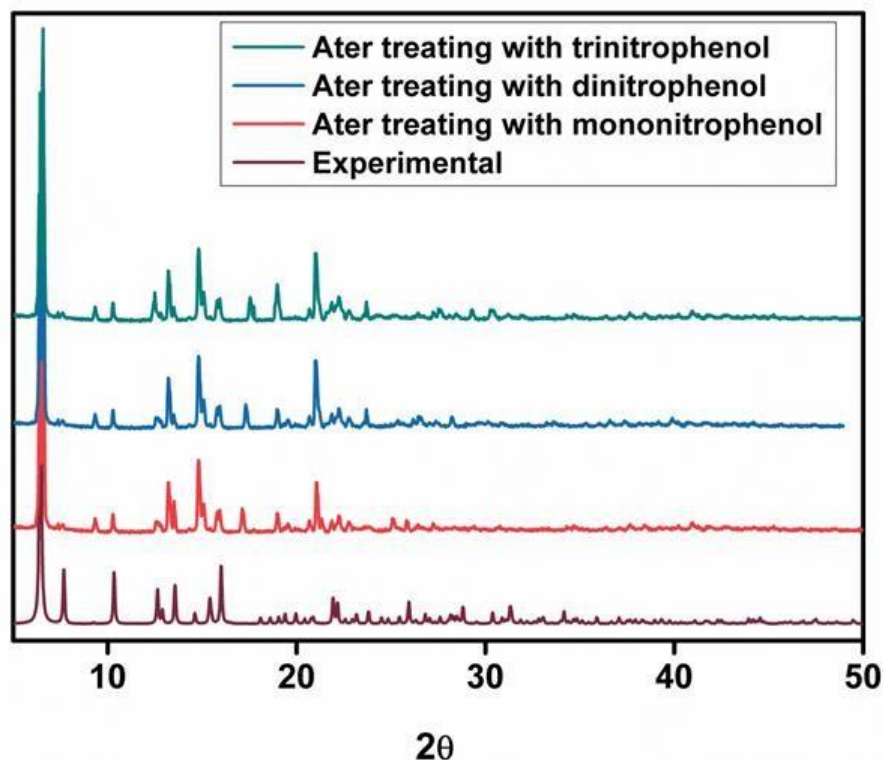


Figure 5.10 PXRD of the nano scaled crystalline Coordination Polymer Particle after catalysis reaction.

Hence, we can say that the coordination polymer $[\text{Cu}_2(\mu_2\text{-OH})_2(\text{DABA})_2]_n$ (**1**), catalyst is successful in acting as an adsorbent catalyst in the reduction process (Figure 5.11; Scheme 5.1).

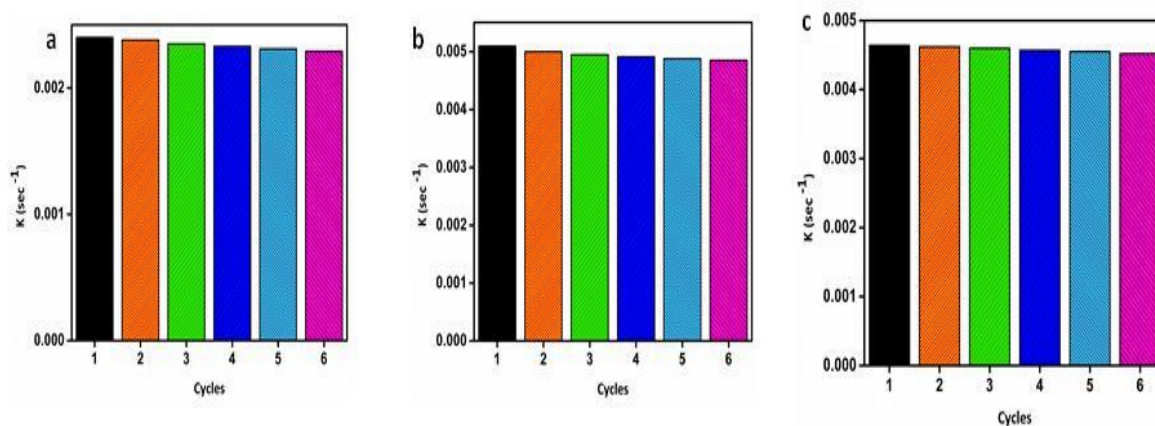
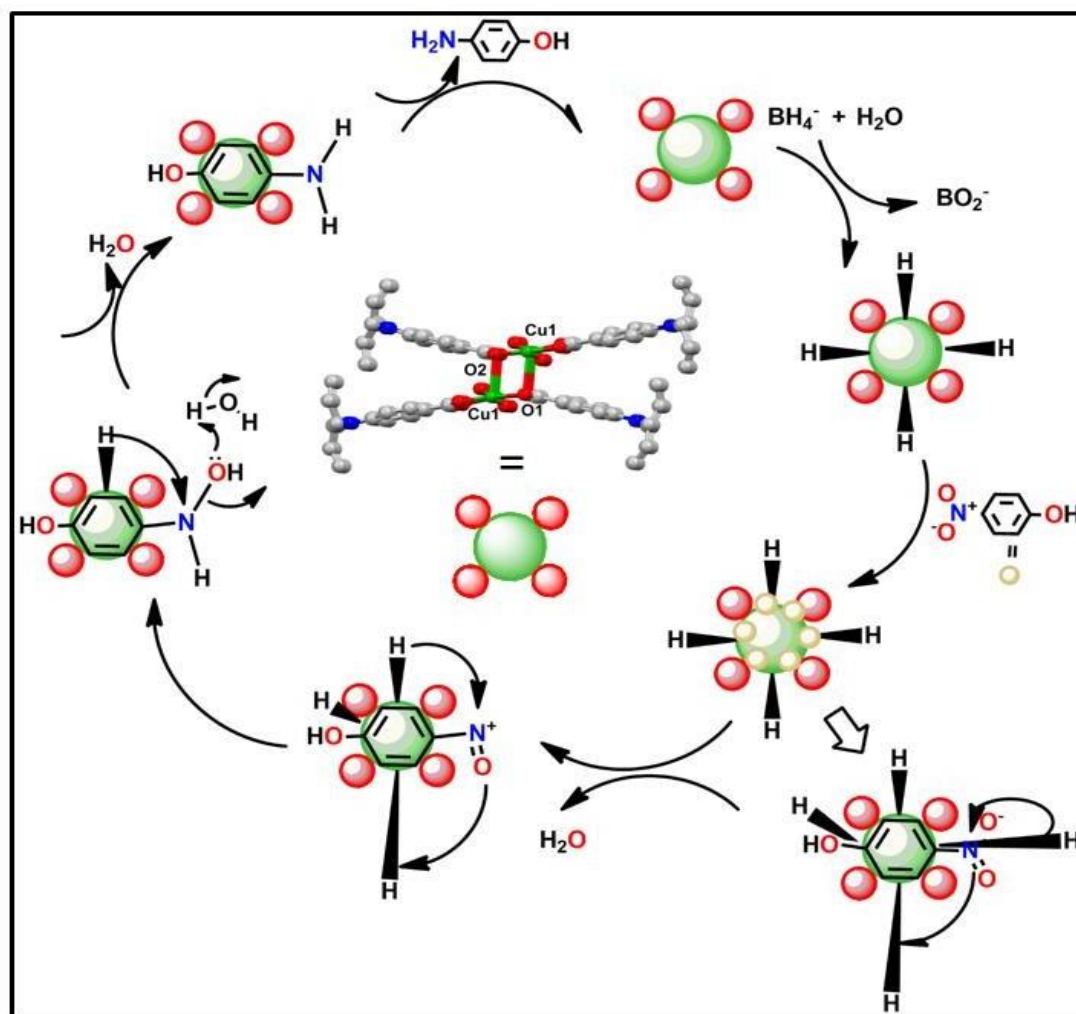


Figure 5.11 Reusability cycles of (a) 4-NP, (b) 2,4-DNP and (c) 2,4,6-TNP.



SCHEME 5.1 Plausible mechanism for nitrophenol reduction by BH_4^- catalysed by nanopolymer

5.3. Experimental Section

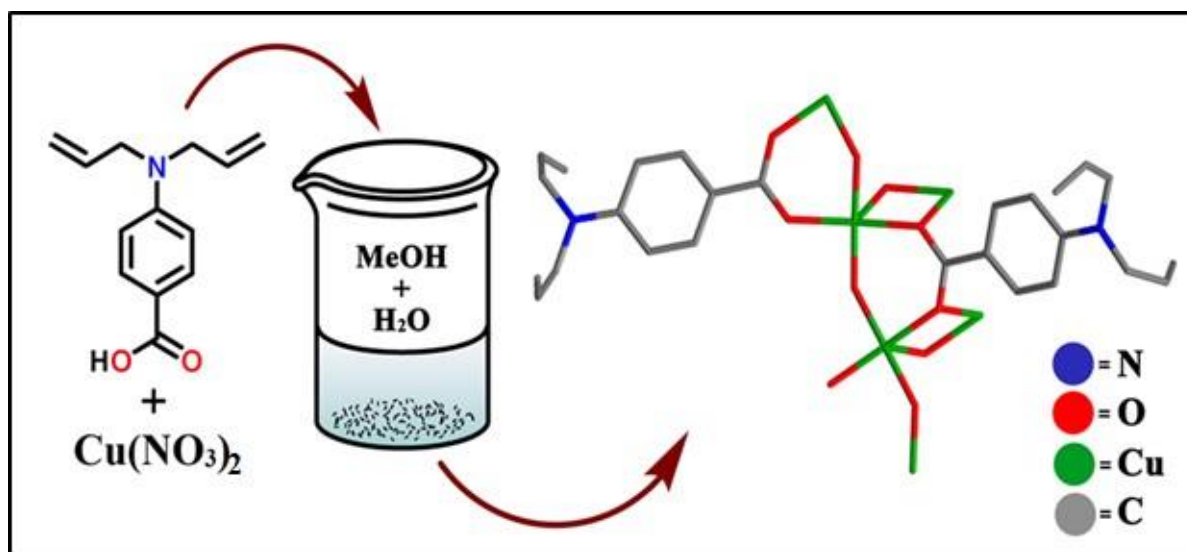
5.3.1. Experimental Methods and Materials

The chemicals required in this research were obtained from Sigma Aldrich and no further refinement was carried out. Microanalytical data (C, H, N) were collected using Perkin-Elmer 2400 CHNS/O elemental analyzer. Perkin-Elmer Pyris Diamond TG/DTA instrument was used for thermogravimetric analysis in the temperature range 30 - 600 °C under N_2 atmosphere at a heating rate of 12 °C min^{-1} . Bruker D8 advance X-ray diffractometer was used for field emission scanning electron microscope (FESEM, S-4800, Hitachi) measurement. The PXRD data were collected on an X-ray diffractometer using Cu $\text{K}\alpha$ radiation ($\lambda = 1.548 \text{ \AA}$) generated at 40 kV and 40 mA. The PXRD spectra were recorded in a 2θ range of 5–50°. Magnetic susceptibility measurement for the compound was carried out on

polycrystalline sample, at the Servei de Magnetoquímica of the University de Barcelona, with a Quantum Design SQUID MPMS-XL susceptometer apparatus working in the range 2-30 K and 30-300 under magnetic field of approximately 500 G and 10000 G, respectively. Diamagnetic corrections were estimated from Pascal Tables.

5.3.2. Synthesis of Coordination Polymer (CP, 1)

4-Diallylamino benzoic acid (HDABA) was prepared by reported procedure.⁴⁸ An ethanolic solution of (2 ml) of HDABA (43.45 mg, 0.2 mmol) neutralized with Et₃N (20.23 mg, 0.2 mmol) was added slowly in drops to water-methanol (1:1, v/v) buffer mixed solvent over the aqueous solution (2 ml) of Cu(NO₃)₂ · 3H₂O, (48.32 mg, 0.2 mmol).⁴⁹⁻⁵³ After week long settling needle-shaped blue coloured crystals were grown on the glass wall. The crystals were isolated mechanically under the microscope and washed several times with methanol and water (1:1) mixture, and dried in a desiccator. The yield of product, [Cu₂(μ₂-OH)₂(DABA)₂]_n (**1**) was 85 % (78.23 mg).



Scheme 5.2 Synthesis of the Coordination polymer [Cu₂(μ₂-OH)₂(DABA)₂]_n (**1**)

Elemental analysis, Calculated (C₂₆H₃₀Cu₂N₂O₆): C, 52.61; H, 5.09; N, 4.72%; Found: C, 52.52; H, 5.0; N, 4.76%. FT-IR (4000–400 cm⁻¹) (Figure S1): 3388 (w), 1637 (s), 1594 (s), 1537 (s), 1385 (s), 1351 (s), 1251 (s), 1199 (s), 1136 (s), 994 (s), 912 (s), 817 (s), 784 (s), 703 (s), 641 (s), 555(w), 512 (w).

5.3.3. X-ray Crystallographic Data Collection and Structure Determination

Bruker Smart Apex diffractometer equipped with CCD and Mo-K α radiation ($\lambda = 0.71073 \text{ \AA}$) was used for crystal data collection of **1** (Table 5.1) at room temperature. Cell refinement, indexing and scaling of the data were done by using programs of Bruker Smart Apex and Bruker Saint packages.⁵⁴ Direct method used for the structure analysis with subsequent Fourier analyses⁵⁵ and refined by the full-matrix least-squares method based on F_0^2 with all observed reflections.⁵⁶ Hydrogen atoms were placed at geometrical positions. All the calculations were performed using the WinGX System, Ver 2018.3.39 Molecular pictures were prepared with program DIAMOND.⁵⁷

5.3.4. Preparation of Nanoscale Cu(II) Coordination Polymer (1)

Solubility of the coordination polymer in common organic solvent and in aqueous medium is a practical problem. There are so many other methods like sonochemical, surfactant mediated synthesis, solvothermal, microemulsion etc. to scale down the particle size but all of them consume time and are non-ecofriendly. So, to handle this problem we take the help of a green hand-grinding strategy.⁵⁸ By applying this we diminish the particle size of the CP, **1**, and surface area will increase accordingly which is very effective for the catalysis. The compound **1** (50 mg) was grinded with the help of mortar pestle for near about 45 mins and extracted with water. The relevant experiments were performed using the aqueous extract. To confirm the structural integrity in nano regime the prepared material is subjected to PXRD analyses. The phase purity and the structural integrity of the nano scaled product (**1**) matches with the PXRD patterns as that of the synthesized ones.

5.3.5. Reduction of Nitrophenols using NaBH₄ catalysed by nano regime **1**

The reduction of nitrophenols (4-NP, 2,4-DNP, 2,4,6-TNP) to corresponding aminophenols were followed by Shimadzu UV- 3101PC UV-Visible spectrophotometer. In a cuvette, nitrophenol (30 μl of 10 mM) in deionized water (3 ml) was added to NaBH₄ (0.16 ml of 0.1 M) solutions followed by the addition of water dispersed nano scaled synthesized compound **1** (1 mg). The solution colour slowly changed from bright yellow to transparent as the reaction proceeds with time. The colour change was followed by spectral measurement with time. Pseudo-first order rate equations were used to calculate the kinetic data.

5.4. Conclusion

In summary, we presented a simple synthetic procedure to prepare a heterogeneous, crystalline Cu(II) nano-catalyst, $[\text{Cu}_2(\mu_2\text{-OH})_2(\text{DABA})_2]_n$ (**1**) (HDABA, 4-Diallylamino-benzoic acid). In the presence of NaBH_4 , the resulting Cu(II) catalyst shows high catalytic activity in the reduction of nitrophenols. Even after 6 cycling experiment, the catalytic activity for reduction was still noteworthy.

5.5. References

- (1) Wu, G.; Liang, X.; Zhang, L.; Tang, Z.; Al-Mamun, M.; Zhao, H.; Su, X. Fabrication Of Highly Stable Metal Oxide Hollow Nanospheres And Their Catalytic Activity Toward 4-Nitrophenol Reduction. *ACS Applied Materials & Interfaces*. **2017**, *9*, 18207-18214.
- (2) Bingwa, N.; Patala, R.; Noh, J.; Ndolomingo, M.; Tetyana, S.; Bewana, S.; Meijboom, R. Synergistic Effects Of Gold–Palladium Nanoalloys And Reducible Supports On The Catalytic Reduction Of 4-Nitrophenol. *Langmuir*. **2017**, *33*, 7086-7095.
- (3) Qiao, X.; Zhang, Z.; Tian, F.; Hou, D.; Tian, Z.; Li, D.; Zhang, Q. Enhanced Catalytic Reduction Of P-Nitrophenol On Ultrathin MoS_2 Nanosheets Decorated With Noble Metal Nanoparticles. *Crystal Growth & Design*. **2017**, *17*, 3538-3547.
- (4) Hirooka, T.; Akiyama, Y.; Tsuji, N.; Nakamura, T.; Nagase, H.; Hirata, K.; Miyamoto, K. Removal Of Hazardous Phenols By Microalgae Under Photoautotrophic Conditions. *Journal of Bioscience and Bioengineering* **2003**, *95*, 200-203.
- (5) Ismail, M.; Khan, M.; Khan, S.; Khan, M.; Akhtar, K.; Asiri, A. Green Synthesis Of Plant Supported Cu Ag And Cu Ni Bimetallic Nanoparticles In The Reduction Of Nitrophenols And Organic Dyes For Water Treatment. *Journal of Molecular Liquids*. **2018**, *260*, 78-91.
- (6) Goyal, A.; Bansal, S.; Singhal, S. Facile Reduction Of Nitrophenols: Comparative Catalytic Efficiency Of MFe_2O_4 ($\text{M} = \text{Ni}, \text{Cu}, \text{Zn}$) Nano Ferrites. *International Journal of Hydrogen Energy* **2014**, *39*, 4895-4908.
- (7) Lee, C.; Alvarez, P.; Nam, A.; Park, S.; Do, T.; Choi, U.; Lee, S. Arsenic(V) Removal Using An Amine-Doped Acrylic Ion Exchange Fiber: Kinetic, Equilibrium, And Regeneration Studies. *Journal of Hazardous Materials*. **2017**, *325*, 223-229.

- (8) Chen, K.; Chen, C.; Ren, X.; Alsaedi, A.; Hayat, T. Interaction Mechanism Between Different Facet TiO_2 And U(VI): Experimental And Density-Functional Theory Investigation. *Chemical Engineering Journal*. **2019**, 359, 944-954.
- (9) Wang, J.; Lou, H.; Xu, Z.; Cui, C.; Li, Z.; Jiang, K.; Zhang, Y.; Qu, L.; Shi, W. Natural Sunlight Driven Highly Efficient Photocatalysis For Simultaneous Degradation Of Rhodamine B And Methyl Orange Using I/C Codoped TiO_2 Photocatalyst. *Journal of Hazardous Materials*. **2018**, 360, 356-363.
- (10) Hao, L.; Zheng, T.; Jiang, J.; Zhang, G.; Wang, P. Removal of As(III) and As(V) from water using iron doped amino functionalized sawdust: characterization, adsorptive performance and UF membrane separation. *Chem. Eng. J.* **2016**, 292, 163–173.
- (11) Shin, K.; Cho, Y.; Choi, J.; Kim, K. Facile Synthesis Of Silver-Deposited Silanized Magnetite Nanoparticles And Their Application For Catalytic Reduction Of Nitrophenols. *Applied Catalysis A: General*. **2012**, 413-414, 170-175.
- (12) Li, Y.; Cao, Y.; Xie, J.; Jia, D.; Qin, H.; Liang, Z. Facile solid-state synthesis of Ag/graphene oxide nanocomposites as highly active and stable catalyst for the reduction of 4-nitrophenol. *Catal. Commun.* **2015**, 58, 21–25
- (13)) Lv, J. J.; Wang, A. J.; Ma, X.; Xiang, R. Y.; Chen, J. R.; Feng, J. J. One-pot synthesis of porous Pt–Au nanodendrites supported on reduced graphene oxide nanosheets toward catalytic reduction of 4-nitrophenol. *J. Mater. Chem. A*, **2015**, 3, 290–296.
- (14) Nakagawa, M.; Crosby, D. G. Photodecomposition of nitrofen. *J. Agric. Food. Chem.* **1974**, 22, 849–853.
- (15) Sarmah, K.; Pal, J.; Maji, T. K.; Pratihari, S. Magnetically Recoverable Heterobimetallic $\text{Co}_2\text{Mn}_3\text{O}_8$: Selective and Sustainable Oxidation and Reduction Reactions. *ACS Sustainable Chem. Eng.* **2017**, 5, 11504–11515.
- (16) Chang, Y.-C.; Chen, D.-H. Catalytic reduction of 4-nitrophenol by magnetically recoverable Au nanocatalyst. *Journal of Hazardous Materials*, **2009**, 165, 664–669.
- (17) Chen, X.; Cai, Z.; Chen, X.; Oyamac, M. AuPd bimetallic nanoparticles decorated on graphene nanosheets: their green synthesis, growth mechanism and high catalytic ability in 4-nitrophenol reduction†. *J. Mater. Chem. A*, **2014**, 2, 5668–5674.

- (18) Lin, F.; Doong, R.; Bifunctional Au-Fe₃O₄ Heterostructures for Magnetically Recyclable Catalysis of Nitrophenol Reduction. *J. Phys. Chem. C*, **2011**, *115*, 6591–6598.
- (19) Jiang, Z.; Xie, J.; Jiang, D.; Jing, J.; Qin, H. Facile route fabrication of nano-Ni core mesoporous-silica shell particles with high catalytic activity towards 4-nitrophenol reduction. *Cryst Eng Comm*. **2012**, *14*, 4601–4611.
- (20) Wang, X.; Liu, D.; Song, S.; Zhang, H. Pt@CeO₂ Multicore@Shell Self-Assembled Nanospheres: Clean Synthesis, Structure Optimization, and Catalytic Applications. *J. Am. Chem. Soc.* **2013**, *135*, 15864–15872.
- (21) Fu, Y.; Huang, T.; Jia, B.; Zhu, J.; Wang, X. Reduction Of Nitrophenols To Aminophenols Under Concerted Catalysis By Au/G-C₃N₄ Contact System. *Applied Catalysis B: Environmental*. **2017**, *202*, 430-437.
- (22) Nguyen, T.; Huang, C.; and Doong, R. Enhanced catalytic reduction of nitrophenols by sodium borohydride over highly recyclable Au@graphitic carbon nitride nanocomposites. *Applied Catalysis B: Environmental*, **2018**, *240*, 337-347.
- (23) Fu, Y.; Xu, P.; Huang, D.; Zeng, G.; Lai, C.; Qin, L.; Li, B.; He, J.; Yi, H. Cheng, M. and Zhang, C. Au nanoparticles decorated on activated coke via a facile preparation for efficient catalytic reduction of nitrophenols and azo dyes. *Applied Surface Science*, **2019**, *473*, 578-588.
- (24) Ma, Y.; Wu, X.; and Zhang, G.; Core-shell Ag@Pt nanoparticles supported on sepiolite nanofibers for the catalytic reduction of nitrophenols in water: Enhanced catalytic performance and DFT study. *Applied Catalysis B: Environmental*. **2017**, *205*, 262-270.
- (25) Sahiner, N.; Ozay, H.; Ozay, O.; Aktas, N. A Soft Hydrogel Reactor For Cobalt Nanoparticle Preparation And Use In The Reduction Of Nitrophenols. *Applied Catalysis B: Environmental* **2010**, *101*, 137-143.
- (26) Liu, J.; Hao, J.; Hu, C.; He, B.; Xi, J.; Xiao, J.; Wang, S.; Bai, Z. Palladium nanoparticles anchored on amine-functionalized silica nanotubes as a highly effective catalyst. *J. Phys. Chem. C*. **2018**, *122*, 2696–2703.
- (27) Zhang, S.; Zhang, H.; Ni, T.; Shen, X. Highly Efficient Au Nanocatalysts for Heterogeneous Continuous-Flow Reactions Using Hollow CeO₂ Microspheres as a Functional Skeleton. *Ind. Eng. Chem. Res.* **2018**, *57*, 3575–3582.

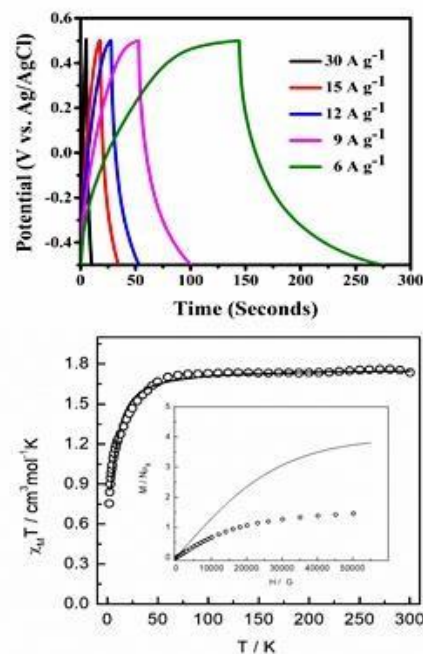
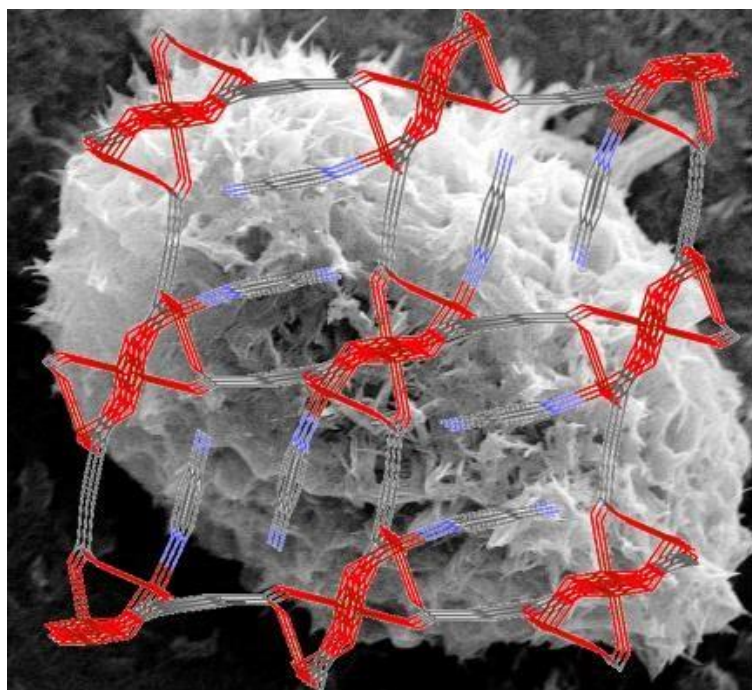
- (28) Kim, J. G.; Cha, M. C.; Lee, J.; Choi, T.; Chang, J. Y. Preparation of a sulfur-functionalized microporous polymer sponge and in situ growth of silver nanoparticles: a compressible monolithic catalyst. *ACS Appl. Mater. Interfaces*. **2017**, *9*, 38081–38088.
- (29) Dutta, B.; Das, D.; Datta, J.; Chandra, A.; Jana, S.; Sinha, C.; Ray, P. P.; Mir, M. H. Synthesis of a Zn(II)-based 1D zigzag coordination polymer for the fabrication of optoelectronic devices with remarkably high photosensitivity. *Inorg. Chem. Front.* **2019**, *6*, 1245–1252.
- (30) Dutta, B.; Dey, A.; Sinha, C.; Ray, P. P.; Mir, M. H. Photochemical Structural Transformation of a Linear 1D Coordination Polymer Impacts the Electrical Conductivity. *Inorg. Chem.* **2018**, *57*, 8029–8032.
- (31) Naskar, K.; Maity, S.; Jana, S.; Dutta, B.; Tanaka, S.; Mallick, D.; Akitsu, T.; Sinha, C. Arylazoimidazole Coordinated and Naphthalene-Dicarboxylato Bridged Polymers of Co(II) and Photochromic Zn(II) Complexes. *Cryst. Growth Des.* **2018**, *18*, 2986–2997.
- (32) Dutta, B.; Jana, R.; Sinha, C.; Ray, P. P.; Mir, M. H. Synthesis of a Cd(II) based 1D coordination polymer by in situ ligand generation and fabrication of a photosensitive electronic device. *Inorg. Chem. Front.* **2018**, *5*, 1998–2005.
- (33) Furukawa, H.; Cordova, K. E.; O’Keeffe, M.; Yaghi, O. M. The chemistry and applications of metal-organic frameworks. *Science*. **2013**, *341*, 123-444.
- (34) Silva, P.; Vilela, S. M. F.; Tome, J. P. C.; Paz, F.; A Multifunctional metal–organic frameworks: from academia to industrial applications. *Chem. Soc. Rev.* **2015**, *44*, 6774–6803.
- (35) Howarth, A. J.; Liu, Y.; Li, P.; Li, Z.; Wang, T. C.; Hupp, J. T.; Farha, O. K. Chemical, thermal and mechanical stabilities of metal–organic frameworks. *Nat. Rev. Mater.* **2016**, *1*, 15018.
- (36) Chandra, A.; Das, M.; Pal, K.; Jana, S.; Dutta, B.; Ray, P. P.; Jana, K.; Sinha, C. Three-Dimensional-Coordination Polymer of Zn(II)-Carboxylate: Structural Elucidation, Photoelectrical Conductivity, and Biological Activity. *ACS Omega*, **2019**, *4*, 17649–17661.
- (37) Sakamoto, N.; Nishimura, F. Y.; Nonaka, T.; Ohashi, M.; Ishida, N.; Kitazumi, K.; Kato, Y.; Sekizawa, K.; Morikawa, T.; Arai, T. Self-assembled Cuprous Coordination Polymer as a Catalyst for CO₂ Electrochemical Reduction into C₂ Products. *ACS Catal.* **2020**, *10*, 10412–10419.

- (38) Tao, B.; Yin, Z. Redox-Responsive Coordination Polymers of Dopamine-Modified Hyaluronic Acid with Copper and 6-Mercaptopurine for Targeted Drug Delivery and Improvement of Anticancer Activity against Cancer Cells. *Polymers*, **2020**, *12*, 1132.
- (39) Duan, J.; Jin, W.; Krishna, R. Natural Gas Purification Using a Porous Coordination Polymer with Water and Chemical Stability. *Inorg. Chem.* **2015**, *54*, 4279–4284.
- (40) Tong, L.; Zhang, L. L.; Wang, C. Y.; Wan, Y. L.; Yan, Q. Q.; Hua, C.; Jiao, J. C.; Zhou, Y. Z.; Ding, W. Y.; Liu, B.; Liang, W. H. Hierarchically Porous Carbons Derived from Nonporous Coordination Polymers. *ACS Appl. Mater. Interfaces*, **2020**, *12*, 25211–25220.
- (41) Meng, J.; Niu, C.; Xu, L.; Li, J.; Liu, X.; Wang, X.; Wu, Y.; Xu, X.; Chen, W.; Li, Q.; Zhu, Z.; Zhao, D.; Mai, L. General oriented formation of carbon nanotubes from metal–organic frameworks. *J. Am. Chem. Soc.* **2017**, *139*, 8212–8221.
- (42) Stassen, I.; Styles, M.; Greci, G.; Gorp, H. V.; Vanderlinden, W.; Feyter, S. D.; Falcaro, P.; Vos, D. D.; Vereecken, P.; Ameloot, R. Chemical vapour deposition of zeolitic imidazolate framework thin films. *Nat. Mater.* **2016**, *15*, 304–310.
- (43) Xu, Y. T.; Xiao, X.; Ye, Z. M.; Zhao, S.; Shen, R.; He, C. T.; Zhang, J. P.; Li, Y.; Chen, X. M. Cage-confinement pyrolysis route to ultrasmall tungsten carbide nanoparticles for efficient electrocatalytic hydrogen evolution. *J. Am. Chem. Soc.* **2017**, *139*, 5285–5288.
- (44) Xia, W.; Qu, C.; Liang, Z.; Zhao, B.; Dai, S.; Qiu, B.; Jiao, Y.; Zhang, Q.; Huang, X.; Guo, W.; Dang, D.; Zou, R.; Xia, D.; Xu, Q.; Liu, M. High-performance energy storage and conversion materials derived from a single metal–organic framework/graphene aerogel composite. *Nano Lett.* **2017**, *17*, 2788–2795.
- (45) Guan, C.; Zhao, W.; Hu, Y.; Lai, Z.; Li, X.; Sun, S.; Zhang, H.; Cheetham, A. K.; Wang, J. Cobalt oxide and N-doped carbon nanosheets derived from a single two-dimensional metal–organic framework precursor and their application in flexible. *Nanoscale Horiz.* **2017**, *2*, 99–105.
- (46) Wang, R.; Dong, X. Y.; Du, J.; Zhao, J. Y.; Zang, S. Q. MOF- Derived Bifunctional Cu₃P Nanoparticles Coated by a N,P- Codoped Carbon Shell for Hydrogen Evolution and Oxygen Reduction. *Adv. Mater.* **2018**, *30*, 1703711.

- (47) Roy, K.; Jana, S.; Ghosh, K. S.; Mahanty, B.; Mallick, Z.; Sarkar, S.; Sinha, C.; Mandal, D. 3D MOF Assisted Self-Polarized Ferroelectret: An Effective Auto-Powered Remote Healthcare Monitoring Approach. *Langmuir*, Just Accepted.
- (48) Jana, S.; Jana, R.; Sil, S.; Dutta, B.; Sato, H.; Ray, P. P.; Datta, A.; Akitsu, T.; Sinha, C. Influence of Axial Linkers on Polymerization in Paddle-Wheel Cu(II) Coordination Polymers for the Application of Optoelectronics Devices. *Cryst. Growth Des.* **2019**, *19*, 6283–6290.
- (49). Kahn, O. *Molecular Magnetism*. VCH, **1993**, p.27.
- (50) Pozun, Z. D.; Rodenbusch, S. E.; Keller, E.; Tran, K.; Tang, W.; Stevenson, K. J.; Henkelman G. A Systematic Investigation of p- Nitrophenol Reduction by Bimetallic Dendrimer Encapsulated Nanoparticles. *J. Phys. Chem. C.* **2013**, *117*, *15*, 7598–7604.
- (51) MirzaHedayat, B.; Noorisepehr, M.; Dehghanifard, E.; Esrafil, A.; Norozi1, R. Evaluation of Photocatalytic Degradation of 2,4-Dinitrophenol from Synthetic Wastewater Using Fe₃O₄@SiO₂@TiO₂/rGO Magnetic Nanoparticles. *Journal of Molecular Liquid.* **2018**, *264*, 571-578).
- (52) Ali, S.; Farrukh, M. A.; Khaleeq-ur-Rahman, M. Photodegradation of 2,4,6-trinitrophenol catalyzed by Zn/MgO nanoparticles prepared in aqueous-organic medium. *Korean J. Chem. Eng.* **2013**, *30*, 2100–2107.
- (53) Jana, S.; Ray, A.; Chandra, A.; Fallah, E. S. M.; Das, S.; Sinha, C. Studies on Magnetic and Dielectric Properties of Antiferromagnetically Coupled Dinuclear Cu(II) in a OneDimensional Cu(II) Coordination Polymer. *ACS Omega*, **2020**, *5*, 274–280.
- (54) Bruker, **2000**. SMART, SAINT. Software Reference Manual Bruker AXS Inc. Madison, Wisconsin, USA.
- (55) Sheldrick, G. M. *Acta Cryst A*, **2008** A64, 112-122.
- (56) Farrugia, L. J. *J. Appl. Crystallogr.* **2012**, *45*, 849-854.
- (57) Brandenburg, K. **1999**, DIAMOND. Crystal Impact GbR, Bonn, Germany.
- (58) Mukherjee, S.; Ganguly, S.; Manna, K.; Mondal, S.; Mahapatra, S.; Das, D. Green Approach To Synthesize Crystalline Nanoscale ZnII-Coordination Polymers: Cell Growth Inhibition and Immunofluorescence Study. *Inorg. Chem.* **2018**, *57*, *7*, 4050–4060.

Abstract

The single crystal X-Ray structure of a Cu based metal–organic framework, $\{[\text{Cu}_4(\text{BTC})_6(4\text{-APy})_2(\mu_3\text{-OH})_2](\text{CH}_3\text{OH})(\text{H}_2\text{O})\}_n$, (Cu-MOF) (H_3BTC = 1,3,5-benzenetricarboxylic acid; 4-APy = 4-Aminopyridine) shows the formation of four Cu(II) connected motif ($[\text{Cu}^{\text{II}}]_4$) via edge sharing of two Cu_3O cores and bridging by six acetato function of BTC^{3-} connector. The $[\text{Cu}^{\text{II}}]_4$ is composed of two five coordinated distorted square pyramidal, CuO_5 and two distorted square planar, CuO_4 units; the Cu(II) knot in later one (CuO_4) is coordinated by pyridyl-N of 4-APy. Remaining donor centres of acetato-O of BTC^{3-} binds adjacent $[\text{Cu}^{\text{II}}]_4$ core to form an infinite 3D network structure. The coordination of CH_3OH and H_2O forms different hydrogen bonding to make a strong superstructure. The surface morphology determination shows nano-flower pattern. The hybrid material, Cu-MOF exhibits very high specific capacitance, 547 F g^{-1} at the scan rate of 2 mV s^{-1} with excellent recycling stability (retains 97.4% after 5000 cycles). The χ_{MT} value for CuMOF at 300 K is $1.735 \text{ cm}^3 \text{ mol}^{-1} \text{ K}$ for four copper(II) ions which is as expected for four isolated copper(II) ion with $g = 2.15$. The χ_{MT} values are almost constant until ca. 55 K and then χ_{MT} decrease sharply, giving the minimum value of $0.753 \text{ cm}^3 \text{ K mol}^{-1}$ at 2K.



6.1. Introduction

Improving Energy storage capacity and miniaturisation of devices are intensive area of research in fundamental and engineering sciences.¹⁻⁵ A capacitor with power density $>100 \text{ W kg}^{-1}$, maintenance free, stable, long life and environmentally benign is the ultracapacitor or supercapacitor.⁶⁻⁹ A supercapacitor cell consists of two electrodes, one separator, and one electrolyte.¹⁰ The electrode is charged and ions from the electrolyte move spontaneously toward the surface to balance overall charges of the system. The metal oxides and hydroxides, polymers (polyaniline and polypyrrole), Carbon based 2D materials (graphene, CNTs, nanowires, nano fibres), areogel etc. are potential energy storage materials because of high surface area and fast electron communication for supercapacitor applications.¹¹⁻¹⁴ Still, it needs more improvement because the energy density of the devices is not satisfactory and poor cycling stability and less electronic conductivity.¹⁵⁻¹⁶ Additionally, they execute a crucial part in fuel cells for renewable energy based electric vehicles. Supercapacitor can store energy in two types of mechanism - Electric Double Layer Capacitor (EDLC, charge separation at an electrode/electrolyte interface is the cause of capacitance) and pseudo-capacitor (the fast and reversible redox reactions at the surfaces of the electroactive materials).¹⁷⁻²³ Hence, the search for high performing energy storage material is in progress.

Metal-organic frameworks, a dynamic family of functional materials, having many advantages due to their high porosity and large surface area such as applications in gas storage, gas separation, catalysis, luminescence, drug delivery and also find use in electronic devices, batteries, insulators, powerbanks and superconductors, memory devices, optical superstructures, mechanical metamaterials etc.²⁴⁻²⁷ The MOFs are employed to construct novel electrodes and electrolyte composites. Supercapacitor MOFs are typically microporous and exhibit the outstanding capacitive performance compared to other storage batteries such as, Li-ion, lead acid, and alkaline batteries.²⁸⁻³⁰ But they have few limitations which hamper the direct use as electrode - low electrical conductivity and large steric hindrance.³¹⁻³³ Hence new strategies are needed to enhance the electrochemical properties of MOF.³⁴ Few 2D MOFs show high supercapacitor activity due to their atomic thickness with short paths, large lateral sizes allowing rapid mass transfer, electron transfer, highly exposed accessible active sites on the surface of MOFs instead of enclosed inside the pores.³⁵⁻³⁶ Thus, the interaction between the active sites in MOF and the electrolytes may be accelerated and hence the electron transfer rate may be improved.³⁷ Electrochemical activity immensely depends upon the stability and efficiency of the electrode material such as, mechanical/chemical stability,

morphology, structural functionality, electronic conductivity etc. Nanoscale engineering, incorporation of pseudo-active component, hierarchical and regular nanocomposites are effective strategy to improve the supercapacitor performance.³⁸⁻³⁹ Better charge transfer within the framework can be achieved by tuning the structure and functionality of the linker whereas better electron transport can be assisted by the redox property of the metal ion inside the MOF.⁴⁰ Steric hindrance can also be eliminated by preparing porous MOF with sufficient large area to facilitate high electrolytic diffusion. The active metal cation inside the MOF must accompany the electrolyte solution so that the predominant charge storage mechanism can be manifested by pseudo-capacitive reaction and exhibit high supercapacitor performance.⁴¹⁻⁴²

Copper(II), a redox non-innocent and magnetically sensitive (d^9) ion, active site of metalloproteins and a precursor to high-nuclearity clusters for the preparation of useful magnetic materials is used for designing of supercapacitors.⁴³ In this work we used to synthesize Cu based metal-organic framework of 1,3,5-benzene tricarboxylic acid (H_3BTC) utilising a facile mixed ligand approach where second ligand is 4-Aminopyridine (4-APy) at room temperature by slow-diffusion method. The single crystal X-Ray structure determination has established tetranuclear Cu based metal-organic framework $\{[Cu_4(BTC)_6(4-APy)_2(\mu_3-OH)_2](CH_3OH)(H_2O)]\}_n$, (Cu-MOF) with nano-flower morphology. Multicarboxylate type linkers are preferably used for the building of multinuclear compounds/MOFs through bridging of $-COO^-$ groups.^{44, 45} Amino-functionalized ligands have high electron density and hence the zeta potential which is useful for quicker charge flow and improved capacitance activity. Tetranuclear copper entity form an infinite 3D network structure through BTC^{3-} linker and 4-APy, which is appended from metal center connected through hydrogen bonding with oxygen atom of adjacent carboxylato group. Magnetic study indicates the presence of a very weak antiferromagnetic coupling between the copper(II) ions. High performance supercapacitor behavior of Cu-MOF makes the material for energy storage application.^{46, 47}

6.2. Results and discussion

6.2.1. Structure and Morphology Analysis of Cu-MOF

Monoclinic system of Cu-MOF is crystallized in $P 2_1/n$ space group with $Z=2$. Single crystal structure reveals that the asymmetric unit contains two Cu(II) node, one 4-aminopyridine (4-APy), one 1,3,5-benzene tricarboxylate (BTC^{3-}) and one bridging $-OH^-$ group (Table 6.1 and

Figure 6.2a). Four Cu(II) atoms form a tetranuclear unit by the coordination with six BTC³⁻, two 4-APy and two μ_3 -OH bridging linkers (Figure 6.2b) along with coordination of CH₃OH and H₂O.

Table 6.1 Crystal data and refinement parameters for Cu-MOF.

CCDC No.	1919988
Formula	C ₃₀ H ₂₇ Cu ₄ N ₄ O ₁₇
Fw	969.76
Crystalsyst	Monoclinic
space group	<i>P</i> 21/ <i>n</i>
<i>a</i> (Å)	10.697(4)
<i>b</i> (Å)	11.948(4)
<i>c</i> (Å)	15.449(6)
β (deg)	94.893(9)
<i>V</i> (Å ³)	1967.4(12)
<i>Z</i>	2
<i>D</i> _{calcd} (g/cm ³)	1.637
μ (mm ⁻¹)	2.207
λ (Å)	0.71073
data[<i>I</i> > 2 σ (<i>I</i>)]/params	3447/259
GOF on <i>F</i> ²	1.033
final <i>R</i> indices[<i>I</i> > 2 σ (<i>I</i>)] ^{<i>a,b</i>}	<i>R</i> 1 = 0.0837 <i>wR</i> 2 = 0.2373

$$^a R1 = \sum ||F_o| - |F_c|| / \sum |F_o|, \quad ^b wR2 = [\sum w(F_o^2 - F_c^2)^2 / \sum w(F_o^2)^2]^{1/2}$$

There are two five coordinated distorted square pyramidal, CuO₅ and two distorted square planar, CuO₄ units are generated by carboxylate bridging of BTC³⁻ to generate [Cu^{II}]₄ unit.⁴⁸⁻

⁵⁰ The Cu(II) knot in CuO₄ is coordinated by pyridyl-N of 4-APy to make distorted square pyramidal CuO₄N motif (Figures 6.1 and 6.2).

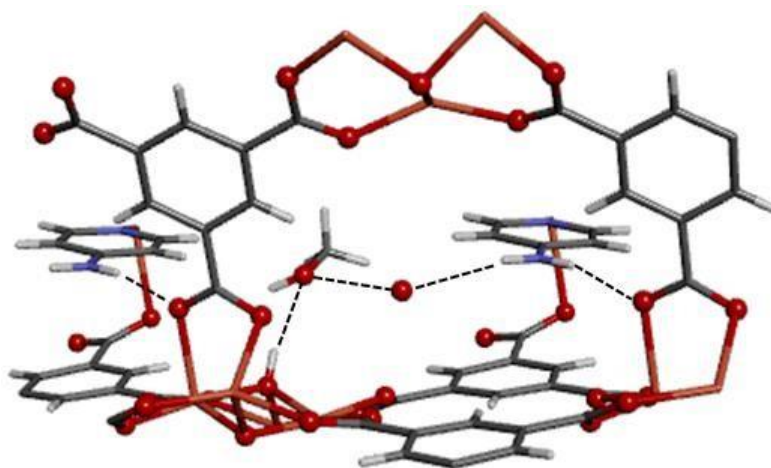


Figure 6.1. Hydrogen bonding interaction in CuMOF.

Remaining donor centres of acetato-O of BTC^{3-} binds six adjacent $[\text{Cu}^{\text{II}}]_4$ cores to form an infinite 3D network structure (Figure 6.2c) and within 3D framework 4-APYy which is appended from copper center connected through hydrogen bonding with oxygen atom of adjacent carboxylate group and solvent water molecule (Figure 6.1).⁵¹⁻⁵³ The short distance $\text{Cu}\cdots\text{Cu}$ in tetramer unit lies between 2.934 Å – 3.264 Å and the bond length of $\mu_3\text{-OH}$ -copper centre appears in the range 1.933 Å - 2.009 Å.⁵⁴⁻⁵⁶ A suitable pathway offers by this functionalized 3D network for charge transfer, which is responsible for efficient electrochemical and magnetic measurements (Figure 6.2d).

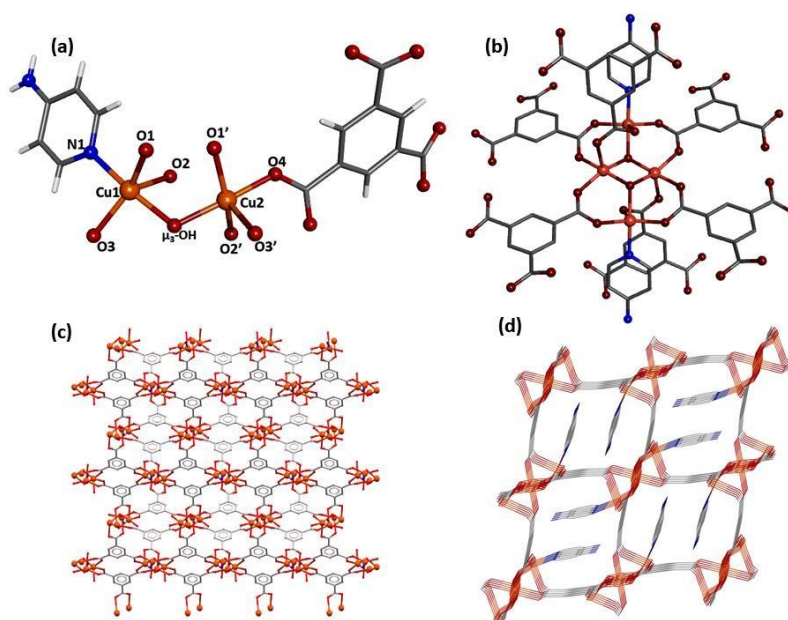


Figure 6.2. (a) Asymmetric unit of CuMOF, (b) Coordination sphere of tetranuclear $[\text{Cu}^{\text{II}}]_4$ unit, (c) View in [001] axis of the infinite $[\text{Cu}^{\text{II}}]_4$ entity connected by 6 ligands of BTC in CuMOF, (d) 3D network along the a^* -axis. Hydrogen atoms have been omitted for picture clarity.

Morphology of Cu-MOF is shown (Figure 6.3(a, b)) by FESEM at different magnifications and shows flower like microsphere.⁵⁷⁻⁵⁹ The morphology of the Cu-MOF has retained even after 5000 cycles of GCD experiment and is shown in Figure 6.3(c-d).⁶⁰⁻⁶¹ This type of morphology allows the electrolyte ions to penetrate deep into the active material and thus improved electrochemical performance can be obtained.

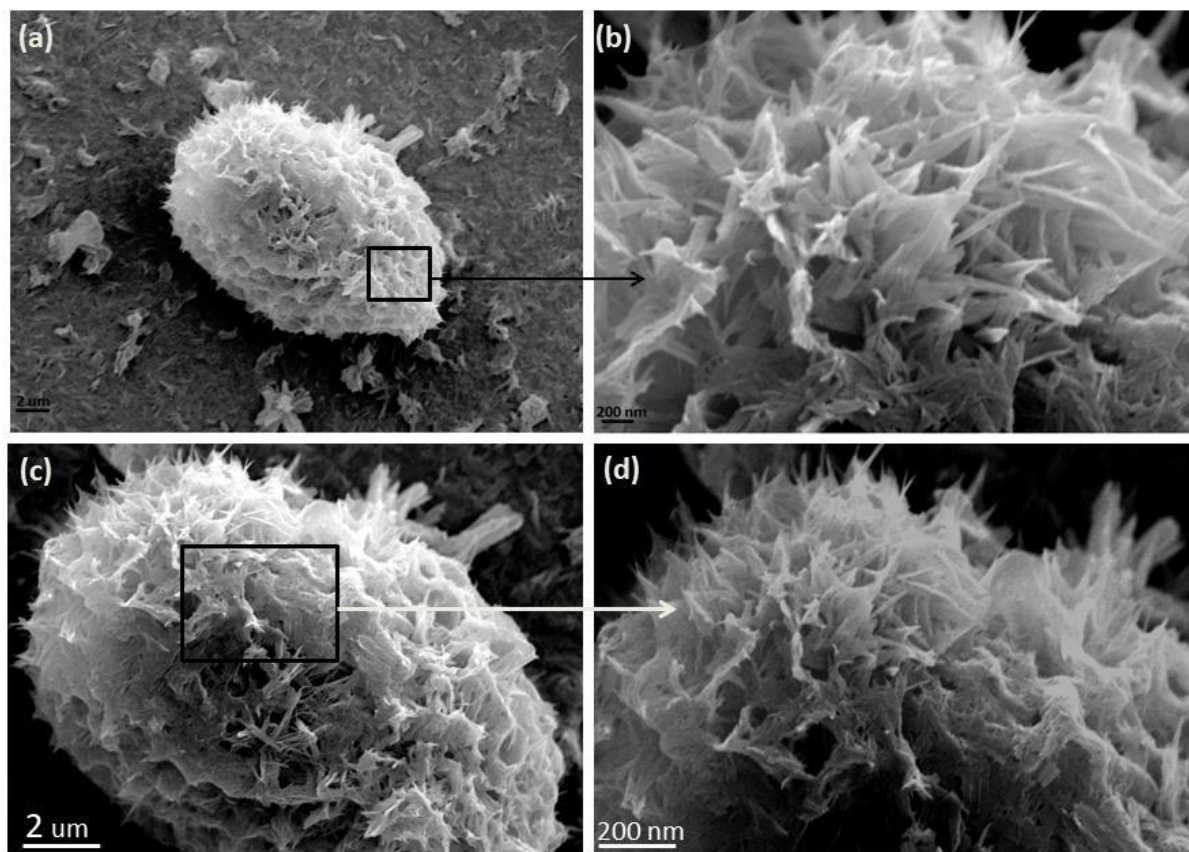


Figure 6.3 (a) Flower-like microsphere of Cu-MOF, (b) enlarge view of selected region of (a). (c) FESEM images after 5000 cycles, (d) enlarge view of selected region of (c).

6.2.2. Supercapacitor Properties

The electrochemical studies of as-fabricated Cu-MOF is examined using a three-electrode setup through cyclic voltammetry (CV) and galvanostatic charge–discharge (GCD) in 1 M KOH aqueous solution as an electrolyte. The CV curves of the Cu-MOF at different scan rates in 1 M KOH electrolyte are displayed in Figure 6.4a. The MOF offers a relatively wide potential window of 1 V in basic electrolyte. No gas evolution was observed from the electrodes at the extreme end of the working potential window. This suggests that the material possess good stability over this potential window. The CV curves are nearly rectangular shaped suggesting good supercapacitive charge storage performance can be

achieved from these electrodes, these exhibits the possible pseudocapacitive behaviour of Cu-MOF.⁶²⁻⁶⁵ Without any deformation of CV curve at higher scan rate suggested good charge storage. The specific capacitance (C_m) of the material can be calculated from the Cyclic Voltammetry by estimating the area within the loop and using the following equation (Eq. 1):

$$C_m = \frac{i}{2mv} \quad (1)$$

here, m is the mass of the active material on the electrode and v is the scan rate. The area within the loop i can be calculated using the following equation (Eq. 2):

$$i = \frac{\int^{v_c} i(v)dv}{(v_c - v_a)} \quad (2)$$

here, $i(v)$ is the response current at different value of the potential, v_c and v_a are the highest and lowest points of the applied potential. The denominator of the above equation can be identified with the potential window of the material under investigation. We have obtained a highest specific capacitance of 547 F g^{-1} at 2 mV s^{-1} scan rate by using equations (1) and (2). Figure 6.4b shows the specific capacitance vs. scan rate plot for the sample. It can be seen that the specific capacitance reduces with the increasing scan rate.⁶⁶ This is mainly because of the fact that at higher scan rate the electrolyte ions cannot get enough time to enter the inner active site of the electrode.⁶⁷ Hence at higher scan rate the redox activity at the electrode decreases and as a result the specific capacitance decrease. The value of specific capacitance can also be estimated from the Galvanostatic Charge Discharge (GCD) experiment using the following equation (Eq. 3):

$$C_m = \frac{i}{(-\frac{dV}{dt})} \quad (3)$$

here, i is the applied current density in the unit of A g^{-1} and $\frac{dV}{dt}$ is the average slope of the discharge curve of the GCD plot. Using equation (3), we have again estimated the value of specific capacitance from the GCD plot.⁶⁸ A highest specific capacitance of 535 F g^{-1} was obtained at the lowest current density of 6 A g^{-1} . This value is relatively close to the specific capacitance value obtained from the CV curves. Figure 6.4c shows the near triangular shaped GCD curves at different current densities. The specific capacitance gradually decreases with increases of current density. This may be due to the increase of internal resistance and lack of active ionic species. The discharge portion of the curves shows little IR drop at the beginning.⁶⁹⁻⁷⁰ This IR drop is mainly because of the material resistance and also due to the

imperfect contact of the active material with the current collector (graphite rod). Noteworthy, retention of initial specific capacitance $\sim 77.8\%$ at the current density 16 A g^{-1} of Cu-MOF has depicted rapid exchange of charge particle between electrode/electrolyte interface. The tetranuclear copper unit of 3D network offers a conductive pathway as result facile charge transportation and improved conductivity (Figure 6.4d). Redox chemistry of Cu-MOF enriched by the participation of tetramer copper unit in redox reaction attributed efficient electrochemical response and high specific capacitance.

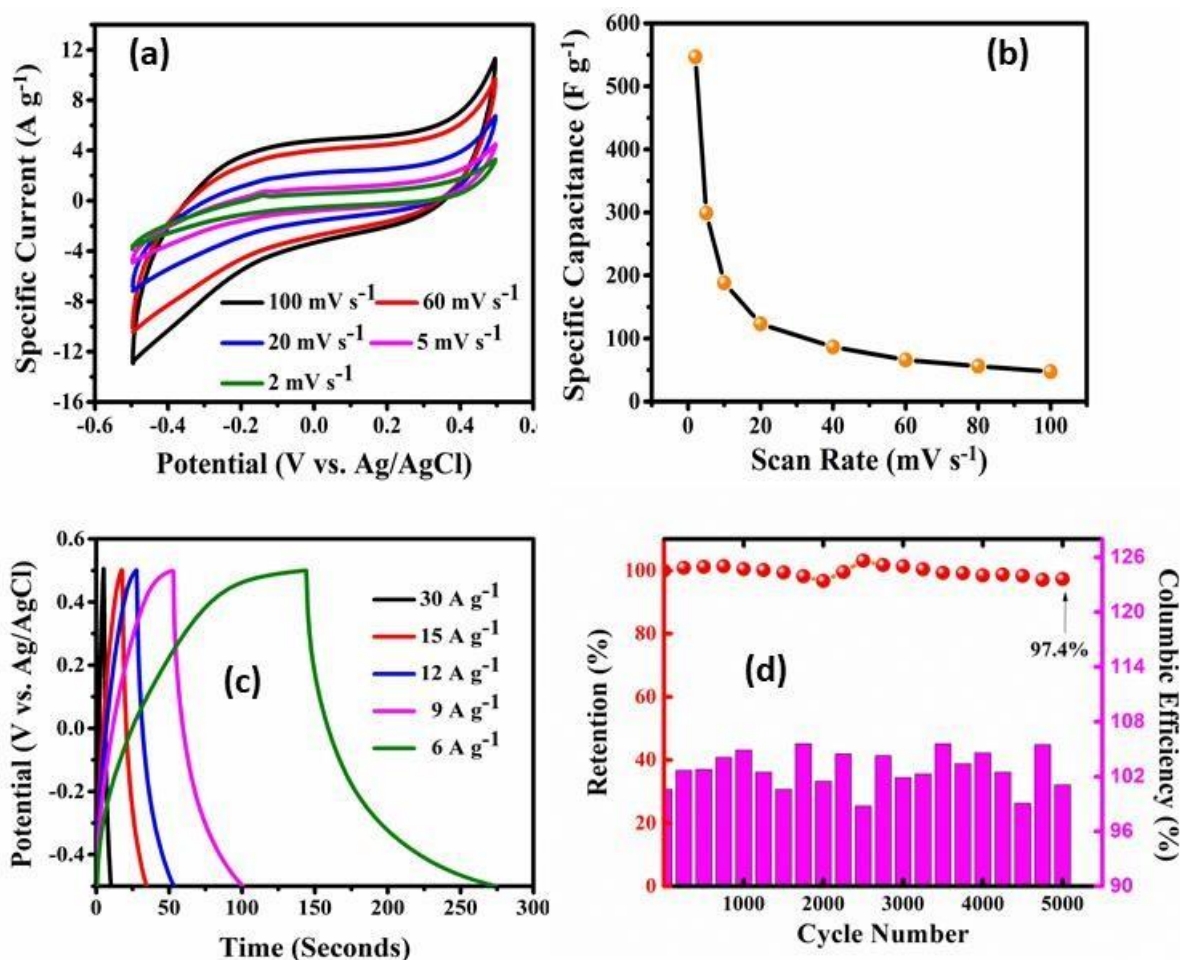


Figure 6.4 (a) CV curves at different scan rates; (b) Specific capacitance vs. Scan rate plot (c) GCD curves at different current densities, (d) Cyclic stability analysis for the CuMOF material.

The GCD experiment has been performed at 18 A g^{-1} for 5000 cycles to check the cycling stability of Cu-MOF. Figure 4b shows retention of specific capacitance is $\sim 97.4\%$ even after 5000 cycles.⁷¹ Initially during the experiment, the specific capacitance of the sample started decreasing and then at around 2500th cycle the specific capacitance started rising and even reached beyond 100%. This is mainly because of the improved redox activity of the electrode

with the increasing cycle number. Any observable physical deformation does not occur in the CV and GCD diagrams before and after cycling suggested excellent performance of Cu-MOF as supercapacitor electrode. Additionally, the flower-like microsphere morphology of Cu-MOF was retained even after 5000 charge/discharge cycles reveals excellent structural stability in 1M KOH electrolyte solution and also finger print region of FTIR spectrum before and after cycles represent the network of CuMOF remains intact (Figure 6.5). Electrochemical impedance spectroscopy is an excellent measurement technique to study the different dynamic processes occurring at the electrode-electrolyte interface.

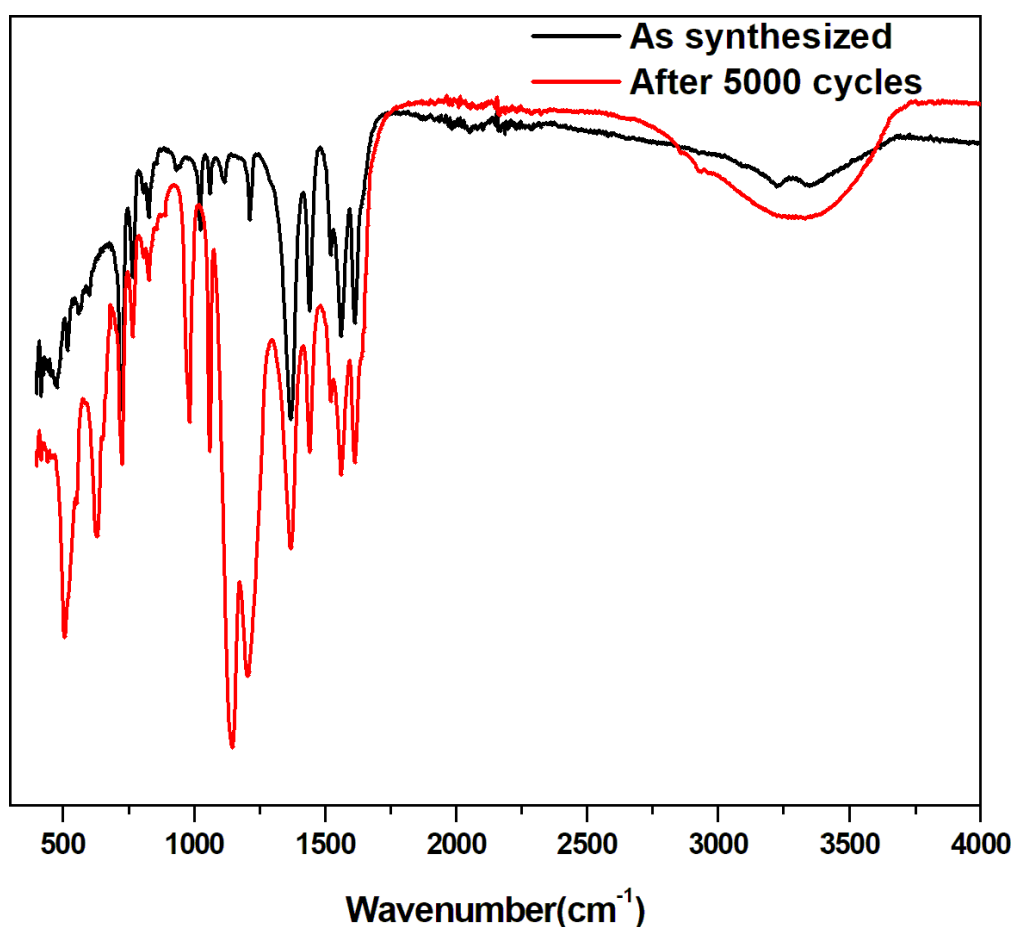


Figure 6.5 FTIR spectra of CuMOF as synthesized and after 5000 cycles.

An AC perturbation signal with magnitude 10 mV and variable frequency from 0.01 Hz to 10⁵ Hz was applied to the working electrode to extract the information regarding the different processes at the interface.⁷²⁻⁷³

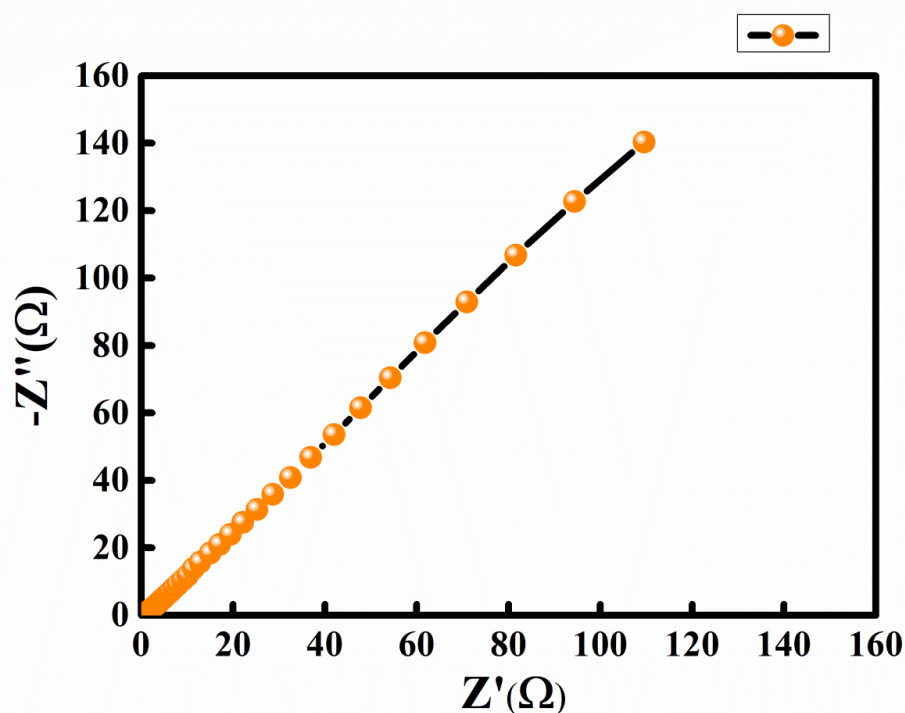


Figure 6.6 Impedance spectra of CuMOF.

Figure 6.6 shows the EIS data in the form of Nyquist plot. A contact resistance of 0.5Ω is offered by the electrode material which is very less and is suitable for good electrochemical performance. In the low frequency region the curve shows a line which is inclined at 45° with respect to the real axis. This region is due to Warburg diffusion resistance.⁷⁴⁻⁷⁵

6.2.3. Magnetic Study

Multinuclear Cu(II) complexes show large variation of magnetic interactions from normal to subnormal, ferro- to antiferromagnetic, spin frustration to remnant magnetism etc. The magnetic property of Cu-MOF shows antiferromagnetic coupling at lower temperature (<50 K). The $\chi_M T$ value for Cu-MOF at 300 K is $1.735 \text{ cm}^3 \text{ mol}^{-1} \text{ K}$ for four copper(II) ions which is as expected for four isolated copper(II) ions with $g = 2.15$. The $\chi_M T$ values are almost constant until ca. 55 K and then $\chi_M T$ decreases sharply, giving the minimum value of $0.753 \text{ cm}^3 \text{ K mol}^{-1}$ at 2K (Figure 6.7).⁷⁶ The drop in $\chi_M T$ at low temperature (<50 K) indicates the presence of a very weak antiferromagnetic coupling between the copper(II) ions.⁷⁷

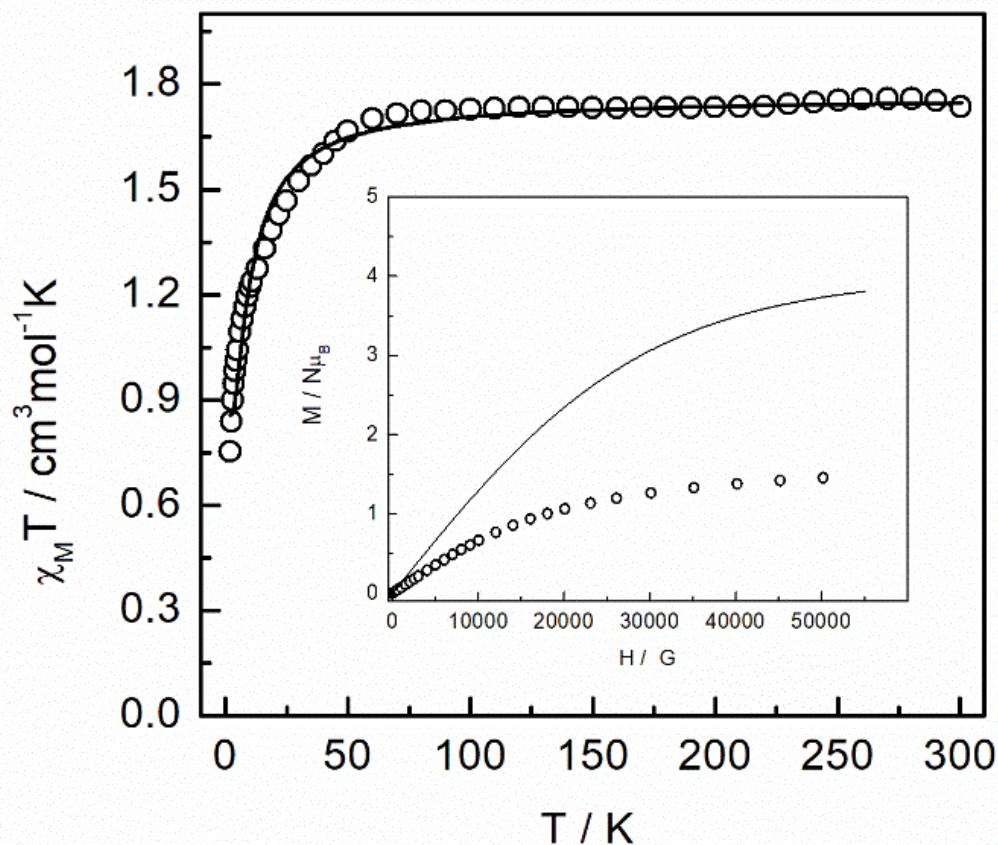


Figure 6.7 Plots of the $\chi_M T$ vs T and $M/N\mu_B$ vs H at 2 K (inset) for complex Cu-MOF (per four Cu atoms). Solid line shows the best fit of the $\chi_M T$ (T) data (see text) and in inset figure continuous line correspond to the Brillouin function for four isolated $S = 1/2$ and $g = 2.0$

As shown in the [Figure 6.2c](#), the structure of Cu-MOF consists of tetramer copper entity connected to six similar adjacent $[\text{Cu}^{\text{II}}]_4$ by six benzene-1,3,5-tricarboxylate ligands to form an infinite 3D network structure. From the magnetic point of view, Cu-MOF behaves as an isolated tetranuclear compound. The short distance $\text{Cu}\cdots\text{Cu}$ between two adjacent $[\text{Cu}^{\text{II}}]_4$ is 7.732 \AA .⁷⁸ Taking into account this topology, we count five exchange pathways as is represented in [Figure 6.8](#), grouped into three averaged different exchange parameters, J_1 , J_2 and J_3 , corresponding to the μ_3 -oxo/carboxylate group, μ_3 -oxo/double carboxylate group and μ_3 -Oxo bridges respectively. As a consequence of the coupling scheme the Hamiltonian to use is $H = -J_1(S_1S_2 + S_3S_4) - J_2(S_2S_3 + S_1S_4) - J_3(S_2S_4)$. The fit on the indicated scheme was performed by means of the computer program *CLUMAG*.⁷⁹

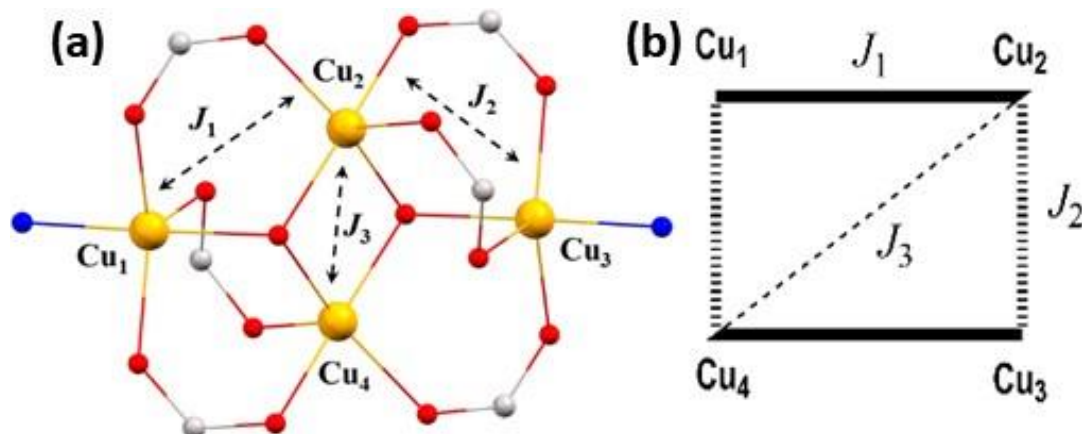


Figure 6.8 Schematic diagrams representing the exchange interaction J_1 , J_2 and J_3 within the tetramer entity in Cu-MOF.

The best fit parameters found were $J_1 = -2.9 \text{ cm}^{-1}$, $J_2 = 2.2 \text{ cm}^{-1}$, $J_3 = 8.5 \text{ cm}^{-1}$ and $g = 2.14$.

The weak antiferromagnetic interaction was confirmed by magnetization measurements at 2 K up to an external field of 5 T. At higher field, the magnetization in $M/N\beta$ units indicates a value of 1.45 0.54 corresponding to four isolated Cu(II) ions (Figure 6.7, inset). Comparison of the overall shape of the plot with the Brillouin plot (solid line plot) for four isolated ions with $S = 1/2$ system and $g = 2$ indicates slower magnetization which is consistent with a weak antiferromagnetic interaction.⁸⁰

6.3. Experimental Section

6.3.1. Materials and general method

Sigma Aldrich helped us by providing all the required chemicals. The PXRD data were collected on a Bruker D8 Advance X-ray diffractometer using Cu $K\alpha$ radiation ($\lambda = 1.548 \text{ \AA}$) generated at 40 kV and 40 mA. The PXRD spectrum was recorded in a 2θ range of 5–50. Bruker D8 advance X-ray diffractometer was used for field emission scanning electron microscope (FESEM, S-4800, Hitachi) measurement. Spectroscopic analysis of the sample was performed using a Fourier transform Infrared (FT-IR) spectrometer (Perkin-Elmer 843) using the KBr pellets in the range of 400–4000 cm^{-1} . Magnetic susceptibility measurements for the compounds were carried out on polycrystalline samples, at the Servei de Magnetoquímica of the Universitat de Barcelona, with a Quantum Design SQUID MPMS-XL susceptometer apparatus working in the range 2–300 K under magnetic field of

approximately 10000 G. and 500 G. Diamagnetic corrections were estimated from Pascal Tables. All the measurements are performed at room temperature.

6.3.2. Synthesis of Cu-MOF

Equimolar concentration of 4-Aminopyridine (4-APy), 1,3,5-benzene tricarboxylic acid (H₃BTC) and Cu(NO₃)₂·3H₂O solutions were prepared in methanol, ethanol and water respectively. Ethanolic solution of BTC was neutralised using equimolar triethylamine. Aqueous solution of metal (5 ml) was taken in a glass tube and 5 ml methanolic solution of 4-Aminopyridine was added slowly using water-methanol (1:1) mixed solvent above the aqueous solution. Ethanolic solution (5ml) of BTC was layered carefully above the methanolic solution to build an undisturbed layer. Separated layers were slowly diffused in the glass tube, after one month green coloured block-shaped crystals were settled on the glass wall. The crystals were separated, washed and collected for single crystal diffraction. The yield of CuMOF was 64%. FT-IR using KBr pallet, cm⁻¹: 3353.56, 3222.11, 1612.20, 1557.30, 1437.45, 1366.31, 1212.43, 1021.44, 824.26, 769.36, 725.28, 632.49, 506.45.

6.3.3. X-Ray crystallographic data collection and structure determination.

Single crystal had mounted for X-Ray diffraction data collection of Cu-MOF at room temperature on a Bruker Smart Apex diffractometer equipped with CCD and Mo-K α radiation ($\lambda = 0.71073 \text{ \AA}$). Cell refinement, indexing and scaling of the data set were done by using programs Bruker Smart Apex and Bruker Saint packages.⁸¹ The structure was solved by direct methods and subsequent Fourier analyses⁸² and refined by the full-matrix least-squares method based on F² with all observed reflections.⁸³ Hydrogen atoms were placed at geometrical positions. All the calculations were performed using the WinGX System, Ver 2018.3.39. Molecular pictures were prepared with program Mercury 3.10.3 and Discovery Studio 2017R2. Crystal data and details of refinements are given in [Table 6.1](#).

6.3.4. Electrochemical Measurements

All the electrochemical measurements were performed in three-electrode system using CS313 (Corrtest) electrochemical workstation. The three-electrode setup consisted of a Pt counter electrode (1 cm x 1 cm), a Ag/AgCl in saturated KCl reference electrode and a working electrode. The working electrode is fabricated by dropcasting the sample gel on the flat side of a teflon coated graphite rod. Before dropcasting the circular flat end of the rod was cleaned and polished. The working gel was prepared by sonication of CuMOF in 1:1 water/isopropyl

alcohol. The gel was then dropcasted directly on the circular flat end of the graphite rod. After the deposition the rods were dried in vacuum for 12h at a temperature of 60^o C. The deposited mass of the material was estimated by weighing the rods before and after deposition. We maintained the deposited mass to be around 5 mg cm⁻² in each of the electrodes.

6.4. Conclusion

To sum-up, here we introduce a facile synthetic route to tetranuclear copper 3D framework for supercapacitor application and magnetic study. The presence of free –NH₂ group of 4-aminopyridine makes this MOF as an important motif for post synthetic modification. This organic-inorganic hybrid material shows very weak antiferromagnetic coupling between the copper(II) ions. High supercapacitor performance (specific capacitance of 547 F g⁻¹ at 2 mV s⁻¹ scan rate) and cycling stability (5000 cycles) makes these material useful for energy storage application.

6.5. References

- (1) Chen, S.; Xing, W.; Duan, J.; Hu, X.; Qiao, Z. S. Nanostructured morphology control for efficient supercapacitor electrodes. *J. Mater. Chem. A*, **2013**, *1*, 2941-2954.
- (2) Simon, P.; Gogotsi, Y.; Materials for electrochemical capacitors. *Nat. Mater.* **2008**, *7*, 845–854.
- (3) Ansari, S. N.; Saraf, M.; Gupta, A. K.; Mobin, S. M. Functionalized Cu MOF@CNT Hybrid: Synthesis, Crystal Structure and Applicability in Supercapacitors. *Chem. - Asian J.* **2019**, *14*, 3566-3571.
- (4) Qin, Y.; Wang, D. X.; Wang, L. Z. Microfibre-nanowire hybrid structure for energy scavenging. *Nature*, **2008**, *451*, 809–813.
- (5) Yang, H. P.; Ding, Y.; Lin, Y. Z.; Chen, W. Z.; Li, Z. Y.; Qiang, F. P.; Ebrahimi, M.; Mai, J. W.; Wong, P. C.; Wang, L. Z. Low-cost high-performance solid-state asymmetric supercapacitors based on MnO₂ nanowires and Fe₂O₃ nanotubes. *Nano Lett.*, **2014**, *14*, 731–736.
- (6) Xue, Y.; Zheng, S.; Xue, H.; Pang, H. Metal–organic framework composites and their electrochemical applications. *J. Mater. Chem. A*, **2019**, *7*, 7301–7327.

- (7) Yan, Y.; Gu, P.; Zheng, S.; Zheng, M.; Pang, H.; Xue, H. Facile synthesis of an accordion-like Ni-MOF superstructure for high performance flexible supercapacitors. *J. Mater. Chem. A* **2016**, *4*, 19078–19085.
- (8) Yan, S. C.; Chen, G.; Sun, X. J.; Lv, D. C.; Pei, J. Edge dislocation surface modification: A new and efficient strategy for realizing outstanding lithium storage performance. *Nano Energy*, **2015**, *15*, 558–566.
- (9) Yan, S. C.; Chen, G.; Zhou, X.; Sun, X. J.; Lv, D. C. Template-Based Engineering of Carbon-Doped Co₃O₄ Hollow Nanofibers as Anode Materials for Lithium-Ion Batteries. *Adv. Funct. Mater.*, **2016**, *26*, 1428–1436.
- (10) Chu, S.; Majumdar, A. Opportunities and challenges for a sustainable energy future. *Nature*, **2012**, *488*, 294–303.
- (11) Mezenov, A. Y.; Krasilin, A. A.; Dzyuba, P. V.; Nominé, A.; Milichko, A. V. Metal–Organic Frameworks in Modern Physics: Highlights and Perspectives, *Adv. Sci.* **2019**, *6*, 1900506.
- (12) Takenaka, T.; Ishihara, K.; Roppongi, M.; Miao, Y.; Mizukami, Y.; Makita, T.; Tsurum, J.; Watanabe, S.; Takeya, J.; Yamashita, M.; Torizuka, K.; Uwatoko, Y.; Sasaki, T.; Huang, X.; Xu, W.; Zhu, D.; Su, N.; Cheng, -G. J.; Shibauchi, T.; Hashimoto, K. Strongly correlated superconductivity in a copper-based metal-organic framework with a perfect kagome lattice. *Sci. Adv.* **2021**, *7*, 3996.
- (13) Wang, S.; Liu, N.; Su, J.; Li, L.; Long, F.; Zou, Z.; Jiang, X.; Gao, Y. Highly Stretchable and Self-Healable Supercapacitor with Reduced Graphene Oxide Based Fiber Springs. *ACS Nano*, **2017**, *11*, 2066–2074.
- (14) Xiong, D.; Li, X.; Bai, Z.; Lu, S. Recent Advances in Layered Ti₃C₂T_x MXene for Electrochemical Energy Storage. *Small*, **2018**, *14*, 1703419.
- (15) Han, X.; Tao, K.; Wang, D.; Han, L. Design of a Porous Cobalt Sulfide Nanosheet Array on Ni Foam from Zeolitic Imidazolate Frameworks as an Advanced Electrode for Supercapacitors. *Nanoscale*, **2018**, *10*, 2735–2741.
- (16) Saraf, M.; Rajak, R.; Mobin, S. M. A Fascinating Multitasking Cu-MOF/rGO Hybrid for High Performance Supercapacitors and Highly Sensitive and Selective Electrochemical Nitrite Sensors. *J. Mater. Chem. A*, **2016**, *4*, 16432–16445.

- (17) Miller, J. R.; Simon, P. Electrochemical capacitors for energy management. *Science* **2008**, *321*, 651–652.
- (18) Zhang, Y.; Yu, S.; Lou, G.; Shen, Y.; Chen, H.; Shen, Z.; Zhao, S.; Zhang, J.; Chai, S.; Zou, Q. Review of macroporous materials as electrochemical supercapacitor electrodes. *J. Mater. Sci.* **2017**, *52*, 11201–11228.
- (19) Saraf, M.; Natarajan, K.; Mobin, S. M. Microwave Assisted Fabrication of a Nanostructured Reduced Graphene Oxide (rGO)/ Fe₂O₃ Composite as a Promising next Generation Energy Storage Material. *RSC Adv.* **2017**, *7*, 309–317.
- (20) Saraf, M.; Dar, R. A.; Natarajan, K.; Srivastava, A. K.; Mobin, S. M. A Binder-Free Hybrid of CuO-Microspheres and rGO Nanosheets as an Alternative Material for Next Generation Energy Storage Application. *ChemistrySelect* **2016**, *1*, 2826–2833.
- (21) Rajak, R.; Saraf, M.; Mobin, M. S. Mixed-Ligand Architected Unique Topological Heterometallic Sodium/Cobalt-Based Metal–Organic Framework for High-Performance Supercapacitors. *Inorg. Chem.* **2020**, *59*, 1642–1652.
- (22) Conway, E. B. *Electrochemical Supercapacitors*. Kluwer, New York, **1999**.
- (23) Wang, X.; Lu, X.; Liu, B.; Chen, D.; Tong, Y.; Shen, G. Flexible Energy-Storage Devices: Design Consideration and Recent Progress. *Adv. Mater.* **2014**, *26*, 4763–4782.
- (24) Wang, G. D.; Liang, Z.; Gao, S.; Qu, C.; Zou, R. Metal-organic framework-based materials for hybrid supercapacitor application. *Coord. Chem. Rev.*, **2020**, *404*, 213093.
- (25) Sundriyal, S.; Kaur, H.; Bhardwaj, K. S.; Mishra, S.; Kim, H. K.; Deep, A. Metal-organic frameworks and their composites as efficient electrodes for supercapacitor applications, *Coord. Chem. Rev.*, **2018**, *369*, 15–38.
- (26) Huang, S.; Shi, R. X.; Sun, C.; Duan, Z.; Ma, P.; Xu, S. The Application of Metal–Organic Frameworks and Their Derivatives for Supercapacitors. *Nanomaterials* **2020**, *10*, 2268.
- (27) Kuppler, J. R.; Timmons, J. D.; Fang, R. Q.; Li, R. J.; Makal, A. T.; Young, D. M.; Yuan, D.; Zhao, D.; Zhuang, W.; Zhou, C. H. Potential applications of metal-organic frameworks. *Coord. Chem. Rev.*, **2009**, *253*, 3042–3066.

- (28) Valade, L.; Tanaka, H.; Bruce, W. D.; O'Hare, D.; Richard I. Molecular Inorganic Conductors and Superconductors, in *Molecular Materials*. Walton, John Wiley & Sons, **2010**.
- (29) Chmiola, J.; Yushin, G.; Gogotsi, Y.; Portet, C.; Simon, P.; Taberna, P.-L. Anomalous Increase in Carbon Capacitance at Pore Sizes Less than 1 Nanometer. *Science* **2006**, *313*, 1760–1763.
- (30) Largeot, C.; Portet, C.; Chmiola, J.; Taberna, P.-L.; Gogotsi, Y.; Simon, P. Relation Between the Ion Size and Pore Size for an Electric Double-Layer Capacitor. *J. Am. Chem. Soc.* **2008**, *130*, 2730–2731.
- (31) Boota, M.; Paranthaman, M. P.; Naskar, A. K.; Li, Y.; Akato, K.; Gogotsi, Y. Waste Tire Derived Carbon-Polymer Composite Paper as Pseudocapacitive Electrode with Long Cycle Life. *ChemSusChem* **2015**, *8*, 3576–3581.
- (32) Qi, K.; Hou, R.; Zaman, S.; Qiu, Y.; Xia, B. Y.; Duan, H. Construction of Metal-Organic Framework/Conductive Polymer Hybrid for All-Solid-State Fabric Supercapacitor. *ACS Appl. Mater. Interfaces* **2018**, *10*, 18021–18028.
- (33) Díaz, R.; Orcajo, M. G.; Botas, J. A.; Calleja, G.; Palma, J. Co⁸- MOF-5 as Electrode for Supercapacitors. *Mater. Lett.* **2012**, *68*, 126–128.
- (34) Jiao, Y.; Pei, J.; Chen, D.; Yan, C.; Hu, Y.; Zhang, Q.; Chen, G. Mixed-metallic MOF based electrode materials for high performance hybrid supercapacitors. *J. Mater. Chem. A* **2017**, *5*, 1094–1102.
- (35) Cherusseri, J.; Pandey, D.; Kumar, S. K.; Thomas, J.; Zhai, L.; Flexible Supercapacitor Electrodes using Metal-Organic Frameworks. *Nanoscale*, **2020**, *12*, 17649-17662.
- (36) Sheberla, D.; Bachman, J. C.; Elias, J. S.; Sun, C.-J.; Shao-Horn, Y.; Dincă, M. Conductive MOF electrodes for stable supercapacitors with high areal capacitance. *Nat. Mater.* **2017**, *16*, 220–224.
- (37) Li, W.-H.; Ding, K.; Tian, H.-R.; Yao, M.-S.; Nath, B.; Deng, W.- H.; Wang, Y.; Xu, G. Conductive Metal–Organic Framework Nanowire Array Electrodes for High-Performance Solid-State Supercapacitors. *Adv. Funct. Mater.* **2017**, *27*, 1702067.
- (38) Feng, D.; Lei, T.; Lukatskaya, M. R.; Park, J.; Huang, Z.; Lee, M.; Shaw, L.; Chen, S.; Yakovenko, A. A.; Kulkarni, A.; Xiao, J.; Fredrickson, K.; Tok, J. B.; Zou, X. D.; Cui, Y.;

Bao, Z. N. Robust and conductive two-dimensional metal–organic frameworks with exceptionally high volumetric and areal capacitance. *Nat. Energy* **2018**, *3*, 30–36.

(39) Zhao, M.; Lu, Q.; Ma, Q.; Zhang, H. Two-Dimensional Metal–Organic Framework Nanosheets. *Small Methods*, **2017**, *1*, 1600030.

(40) Tan, C.; Cao, X.; Wu, X. J.; He, Q.; Yang, J.; Zhang, X.; Chen, J.; Zhao, W.; Han, S.; Nam, G. H.; Sindoro, M.; Zhang, H. Recent Advances in Ultrathin Two-Dimensional Nanomaterials. *Chem. Rev.* **2017**, *117*, 6225–6331.

(41) Sun, L.; Campbell, M. G.; Dincă, M. Electrically Conductive Porous Metal–Organic Frameworks. *Angew. Chem., Int. Ed.* **2016**, *55*, 3566–3579.

(42) Zhao, S.; Wang, Y.; Dong, J.; He, C.-T.; Yin, H.; An, P.; Zhao, K.; Zhang, X.; Gao, C.; Zhang, L.; Lv, J.; Wang, J.; Zhang, J.; Khattak, A. M.; Khan, N. A.; Wei, Z.; Zhang, J.; Liu, S.; Zhao, H.; Tang, Z. Y. Ultrathin metal–organic framework nanosheets for electrocatalytic oxygen evolution. *Nat. Energy* **2016**, *1*, 16184.

(43) Qin, W.; Zhou, N.; Wu, C.; Xie, M.; Sun, H.; Guo, Y.; Pan, L. Mini-Review on the Redox Additives in Aqueous Electrolyte for High Performance Supercapacitors, *ACS Omega* **2020**, *5*, 3801–3808

(44) Song, W.; Teng, X.; Liu, Y.; Wang, J.; Niu, Y.; He, X.; Zhang, C.; Chen, Z. Rational Construction of Self-Supported Triangle-like MOF-Derived Hollow (Ni,Co)Se₂ Arrays for Electrocatalysis and Supercapacitors. *Nanoscale* **2019**, *11*, 6401–6409.

(45) Li, Q.; Zheng, S.; Xu, Y.; Xue, H.; Pang, H. Ruthenium Based Materials as Electrode Materials for Supercapacitors. *Chem. Eng. J.* **2018**, *333*, 505–518.

(46) Darmanin, T.; Guittard, F. Wettability of Conducting Polymers: From Superhydrophilicity to Superoleophobicity. *Prog. Polym. Sci.* **2014**, *39*, 656–682.

(47) Kwon, Y. H.; Park, J. J.; Housel, L. M.; Minnici, K.; Zhang, G.; Lee, S. R.; Lee, S. W.; Chen, Z.; Noda, S.; Takeuchi, E. S.; Takeuchi, K. J.; Marschlok, A. C.; Reichmanis, E. Carbon Nanotube Web with Carboxylated Polythiophene “Assist” for High-Performance Battery Electrodes. *ACS Nano* **2018**, *12*, 3126–3139.

(48) Dutta, B.; Das, D.; Datta, J.; Chandra, A.; Jana, S.; Sinha, C.; Ray, P. P.; Mir, M. H. Synthesis of a Zn(II)-based 1D zigzag coordination polymer for the fabrication of

optoelectronic devices with remarkably high photosensitivity. *Inorg. Chem. Front.* **2019**, *6*, 1245-1252.

(49) Dutta, B.; Dey, A.; Sinha, C.; Ray, P. P.; Mir, M. H. Photochemical Structural Transformation of a Linear 1D Coordination Polymer Impacts the Electrical Conductivity. *Inorg. Chem.* **2018**, *57*, 8029–8032.

(50) Naskar, K.; Maity, S.; Jana, S.; Dutta, B.; Tanaka, S.; Mallick, D.; Akitsu, T.; Sinha, C. Arylazoimidazole Coordinated and Naphthalene-Dicarboxylato Bridged Polymers of Co(II) and Photochromic Zn(II) Complexes. *Cryst. Growth. Des.* **2018**, *18*, 2986–2997.

(51) Dutta, B.; Jana, R.; Sinha, C.; Ray, P. P.; Mir, M. H. Synthesis of a Cd(II) based 1D coordination polymer by in situ ligand generation and fabrication of a photosensitive electronic device. *Inorg. Chem. Front.* **2018**, *5*, 1998-2005.

(52) Chandra, A.; Das, M.; Pal, K.; Jana, S.; Dutta, B.; Ray, P. P.; Jana, K.; Sinha, C. Three-Dimensional-Coordination Polymer of Zn(II)-Carboxylate: Structural Elucidation, Photoelectrical Conductivity, and Biological Activity. *ACS Omega*, **2019**, *4*, 17649–17661.

(53) Dutta, B.; Ghosh, R. S.; Ray, A.; Jana, S.; Sinha, C.; Das, S.; Jana, D. A.; Mir, H. M. Stabilization of cyclic water tetramers and dimers in the crystal host of 2D coordination networks: electrical conductivity and dielectric studies. *New J. Chem.*, **2020**, *44*, 15857-15870.

(54) Naskar, K.; Dey, A.; Maity, S.; Ray, P. P.; Sinha, C. Charge Transportation in Zn(II)/Cd(II)-Based 2D MOFs of 5-Nitro-isophthalate with Isonicotinic Hydrazide. *Cryst. Growth. Des.* **2021**, DOI: 10.1021/acs.cgd.1c00018

(55) Jana, S.; Datta, J.; Maity, S.; Thakurta, B.; Ray, P. P.; Sinha, C. Tetrameric and Polymeric Zn(II) Coordination Complexes of 4-Diallylaminobenzoic Acid and Their Applications in the Electroreduction of CO₂ and Schottky Diode Behavior. *Cryst. Growth. Des.* **2021**, DOI: 10.1021/acs.cgd.1c00581.

(56) Chandra, A.; Das, D.; Castro, O. J.; Naskar, K.; Jana, S.; Frontera, A.; Ray, P. P.; Sinha, C. Cd(II) coordination polymer of fumaric acid and pyridyl-hydrazide Schiff base: Structure, photoconductivity and theoretical interpretation. *Inorganica Chimica Acta*, **2021**, *518*, 120253.

- (57) Xu, X.; Shi, W.; Liu, W.; Ye, S.; Yin, R.; Zhang, L.; Xu, L.; Chen, M.; Zhong, M.; Cao, X. Preparation of two-dimensional assembled Ni–Mn–C ternary composites for high-performance all-solid-state flexible supercapacitors. *J. Mater. Chem. A*, **2018**, *6*, 24086.
- (58) Cao, X.; Cui, L.; Liu, B.; Liu, Y.; Jia, D.; Yang, W.; Razal, M. J.; Liu, J. Reverse synthesis of star anise-like cobalt doped Cu-MOF/Cu₂O hybrid materials based on a Cu(OH)₂ precursor for high performance supercapacitors. *J. Mater. Chem. A*, **2019**, *7*, 3815.
- (59) Bahaa, A.; Balamurugan, J.; Kim, H. N.; Lee, H. J. Metal–organic framework derived hierarchical copper cobalt sulfide nanosheet arrays for highperformance solid-state asymmetric supercapacitors. *J. Mater. Chem. A*, **2019**, *7*, 8620.
- (60) Li, -L. Y.; Zhou, -J. J.; Wu, -K. M.; Chen, C.; Tao, K.; Yi, -Y. F.; Han, L. Hierarchical Two-Dimensional Conductive Metal–Organic Framework/Layered Double Hydroxide Nanoarray for a High- Performance Supercapacitor. *Inorg. Chem.* **2018**, *57*, 6202–6205.
- (61) Gupta, K. A.; Saraf, M.; Bharadwaj, K. P.; Mobin, M. S. Dual Functionalized CuMOF-Based Composite for High-Performance Supercapacitors. *Inorg. Chem.* **2019**, *58*, 9844–9854.
- (62) Wang, J.; Zhong, Q.; Xiong, Y.; Cheng, D.; Zeng, Y.; Bu, Y. Fabrication of 3D Co-Doped Ni-Based MOF Hierarchical Micro- Flowers as a High-Performance Electrode Material for Supercapacitors. *Appl. Surf. Sci.* **2019**, *483*, 1158–1165.
- (63) Gao, H.; Shen, H.; Wu, H.; Jing, H.; Sun, Y.; Liu, B.; Chen, Z.; Song, J.; Lu, L.; Wu, Z.; Hao, Q. Review of Pristine Metal–Organic Frameworks for Supercapacitors: Recent Progress and Perspectives. *Energy Fuels*, 2021, <https://doi.org/10.1021/acs.energyfuels.1c01722>.
- (64) Pan, Y.; Shi, C.; Chen, Y.; Li, D.; Tian, Z.; Guo, L.; Wang, Y. Fishbone-like Ni₃S₂/Co₃S₄ integrated with nickel MOF nanosheets for hybrid supercapacitors. *Appl. Surf. Sci.* **2021**, *566*, 150744.
- (65) Jing, Q.; Li, W.; Wang, J.; Chen, X.; Pang, H. Calcination activation of three-dimensional cobalt organic phosphate nanoflake assemblies for supercapacitors. *Inorg. Chem. Front.*, **2021**, <https://doi.org/10.1039/D1QI00797A>.
- (66) Duan, H.; Zhao, Z.; Lu, J.; Hu, W.; Zhang, Y.; Li, S.; Zhang, M.; Zhu, R.; Pang, H. When Conductive MOFs Meet MnO₂: High Electrochemical Energy Storage Performance in

an Aqueous Asymmetric Supercapacitor. *ACS Appl. Mater. Interfaces* **2021**, *13*, 33083–33090.

(67) babu, S.; Jayachandran, M.; Maiyalagan, T.; Vijayakumar, T.; Gunasekaran, B. Metal-organic framework (MOF-5) incorporated on NiCo₂O₄ as electrode material for supercapacitor application. *Materials Letters*, **2021**, *302*, 130338.

(68) Rajak, R.; Saraf, M.; Mobin, S. M. Robust Heterostructures of a Bimetallic Sodium-Zinc Metal-Organic Framework and Reduced Graphene Oxide for High-Performance Supercapacitors. *J. Mater. Chem. A* **2019**, *7*, 1725–1736.

(69) Ye, C.; Qin, Q.; Liu, J.; Mao, W.; Yan, J.; Wang, Y.; Cui, J.; Zhang, Q.; Yang, L.; Wu, Y. Coordination Derived Stable Ni-Co MOFs for Foldable All-Solid-State Supercapacitors with High Specific Energy. *J. Mater. Chem. A* **2019**, *7*, 4998–5008.

(70) Gao, S.; Sui, Y.; Wei, F.; Qi, J.; Meng, Q.; Ren, Y.; He, Y. Dandelion-Like Nickel/Cobalt Metal-Organic Framework based Electrode Materials for High Performance Supercapacitors. *J. Colloid Interface Sci.* **2018**, *531*, 83–90.

(71) Saha, S.; Maji, P.; Pethsangave, A. D.; Roy, A.; Ray, A.; Some, S.; Das, S. Effect of morphological ordering on the electrochemical performance of MnO₂-Graphene oxide composite. *Electrochimica Acta*, **2019**, *317*, 199-210.

(72) Saraf, M.; Natarajan, K.; Mobin, S. M. Emerging Robust Heterostructure of MoS₂-rGO for High-Performance Supercapacitors. *ACS Appl. Mater. Interfaces* **2018**, *10*, 16588–16595.

(73) Saha, S.; Roy, A.; Ray, A.; Das, T.; Nandi, M.; Ghosh, B.; Das, S. Effect of particle morphology on the electrochemical performance of hydrothermally synthesized NiMn₂O₄. *Electrochimica Acta*, **2020**, *353*, 136515.

(74) Liu, S.; Zhou, J.; Cai, Z.; Fang, G.; Cai, Y.; Pan, A.; Liang, S. Nb₂O₅ quantum dots embedded in MOF derived nitrogen-doped porous carbon for advanced hybrid supercapacitor applications. *J. Mater. Chem. A* **2016**, *4*, 17838–17847.

(75) Saha, S.; Sadhukhan, P.; Chowdhury, R. S.; Das, S.; Rotary-Jet spin assisted fabrication of MnO₂ microfiber for supercapacitor electrode application. *Materials Letters*, **2020**, *277*, 128342.

- (76) Jana, S. M.; Dey, S.; Priego, L. J.; Aparicio, J. R.; Mondal, K. T.; Roy, P. Synthesis, characterization and magnetic properties of an oxido-bridged tetranuclear copper(II) complex. *Polyhedron*, **2019**, *59*, 101 – 106.
- (77) Jana, S.; Ray, A.; Chandra, A.; Fallah, E. S. M.; Das, S.; Sinha, C. Studies on Magnetic and Dielectric Properties of Antiferromagnetically Coupled Dinuclear Cu(II) in a OneDimensional Cu(II) Coordination Polymer. *ACS Omega*, **2020**, *5*, 274–280.
- (78) Jana, S.; Jana, R.; Sil, S.; Dutta, B.; Sato, H.; Ray, P. P.; Datta, A.; Akitsu, T.; Sinha, C. Influence of Axial Linkers on Polymerization in Paddle-Wheel Cu(II) Coordination Polymers for the Application of Optoelectronics Devices. *Cryst. Growth Des.* **2019**, *19*, 6283–6290.
- (79) Gatteschi, D.; Pardi, L. The series of calculations were made using the computer program CLUMAG which uses the irreducible tensor operator formalism (ITO). *Gazz. Chim. Ital.* **1993**, *123*, 231.
- (80) Jana, S.; Karim, S.; Paul, S.; Zangrando, E.; Fallah, E. S. M.; Das, D.; Sinha, C. Carboxylato bridging Cu(II) coordination polymer: Structure, magnetism and catalytic reduction of nitrophenols. *J. Mol. Struct.*, **2021**, *1245*, 131058.
- (81) Bruker, **2000**. SMART, SAINT. Software Reference Manual Bruker AXS Inc. Madison, Wisconsin, USA.
- (82) Sheldrick, G. M. *Acta Cryst A*, **2008** *A64*, 112-122.
- (83) Farrugia, L. J. *J. Appl. Crystallogr.* **2012**, *45*, 849-854.

7.1 Summary

The CPs and MOFs attract diverse applications because of high porosity, structural stability, and versatility in the design and synthesis. Depending upon the structural architecture and chemical behavior, they have been used in gas sorption and separation, catalysis, electrical conductivity, drug delivery, proton conduction, chemical separation, variable temperature magnetism, sensing, storage device, bio-imaging, etc. This has drawn our attention to design CPs/MOFs for application in energy storage devices, catalytic reduction of aromatic nitro compounds, photo-switching applications and magnetic study. In this work, various mono, di and tritopic carboxylato acid bridging linkers have been used to integrate 0D, 1D, 2D and 3D coordination polymers of d-block metal ions (e.g. Cu(II), and Zn(II) along with mono/di-dentate pyridyl based ligands.

In this contest (Chapter-2) two cu-based electro-conductive 0D, 1D coordination polymers $[\text{Cu}_2(\text{DABA})_4(4,4'\text{-BPY})]_n$ (**1**) and $[\text{Cu}_4(\text{DABA})_8(\text{PYZ})(\text{H}_2\text{O})_2]$ (**2**) (HDABA = 4-Diallylamino-benzoic acid) have been synthesized by varying axial linkers, 4,4'-Bipyridine (4,4'-BPY) and Pyrazine (PYZ). Upon light irradiation the thin film of the compounds increases the electrical conductivity with respect to the dark phase and the conductivity of **1** is ~150 times higher than **2**. Magnetic properties were investigated at an applied field 0.5 T in a temperature range 5–300 K. Compound **1** exhibits ferromagnetic behavior and compound **2** is antiferromagnetic at 300 K and the effective magnetic moment at 300 K, is 1.94 and 0.93 BM, respectively. Changing of axial linkers leads to the formation of charge transfer complexes which significantly enhances its magnetic moment and improves its electrical properties.

In this Chapter-3, a 1D Cu(II) coordination polymer with encapsulated antiferromagnetically coupled binuclear Cu(II) has been synthesized by using 5-nitroisophthalic acid (5-N-IPA) and 4-aminopyridine (4-APY) $[\text{Cu}_2(5\text{-N-IPA})_2(4\text{-APY})_4]_n$ (**1**). This complex has the potential to form higher dimensional structures throughout H-bonding (2.865–3.3320 Å) and Supramolecular (aromatic $\pi\cdots\pi$) interactions (3.869–4.148 Å). The charge transfer mechanism and dielectric relaxation throughout the CP have been established. The shape of the $\chi_M T$ vs T curve indicates dominant antiferromagnetic coupling, which results from the interaction between the copper(II) atoms. The overall electromagnetic properties and the effect of temperature on electromagnetic behaviour of compound **1** reveals that our synthesized polymer will be a suitable for energy storage applications

In Chapter-4, tetranuclear (0D) $[\text{Zn}_4(\mu_4\text{-O})(\text{DABA})_6]$ (**1**) and polynuclear (1D) $[\text{Zn}_2(\text{DABA})_4(4,4'\text{-BPY})]_n$ (**2**), in one pot (HDABA = 4-Diallylamino-benzoic acid and 4,4'-BPY = 4,4'-Bipyridine) complexes have been synthesized and characterized by single crystal X-ray diffraction measurements and other spectroscopic data. The tetranuclear Zn(II) complex (**1**) shows Zn···Zn separation in the range 3.122-3.186 Å, and the $\mu_4\text{-O}$ Zn distance lies in the range 1.927-1.944 Å (Figure 4.4). The structure analysis of **2** shows that a carboxylato bridged Zn(II) paddle wheel $[\text{Zn}_2(\text{DABA})_4]$ unit is connected by the 4, 4'-bipyridine at the axial coordination position and helps to form 1D polymeric chain. This research discovered the high efficiency and selectivity in electrocatalytic CO_2 reduction to methanol, formaldehyde and formic acid. Also due to the polymeric nature of compound **2** (1D), the conductivity based on diode derived from J-V characteristics has promisingly increased by 10^4 times than tetranuclear complex.

In the successive chapters we have successfully studied the role of supramolecular interactions in the construction of a 1D coordination polymer, $[\text{Cu}_2(\mu_2\text{-OH})_2(\text{DABA})_2]_n$ (**1**), (HDABA = 4-Diallylamino-benzoic acid) and this was extended in the 3D array by hydrogen bonds (bonding) and $\pi\cdots\pi$ interactions along with weak C-H··· π interactions. Hand grinding aqueous suspension of the coordination polymer, **1** shows catalytic performance in the reduction of toxic nitrophenols to corresponding aminophenols by NaBH_4 . The susceptibility measurements (χ_{MT}) of Cu(II) coordination polymer indicates the presence of a very weak antiferromagnetic coupling between the metal centres.

In this chapter (Chapter-6), a Cu based metal-organic framework, $\{[\text{Cu}_4(\text{BTC})_6(4\text{-APy})_2(\mu_3\text{-OH})_2](\text{CH}_3\text{OH})(\text{H}_2\text{O})\}_n$, (Cu-MOF) (H_3BTC = 1,3,5-benzenetricarboxylic acid; 4-APy = 4-Aminopyridine) has been synthesized and the single crystal X-ray structure shows the formation of four Cu(II) connected motif ($[\text{Cu}^{\text{II}}]_4$) via edge sharing of two Cu_3O cores and bridging by six acetato function of BTC^{3-} connector. The hybrid material, Cu-MOF exhibits very high specific capacitance, 547 F g^{-1} at the scan rate of 2 mV s^{-1} with excellent recycling stability (retains 97.4% after 5000 cycles). The χ_{MT} value for CuMOF at 300 K is 1.735 $\text{cm}^3 \text{mol}^{-1} \text{K}$ for four copper(II) ions which is as expected for four isolated copper(II) ion with $g = 2.15$. The χ_{MT} values are almost constant until ca. 55 K and then χ_{MT} decrease sharply, giving the minimum value of 0.753 $\text{cm}^3 \text{K mol}^{-1}$ at 2K. These material useful for energy storage application.

Rights and Permissions**Chapter 2:**

Reprinted (adapted) with permission from *Cryst. Growth Des.* **2019**, *19*, 6283-6290.
Copyright © 2020, American Chemical Society.

Chapter 3:

Reprinted (adapted) with permission from *ACS Omega*, **2020**, *5*, 274-280. Copyright ©
2019, American Chemical Society.

Chapter 4:

Reprinted (adapted) with permission from *Cryst. Growth Des.* **2021**, *21*, 5240–5250.
Copyright ©2017, American Chemical Society.

Chapter 5:

Reprinted (adapted) with permission from *J. Mol. Struct.* **2021**, *1245*, 131058. Copyright
©2021 Published by Elsevier B.V.

Chapter 6:

Reprinted (adapted) with permission from *Cryst. Growth Des.* Revision. Copyright ©2021,
American Chemical Society.

Srikanta Jana

Research Publications

- (1) **Srikanta Jana**, Samik Saha, Angeera Chandra, Mohamed Salah El Fallah, Sachindranath Das, Chittaranjan Sinha, Supercapacitance Efficiency of Tetranuclear Cu-MOF and its Magnetism. **Crystal Growth & Design** (Revision).
- (2) **Srikanta Jana**, Joydeep Datta, Suvendu Maity, Baishali Thakurta, Partha Pratim Ray, and Chittaranjan Sinha. Tetrameric and Polymeric Zn(II) Coordination Complexes of 4-Diallylaminobenzoic Acid and Their Applications in the Electroreduction of CO₂ and Schottky Diode Behavior. **Crystal Growth & Design**, 2021, 21, 9, 5240–5250.
- (3) **Srikanta Jana**, Rajkumar Jana, Sayantan Sil, Basudeb Dutta, Hiroki Sato, Partha Ray, Ayan Datta, Takashiro Akitsu, Chittaranjan Sinha. "Influence of Axial Linkers on Polymerization in Paddle Wheel Cu(II) Coordination Polymers for the Application of Optoelectronics Devices" **Crystal Growth & Design**, 2019, 19, 11, 6283-6290.
- (4) **Srikanta Jana**, Apurba Ray, Angeera Chandra, M. Salah El Fallah, Sachindranath Das, Chittaranjan Sinha. "Studies on Magnetic and Dielectric Properties of Antiferromagnetically Coupled Dinuclear Cu(II) in a One-Dimensional Cu(II) Coordination Polymer" **ACS Omega**, 2020, 5, 1, 274-280.
- (5) **Srikanta Jana**, Suhana Karim, Sukanya Paul, Ennio Zangrando, M. Salah El Fallah, Debasis Das, Chittaranjan Sinha. "Antiferromagnetically coupled Cu(II) coordination polymer for the heterogeneous and efficient reduction of nitrophenols". **Journal of molecular structure**. 2021, 1245, 131058.
- (6) Kritish Roy, **Srikanta Jana**, Zinnia Mallick, Sujoy Ghosh, Basudeb Dutta, Subrata Sarkar, Chittaranjan Sinha, Dipankar Mandal. "2D MOF Modulated Fiber Nanogenerator for Effective Acoustoelectric Conversion and Human Motion Detection". **Langmuir**, 2021, 37, 7107–7117.
- (7) Kritish Roy, **Srikanta Jana**, Sujoy Kumar Ghosh, Biswajit Mahanty, Subrata Sarkara, Chittaranjan Sinha, Dipankar Mandal. "3D MOF Assisted Self-polarized Electret: An Effective Self-powered Remote Healthcare Monitoring Approach" **Langmuir** 2020, 36, 39, 11477–11489.
- (8) Angeera Chandra, Dhananjay Das, Joaquín-Ortega Castro, Kaushik Naskar, **Srikanta Jana**, Antonio Frontera, Partha Pratim Ray, Chittaranjan Sinha. "Cd(II) Coordination

Polymer of Fumeric Acid and Pyridyl-hydrazide Schiff base : Structure, Photoconductivity and Theoretical Interpretation”. **Inorganica Chimica Acta**, 518 (2021) 120253.

(9) Angeera Chandra, Mrinmay Das, Kunal Pal, **Srikanta Jana**, Basudeb Dutta, Partha Ray, Kuladip Jana, Chittaranjan Sinha. "3D-Coordination Polymer of Zn(II)-carboxylate : Structural Elucidation, Photo-electrical Conductivity and Biological Activity" **ACS Omega** 2019, 4, 18, 17649-1766.

(10) Basudeb Dutta, Dhananjay Das, Joydeep Datta, Angeera Chandra, **Srikanta Jana**, Chittaranjan Sinha, Partha Pratim Ray, Mohammad Hedayetullah Mir. “Synthesis of a Zn (ii)-based 1D zigzag coordination polymer for the fabrication of optoelectronic devices with remarkably high photosensitivity” **Inorganic Chemistry Frontiers**, 2019, 6, 1245-1252.

(11) Basudeb Dutta, Saied Md Pratik, **Srikanta Jana**, Chittaranjan Sinha, Ayan Datta, and Mohammad Hedayetullah Mir “Novel Br···p(Chelate) Interaction in a 1D Coordination Polymer Revealing Aromaticity” **ChemistrySelect** 2018, 3, 4289 – 4291.

(12) Basudeb Dutta, Sourav Ranjan Ghosh, Apurba Ray, **Srikanta Jana**, Chittaranjan Sinha, Sachindranath Das, Atish Dipankar Jana, Mohammad Hedayetullah Mir. Stabilization of cyclic water tetramers and dimers in the crystal host of 2D coordination networks: electrical conductivity and dielectric studies. *New J. Chem.*, 2020, 44, 15857-15870.

(13) Kaushik Naskar, Suwendu Maity, **Srikanta Jana**, Basudeb Dutta, Shinnosuke Tanaka, Debashis Mallick, Takashiro Akitsu and Chittaranjan Sinha “Arylazoimidazole Coordinated and Naphthalene-Dicarboxylato Bridged Polymers of Co(II) and Photochromic Zn(II) Complexes” **Cryst. Growth Des.** 2018, 18, 2986–2997.

(14) Apurba Ray, Atanu Roy, Swarupananda Bhattacharjee , **Srikanta Jana** ,Chandan Kumar Ghosh , Chittaranjan Sinha , Sachindranath Das , “Correlation between the dielectric and electrochemical properties of TiO₂-V₂O₅ nanocomposite for energy storage application” **Electrochimica Acta** 2018,266, 404 – 413.

(15) Debashis Mallick, Bharati Chowdhury , Chandana Sen , Kamal Krishna Sarkar , **Srikanta Jana** , Sudipa Mondal , Chittaranjan Sinha “Arylazoimidazole complexes of lead(II)-halide and their photochromism” **Indian Journal of Chemistry**. 2018,57, 418 – 426.

(16) Debashis Mallick , Uttam Panda, **Srikanta Jana**, Chandana Sen, Tapan Kumar Mondal, Chittaranjan Sinha “Lead(II) complexes of 1-alkyl-2-(arylo)imidazole: Synthesis, structure, photochromism and metallomesogenic properties” **Polyhedron** 2016,117, 318–326.

(17) Uttam Panda, **Srikanta Jana**, Bikas Kumar Sarkar, Chittaranjan Sinha, Debashis Mallick.“Effect of micelle environment on the photochromism of 1-alkyl-2-{(o-thioalkyl) phenylazo}imidazole” JOURNAL OF THE INDIAN CHEMICAL SOCIETY 2016, 93, 613-620.

Conference Attended

1. Participation: International seminar on recent advances in molecules & materials (RAM-2018). H. I. T Haldia.

2. Participation: National seminar on current developments in chemical sciences (CDCS-2018). Jadavpur University, Kolkata.

3. Participation: National seminar on chemical sciences: today and tomorrow (CSTT-2019). Jadavpur University, Kolkata.

4. Participation: National seminar on celebration of the international year of the periodic table (CIYPT-2019). Jadavpur University, Kolkata.

Awards and Recognitions

1. CSIR Research Fellow (NET, JRF), CSIR EMR-I, Govt. of India.

Srikanta Jana

Chapter 1

INTRODUCTION

Importance and problems of Coordination Polymers (CPs)/Metal Organic Frameworks (MOFs) are reviewed with reference to focus of present research.

Chapter 2

**Influence of Axial Linkers on Polymerization in Paddle
Wheel Cu(II) Coordination Polymers for the Application
of Optoelectronics Devices**

Chapter 3

**Studies on Magnetic and Dielectric Properties of
Antiferromagnetically Coupled Dinuclear Cu(II) in one
Dimensional Cu(II) Coordination Polymer (CP)**

Chapter 4

**Tetrameric and Polymeric Zn(II) Coordination
Complexes of 4-Diallylaminobenzoic Acid and their
Applications in the Electroreduction of CO₂ and Schottky
Diode Behavior**

Chapter 5

**Carboxylato bridging Cu(II) coordination polymer :
Structure, magnetism and catalytic reduction of
nitrophenols**

Chapter 6

**A Cu(II)-Metal Organic Framework with tetranuclear
core : Structure, Magnetism and Supercapacitor Activity**

Chapter 7

Summary of Research Work